

New Ideas for Effective Higgs Measurements

Dissertation

Johann Brehmer

Dissertation

submitted to the

Combined Faculties for the Natural Sciences and for Mathematics
of the Ruperto-Carola University of Heidelberg, Germany

for the degree of

Doctor of Natural Sciences

Put forward by

Johann Brehmer

born in Bremen, Germany

Referees:

Prof. Dr. Tilman Plehn

Prof. Dr. Björn Malte Schäfer

Oral examination:

July 26, 2017

Corrected version from July 19, 2017

New Ideas for Effective Higgs Measurements

Abstract in deutscher Übersetzung

Mit einer effektiven Feldtheorie können die Signaturen neuer Physik im Higgs-Sektor ohne starke Theorieannahmen parametrisiert werden. In dieser Arbeit untersuchen wir zwei Aspekte dieses Ansatzes, die für Messungen der Eigenschaften des Higgs-Bosons während Run 2 des LHC relevant sind.

Aufgrund der beschränkten Präzision dieser Messungen kann neue Physik im Higgs-Sektor nur dann entdeckt werden, wenn deren typische Energieskala nah am experimentellen Impulsübertrag liegt. Die Näherungen der effektiven Theorie sind daher möglicherweise ungültig. Im ersten Teil dieser Arbeit vergleichen wir die Signaturen mehrerer Modelle von Physik jenseits des Standardmodells mit den entsprechenden Beschreibungen in der effektiven Theorie, untersuchen die Nützlichkeit des effektiven Modells und zeigen, wie dessen Gültigkeitsbereich vergrößert werden kann.

Im zweiten Teil verwenden wir Methoden aus der Informationsgeometrie, um Messungen von Higgs-Eigenschaften zu optimieren. Unser Ansatz basiert auf der Fisher-Information, die die maximale Präzision angibt, mit der Parameter in einem Experiment gemessen werden können. Wir entwickeln Methoden zur Berechnung der Fisher-Information in der Teilchenphysik und wenden sie auf verschiedenen Higgs-Prozesse an. Dabei zeigen wir, wie mit Informationsgeometrie Selektionsschnitte optimiert, die wichtigsten kinematischen Observablen definiert und das Potential von modernen multivariaten Methoden mit dem von Histogramm-basierten Analysen verglichen werden kann.

Abstract

An effective field theory provides a model-independent and phenomenologically powerful parametrisation of new physics in the Higgs sector. We analyse two aspects of this framework that are relevant for measurements of the Higgs properties during Run 2 of the LHC.

First, the limited precision of the LHC analyses cannot guarantee a clear hierarchy between the experimental momentum transfer and the probed new physics scales, casting doubt on the validity of the effective model. By comparing a range of new physics scenarios to their dimension-six approximation, we analyse if an effective description of the Higgs sector is useful, where it breaks down, and how its validity can be improved.

Second, we use information geometry to understand and optimise Higgs measurements at the LHC. Our novel approach is based on the Fisher information, which encodes the maximum precision with which theory parameters can be measured in an experiment. We develop an algorithm to calculate the Fisher information in LHC processes and compute the information on dimension-six operators in different Higgs signatures. We demonstrate how information geometry lets us improve event selections, determine the most powerful observables, and compare the power of modern multivariate techniques to that of traditional histogram-based analyses.

Contents

Preface	xi
1 Introduction	1
2 An effective theory for Higgs physics	5
2.1 The Higgs boson at the LHC	5
2.1.1 The Standard Model Higgs sector	5
2.1.2 Production and decay	6
2.1.3 To new physics through Higgs measurements	9
2.2 The effective field theory idea	12
2.2.1 Different physics at different scales	13
2.2.2 EFT construction and the bottom-up approach	15
2.2.3 Top-down approach and matching	20
2.3 Dimension-six operators for Higgs physics	24
2.3.1 Motivation	24
2.3.2 Operators	25
2.3.3 Phenomenology	30
2.3.4 Alternative frameworks	34
3 Higgs effective theory at its limits	43
3.1 Introduction	43
3.2 Matching intricacies	46
3.2.1 Ambiguities	46
3.2.2 Default vs. v -improved matching	48
3.2.3 Making sense of v -improvement	48
3.3 Full models vs. effective theory	50
3.3.1 Setup	51
3.3.2 Singlet extension	53

3.3.3	Two-Higgs-doublet model	60
3.3.4	Scalar top partners	68
3.3.5	Vector triplet	73
3.4	Practical questions	81
3.4.1	Weak boson fusion observables	82
3.4.2	To square or not to square	85
3.4.3	Limit setting	87
3.5	Conclusions	88
4	Better Higgs measurements through information geometry	93
4.1	Introduction	93
4.2	Essential statistics	96
4.2.1	Fisher information and Cramér-Rao bound	96
4.2.2	Information geometry	99
4.3	Tools for the LHC	100
4.3.1	Information in total rates	100
4.3.2	Information in distributions	100
4.3.3	Information in full kinematics	101
4.3.4	Distribution of differential information	102
4.3.5	Nuisance parameters and profiled information matrix	103
4.3.6	Geometry of effective field theories	105
4.3.7	The MadFisher algorithm	106
4.4	Higgs measurements	109
4.4.1	Weak-boson-fusion Higgs to taus	110
4.4.2	Weak-boson-fusion Higgs to four leptons	124
4.4.3	Higgs plus single top	131
4.5	Extensions	140
4.5.1	Systematic uncertainties	140
4.5.2	Comparison with other tools	141
4.6	Conclusions	145
5	Conclusions	147
Acknowledgements		151
Appendices		153
A.1	Standard model conventions	153
A.2	Phenomenology glossary	157

A.3	EFT fundamentals	158
A.3.1	Nonlinear field redefinitions	158
A.3.2	Functional matching	159
A.4	SILH basis	163
A.5	Model fine print	164
A.5.1	Singlet extension	164
A.5.2	Two-Higgs-doublet model	165
A.5.3	Scalar top partners	167
A.5.4	Vector triplet	168
A.6	Information geometry	172
A.6.1	Cramér-Rao bound	172
A.6.2	A simple example	173
A.6.3	Detector response	175

References

177

Preface

This thesis is based on research conducted between 2014 and 2017 at the Institute for Theoretical Physics at Heidelberg University. Chapter 3 is based on two articles, parts of which were incorporated into a CERN report:

- [1] J. Brehmer, A. Freitas, D. López-Val, and T. Plehn:
Pushing Higgs effective theory to its limits.
Phys. Rev. D93 (7), p. 075014, 2016. arXiv:1510.03443.
- [2] A. Biekötter, J. Brehmer, and T. Plehn:
Extending the limits of Higgs effective theory.
Phys. Rev. D94 (5), p. 055032, 2016. arXiv:1602.05202.
- [3] D. de Florian, C. Grojean, F. Maltoni, et al.:
Handbook of LHC Higgs cross sections: 4. Deciphering the nature of the Higgs sector.
LHC Higgs Cross Section Working Group Yellow Report. arXiv:1610.07922.

Chapter 4 is based on the following publication:

- [4] J. Brehmer, K. Cranmer, F. Kling, and T. Plehn:
Better Higgs boson measurements through information geometry.
Phys. Rev. D95 (7), p. 073002, 2017. arXiv:1612.05261.

Chapter 2 consists of introductory material that can be found in textbooks and review articles, and is partly based on a short lecture I gave to fellow PhD students:

- [5] J. Brehmer:
Higgs effective field theory.
Student lecture, research training group ‘Particle Physics Beyond the Standard Model’.

Finally, some of the work done during my PhD is not included in this thesis:

- [6] J. Brehmer, J. Hewett, J. Kopp, T. Rizzo, and J. Tattersall:
Symmetry restored in dibosons at the LHC?
JHEP 1510, p. 182, 2015. arXiv:1507.00013.
- [7, 8] G. Brooijmans, C. Delaunay, A. Delgado, et al.:
Les Houches 2015: Physics at TeV colliders — New Physics Working Group report.
arXiv:1605.02684.
Part of these proceedings were published separately as
J. Brehmer, G. Brooijmans, G. Cacciapaglia, et al.:
The diboson excess: Experimental situation and classification of explanations; a Les Houches pre-proceeding.
arXiv:1512.04357.

Chapter 1

Introduction

THE HIGGS BOSON [9–13] is the cornerstone of the Standard Model of particle physics (SM) [14–16]. Its experimental discovery in 2012 [17, 18] is a triumph for a decades-old model, but it also defines a way forward: the Higgs provides us with an unprecedented chance to understand some of the biggest unsolved mysteries of physics.

As the only known fundamental scalar, it suffers from the famous electroweak hierarchy problem: why is its mass scale (and therefore the electroweak scale) so much smaller than the Planck scale, while there is no sign of a symmetry protecting it against quantum corrections? In addition, the Higgs sector is intimately tied to the stability of the electroweak vacuum and to the unexplained large hierarchy between the fermion masses. It might also be related to the open questions of the baryon asymmetry, of the nature of dark matter, and of inflation.

Many models of physics beyond the Standard Model have been proposed to explain at least some of these aspects. Often they predict Higgs coupling patterns different from the SM. A precise measurement of the Higgs properties thus provides a crucial probe of such models, and might be one of the most important goals for present and future runs of the Large Hadron Collider (LHC).

This prospect poses two immediate phenomenological questions:

1. Which framework should be used to parametrise the Higgs properties?
2. How can these parameters be measured efficiently at the LHC?

The research presented in this thesis consists of two major parts, each driven by one of these questions.

All Higgs measurements should ideally use the same universal language to parametrise their results, allowing for their efficient comparison, combination, and interpretation. Such a framework should be general enough to describe the effects of many interesting new physics (NP)

scenarios without strong model assumptions. On the other hand, practical considerations such as computational resources limit the number of parameters.

A simple example for such a universal parametrisation that was widely used during Run 1 of the LHC is the κ framework. It is based on the SM Lagrangian, but promotes all Higgs couplings to free parameters. The main limitation of this approach is that it can only describe structures that are already present in the SM. While a measurement based on the κ framework can be useful for total rates, it is not able to utilise information in kinematic distributions.

Instead, we parametrise new physics signatures with an effective field theory (EFT) [19–21]. Based only on the assumption that new physics has a typical energy scale significantly larger than the experimental energies, all new physics effects are captured by a tower of higher-dimensional operators. The leading effects for Higgs physics should come from a handful of operators with mass dimension six [22–24]. These operators describe both coupling rescalings as well as novel kinematic structures not present in the SM, allowing us to access information in distributions in addition to total rates [25, 26]. Effective operators also let us combine Higgs measurements with constraints from other processes, including electroweak precision data or gauge boson production at the LHC [27].

However, due to their limited precision LHC Higgs measurements are only sensitive to signatures from models that are either strongly coupled or relatively light. In the latter case, the characteristic energy scale of new physics is not clearly separated from the momentum transfer in the experiments, casting doubt on the validity of the EFT approach.

We analyse the usefulness of higher-dimensional operators at the LHC by comparing the predictions of specific scenarios of new physics to their dimension-six approximations [1]. Our analysis covers additional scalar singlets, a two-Higgs-doublet model, scalar top partners, and heavy vector bosons, focusing on parameter ranges that the LHC will be sensitive to. We take into account rates and distributions in the most important Higgs production modes and representative decay channels as well as in Higgs pair production. For this array of models, benchmark points, and observables, we ask if and where the effective description of new physics breaks down, and how it can be improved.

As it turns out, the performance of the effective model strongly depends on the matching procedure that links the coefficients of the dimension-six operators to the full theory. We analyse how electroweak symmetry breaking affects the validity of the effective theory, and discuss how the standard matching procedure can be adapted to situations where these effects are large. In addition, we discuss whether squared amplitudes from dimension-six operators should be included in calculations, and which observables provide the best probes of the momentum transfer in Higgs production in weak boson fusion [2].

Having chosen a parametrisation of the Higgs properties, the second part of this thesis focuses on the question of how its parameters can be measured optimally. Higgs processes are sensitive to many effective operators. Each of them affects different couplings, typically introducing non-

trivial kinematic structures. This leads to a complicated relation between the high-dimensional model parameter space and the often also high-dimensional phase space.

Conventional analyses based on selection cuts and histograms of kinematic observables are in many cases not sensitive to such subtle signatures. At the other end of the spectrum, experiments resort more and more to high-level statistical tools, including machine learning techniques [28–49] or matrix-element-based methods [50–65]. While these multivariate techniques are powerful, it is often not transparent which physical properties they probe. It is therefore increasingly important to be able to characterise the information contained in LHC signatures.

We use information geometry [66–68] to understand and optimise the measurement of Higgs properties at the LHC [4]. The central building block of our approach is the Fisher information matrix, which according to the Cramér-Rao bound [69, 70] encodes the maximal knowledge on theory parameters we can derive from an experiment. We show that the properties of the Fisher information make it especially well-suited to continuous, high-dimensional parameter spaces, and in particular to effective field theories.

We develop an algorithm to calculate the Fisher information in particle physics processes based on Monte-Carlo methods. It allows us to calculate the maximum precision with which continuous parameters can be measured in a process. We also analyse how the differential information is distributed over phase space and how much information is carried by individual kinematic distributions. This defines the most powerful phase-space regions and observables for an analysis. It also allows us to compare how much we can learn from a simple fit to histograms compared to fully multivariate methods.

These new instruments are applied to Higgs measurements in three different channels. We calculate the information on dimension-six operators in Higgs production in weak boson fusion with decays into tau pairs and four leptons, and in Higgs production in association with a single top quark. Finally, we show how our approach can be extended to include systematic and theory uncertainties, and compare it to the likelihood ratio.

This thesis begins with a synopsis of essential aspects of Higgs physics and effective field theories in Chapter 2. In Chapter 3, we discuss the validity of the effective field theory for LHC Higgs measurements and the matching between full models and effective operators. Chapter 4 presents our work on information geometry and efficient measurements of Higgs properties. Both these chapters contain separate, detailed introductions and conclusions. We summarise our results in Chapter 5. In a set of appendices we list our conventions, explain technical details, and provide additional examples.

Chapter 2

An effective theory for Higgs physics

IN THIS CHAPTER we review some of the essential concepts that underlie the research presented in this thesis. First, we briefly summarise the role of the Higgs boson in the Standard Model (SM) and its phenomenology at the LHC. Section 2.2 then presents a pedagogical introduction to effective field theories (EFTs). In Section 2.3 we combine these ideas and construct an effective field theory for the Higgs sector.

Our introduction to Higgs physics is superficial, and the EFT part eschews mathematical rigour in favour of a broad picture of the central ideas. For a more thorough introduction to Higgs physics, see for instance Reference [71]. For an extensive introduction to EFTs, see References [72, 73]. Note that Section 2.2 is largely identical to Reference [5]. Some of the examples are taken from References [72, 73].

2.1 The Higgs boson at the LHC

2.1.1 The Standard Model Higgs sector

In the Standard Model, the Higgs boson is part of a scalar $SU(2)_L$ doublet ϕ . The relevant terms in the Lagrangian are

$$\begin{aligned} \mathcal{L}_{\text{SM}} \supset & (D_\mu \phi)^\dagger (D^\mu \phi) - \mu^2 \phi^\dagger \phi - \lambda (\phi^\dagger \phi)^2 \\ & - \sum_{\text{generations}} \left(y_u \begin{pmatrix} \bar{u} \\ \bar{d} \end{pmatrix}_L \tilde{\phi} u_R + y_d \begin{pmatrix} \bar{u} \\ \bar{d} \end{pmatrix}_L \phi d_R + y_\ell \begin{pmatrix} \bar{\nu} \\ \bar{\ell}^- \end{pmatrix}_L \phi \ell_R + \text{h. c.} \right). \end{aligned} \quad (2.1)$$

Here u , d , and ℓ are the up-type quarks, down-type quarks, and leptons of the three generations, all appearing in a left-handed and right-handed version marked by the subscripts L and R . The Higgs potential is defined by the real parameters μ^2 and λ , while the Yukawa couplings y_i are

complex-valued matrices in flavour space. The covariant derivatives are defined as

$$D_\mu \phi = \left(\partial_\mu - i g \frac{\sigma^a}{2} W_\mu^a - i \frac{g'}{2} B_\mu \right) \phi \quad (2.2)$$

with $SU(2)_L$ gauge bosons W_μ^a and $U(1)_Y$ gauge boson B_μ . The corresponding coupling constants are g and g' , and σ_i denote the Pauli matrices. Finally,

$$\tilde{\phi} \equiv i\sigma_2 \phi^*. \quad (2.3)$$

The Lagrangian in Equation (2.1) shows the SM in the unbroken phase of the electroweak symmetry. For a detailed account including all definitions and conventions, see Appendix A.1.

For $\mu^2 < 0$, the Higgs doublet develops a non-zero vacuum expectation value (VEV)

$$v^2 \equiv 2 |\langle \phi \rangle|^2 = -\frac{\mu^2}{\lambda}, \quad (2.4)$$

spontaneously breaking the electroweak symmetry. Using some of the gauge freedom, we can rotate the scalar doublet such that

$$\phi = \frac{1}{\sqrt{2}} \begin{pmatrix} -w^2 - iw^1 \\ v + h + iw^3 \end{pmatrix}. \quad (2.5)$$

Here w^a are the would-be Goldstone bosons resulting from the spontaneous breaking of the electroweak symmetry. They combine with the gauge bosons W^a and B to the mass eigenstates γ , W^\pm , and Z . The remaining degree of freedom, the scalar field h , is the physical Higgs boson. Plugging Equation (2.5) into Equation (2.1), we find its mass

$$m_h^2 = -2\mu^2 = 2\lambda v^2. \quad (2.6)$$

In this broken phase of the electroweak symmetry, the fermions and the vector bosons W^\pm and Z also acquire mass terms proportional to v , as well as couplings to the Higgs boson h . Since both terms stem from the same coupling to $\phi \sim v + h$, the Higgs couplings to other particles x are always proportional to $g_{hx} \sim m_x/v$. Finally, there are h^3 and h^4 self-couplings.

The SM Higgs sector is very predictive. Weak interactions fix the VEV to $v = 246$ GeV. With the measurement of the Higgs mass $m_h = 125$ GeV [17, 18, 74], there are no free parameters in the SM left and all couplings are fixed.

2.1.2 Production and decay

At the LHC, most Higgs bosons are produced in **gluon fusion** (ggF) as shown in the left panel of Figure 2.1. Due to its large Yukawa coupling, the top plays the dominant role in the loop, with small contributions from the bottom. The total cross section for this process in proton-proton

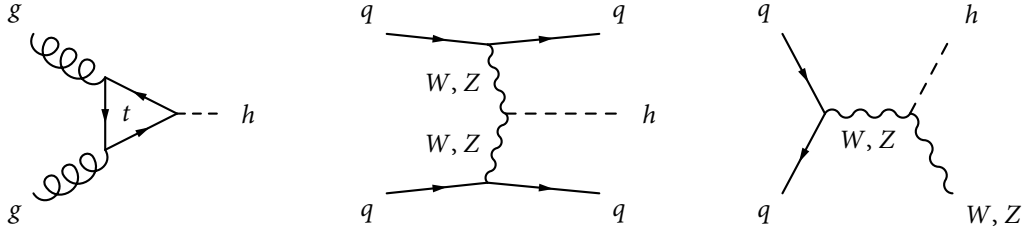


Figure 2.1: Feynman diagrams for the most important Higgs production modes considered in this thesis. Left: gluon fusion. Middle: weak boson fusion. Right: Higgs-strahlung.

collisions at $\sqrt{s} = 13$ TeV is approximately 49 pb [3], a large part of which comes from loop corrections at next-to-leading order (NLO) or next-to-next-to-leading order (NNLO) in α_s . This sizeable rate comes at the price of a lack of discerning kinematic features that could help to separate the Higgs signal from QCD backgrounds.

This is certainly different for Higgs production in **weak boson fusion** (WBF)¹, as shown in the middle panel of Figure 2.1. The production rate for this quark-initiated process is only 3.8 pb [3], but the Higgs is accompanied by two highly energetic jets that point nearly back-to-back into the two forward regions of the detector. This translates to a large invariant mass m_{jj} between them as well as a large separation in pseudorapidity² $\Delta\eta_{jj}$. A second important property is provided by the colour structure of the process: at leading order, there is no colour exchange between the two quark lines, which leads to little QCD radiation in this process [71]. Both of these features set the WBF process apart from QCD backgrounds, which typically have many central jets. Such backgrounds can therefore be reduced significantly by requiring two so-called ‘tagging jets’ with large $\Delta\eta_{jj}$ and large m_{jj} , and vetoing any additional central jets [75–81].

But the tagging jets are not only useful to discriminate Higgs production from non-Higgs backgrounds. Since they recoil against the intermediate vector bosons that couple to the Higgs, they provide access to the momentum flow through the Higgs production vertex. Their properties, in particular their transverse momenta and the angular correlations between them, thus provide probes of the Higgs-gauge coupling [82–89]. We revisit this important feature from different perspectives in this thesis.

The right panel of Figure 2.1 shows Higgs production in association with a vector boson, or **Higgs-strahlung**. The rate is 1.4 pb for a Wh final state plus 0.9 pb for Zh . Similarly to the tagging jets in WBF, the final-state gauge boson both helps to discriminate the Higgs signal from backgrounds and provides a handle on the momentum flow through the virtual intermediate

¹This channel is also known as Vector Boson Fusion or VBF. But this is slightly misleading since the gluon also has spin 1.

²See Appendix A.2 for a glossary of phenomenology lingo, in particular for definitions of common kinematic quantities and of typical units.

vector boson.

Higgs production in association with a $t\bar{t}$ pair is another production mode relevant for the LHC, but we do not discuss it in this thesis. Instead, we briefly analyse **Higgs production with a single top quark**. This process exists as an s -channel and a t -channel version with very different kinematic features. It can be calculated either in the four-flavour scheme (with a gluon in the partonic initial state) or in the five-flavour scheme (with a b quark in the partonic initial state, described by a bottom parton density function). We focus on the dominant t -channel process and calculate it in the five-flavour scheme, as shown in Figure 2.2. Diagrams where the Higgs is radiated off a top quark interfere destructively with amplitudes in which the Higgs couples to a W . The SM rate is small at 74 fb [3], but this interference pattern makes it very sensitive to modified Higgs couplings. In fact, this process is the only direct probe of the sign or complex phase of the top Yukawa coupling [90] ($t\bar{t}h$ production is only sensitive to the absolute value of the top Yukawa, while the total rate in gluon fusion can be influenced by many effects such as new particles in the loop).

Our final channel is **Higgs pair production**, shown in Figure 2.3, which allows us to directly measure the cubic Higgs self-coupling [91, 92]. It provides another example of destructive interference between different amplitudes: diagrams in which the two Higgs bosons couple to a top box loop interfere with those in which a single Higgs is produced in gluon fusion and then splits into two Higgs bosons through the self-coupling. Close to threshold, these two contributions approximately cancel in the SM [91, 93], and the total rate is very small at 33 fb. But modified Higgs sectors can spoil this cancellation and drastically increase the rate, as we demonstrate in the next chapter.

The Higgs boson interacts with all massive particles of the SM, leading to a wide variety of decay modes. Since it couples to all particles proportional to their mass, it prefers to decay into the heaviest particles allowed by phase space. The dominant decay mode with a branching ratio of 58% [3] is therefore $h \rightarrow b\bar{b}$. This signature is clearly useless for Higgs bosons produced in gluon fusion because of the overwhelming QCD $gg \rightarrow b\bar{b}$ background. WBF and Vh production provide handles to tame these backgrounds, but the final state is still challenging. A decay

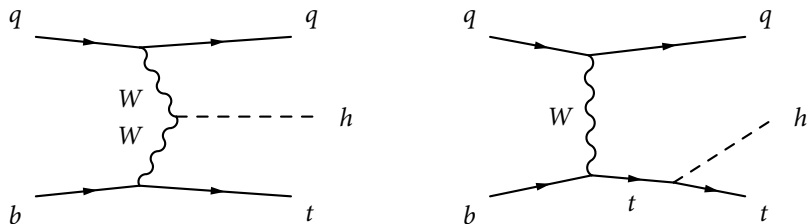


Figure 2.2: Feynman diagrams for Higgs production with a single top quark.

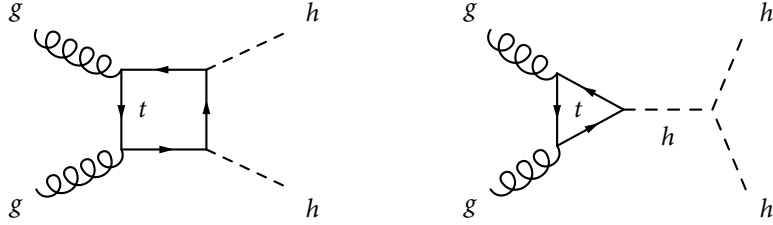


Figure 2.3: Feynman diagrams for Higgs pair production.

mode that is easier to detect is $h \rightarrow \tau^+ \tau^-$ with a branching ratio of 6.3%. The semi-leptonic and purely leptonic decays of tau pairs involve neutrinos. But when the taus are boosted and not exactly back-to-back, their momenta can be reconstructed for instance using a collinear approximation [71].

The decays through $W^+ W^-$ or ZZ pairs into four-lepton final states are particularly important due to their clean signatures and because they provide access to the Higgs-gauge couplings. Since the Higgs mass is below the $W^+ W^-$ and ZZ thresholds, one of the vectors has to be off-shell.³ The channel $h \rightarrow W^+ W^- \rightarrow (\ell^+ \nu)(\ell^- \bar{\nu})$ with $\ell = e, \mu$ has a respectable branching fraction of 1.1% [3], but comes with two neutrinos in the final state. Still, it is one of the most important modes for WBF Higgs production. The decay $h \rightarrow ZZ \rightarrow 4\ell$ with $\ell = e, \mu$ provides an extremely clean signal. Despite its small branching ratio of $1.3 \cdot 10^{-4}$, it was one of the most important channels for the discovery of the Higgs boson [17, 74]. From a post-discovery perspective, its four leptons provide a rich spectrum of angular correlations and other observables that allow us to measure the Higgs behaviour in detail. We discuss this feature in more detail in Chapter 4.

Finally, the small couplings of the Higgs to light fermions mean that the loop-induced decay into photon pairs can compete with the tree-level decay channels. The dominant contribution to the $h \rightarrow \gamma\gamma$ amplitude comes from a W loop, which interferes destructively with a top loop, resulting in a branching ratio of 0.23% [3]. This large signal on top of a smooth background made the di-photon mode the second crucial channel for the experimental discovery [17, 74].

2.1.3 To new physics through Higgs measurements

There are several facets that set the Higgs boson apart from the other SM particles. From an experimental point of view, the properties of this shiny new thing in particle physics are still relatively unknown. Its couplings to vector bosons and heavy fermions are constrained at the $\mathcal{O}(10\%)$ level, while for the couplings to light fermions, invisible decays, and the total decay width of the Higgs there are only weak upper bounds [26, 74]. Many of these limits also rely on

³This also means that the branching ratios for $h \rightarrow ZZ$ and $h \rightarrow WW$ are not well-defined. What is often quoted is in fact a term like $\text{BR}(h \rightarrow 4\ell)/(\text{BR}(Z \rightarrow \ell^+ \ell^-))^2$.

specific model assumptions. The top Yukawa coupling, for instance, can be tightly constrained from the total Higgs production rate under the assumption that no new physics plays a role in the gluon-fusion loop. Allowing for such new physics effects in a fit significantly relaxes the bounds on y_t , and information from $t\bar{t}h$ production and the $h \rightarrow \gamma\gamma$ decay is needed to break this degeneracy [26]. Similarly, the total Higgs width can be constrained indirectly from the contribution of $gg \rightarrow h \rightarrow ZZ \rightarrow 4\ell$ in the off-shell Higgs region, again relying on strong model assumptions. All in all, the Higgs is still the least well measured elementary particle (in some sense with the exception of neutrinos), leaving plenty of room for physics beyond the Standard Model.

From a theory perspective, there are several reasons to expect manifestations of new physics (NP) in the Higgs sector. On rather general grounds, the Higgs doublet is the key component of electroweak symmetry breaking (EWSB), the centrepiece of the SM. A test of the Higgs properties therefore provides a test of the fundamental structure of Nature.

The Higgs boson is the only fundamental scalar discovered so far. This is interesting in its own right, but also leads to the famous electroweak **hierarchy problem**: in the absence of any protective symmetry, the mass of a scalar field should receive quantum corrections of the order of the largest scale in the theory. If the SM is valid all the way up to the Planck scale, severe fine-tuning between the bare parameter and these quantum corrections is necessary to keep the electroweak mass scale at the observed value. Note that this argument interchangeably applies to the mass parameter of the Higgs doublet μ^2 , the physical Higgs mass m_h , or the electroweak VEV v . Since the strength of the weak force is suppressed by powers of $m_W \sim v$, and the gravitational force by the Planck scale, the hierarchy problem is often phrased in terms of the surprising weakness of gravity compared to the weak force. This naturalness problem is of a purely aesthetic nature, but similar aesthetic problems have in the past led to new insights. For instance, the surprising smallness of the electron mass compared to its large self-energy in classical electrodynamics pointed to ‘new physics’ close to 511 keV, and was finally resolved with the introduction of positrons in quantum electrodynamics [94]. Many models have been proposed to solve the electroweak hierarchy problem by introducing a new symmetry that protects the Higgs mass against quantum corrections.^{4,5} Famous examples are

⁴An entirely different and somewhat metaphysical argument is based on the (weak) anthropic principle that observations of the universe are conditional upon its laws of physics allowing conscious life [95, 96]. First, this explanation requires some mechanism that generates many different vacua with different values of the physics parameters, including the Higgs mass. Most of these vacua have ‘natural’ parameters in which the weak and gravitational scales are comparable. String theory is hypothesised to provide such a sampling mechanism (the ‘multiverse’). Second, there has to be a reason why larger (and thus more abundant) values of the weak scale would not allow any type of intelligent life to form and make observations. This question is difficult to answer, and the jury is still out [97–103]. Given the speculative nature of the two questions, anthropic reasoning is being criticised as unverifiable or as based on arguments from lack of imagination.

⁵The smallness of the Higgs VEV can also be explained with a modified cosmological evolution. Relaxion mod-

supersymmetry [106–108], composite Higgs models in which the Higgs is often the pseudo-Goldstone boson of some broken symmetry [109–113], conformal symmetries [114], or extra dimensions [115–118]. To reduce tuning to an acceptable level, such new physics should reside at energy scales not too far from the electroweak scale. These models usually modify the Higgs sector in a way that translates into Higgs couplings different from their SM values.

Another hierarchy unexplained in the SM is the large difference between the **fermion masses**. There are more than five orders of magnitude between the top and the electron mass, and neutrinos are even lighter. Since the fermion masses are generated by the Yukawa couplings of the Higgs doublet, models that explain the fermion masses often also shift the Higgs-fermion coupling patterns [119].

The question of **vacuum stability** is still being discussed. If, after including quantum corrections, the potential for the Higgs doublet ϕ has another minimum at a different field value than the electroweak VEV $v = 246$ GeV with lower energy, the known vacuum is unstable and can tunnel into this lower-energy state. The renormalisation group (RG) allows us to link the potential at large values of ϕ to the running of the quartic coupling λ to higher energies. Current results [120] indicate that in the SM indeed such a lower vacuum exists. Fortunately for us, the tunnelling probability is very small, and ‘our’ vacuum seems to be metastable with a lifetime longer than the age of the universe. While this means that there is no pressing need for physics below the Planck scale to save the electroweak vacuum from a horrible fate, this result crucially depends on the measured top and Higgs masses, higher-order corrections to the beta functions, and higher-dimensional operators stemming from ultra-violet (UV) physics [121].

In addition to these theoretical and to some degree aesthetic arguments, there is solid experimental evidence for physics beyond the SM that might be linked to the Higgs sector. First, the nature of **dark matter** [122] is still unclear. It is experimentally established that this form of matter is electromagnetically neutral, is stable over cosmological timescales, clumps (i. e. is now non-relativistic), and makes up roughly a fourth of the energy density of the universe. In many models dark matter is in thermal equilibrium with ordinary matter in the early universe. Interestingly, the observed dark matter density is in good agreement with electroweak-scale masses and weak couplings. This ‘WIMP miracle’ is one main reason behind the popularity of weakly interacting massive particles (WIMPs) as dark matter candidates. In this scenario, good candidates for the mediator between dark matter and the SM are the Higgs boson or other (pseudo-)scalars in an extended Higgs sector [123]. Such ‘Higgs portal’ scenarios often predict

els [104] introduce a new scalar field with a vacuum expectation value that changes during the cosmological history. Since it couples to the Higgs, this effectively corresponds to a scan over values of the mass parameter μ^2 . Once this term turns negative and the electroweak symmetry is broken, a feedback mechanism freezes the evolution of the scalar, and the electroweak scale remains at a seemingly unnatural value. Nnaturalness [sic] [105] postulates that there are many different copies of the SM with different values of the electroweak scale, a few of which will naturally have a small Higgs mass. The model is set up such that during reheating most of the energy ends up in the copy with the smallest negative value of μ^2 .

signatures in Higgs physics such as modified couplings or invisible Higgs decays.

Another mystery is the **baryon asymmetry** of the universe. Assuming that the cosmos was initially perfectly balanced between matter and antimatter, the observed excess of matter can be generated dynamically if the three Sakharov conditions are satisfied: there have to be processes with baryon-number violation as well as C and CP violation, which take place out of thermal equilibrium [124]. In the SM, these effects are too small to account for the observed asymmetry [125–128]. Models that accommodate larger effects often affect the Higgs sector. In particular, extended Higgs sectors allow for electroweak symmetry breaking to be a strong first-order phase transition, providing the required out-of-equilibrium dynamics [129–131]. Again, such scenarios predict signatures in Higgs measurements.

Finally, the Higgs could play another role in the cosmological evolution of the universe. The origin of the large-scale structure of the cosmos, the surprising isotropy of the cosmic microwave background (CMB), and the flatness of the Universe are all explained by an epoch of exponential expansion of space in the early universe called **inflation**. This process is often thought to be caused by a scalar field, the inflaton, slowly rolling down a potential of a certain shape. In a particularly economical model, the Higgs boson is the inflaton [132], and no new particles beyond the Standard Model are required. However, large couplings of the Higgs to the Ricci scalar are essential for this scenario of Higgs inflation; the model consequently suffers from unitarity problems and requires a ultraviolet (UV) completion.

The null results of the LHC searches for new particles have led to some disappointment among particle physicists. But through the discovery of the Higgs boson, the LHC might not only have completed the Standard Model, but rather opened the door to the unknown. The Higgs boson is not just another SM particle. Some of the big open questions of fundamental physics are deeply rooted in the Higgs sector, and many other ideas can at least be linked to the Higgs sector under some assumptions. At the same time, the current experimental precision leaves quite some room for signatures of new physics in Higgs observables. A precise determination of the Higgs properties might be one of the most exciting measurements at the LHC and may improve our understanding of Nature significantly. Hopefully, the Higgs boson is not just the last puzzle piece of the Standard Model, but the first sign of what lies beyond.

2.2 The effective field theory idea

This plethora of possible BSM scenarios means that a model-independent description is invaluable for TeV signatures of new physics. We consider such an approach based on the effective field theory (EFT) paradigm. Before discussing the specific realisation for Higgs physics in the next section, we here introduce the EFT idea in general.

2.2.1 Different physics at different scales

Our world behaves very differently depending on which energy and length scales we look at. At extremely high energies (or short distances), Nature might be described by a quantum theory of gravity. At energies of a few hundred GeV, the Standard Model is (disappointingly) in agreement with all measurements. Going to lower energies (or larger distances), we do not have to worry about the Higgs or W bosons anymore: electromagnetic interactions are described by QED, weak interactions by Fermi theory, strong physics by QCD. Below a GeV, quarks and gluons are replaced by pions and nucleons as the relevant degrees of freedom. Then by nuclei, atoms, molecules. At this point most physicists give up and let chemists (and ultimately biologists and sociologists) analyse the emergent systems.

The important point here is that the observables at one scale are not directly sensitive to the physics at significantly different scales. This is nothing new: for molecules to stick together, the details of the Higgs sector are not relevant, just as we can calculate how an apple falls from a tree without knowing about quantum gravity. To do physics at one scale, we do not have to (and often cannot) take into account the physics from all other scales. Instead, we isolate only those features that play a role at the scale of interest.

An effective field theory is a physics model that includes all effects relevant at a given scale, but not those that only play a role at significantly different scales. In particular, EFTs ignore spatial substructures much smaller than the lengths of interest, or effects at much higher energies than the energy scale considered.

We often use examples with one full or underlying theory and one effective theory. For simplicity, we pretend that the full theory describes physics correctly at all scales. The EFT is a simpler model than the full theory and neglects some phenomena (such as heavy particles) at an energy scale Λ . However, it correctly describes the physics as long as the observables probe energy scales

$$E \ll \Lambda, \tag{2.7}$$

within some finite precision. This **scale hierarchy** between the energy of interest and the scale of high-energy physics not included in the EFT is the basic requirement for the EFT idea. A validity range (2.7) is an intrinsic property of effective theories. In this simple scenario we ignore that the full theory will also typically break down at even higher energies, and that at some very small energy the effective model should be replaced with another effective theory designed for those energy scales.

Fermi theory

The textbook example for an EFT in particle physics is Fermi theory, which describes the charged current interactions between quarks (or hadrons), leptons and neutrinos at low energies. The

underlying model here is the SM, in which this weak interaction is mediated by the exchange of virtual W bosons with mass m_W and coupling constant g :

$$\mathcal{M}_{\text{full}} \sim \begin{array}{c} f_1 \\ \diagdown \\ \text{---} \end{array} \begin{array}{c} g \\ \diagup \\ \text{---} \end{array} \begin{array}{c} p \\ \curvearrowright \\ W \\ \curvearrowleft \\ \text{---} \end{array} \begin{array}{c} g \\ \diagdown \\ \text{---} \end{array} \begin{array}{c} f_3 \\ \diagup \\ \text{---} \end{array} \sim \frac{g^2}{p^2 - m_W^2}. \quad (2.8)$$

In Fermi theory, there are no W bosons, just a direct interaction between four fermions with coupling constant $G_F \propto g^2/m_W^2$:

$$\mathcal{M}_{\text{EFT}} \sim \begin{array}{c} f_1 \\ \diagdown \quad \diagup \\ \bullet G_F \\ \diagup \quad \diagdown \\ f_3 \quad f_4 \\ \diagdown \quad \diagup \\ f_2 \end{array} \sim G_F \propto \frac{g^2}{m_W^2}. \quad (2.9)$$

So the EFT turns the W propagator into a contact interaction between the fermions, shrinking the distance bridged by the virtual W to zero. Clearly, the two amplitudes agree as long as the momentum transfer through the vertex is small, $E^2 = p^2 \ll \Lambda^2 = m_W^2$.

One process described by this interaction is muon decay. Its typical energy scale $E \approx m_\mu$ is well separated from $\Lambda = m_W$, and Fermi theory describes the process quite accurately. The relative **EFT error**, i. e. the inaccuracy of a calculation with the EFT rather than with the full model, should be of order $\Delta_{\text{EFT}} = \Gamma_{\text{EFT}}/\Gamma_{\text{full}} \sim E^2/\Lambda^2 \sim m_\mu^2/m_W^2 \approx 10^{-6}$.

In proton collisions at the LHC the same interaction takes place, but at potentially much larger momentum transfer $E \lesssim 13$ TeV. The EFT error increases with E . For $E \gtrsim m_W$, the full model allows on-shell W production, a feature entirely missing in the EFT. Here the two descriptions obviously diverge and Fermi theory is no longer a valid approximation of the weak interaction.

Down and up the theory ladder

In reality there are of course more than two theories, and the notion of underlying and effective model becomes relative. The SM itself is not valid up to arbitrary large energies: it does not explain dark matter, the matter-antimatter asymmetry, or gravity. It is probably also internally inconsistent since at some very large energy the quartic coupling λ and the coupling constant g' hit Landau poles. So the SM is an effective theory with validity range $E \ll \Lambda \leq M_{Pl}$ and has to be replaced by some other description at larger energies. On the other hand, going to energies lower than a few GeV, the relevant physics changes again and we should switch to a new effective theory. In this way, all theories can be thought of as a series of EFTs, where the model valid at one scale is the underlying model for the effective theory at the next lower scale.

If you think you know a theory that describes our world at sufficiently large energies, then in principle there is no need to use effective theories: you can calculate every single observable in

your full model (at least if the full model is perturbative at these energies or other approximations such as lattice calculations are available). This however makes complex calculations necessary even for the simplest low-energy processes. One can save a lot of computational effort and focus on the relevant physics by dividing the phase space into regions with different appropriate effective descriptions. If the underlying theory becomes non-perturbative at small energies, or the number of its degrees of freedom too large, constructing an effective theory becomes a bare necessity.

Starting from a high energy scale where the parameters of the fundamental theory are defined, these parameters are run to lower energies until the physics changes substantially or some degrees of freedom become irrelevant. At this matching scale an effective theory is constructed from the full model, and its coefficients are determined from, or matched to, the underlying model. Then the coefficients of this EFT are run down to the next matching scale, where a new EFT is defined and its parameters are calculated, and so on. This is the **top-down** view of EFTs. For instance, we can start from the SM and construct Fermi theory as a simpler model valid at low energies. While we can certainly use the SM to calculate the muon lifetime, it is not necessary, and a calculation in Fermi theory is quite accurate and shorter.

Yet often we do not know the underlying theory. As mentioned above, there has to be physics beyond the SM, and there is still hope it will appear around a few TeV. If we want to parametrise the effects of such new physics on electroweak-scale observables, as we do in this thesis, we do not know what the full model looks like. But even without knowing the underlying model, we can still construct an effective field theory based on a few general assumptions. We go through these ingredients in the next section. For this **bottom-up** approach, an effective theory is not only useful, but actually the only way we can discuss new physics without choosing a particular model of BSM physics.

High-energy physics can be seen as the field of working ourselves up a chain of theories to ever higher energies. The EFT framework provides us with the tools to do this in an organised way.

2.2.2 EFT construction and the bottom-up approach

EFTs are especially useful in the framework of quantum field theory (QFT). Before showing how to construct the effective operators of such a theory in a bottom-up approach, let us recapitulate how QFTs are organised. The basic object describing perturbative QFTs in $d = 4$ flat space-time dimensions is the action

$$S = \int d^4x \mathcal{L}(x), \quad (2.10)$$

where the Lagrangian $\mathcal{L}(x)$ consists of a sum of couplings times local operators. A key property of each coupling or operator is its **canonical dimension** or mass dimension. In simple terms

this can be phrased as the following question: if you assign a value to a quantity, which power of a mass unit such as GeV would this value carry? Since we work in units with $\hbar = c = 1$, length and distance dimensions are just the inverse of mass dimensions. We denote the mass dimension of any object with squared brackets, where $[\mathcal{O}] = D$ means that \mathcal{O} is of dimension mass ^{D} , or mass dimension D .

Since in the partition function the action appears as e^{iS} , it must be dimensionless, $[S] = 0$. The space-time integral in Equation (2.10) then implies $[\mathcal{L}] = d = 4$, so every term in the Lagrangian has to be of mass dimension 4. Applying this to the kinetic terms, we can calculate the mass dimension of all fields. This then allows us to calculate the dimension of all operators and couplings in the theory.

The canonical dimension of an operator has two important consequences. First, the renormalisation group flow of a theory, i. e. the running of the couplings between different energy scales, largely depends on the mass dimensions of the operators. Operators with mass dimension $D < d$ ('relevant' operators) receive substantial quantum corrections when going from high to low energies. This is a key argument for many fine-tuning problems such as the hierarchy problem or the cosmological constant problem. On the other hand, operators with $D > d$ ('irrelevant' ones) are typically suppressed when going to lower energies. Operators with $D = d$ are called 'marginal'. The second consequence of the mass dimension affects the renormalisability of a theory. Theories with operators with $D > d$ are non-renormalisable:⁶ particles in loops with energies $E \rightarrow \infty$ lead to infinities in observables, too many to be hidden in a renormalisation of the parameters.

Effective operators

From now on we only consider EFTs realised as a local QFT in 4 space-time dimensions, an approach that has proven very successful in high-energy physics so far. EFTs are then defined as a sum of operators \mathcal{O}_i , each with a specific canonical dimension D_i . We can split the coupling in front of each operator into a dimensionless constant, the **Wilson coefficient** f_i , and some powers of a mass scale, for which we use the scale of heavy physics Λ :

$$\mathcal{L}_{\text{EFT}} = (\text{kinetic and mass terms}) + \sum_i \frac{f_i}{\Lambda^{D_i-d}} \mathcal{O}_i. \quad (2.11)$$

Why do we force Λ to appear in front of the operators like this? If we do not know anything about the underlying model at scale Λ , our best guess (which can be motivated with arguments based on the renormalisation group flow) is that it consists of dimensionless couplings g , roughly of up to $\mathcal{O}(1)$ for weakly interacting underlying physics, and mass scales $M \sim \mathcal{O}(\Lambda)$. Indirect effects mediated by the high-energy physics should therefore be proportional to a combination

⁶The opposite is not true: some theories contain only operators with $D \leq d$, but are still not renormalisable.

of these factors, as given in Equation (2.11) with Wilson coefficients f_i of a size dictated by the underlying couplings g . This is certainly true in Fermi theory, where the effective four-fermion interaction is suppressed by $G_F \propto 1/m_W^2 = 1/\Lambda^2$.

Ingredients

What the operators \mathcal{O}_i look like may be clear in a top-down situation where we know the underlying theory. In a bottom-up approach, however, we need a recipe to construct a list of operators in a model-independent way. It turns out that this is surprisingly straightforward, and the list of operators we need to include in the EFT is defined by three ingredients: the particle content, the symmetries, and a counting scheme that decides which operators are relevant at the scale of interest. We go through them one by one.

1. **Particle content:** one has to define the fields that are the dynamical degrees of freedom in the EFT, i. e. that can form either external legs or internal propagators in Feynman diagrams. At least all particles with masses $m \ll \Lambda$ should be included. The operators are then combinations of these fields and derivatives.
2. **Symmetries:** some symmetry properties of the world have been measured with high precision, and we can expect that a violation of these symmetries has to be extremely small or happens at very high energies. These can be gauge symmetries (such as the $SU(3) \times SU(2) \times U(1)$ of the SM), space-time symmetries (such as Lorentz symmetry), or other global symmetries (such as flavour symmetries). Requiring that the effective operators do not violate these symmetries is well motivated and can reduce the complexity of the theory significantly.
3. **Counting scheme:** with a set of particles and some symmetry requirements we can construct an infinite tower of different operators. We therefore need some rule to decide which of the operators we can neglect. We mostly use a counting scheme based on the canonical dimension of the operators. As argued above, we expect an operator with mass dimension $D > d$ to be suppressed by a factor of roughly $1/\Lambda^{D-d}$. Operators of higher mass dimension are therefore more strongly suppressed. Setting a maximal operator dimension is thus a way of limiting the EFT to a finite number of operators that should include the leading effects at energies $E \ll \Lambda$.

One property that is often required of theories is missing in this list: an EFT (with its intrinsic UV cutoff Λ) does not have to be renormalisable in the traditional sense. In fact, most EFTs include operators with mass dimension $D > d$ and are thus non-renormalisable. However, EFTs are still **renormalisable order by order** in the counting scheme: at a given order in the EFT expansion, for instance in $1/\Lambda$, only a finite number of divergences appears and can be absorbed in a renormalisation of the parameters [133]. In this way, loop effects can be calculated without any fundamental issues.

Basis choices

Usually not all operators that can be constructed in this way are independent. This can be seen from a field redefinition of the form

$$\phi(x) \rightarrow \phi'(x) = \phi(x) + \varepsilon f(x) \quad (2.12)$$

where ε is some small parameter and $f(x)$ can contain any combination of fields evaluated at x . The action in terms of the new field is (after integration by parts)

$$\int d^4x \mathcal{L}[\phi] \rightarrow \int d^4x \mathcal{L}[\phi'] = \int d^4x \left(\mathcal{L}[\phi] + \varepsilon \left[\frac{\delta \mathcal{L}}{\delta \phi} - \partial_\mu \frac{\delta \mathcal{L}}{\delta \partial_\mu \phi} \right] f + \mathcal{O}(\varepsilon^2) \right). \quad (2.13)$$

We demonstrate this in a concrete example in Appendix A.3.1. Such a transformation does not change the physics, i. e. the S -matrix elements, so we can equivalently use the new action instead of the original one [134–137]. In this way, each equation of motion provides us with a degree of freedom to swap operators for a combination of other operators. Similarly, Fierz identities and integration by parts can be used to manipulate the form of operators. Together these tools reduce the number of operators and coefficients necessary in an EFT basis, and lead to some freedom to choose which operators to work with.

Why is the sky blue?

Following Reference [73], we demonstrate this bottom-up approach by deriving the colour of the sky. In other words, we answer the question why blue light coming from the sun is scattered more strongly by particles in the atmosphere than red light. A full derivation of this takes some time and requires knowledge of the underlying electrodynamic interactions. Instead, we write down an effective field theory for this process of Rayleigh scattering. The only thing we have to know are the basic scales of the process: photons with energy E_γ scatter off basically static nuclei characterised by an excitation energy ΔE , mass M and radius a_0 . These scales are clearly separated:

$$E_\gamma \ll \Delta E, a_0^{-1} \ll M. \quad (2.14)$$

This is good news, since such a scale hierarchy is the basic requirement for an EFT. We are interested in elastic scattering, so we set the cutoff of the EFT as⁷

$$\Lambda \sim \Delta E, a_0^{-1}. \quad (2.15)$$

With this we can put together the building blocks for our EFT as discussed above:

⁷In reality there are two orders of magnitude between ΔE and a_0^{-1} , but this does not affect the line of argument at all and we choose to ignore this fact.

1. As fields we need photons and atoms, where we can approximate the latter as infinitely heavy.
2. The relevant symmetries are the $U(1)_{\text{em}}$ and Lorentz invariance. At these energies atoms can neither be created nor destroyed, which can be seen as another symmetry requirement on the effective Lagrangian.
3. We include the lowest-dimensional operators that describe photon-atom scattering.

The kinetic part of such an EFT reads

$$\mathcal{L}_{\text{kin}} = \phi_v^\dagger i v^\alpha \partial_\alpha \phi_v - \frac{1}{4} F_{\mu\nu} F^{\mu\nu}, \quad (2.16)$$

where ϕ_v is the field operator representing an infinitely heavy atom at constant velocity v^μ , and $F_{\mu\nu}$ is the photon field strength tensor. Boosting into the atom's rest frame, $v^\mu = (1, 0, 0, 0)$ and the first term becomes the Lagrangian of the Schrödinger equation.

The usual power counting based on $[\mathcal{L}] = 4$ gives the mass dimensions

$$[\partial_\mu] = 1, \quad [v^\mu] = 0, \quad [\phi] = \frac{3}{2}, \quad \text{and} \quad [F_{\mu\nu}] = 2. \quad (2.17)$$

The interaction operators must be Lorentz-invariant combinations of $\phi^\dagger \phi$, $F_{\mu\nu}$, v_μ , and ∂_μ . Note that operators directly involving A_μ instead of $F_{\mu\nu}$ are forbidden by gauge invariance, and single instances of ϕ correspond to the creation or annihilation of atoms, which is not possible at these energies. The first such operators appear at mass dimension 7:

$$\mathcal{L}_{\text{int}} = \frac{f_1}{\Lambda^3} \phi_v^\dagger \phi_v F_{\mu\nu} F^{\mu\nu} + \frac{f_2}{\Lambda^3} \phi_v^\dagger \phi_v v^\alpha F_{\alpha\mu} v_\beta F^{\beta\mu} + \mathcal{O}(1/\Lambda^4), \quad (2.18)$$

with Wilson coefficients f_1 and f_2 . These two operators should capture the dominant effects of Rayleigh scattering at energies $E_\gamma \ll \Lambda$.

The scattering amplitude of light off the atmospheric atoms should therefore scale as $\mathcal{M} \sim 1/\Lambda^3$, which means that the cross section scales with $\sigma \sim 1/\Lambda^6$. Since the cross section has the dimension of an area, $[\sigma] = -2$, and since the only other mass scale in this low-energy process is the photon energy E_γ , we know that the effective cross section must be proportional to

$$\sigma \propto \frac{E_\gamma^4}{\Lambda^6} (1 + \mathcal{O}(E_\gamma/\Lambda)). \quad (2.19)$$

In other words, blue light is much more strongly scattered than red light. Our effective theory, built just from a few simple assumptions, explains the colour of the sky.

Finally, we should check the validity range of our EFT. We expect it to work as long as

$$E_\gamma \ll \Lambda \sim \Delta E \sim \mathcal{O}(\text{eV}), \quad (2.20)$$

equivalent to wavelengths above $\mathcal{O}(100 \text{ nm})$. Our approximation is probably safe for visible light. In the near ultraviolet we expect deviations from the E_γ^4 proportionality and the EFT to lose its validity.

2.2.3 Top-down approach and matching

In the top-down approach to effective field theories, we start from a known model of UV physics and calculate the corresponding effective operators and Wilson coefficients in the EFT. The defining criterion of this **matching procedure** is that at low energies the effective and underlying descriptions agree, at least up to a given order in the loop expansion (e.g. in α_s) and up to a given order in the EFT expansion in $1/\Lambda$.

This can be achieved either by functional methods or with Feynman diagrams. Here we sketch the conceptual foundation involving functional methods, before arriving at a simple diagrammatic method. Note that the matching cannot be reversed: one cannot uniquely reconstruct a full theory only based on the EFT. Details of the matching procedure play a crucial role in Chapter 3.

The effective action

The central object that allows us to systematically analyse the low-energy effects of heavy physics is the effective action S_{eff} . Following References [138, 139], we now outline its calculation at the one-loop level. Note that this is just a conceptual sketch and not mathematically rigorous, and that we omit higher-order terms irrelevant for this thesis as well as certain cases of mixed loops with light and heavy particles [140]. For a more thorough derivation see the quantum field theory textbook of your choice, e.g. References [141, 142].

For simplicity, let us assume that our theory $S[\phi, \Phi]$ consists of light particles ϕ and a heavy scalar Φ that we want to remove as a dynamical degree of freedom in the effective theory. The effective action is calculated by **integrating out** the heavy particles from the partition function,

$$e^{iS_{\text{eff}}[\phi]} = \int \mathcal{D}\Phi e^{iS[\phi, \Phi]}. \quad (2.21)$$

While the path integral over the heavy fields is computed, the light fields are kept fixed as ‘background fields’.

The effective action can be calculated with a saddle-point approximation. For this we expand Φ around its classical value Φ_c :

$$\Phi(x) = \Phi_c(x) + \eta(x). \quad (2.22)$$

Φ_c is defined by the classical equation of motion

$$\frac{\delta S[\phi, \Phi]}{\delta \Phi} \Bigg|_{\Phi=\Phi_c} = 0, \quad (2.23)$$

so expanding the action around this extremum leads to

$$S[\phi, \Phi_c + \eta] = S[\phi, \Phi_c] + \frac{1}{2} \frac{\delta^2 S[\phi, \Phi]}{\delta \Phi^2} \Bigg|_{\Phi=\Phi_c} \eta^2 + \mathcal{O}(\eta^3). \quad (2.24)$$

Plugging this into Equation (2.21), we find

$$e^{iS_{\text{eff}}[\phi]} \approx e^{iS[\phi, \Phi_c]} \int \mathcal{D}\eta \exp\left(\frac{1}{2} \frac{\delta^2 S[\phi, \Phi]}{\delta \Phi^2} \Big|_{\Phi=\Phi_c} \eta^2\right). \quad (2.25)$$

The last term is a Gaussian integral with a known solution,

$$e^{iS_{\text{eff}}[\phi]} \approx e^{iS[\phi, \Phi_c]} \left[\det\left(-\frac{\delta^2 S}{\delta \Phi^2} \Big|_{\Phi=\Phi_c}\right) \right]^{-1/2} \quad (2.26)$$

and finally

$$S_{\text{eff}}[\phi] \approx S[\phi, \Phi_c] + \frac{i}{2} \text{tr} \log\left(-\frac{\delta^2 S}{\delta \Phi^2} \Big|_{\Phi=\Phi_c}\right), \quad (2.27)$$

where the functional trace is defined as an integral over momentum space k together with a sum over internal states i such as spin or flavour,

$$\text{tr } x \equiv \sum_i \int \frac{d^4 k}{(2\pi)^4} \langle k, i | x | k, i \rangle. \quad (2.28)$$

This result can be directly evaluated with functional methods, see Appendix A.3.2 for an explicit example. The first term in Equation (2.27) can be easily calculated by solving the classical equations of motion in Equation (2.23). Computing the functional trace is more involved, but can be simplified with a procedure called covariant derivative expansion [138, 143, 144]. Universal results that can be adapted to many scenarios are available in the literature [139, 140, 145].

The effective action is in general non-local, visible as (covariant) derivatives D appearing in the denominator (formally defined as Green's functions). We expand these terms schematically as

$$\phi^\dagger \frac{1}{D^2 - M^2} \phi = -\phi^\dagger \frac{1}{M^2} \left[1 + \frac{D^2}{M^2} \right] \phi + \mathcal{O}(1/M^6), \quad (2.29)$$

so that only a rest term of higher order in $1/\Lambda = 1/M$ remains non-local [140]. In a last step, we truncate the resulting tower of operators at some order in the counting scheme, in this case in the expansion in $1/\Lambda$. The resulting effective theory consists of a finite set of local operators up to some order in a counting scheme, compatible with our definition of effective theories in the previous section. Unlike in the bottom-up approach, not all operators have to appear, and we can calculate the Wilson coefficients based on the parameters of the underlying theory.

Diagrammatic matching

The effective action in Equation (2.27) can be calculated in an intuitive diagrammatic way. Since the light fields are kept fixed in Equation (2.21), the effective action is given by all connected Feynman diagrams with only ϕ as external legs and only Φ fields as internal propagators. A more rigorous derivation than the one in the previous section in fact reveals that also certain connected loop diagrams with only ϕ as external legs and both Φ and ϕ fields as internal propagators contribute if they cannot be disconnected by cutting a single internal ϕ line [140]. The first term in Equation (2.27) corresponds to all such tree-level diagrams, the second term describes one-loop pieces. Higher-loop corrections, which play no role in this thesis, are left out.

In practice, the effective operators and their Wilson coefficients can be calculated without the need for any functional methods as follows:

1. Start with the particle content of the full model. Choose the cutoff Λ and divide the particles of the full model into light and heavy fields. Light fields, which should include at least those with masses below Λ , make up the particle content of the effective theory. Heavy fields are integrated out, i. e. removed as dynamical degrees of freedom in the EFT.
2. Based on the particles and interactions of the full model, draw all connected Feynman diagrams that satisfy two conditions:
 - all external legs are light fields; and
 - the diagram cannot be disconnected by cutting a single internal light-field line. For tree-level diagrams this is equivalent to requiring that only heavy fields appear as internal lines.

Using the Feynman rules of the full model, calculate the expressions for these diagrams. Do not treat the external legs as incoming or outgoing particles, but keep the field operator expressions.

3. Express quantities of the full model in terms of Λ . Truncate this infinite series of diagrams at some order in $1/\Lambda$, corresponding to the dimension of the operators we want to keep. Together with kinetic and mass terms for the light fields, these form the Lagrangian of the EFT.

Fermi theory again

Let us apply this top-down procedure to our standard example of Fermi theory. For simplicity, we do not take the full SM, but just the interactions between massive W bosons and fermions as the underlying theory.

1. Our full model consists of quarks and leptons and the W boson. We want to analyse weak interactions below the W mass, so we set $\Lambda = m_W$. The light particles of the EFT thus

consist of the quarks and leptons except for the top, while the W boson and the top quark are heavy and are integrated out.

2. The only diagram with the requested features that has only one heavy propagator has the form



Double lines denote a heavy field. There are additional diagrams with W self-interactions or W loops, but they involve at least two W propagators, which means that all contributions from them are of order $\mathcal{O}(1/\Lambda^4)$, which we neglect.

Applying the SM Feynman rules, this diagram evaluates to

$$\begin{aligned} & \left(\bar{f}_i \frac{i g}{\sqrt{2}} \frac{1 - \gamma_5}{2} \gamma^\mu f_j \right) \frac{-g_{\mu\nu}}{p^2 - m_W^2} \left(\bar{f}_k \frac{i g}{\sqrt{2}} \frac{1 - \gamma_5}{2} \gamma^\nu f_l \right) \\ &= \frac{g^2 (\bar{f}_i (1 - \gamma_5) \gamma^\mu f_j) (\bar{f}_k (1 - \gamma_5) \gamma_\mu f_l)}{8(p^2 - m_W^2)}. \end{aligned} \quad (2.31)$$

3. The only dimensionful parameter is $m_W = \Lambda$, and for the EFT to be valid we assume $p^2 \ll \Lambda^2$. We can then expand this expression as

$$\frac{g^2}{8m_W^2} (\bar{f}_i (1 - \gamma_5) \gamma^\mu f_j) (\bar{f}_k (1 - \gamma_5) \gamma_\mu f_l) + \mathcal{O}(1/\Lambda^4). \quad (2.32)$$

With this, we rediscover the dimension-six EFT matched to the weak interactions of the SM:

$$\mathcal{L} = i \bar{f}_i \gamma^\mu \partial_\mu f_i - m_i \bar{f}_i f_i + \frac{c}{\Lambda^2} (\bar{f}_i (1 - \gamma_5) \gamma_\mu f_j) (\bar{f}_k (1 - \gamma_5) \gamma^\mu f_l), \quad (2.33)$$

with heavy scale $\Lambda = m_W$ and Wilson coefficient $c = g^2/8$. Replacing c/Λ^2 by $G_F/\sqrt{2} = g^2/(8m_W^2)$ restores the historic form of Fermi theory.

Operator mixing

So far we neglected that — like all parameters in a QFT — the value of the Wilson coefficients depends on the energy scale. Running the model from one energy to a different one leads to operator mixing: loop effects from one operator affect the coefficients of other operators. If the Wilson coefficients are given at the matching scale Λ (we use this symbol since the matching

scale is usually chosen only slightly below the EFT cutoff), at the scale of interest E they take on values of the form

$$f_i(E) \sim f_i(\Lambda) \pm \sum_j \frac{g_j^2}{16\pi^2} \log\left(\frac{\Lambda^2}{E^2}\right) f_j(\Lambda), \quad (2.34)$$

where g are the typical couplings in the loops.

If the matching scale is not too far away from the energy scale of interest and if all Wilson coefficients are already sizeable at the matching scale, this is often negligible. One exception arises when operators are generated through strong interactions. Their Wilson coefficients will depend on α_s and pick up the large scale dependence of the strong coupling. Another important consequence is that even if an operator is zero at the matching scale, operator mixing will often give it a small but non-zero value at lower energies. So regardless of what the underlying model is, it can be expected that eventually all effective operators allowed by the symmetries receive contributions from it.

2.3 Dimension-six operators for Higgs physics

We now apply these general ideas to electroweak and in particular Higgs physics at the TeV scale and construct the Standard Model effective field theory (interchangeably called linear Higgs effective field theory) up to dimension six [22–24, 146]. This is the framework we use throughout this thesis. We first argue in Section 2.3.1 why such an effective theory is very useful, and then construct its effective operators in Section 2.3.2 following the recipe laid out in Section 2.2.2. Section 2.3.3 takes a closer look at the phenomenology of these operators. Finally, in Section 2.3.4 we briefly discuss a few alternative parametrisations of Higgs properties.

2.3.1 Motivation

As argued in Section 2.1.3, there are many reasons to expect new physics signatures in the Higgs sector. Some of these arguments, such as the hierarchy problem or the WIMP miracle of dark matter, point towards BSM physics close to the electroweak scale or, depending on the level of acceptable fine-tuning, up to a few TeV. Unfortunately these (purely aesthetic) arguments do not tell us what exactly such physics should look like.

This leaves us with a question highly relevant for upcoming ATLAS and CMS analyses: what is the best language to discuss indirect signs of new physics at the electroweak scale, in particular in the Higgs sector? Which parametrisation of Higgs properties provides a good interface between different experiments, and between experiment and theory?

Directly interpreting measurements in complete models of new physics is impractical: for $n_c \gg 1$ experimental channels and $n_m \gg 1$ models this requires $n_c n_m$ limits to be derived. Also,

the parameter space of such models (think of the relatively simple MSSM) can be huge, and many of their features do not matter at the electroweak scale at all. It makes more sense to define an intermediate framework that can be linked both to measurements and to full theories, so that only n_c sets of limits plus n_m translation rules from complete theories to the intermediate language have to be calculated. Such a framework should include all necessary physics, but no phenomena irrelevant at this scale. This is exactly the defining feature of an effective field theory.

2.3.2 Operators

Building blocks

Since we do not know what physics lays beyond the SM, we have to construct our EFT from a bottom-up perspective. As discussed above, this means we have to write down all operators based on a set of particles that are compatible with certain symmetries and are important according to some counting scheme:

1. As degrees of freedom we use the SM fields. In particular, we assume that the Higgs boson h and the Goldstone bosons w^a are combined in an $SU(2)_L$ doublet ϕ as in the SM, see Equation (2.5). This is the case in many well-studied models of new physics and consistent with data. We discuss an alternative construction in which the physical scalar h and the Goldstones w^a are independent in Section 2.3.4.
2. All operators have to be invariant under proper orthochronous Poincaré transformations and under the SM gauge group $SU(3)_C \times SU(2)_L \times U(1)_Y$, and have to conserve lepton and baryon number.
3. We arrange the operators by their mass dimension and thus their suppression in powers of $1/\Lambda$. We keep those up to mass dimension 6, i. e. $\mathcal{O}(1/\Lambda^2)$.

Simple dimensional analysis of the kinetic terms of the SM fields tells us the mass dimensions of all building blocks:

$$[f] = \frac{3}{2}, \quad [V_\mu] = 1, \quad [V_{\mu\nu}] = 2, \quad [\phi] = 1, \quad [\partial_\mu] = 1 \quad \text{and} \quad [D_\mu] = 1, \quad (2.35)$$

The only dimension-five operator that can be built from the SM fields is the ‘Weinberg operator’ $(\bar{L}_L \tilde{\phi}^*) (\tilde{\phi}^\dagger L_L)$. It generates a Majorana mass term for the neutrinos, violates lepton number, and is entirely irrelevant for Higgs physics. There the leading effects are expected to come from dimension-six operators:

$$\mathcal{L}_{\text{EFT}} = \mathcal{L}_{\text{SM}} + \sum_i \frac{f_i}{\Lambda^2} \mathcal{O}_i + \mathcal{O}(1/\Lambda^4) \quad (2.36)$$

with the unknown cutoff scale Λ and Wilson coefficients f_i . The convergence of this series in $1/\Lambda$ is a central topic of Chapter 3. For convenience, from now on we drop the higher-order terms.

$\mathcal{O}_{\phi,1} = (D_\mu \phi)^\dagger \phi \phi^\dagger D^\mu \phi$	$\mathcal{O}_{GG} = (\phi^\dagger \phi) G_{\mu\nu}^a G^{\mu\nu a}$
$\mathcal{O}_{\phi,2} = \frac{1}{2} \partial_\mu (\phi^\dagger \phi) \partial^\mu (\phi^\dagger \phi)$	$\mathcal{O}_{BB} = -\frac{g'^2}{4} (\phi^\dagger \phi) B_{\mu\nu} B^{\mu\nu}$
$\mathcal{O}_{\phi,3} = \frac{1}{3} (\phi^\dagger \phi)^3$	$\mathcal{O}_{WW} = -\frac{g^2}{4} (\phi^\dagger \phi) W_{\mu\nu}^a W^{\mu\nu a}$
$\mathcal{O}_{\phi,4} = (\phi^\dagger \phi) (D_\mu \phi)^\dagger D^\mu \phi$	$\mathcal{O}_{BW} = -\frac{g g'}{4} (\phi^\dagger \sigma^a \phi) B_{\mu\nu} W^{\mu\nu a}$
	$\mathcal{O}_B = \frac{i g'}{2} (D^\mu \phi)^\dagger D^\nu \phi B_{\mu\nu}$
	$\mathcal{O}_W = \frac{i g}{2} (D^\mu \phi)^\dagger \sigma^a D^\nu \phi W_{\mu\nu}^a$

 Table 2.1: Bosonic CP -conserving dimension-six operators relevant for Higgs physics.

As discussed in Section 2.2.2, field redefinitions (or, relatedly, equations of motion), Fierz identities and integration by parts provide equivalence relations between certain operators and give us some freedom to define a basis of operators. Taking these into account, there are 59 independent types of dimension-six operators, not counting flavour structures and Hermitian conjugation [147]. Counting all possible flavour structures, there are 2499 distinct operators. Fortunately, in practice only a small subset of these are relevant: first, the strong constraints on flavour-changing neutral currents motivate the assumption of flavour-diagonal or even flavour-universal Wilson coefficients. Second, only a small number of these operators directly affect Higgs physics. At higher orders in the EFT expansion, the number of operators increases rapidly, explaining why we stick to the leading effects at dimension six: not counting flavour structures, there are $\mathcal{O}(10^3)$ operators at dimension eight and $\mathcal{O}(10^4)$ dimension-ten operators [148].

Three different conventions have become popular: the complete ‘Warsaw’ basis [147], the ‘Strongly Interacting Light Higgs’ convention (SILH) [149, 150] and the Hagiwara-Ishihara-Szalapski-Zeppenfeld basis (HISZ) [151]. All three maximise the use of bosonic operators to describe Higgs and electroweak observables. For a comparison of and conversion between different bases see Appendix A.4 and References [1, 152]. Throughout this thesis we use the basis developed in References [25, 153, 154], which is virtually identical to the HISZ basis and now widely used in global fits [26, 27, 155, 156].

Operator basis

Finally, we list the dimension-six operators of the SM effective field theory relevant for this thesis. We include some redundancies in this list before using the equations of motion to define a basis. The operators are classified based on their field content and on their behaviour under

$\mathcal{O}_\ell = (\phi^\dagger \phi) \bar{L}_L \phi \ell_R$	$\mathcal{O}_{\phi L}^{(1)} = i(\phi^\dagger \overleftrightarrow{D}_\mu \phi)(\bar{L}_L \gamma^\mu L_L)$	$\mathcal{O}_{\phi L}^{(3)} = i(\phi^\dagger \overleftrightarrow{D}_\mu^a \phi)(\bar{L}_L \gamma^\mu \sigma_a L_L)$
$\mathcal{O}_u = (\phi^\dagger \phi) \bar{Q}_L \tilde{\phi} u_R$	$\mathcal{O}_{\phi Q}^{(1)} = i(\phi^\dagger \overleftrightarrow{D}_\mu \phi)(\bar{Q}_L \gamma^\mu Q_L)$	$\mathcal{O}_{\phi Q}^{(3)} = i(\phi^\dagger \overleftrightarrow{D}_\mu^a \phi)(\bar{Q}_L \gamma^\mu \sigma_a Q_L)$
$\mathcal{O}_d = (\phi^\dagger \phi) \bar{Q}_L \phi d_R$	$\mathcal{O}_{\phi \ell}^{(1)} = i(\phi^\dagger \overleftrightarrow{D}_\mu \phi)(\bar{\ell}_R \gamma^\mu \ell_R)$	
	$\mathcal{O}_{\phi u}^{(1)} = i(\phi^\dagger \overleftrightarrow{D}_\mu \phi)(\bar{u}_R \gamma^\mu u_R)$	
	$\mathcal{O}_{\phi d}^{(1)} = i(\phi^\dagger \overleftrightarrow{D}_\mu \phi)(\bar{d}_R \gamma^\mu d_R)$	
	$\mathcal{O}_{\phi ud}^{(1)} = i(\phi^\dagger \overleftrightarrow{D}_\mu \phi)(\bar{u}_R \gamma^\mu d_R)$	

Table 2.2: CP -conserving dimension-six operators relevant for the Higgs-fermion couplings. All operators contain an implicit Hermitian conjugation. For readability, flavour indices are omitted.

CP transformations. This combined charge conjugation and parity inversion is an approximate symmetry of the SM that is only violated by the complex phase of the CKM matrix. In addition, there are rather tight bounds on CP violation in many processes. This motivates many analyses to restrict their set of operators to the CP -conserving ones. On the other hand, new sources of CP violation are needed to explain the matter-antimatter asymmetry in the universe, and their effects at low energies might be visible as CP -violating effective operators.

We begin with the CP -conserving dimension-six operators relevant for Higgs physics, following References [25, 153, 154]. In Table 2.1 we list the bosonic ones, Table 2.2 gives the Higgs-fermion operators, and the ‘dipole operators’ made of Higgs fields, gauge bosons, and fermions are listed in Table 2.3. We use the convention for the sign in the covariant derivative given in Equation (2.2). T^a are the $SU(3)$ generators, and we define

$$\phi^\dagger \overleftrightarrow{D}_\mu \phi \equiv \phi^\dagger D_\mu \phi - (D_\mu \phi)^\dagger \phi \quad \text{and} \quad \phi^\dagger \overleftrightarrow{D}_\mu^a \phi \equiv \phi^\dagger \sigma^a D_\mu \phi - (D_\mu \phi)^\dagger \sigma^a \phi. \quad (2.37)$$

All other symbols appearing in these operators are defined in Appendix A.1.

In addition to these CP -conserving structures, there are a number of CP -violating operators. We only list the bosonic ones relevant for Higgs physics [84, 157] in Table 2.4. They involve the dual field strength tensors

$$\widetilde{V}_{\mu\nu} = \frac{1}{2} \epsilon_{\mu\nu\rho\sigma} V^{\rho\sigma}, \quad V = B, W, G. \quad (2.38)$$

Finally, there are a few CP -even and CP -odd pure gauge operators made from field strength tensors and (covariant) derivatives, and a large number of four-fermion operators similar to the

$\mathcal{O}_{uW} = (\bar{Q}_L \sigma^{\mu\nu} u_R) \sigma^a \tilde{\phi} W_{\mu\nu}^a$	$\mathcal{O}_{uB} = (\bar{Q}_L \sigma^{\mu\nu} u_R) \tilde{\phi} B_{\mu\nu}$	$\mathcal{O}_{uG} = (\bar{Q}_L \sigma^{\mu\nu} T^a u_R) \tilde{\phi} G_{\mu\nu}^a$
$\mathcal{O}_{dW} = (\bar{Q}_L \sigma^{\mu\nu} d_R) \sigma^a \phi W_{\mu\nu}^a$	$\mathcal{O}_{dB} = (\bar{Q}_L \sigma^{\mu\nu} d_R) \phi B_{\mu\nu}$	$\mathcal{O}_{dG} = (\bar{Q}_L \sigma^{\mu\nu} T^a d_R) \phi G_{\mu\nu}^a$
$\mathcal{O}_{\ell W} = (\bar{L}_L \sigma^{\mu\nu} \ell_R) \sigma^a \phi W_{\mu\nu}^a$	$\mathcal{O}_{\ell B} = (\bar{L}_L \sigma^{\mu\nu} \ell_R) \phi B_{\mu\nu}$	

Table 2.3: Dipole operators affecting the Higgs-gauge-fermion couplings. All operators contain an implicit Hermitian conjugation. For readability, flavour indices are omitted.

one in Equation (2.33), which are not important in this thesis. See Reference [147] for a complete basis of dimension-six operators.

As argued above, not all of these operators are independent. The equations of motion for the Higgs field and the electroweak gauge bosons read [147]

$$D^2 \phi = -\mu^2 \phi - 2\lambda(\phi^\dagger \phi)\phi - \sum_f y_f \bar{f}_R f_L + \mathcal{O}(1/\Lambda^2), \quad (2.39)$$

$$\partial^\rho B_{\rho\mu} = -\frac{ig'}{2} \phi^\dagger \overleftrightarrow{D}_\mu \phi - \sum_f g' Y_f \bar{f} \gamma_\mu f + \mathcal{O}(1/\Lambda^2), \quad \text{and} \quad (2.40)$$

$$(D^\rho W_{\rho\mu})^a = -\frac{ig}{2} \phi^\dagger \overleftrightarrow{D}_\mu^a \phi - \frac{g}{2} \sum_f \bar{f}_L \gamma_\mu \sigma^a f_L + \mathcal{O}(1/\Lambda^2), \quad (2.41)$$

where Y_f are the weak hypercharges of the fermions. Following Equation (2.13) and Appendix A.3.1, this provides us with three equivalence relations between dimension-six operators [25, 153, 154]:

$$2\mathcal{O}_{\phi,2} + 2\mathcal{O}_{\phi,4} - 2\mu^2(\phi^\dagger \phi)^2 - 12\lambda\mathcal{O}_{\phi,3} \simeq \sum_f y_f \mathcal{O}_f + \mathcal{O}(1/\Lambda^2) \quad (2.42)$$

$$\mathcal{O}_{BB} + \mathcal{O}_{BW} - 2\mathcal{O}_B + g'^2 \left(\mathcal{O}_{\phi,1} - \frac{1}{2} \mathcal{O}_{\phi,2} \right) \simeq -\frac{g'^2}{2} \sum_f Y_f \mathcal{O}_{\phi f}^{(1)} + \mathcal{O}(1/\Lambda^2) \quad (2.43)$$

$$\mathcal{O}_{WW} + \mathcal{O}_{BW} - 2\mathcal{O}_W + g^2 \left(\mathcal{O}_{\phi,4} - \frac{1}{2} \mathcal{O}_{\phi,2} \right) \simeq -\frac{g^2}{4} \sum_{F=L,Q} \mathcal{O}_{\phi F}^{(3)} + \mathcal{O}(1/\Lambda^2). \quad (2.44)$$

Here the symbol \simeq means ‘physically equivalent’ in the sense that exchanging operators with these relations does not affect any S-matrix elements. This allows us to eliminate three of the operators listed in Tables 2.1 to 2.4.

There are different strategies for picking the operators to keep. In a top-down approach, one may choose operators based on the underlying physics. In a bottom-up approach, calculations can be simplified if the operators are chosen based on their contributions to physical observables, for instance to avoid non-trivial blind directions. Following Reference [25], we choose to discard $\mathcal{O}_{\phi L}^{(1)}$, $\mathcal{O}_{\phi L}^{(3)}$, and $\mathcal{O}_{\phi,4}$.

$\mathcal{O}_{G\widetilde{G}} = (\phi^\dagger \phi) G_{\mu\nu}^a \widetilde{G}^{\mu\nu a}$	$\mathcal{O}_{\widetilde{B}} = \frac{i g}{2} (D^\mu \phi^\dagger)(D^\nu \phi) \widetilde{B}_{\mu\nu}$
$\mathcal{O}_{B\widetilde{B}} = -\frac{g'^2}{4} (\phi^\dagger \phi) B_{\mu\nu} \widetilde{B}^{\mu\nu}$	$\mathcal{O}_{B\widetilde{W}} = -\frac{g g'}{4} (\phi^\dagger \sigma^a \phi) B_{\mu\nu} \widetilde{W}^{\mu\nu a}$
$\mathcal{O}_{W\widetilde{W}} = -\frac{g^2}{4} (\phi^\dagger \phi) W_{\mu\nu}^a \widetilde{W}^{\mu\nu a}$	

Table 2.4: Bosonic CP -violating dimension-six operators relevant for Higgs physics. The dual field strengths $\widetilde{V}_{\mu\nu}$ with $V = G, B, W$ are defined in Equation (2.38).

Constraints

Some of the remaining operators are tightly constrained from experimental data. Electroweak precision measurements limit the Wilson coefficients of $\mathcal{O}_{\phi,1}$, \mathcal{O}_{BW} , $\mathcal{O}_{B\widetilde{W}}$, $\mathcal{O}_{\widetilde{B}}$, $\mathcal{O}_{\phi L}^{(3)}$, and the remaining $\mathcal{O}_{\phi f}^{(1)}$ to a level where their effects in Higgs physics are small. Measurements of electric dipole moments put tight constraints on the dipole operators. We therefore mostly ignore these operators in this thesis.⁸

Limits on flavour-changing neutral currents constrain off-diagonal fermion-Higgs couplings. Moreover, flavour-diagonal \mathcal{O}_f involving fermions of the first and second generations are irrelevant for many signatures considered in this thesis. We therefore only keep the Higgs-fermion operators \mathcal{O}_f of the third generation.

This leaves us with a list of thirteen operators relevant for LHC Higgs physics: ten CP -even operators,

$$\mathcal{O}_{\phi,2}, \quad \mathcal{O}_{\phi,3}, \quad \mathcal{O}_{GG}, \quad \mathcal{O}_{BB}, \quad \mathcal{O}_{WW}, \quad \mathcal{O}_B, \quad \mathcal{O}_W, \quad \mathcal{O}_\tau, \quad \mathcal{O}_t, \quad \text{and} \quad \mathcal{O}_b; \quad (2.45)$$

and three CP -odd ones,

$$\mathcal{O}_{G\widetilde{G}}, \quad \mathcal{O}_{B\widetilde{B}}, \quad \text{and} \quad \mathcal{O}_{W\widetilde{W}}. \quad (2.46)$$

Renormalisation group evolution

The Wilson coefficients of these operators depend on the energy scale. During the last years, the contributions of all dimension-six operators on the running of the SM parameters, as well as the whole 59×59 anomalous dimension matrix of dimension-six operators, have been calculated at

⁸This simple argument is suitable for our rather conceptual work. In a thorough global fit, however, it should be checked carefully whether these constraints are actually strong enough to make these operators irrelevant for Higgs physics in all cases. Such a check should include RG effects when comparing constraints from different scales. The increasing precision in Higgs observables means that many of these operators will become relevant again in the future.

one-loop level [158–160]. This provides all necessary tools to run the EFT parameters from the matching scale Λ to the experimental scale E . Following Equation (2.34), this shifts the Wilson coefficients by a term proportional to a loop factor times $\log \Lambda^2/E^2$.

As we discuss at some length in Chapter 3, the LHC Higgs measurements are only sensitive to new physics scales between the electroweak scale and the TeV scale. The corresponding logarithm typically cannot compensate for the loop factor, and the RG effects on Wilson coefficients that are already non-zero at the matching scale and that do not explicitly depend on α_s are small. This means that for our analyses we can often neglect the RG running of the Wilson coefficients.

2.3.3 Phenomenology

Having picked a set of operators, the next question is how they affect Higgs observables. We first discuss two examples, $\mathcal{O}_{\phi,2}$ and \mathcal{O}_W , in detail, before listing the effects of all operators in Equations (2.45) and (2.46).

$\mathcal{O}_{\phi,2}$: rescaled Higgs couplings

Our first example is the operator $\mathcal{O}_{\phi,2}$. Ignoring the Goldstones, it consists only of derivatives and Higgs fields $\phi^\dagger \phi = (v^2 + 2v\tilde{h} + \tilde{h}^2)/2$, where we use a tilde on h because this field is not yet a mass eigenstate. Its contribution to the Lagrangian reads

$$\begin{aligned}\mathcal{L}_{\text{EFT}} &\supset \frac{f_{\phi,2}}{2\Lambda^2} \partial_\mu (\phi^\dagger \phi) \partial^\mu (\phi^\dagger \phi) \\ &= \frac{f_{\phi,2} v^2}{2\Lambda^2} \partial_\mu \tilde{h} \partial^\mu \tilde{h} + \frac{f_{\phi,2} v}{\Lambda^2} \tilde{h} \partial_\mu \tilde{h} \partial^\mu \tilde{h} + \frac{f_{\phi,2} v}{2\Lambda^2} \tilde{h}^2 \partial_\mu \tilde{h} \partial^\mu \tilde{h}.\end{aligned}\quad (2.47)$$

The first term rescales the kinetic term of the Higgs boson:

$$\mathcal{L}_{\text{EFT}} \supset \left(1 + \frac{f_{\phi,2} v^2}{\Lambda^2}\right) \frac{1}{2} \partial_\mu \tilde{h} \partial^\mu \tilde{h}. \quad (2.48)$$

To restore the canonical form of the kinetic term, we have to rescale the Higgs boson \tilde{h} to

$$h = \sqrt{1 + \frac{f_{\phi,2} v^2}{\Lambda^2}} \tilde{h}. \quad (2.49)$$

This universally shifts all Higgs couplings to other particles as

$$g_{hxx} = \frac{1}{\sqrt{1 + \frac{f_{\phi,2} v^2}{\Lambda^2}}} g_{hxx}^{\text{SM}}. \quad (2.50)$$

There is an additional, more involved effect on the Higgs self-coupling. The rescaling in Equation (2.49) also affects the Higgs mass term given in Equation (2.6). For fixed v and m_h , this amounts to shifting the Higgs self-coupling λ to

$$\lambda = \frac{m_h^2}{2v^2} \left(1 + \frac{f_{\phi,2}v^2}{\Lambda^2} \right). \quad (2.51)$$

Moreover, the second term in Equation (2.47) introduces a new Lorentz structure into the cubic Higgs self-interaction that depends on the Higgs momenta. A non-zero Wilson coefficient $f_{\phi,2}$ therefore has a strong impact on Higgs pair production, changing not only the total rate, but also kinematic shapes.

\mathcal{O}_W : new Higgs-gauge structures

Our second example is \mathcal{O}_W , which contracts covariant derivatives acting on Higgs doublets, defined in Equation (2.2), with a field strength tensor $W_{\mu\nu}^k = \partial_\mu W_\nu^k - \partial_\nu W_\mu^k + g\epsilon^{kmn}W_\mu^m W_\nu^n$. Expanding \mathcal{O}_W and only keeping the pieces that affect the hWW coupling, we find

$$\begin{aligned} \mathcal{L}_{\text{EFT}} &\supset \frac{f_W}{\Lambda^2} \frac{\text{i}g}{2} (D^\mu \phi)^\dagger \sigma^k (D^\nu \phi) W_{\mu\nu}^k \\ &= \frac{\text{i}g f_W}{2\Lambda^2} \left(\partial^\mu \phi^\dagger + \frac{\text{i}g}{2} W^{m\mu} \phi^\dagger \sigma^m + \frac{\text{i}g'}{2} B^\mu \phi^\dagger \right) \sigma^k \left(\partial^\nu \phi - \frac{\text{i}g}{2} \sigma^n W^{n\nu} \phi - \frac{\text{i}g'}{2} B^\nu \phi \right) W_{\mu\nu}^k \\ &\supset \frac{\text{i}g f_W}{2\Lambda^2} \left\{ \frac{\partial^\mu h}{\sqrt{2}} [\sigma^k \sigma^n]_{22} \frac{-\text{i}g}{2} W^{n\nu} \frac{v}{\sqrt{2}} + \frac{\text{i}g}{2} W^{m\nu} \frac{v}{\sqrt{2}} [\sigma^m \sigma^k]_{22} \frac{\partial^\mu h}{\sqrt{2}} \right\} W_{\mu\nu}^k \\ &= \frac{f_W}{\Lambda^2} \frac{g^2 v}{8} [\sigma^k \sigma^n]_{22} (\partial^\mu h) W^{n\nu} W_{\mu\nu}^k \\ &= \frac{f_W}{\Lambda^2} \frac{\text{i}g^2 v}{4} \epsilon^{nk3} (\partial^\mu h) W^{n\nu} W_{\mu\nu}^k. \end{aligned} \quad (2.52)$$

With $m_W = gv/2$ and $W_\mu^\pm = (W_\mu^1 \mp \text{i}W_\mu^2)/\sqrt{2}$ this finally yields

$$\mathcal{L}_{\text{EFT}} \supset \frac{f_W}{\Lambda^2} \frac{\text{i}gm_W}{2} (\partial^\mu h) (W^{+\nu} W_{\mu\nu}^- + W^{-\nu} W_{\mu\nu}^+). \quad (2.53)$$

This is another contribution to the hWW vertex. But unlike the SM-like coupling

$$\mathcal{L}_{\text{SM}} \supset gm_W h W^{+\mu} W_\mu^-, \quad (2.54)$$

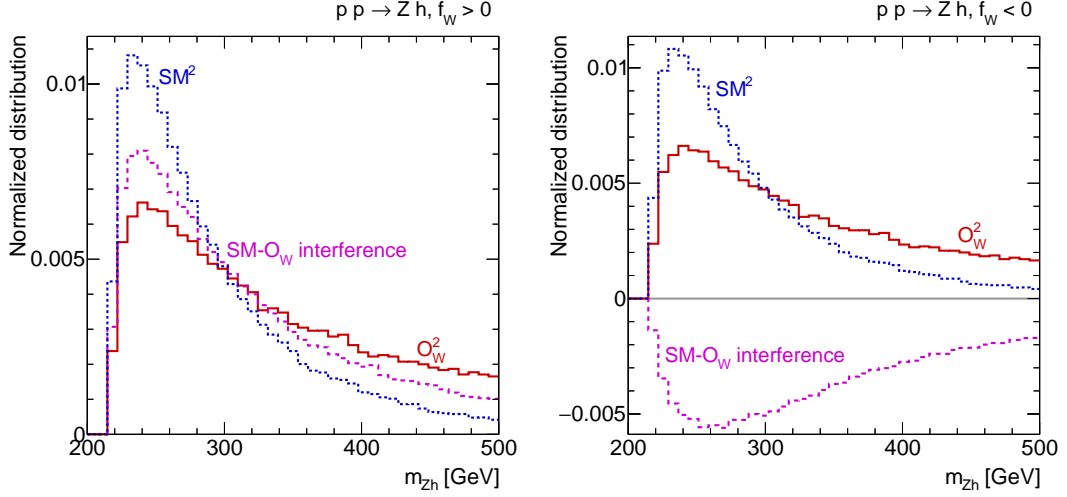


Figure 2.4: Distribution of the Zh invariant mass in the Higgs-strahlung process $pp \rightarrow Zh$ at LHC conditions at $\sqrt{s} = 13$ TeV. We compare the SM contributions to the squared amplitude from the operator \mathcal{O}_W and to their interference. Depending on the sign of the Wilson coefficient f_W , the latter can be constructive (left) or destructive (right).

the \mathcal{O}_W term includes derivatives. This means that the interaction gains a momentum dependence:

$$H \text{---} \begin{array}{c} \text{---} \\ \text{---} \end{array} \begin{array}{c} W_\mu^+ \\ \text{---} \\ W_\nu^- \end{array} = ig m_W \left[g_{\mu\nu} + \frac{f_W}{2\Lambda^2} p_H^2 g_{\mu\nu} + \frac{f_W}{2\Lambda^2} (p_\mu^H p_\nu^+ + p_\mu^- p_\nu^H) \right], \quad (2.55)$$

where p_μ^\pm and p_μ^H are the incoming momenta of the W^\pm and the H , respectively.

This operator illustrates two key features of the EFT approach. First, \mathcal{O}_W does not only affect the hWW vertex, but also hZZ interactions and triple-gauge couplings such as WWZ . This means that the dimension-six operator language allows us to combine different measurements in a global fit.

Second, \mathcal{O}_W changes the shape of distributions, for instance in Higgs-strahlung at the LHC,

$$pp \rightarrow Zh. \quad (2.56)$$

In this process, the intermediate Z can carry arbitrarily large energy and momentum, which we can measure for instance as the invariant mass of the final Zh system. From Equation (2.55) we

expect the effect from \mathcal{O}_W to grow with m_{Zh} . In Figure 2.4 we demonstrate this by comparing the distribution of m_{Zh} based on the SM diagrams alone with the squared amplitudes from the dimension-six operator \mathcal{O}_W and the interference between the two components. Indeed we see that \mathcal{O}_W contributes mostly in the high-energy tail of the distribution.

All those couplings

After these two worked-out examples, we now give the complete list of single-Higgs couplings induced by the dimension-six operators of Equations (2.45) and (2.46) [25, 153, 154].⁹

These interactions read

$$\begin{aligned} \mathcal{L}_{\text{EFT}} \supset & g_{hgg}^{(1)} h G_{\mu\nu}^a G^{a\mu\nu} + g_{hgg}^{(2)} \varepsilon_{\mu\nu\rho\sigma} h G^{a\mu\nu} G^{a\rho\sigma} + g_{hyy} h A_{\mu\nu} A^{\mu\nu} \\ & + g_{hZy}^{(1)} A_{\mu\nu} Z^\mu \partial^\nu h + g_{hZy}^{(2)} h A_{\mu\nu} Z^{\mu\nu} \\ & + g_{hZZ}^{(1)} Z_{\mu\nu} Z^\mu \partial^\nu h + g_{hZZ}^{(2)} h Z_{\mu\nu} Z^{\mu\nu} + g_{hZZ}^{(3)} h Z_\mu Z^\mu + g_{hZZ}^{(4)} h \varepsilon_{\mu\nu\rho\sigma} Z^{\mu\nu} Z^{\rho\sigma} \\ & + g_{hWW}^{(1)} (W_{\mu\nu}^+ W^{-\mu} \partial^\nu h + \text{h. c.}) + g_{hWW}^{(2)} h W_{\mu\nu}^+ W^{-\mu\nu} + g_{hWW}^{(3)} h W_\mu^+ W^{-\mu} \\ & + g_{hWW}^{(4)} h \varepsilon_{\mu\nu\rho\sigma} W^{+\mu\nu} W^{-\rho\sigma} + \sum_{f=\tau,t,b} (g_{hff} h \bar{f}_L f_R + \text{h. c.}) \end{aligned} \quad (2.57)$$

with couplings

$$\begin{aligned} g_{hgg}^{(1)} &= \frac{f_{GG} v}{\Lambda^2} \left(1 + \frac{v^2 f_{\phi,2}}{\Lambda^2} \right)^{-1/2}, \\ g_{hgg}^{(2)} &= \frac{f_{G\tilde{G}} v}{2\Lambda^2} \left(1 + \frac{v^2 f_{\phi,2}}{\Lambda^2} \right)^{-1/2}, \\ g_{hyy} &= -\frac{g^2 v s_W^2 (f_{WW} + f_{BB})}{4\Lambda^2} \left(1 + \frac{v^2 f_{\phi,2}}{\Lambda^2} \right)^{-1/2}, \\ g_{hZy}^{(1)} &= -\frac{g^2 v s_W (f_W - f_B)}{4c_W \Lambda^2} \left(1 + \frac{v^2 f_{\phi,2}}{\Lambda^2} \right)^{-1/2}, \\ g_{hZy}^{(2)} &= \frac{g^2 v s_W (2s_W^2 f_{BB} - 2c_W^2 f_{WW})}{4c_W \Lambda^2} \left(1 + \frac{v^2 f_{\phi,2}}{\Lambda^2} \right)^{-1/2}, \\ g_{hZZ}^{(1)} &= -\frac{g^2 v (c_W^2 f_W + s_W^2 f_B)}{4c_W^2 \Lambda^2} \left(1 + \frac{v^2 f_{\phi,2}}{\Lambda^2} \right)^{-1/2}, \\ g_{hZZ}^{(2)} &= -\frac{g^2 v (s_W^4 f_{BB} + c_W^4 f_{WW})}{4c_W^2 \Lambda^2} \left(1 + \frac{v^2 f_{\phi,2}}{\Lambda^2} \right)^{-1/2}, \end{aligned}$$

⁹When comparing with References [25, 153, 154], note the different sign conventions in the covariant derivative.

$$\begin{aligned}
 g_{hZZ}^{(3)} &= \frac{g^2 v}{4c_W^2} \left(1 + \frac{v^2 f_{\phi,2}}{\Lambda^2} \right)^{-1/2}, \\
 g_{hZZ}^{(4)} &= -\frac{g^2 v (s_W^4 f_{B\widetilde{B}} + c_W^4 f_{W\widetilde{W}})}{8c_W^2 \Lambda^2} \left(1 + \frac{v^2 f_{\phi,2}}{\Lambda^2} \right)^{-1/2}, \\
 g_{hWW}^{(1)} &= -\frac{g^2 v f_W}{4\Lambda^2} \left(1 + \frac{v^2 f_{\phi,2}}{\Lambda^2} \right)^{-1/2}, \\
 g_{hWW}^{(2)} &= -\frac{g^2 v f_{WW}}{2\Lambda^2} \left(1 + \frac{v^2 f_{\phi,2}}{\Lambda^2} \right)^{-1/2}, \\
 g_{hWW}^{(3)} &= \frac{g^2 v}{2} \left(1 + \frac{v^2 f_{\phi,2}}{\Lambda^2} \right)^{-1/2}, \\
 g_{hWW}^{(4)} &= -\frac{g^2 v f_{W\widetilde{W}}}{4\Lambda^2} \left(1 + \frac{v^2 f_{\phi,2}}{\Lambda^2} \right)^{-1/2}, \quad \text{and} \\
 g_{hf} &= -\frac{m_f}{v} \left(1 + \frac{v^2 f_{\phi,2}}{\Lambda^2} \right)^{-1/2} + \frac{v^2 f_f}{\sqrt{2}\Lambda^2}. \tag{2.58}
 \end{aligned}$$

Here $s_W = g'/\sqrt{g^2 + g'^2}$ and $c_W = g/\sqrt{g^2 + g'^2}$ are the sine and cosine of the weak mixing angle, and $V_{\mu\nu} = \partial_\mu V_\nu - \partial_\nu V_\mu$ for $V = A, W^\pm, Z$.

Note that the clear majority of the couplings in Equation (2.57) does not exist in the SM and contains derivatives. Dimension-six operators predict a variety of novel kinematic features in Higgs interactions, making their measurement at the LHC both exciting and challenging.

2.3.4 Alternative frameworks

The linear Higgs EFT discussed above is not the only useful parametrisation of Higgs properties. We briefly go through some of the alternative frameworks and explain their main properties, before concluding this chapter with a comparison between the different approaches.

Non-linear Higgs effective field theory

In the SM EFT (or linear Higgs EFT), constructed in Section 2.3.2, the Higgs boson h and the Goldstone bosons w^a form an $SU(2)_L$ doublet ϕ as given in Equation (2.5). But in some models of new physics the Higgs¹⁰ is not part of an elementary doublet. Typical examples are composite Higgs models in which the Higgs boson is a pseudo-Goldstone from some strongly interacting dynamics [109–113]. Non-linear Higgs EFT, sometimes simply called ‘Higgs EFT’, is

¹⁰In many scenarios of new physics the observed scalar at 125 GeV is, of course, not the Higgs boson of the Standard Model. We nevertheless refer to it as ‘Higgs boson’.

an effective theory designed for these scenarios [157, 161–170]. This model is also often referred to as ‘chiral Lagrangian’, and indeed its structure is similar to that of chiral perturbation theory, for an introduction see for instance References [171, 172]. Again, we begin by going through the ingredients to the effective theory before constructing the Lagrangian.

The **particle content** of the non-linear Higgs EFT constitutes the main difference to the linear Lagrangian: the physical scalar h is separated from the Goldstones w^a , both are included as independent degrees of freedom rather than as part of the doublet ϕ . The Higgs boson h is now a singlet under the SM gauge symmetry. The Goldstone bosons w^a are organised in the exponential form

$$U = e^{i\sigma^a w^a/v}, \quad (2.59)$$

where σ^a are the Pauli matrices. The Goldstones transform non-linearly under the (approximate) global custodial symmetry $SU(2)_L \times SU(2)_R$, giving the EFT its name.

The **symmetries** are the same as in the linear case. We require invariance under Lorentz transformations as well as under the SM gauge group $SU(3)_C \times SU(2)_L \times U(1)_Y$ and baryon and lepton number conservation. For simplicity, we also focus our brief discussion on CP -even operators that conserve lepton flavour.

Choosing the **counting scheme** is a little more complex. To account for strongly interacting scenarios, we now have to distinguish three different scales [167]:

- the electroweak scale $v = 246$ GeV, which defines the W and Z mass, but is not necessarily the Higgs VEV;
- the scale f associated to the Goldstone bosons w^a and the Higgs boson h due to some breaking of the underlying dynamics¹¹, in analogy to the pion decay constant f_π ; and
- the cut-off Λ of the theory. For weakly coupled physics its value is arbitrary. But it can be calculated that the low-energy effective theories from spontaneously broken strongly coupled dynamics break down around $\Lambda \approx 4\pi f$ [171]. A cut-off of this size guarantees that the EFT is renormalisable order by order.

The existence of three scales means there are two dimensionless parameters, so in general the EFT terms are organised in a double expansion [167]. The first is

$$\xi \equiv \frac{v^2}{f^2}. \quad (2.60)$$

The value of ξ defines the non-linearity of the model: the limit $\xi \rightarrow 0$ restores the linear Lagrangian. An expansion in ξ exactly corresponds to the power-counting scheme of the linear EFT, i. e. it orders operators by their canonical dimension.

¹¹In general, the scales associated with w^a and h , f_w and f_h , can be different, making the power-counting even more complicated.

The second dimensionless parameter is

$$\frac{f^2}{\Lambda^2} \approx \frac{1}{16\pi^2} \quad (2.61)$$

for strongly coupled scenarios. Since this is of the same size as a loop factor, expanding in f^2/Λ^2 corresponds to a loop expansion, similar to that in chiral perturbation theory. Equivalently, one can define a **chiral dimension** $\chi = [\mathcal{O}]_c$ for each operator \mathcal{O} with the assignments [167]

$$\begin{aligned} [f]_c &= 1, & [A_\mu]_c &= 0, & [F_{\mu\nu}]_c &= 1, & [U]_c &= 0, & [h]_c &= 0, \\ [\partial_\mu]_c &= 1, & [D_\mu]_c &= 1, & [g]_c &= 1, & [y_f]_c &= 1, \end{aligned} \quad (2.62)$$

where we use A_μ and $F_{\mu\nu}$ to denote any vector boson, since the symbol V_μ is conventionally used for a different purpose in this context. The loop order L of an operator is equivalent to the chiral dimension $\chi = 2L + 2$. This chiral counting can also be linked to an expansion in \hbar [173].

The correct expansion scheme depends on the value of ξ . For $\xi \gg 1/16\pi^2$ or $f \ll 3$ TeV, the chiral expansion is more appropriate. For $\xi \ll 1/16\pi^2$ or $f \gg 3$ TeV, the canonical expansion is correct. In the intermediate region, a combined expansion gives the best results. Since LHC Higgs physics is mostly sensitive to new physics scenarios with $f \ll 3$ TeV, the chiral expansion can be considered phenomenologically more relevant. For a more thorough discussion of power counting in this framework, see Reference [174].

At the leading chiral order $\chi = 2$ or $L = 0$, the Higgs sector of the Lagrangian is given by [165]¹²

$$\begin{aligned} \mathcal{L}_{\text{non-linear EFT}} \supset & \frac{1}{2} \partial_\mu h \partial^\mu h (1 + c_H \xi \mathcal{F}_H(h)) - V(h) \\ & - \frac{v^2}{4} \text{tr}[V_\mu V^\mu] \mathcal{F}_C(h) + c_T \xi \frac{v^2}{4} \text{tr}[TV^\mu] \text{tr}[TV_\mu] \mathcal{F}_T(h) \\ & - \frac{v}{\sqrt{2}} \left[\sum_f \bar{f}_L U y_f \mathcal{F}_Y^f(h) P_f f_R + \text{h. c.} \right] \end{aligned} \quad (2.63)$$

with $V_\mu \equiv (D_\mu U)U^\dagger$, $T \equiv U\sigma_3 U^\dagger$ and projectors $P_u = (\mathbb{1} + \sigma_3)/2$, $P_d = P_\ell = (\mathbb{1} - \sigma_3)/2$. The functions $\mathcal{F}_C(h)$, $V(h)$, $\mathcal{F}_T(h)$, $\mathcal{F}_T(h)$, $\mathcal{F}_Y^u(h)$, $\mathcal{F}_Y^d(h)$, and $\mathcal{F}_Y^\ell(h)$ encode the coupling of the Higgs h and are arbitrary functions. They can be expanded as a power series in h/f , or to simplify the expressions in h/v , for instance

$$\mathcal{F}_C(h) = 1 + 2a_C \frac{h}{v} + b_C \left(\frac{h}{v} \right)^2 + \dots \quad (2.64)$$

¹²Two comments on this Lagrangian are in order. First, in principle there could be further functions of h coupling to the kinetic terms of the gauge bosons. Such interactions arise in typical strongly coupled theories at one-loop level with a coefficient $\sim 1/(16\pi^2)$ and are therefore usually classified as NLO operators [165, 166]. Second, the function $\mathcal{F}_C(h)$ (and a corresponding one for the fermion kinetic terms) can be removed with field redefinitions, shifting its effects into the other couplings [166, 170].

At next-to-leading order in the chiral expansion, many more terms relevant for Higgs physics appear. We do not list them here and refer the interested reader for example to Reference [168].

Finally, the relationship between the linear and non-linear effective theories deserves some discussion. The two approaches in principle provide different parametrisations of the same physics, as can be seen by expanding the non-linear Lagrangian in ξ rather than χ . The difference is the ordering of the operators in the EFT expansion and, equivalently, the expected size of different effects. Operators that appear at one order in the $1/\Lambda$ expansion of the linear EFT may appear at a very different order in the chiral expansion of the non-linear EFT.

Since the symmetry requirements on the non-linear setup are smaller, we expect it to be more general than the linear Lagrangian at a comparable order in the expansions. This is exactly what is found when comparing the linear dimension-six operators to the NLO chiral Lagrangian: the dimension-six operators predict certain correlations, while the non-linear description has more operators that can break these correlations [168]. A straightforward example is the relation between h_{xx} and hh_{xx} couplings. For dimension-six operators of the form $\phi^\dagger \phi_{xx}$, this ratio is fixed to $2v$, since $\phi^\dagger \phi \sim (v^2 + 2vh + h^2)/2$. In the chiral approach, these couplings are always independent, as can be seen in Equation (2.63).

The current experimental limits leave room for both strongly or weakly coupled new physics, for ξ smaller or larger than $1/(16\pi^2)$, for scenarios in which the linear or non-linear effective theories work better. Only a precise measurement of the Higgs properties and a global analysis of correlations will tell us which approach is correct. As a general rule, more SM-like results favour the linear approach that we follow throughout this thesis [174]. On the other hand, certain deviations that do not follow the correlations predicted by dimension-six operators point towards non-linear physics [168].

κ framework

Effective field theories are of course not the only way to describe the Higgs sector. During Run 1 of the LHC, the most widely used parametrisation was the κ framework [175] or the closely related Δ framework [176]. Its construction is remarkably simple: starting from the SM Higgs sector, all Higgs couplings are dressed with form factors,

$$g_{h_{xx}} = \kappa_x g_{h_{xx}}^{\text{SM}} \equiv (1 + \Delta_x) g_{h_{xx}}^{\text{SM}}, \quad (2.65)$$

such that $\kappa_x = 1$ or $\Delta_x = 0$ corresponds to the SM couplings. Some care has to be taken to treat the Higgs-gluon and Higgs-photon couplings consistently, where indirect effects of shifted Higgs-top or Higgs- W couplings compete with direct effects from new physics [176].

From a theoretical point of view, the κ framework is not gauge-invariant and does not present a consistent quantum field theory. In particular, calculating electroweak loop effects in the κ

framework can introduce divergences that cannot be renormalised [177]. This problem can be solved by embedding the κ framework in a UV completion [178].

From a more phenomenological point of view, this approach is well suited to parametrise measurements of total rates. Simple shifts of SM-like Higgs coupling structures are expected in some scenarios of new physics, for instance in many scalar extensions of the Higgs sector [178]. But many other models predict new kinematic features, visible as changed kinematic shapes, and the κ framework is unable to describe these. For better or worse, it is also agnostic about correlations between different Higgs couplings, and about correlations between Higgs observables and triple gauge vertices or electroweak precision measurements.

The strength of the κ framework is clearly not its theoretical foundation. Its allure comes from its simplicity and the fact that it is designed around the simple question of measuring the couplings of the (SM-like) Higgs boson. This parametrisation made sense as a common denominator for the first Higgs measurements with limited statistics of Run 1 of the LHC. But the increased amount of data and crucial kinematic information collected during Run 2 require a different, more sophisticated language.

Pseudo-Observables

Higgs pseudo-observables (POs) [179–181] are designed as a generalisation of the κ framework to include BSM kinematic features. In a very broad sense, this term encompasses any quantity that is field theoretically defined and can be experimentally accessed [174]. Signal strengths, cross sections, partial widths, total widths, and individual form factors or couplings all fall under this umbrella term. Here we follow the more narrow definition of effective-coupling POs [3]. They are defined process by process by writing down all contributing amplitudes under some broad assumptions on new physics. These expressions are then decomposed in a pole expansion, and the resulting residues are identified as pseudo-observables. This procedure also requires an expansion in the inverse of the new physics scale Λ . Just as the EFT approach, pseudo-observables thus rely on new physics being heavy, $E \ll \Lambda$. So far, this framework has been developed for Higgs production in WBF and Higgs-strahlung, as well as for all phenomenologically relevant Higgs decays.

Phenomenologically, pseudo-observables can describe shifts in SM couplings as well as kinematic shapes. Like the EFT approach, their construction requires certain minimal assumptions on the symmetries of new physics as well as an expansion in $1/\Lambda$. In fact, at tree level pseudo-observables can be mapped directly to the Wilson coefficients of an EFT constructed with the same ingredients (which is the non-linear Higgs EFT discussed above).

The main difference between pseudo-observables and the EFT approach is a conceptual one. Pseudo-observables are designed from the perspective of a given process: they describe the coefficients of the different contributing amplitudes. They are not parameters of a Lagrangian and do not define a consistent quantum field theory. In particular, the values of POs measured

in one process have no meaning for other processes. Effective operators on the other hand are a proper, gauge-invariant quantum field theory that universally describes any physics below the cutoff scale, and the same Wilson coefficients predict the behaviour of very different processes.

Proponents of the PO approach favour a multi-layer interpretation of LHC data, where the data is first presented in terms of pseudo-observables, and can then be interpreted in terms of EFTs or specific models of UV physics. They argue that this approach provides a clear separation between measurement and interpretation [3]. On the other hand, proponents of the ‘direct EFT approach’ argue that there is no need for such an intermediate layer, and suggest to directly fit effective operators. The debate about which approach is better is still ongoing [3]. Ultimately, both effective operators and POs are well-defined frameworks that can describe all relevant kinematic effects, and thus present a suitable interface between experiment and theory.

Simplified models

The parametrisations discussed so far have in common that they assume the absence of new light particles. Simplified models are designed to close this gap and to describe kinematic effects from new light resonances. In addition to resonance peaks, these include threshold effects in loops and Higgs decays into (invisible) new light degrees of freedom. Simplified models thus allow to combine information from direct searches with indirect measurements. Except for the key element of adding new light propagating degrees of freedom to the SM, the term is not particularly well-defined, and there is a lot of freedom to construct such models.

The simplest version of a simplified model consists of the SM supplemented with another particle, with ad-hoc coupling structures based on phenomenological requirements [2]. Such a setup might even be not gauge-invariant and thus inconsistent beyond tree level. At the other end of the spectrum, simplified models can be consistently defined quantum field theories, potentially involving higher-dimensional operators. The only difference to the linear and non-linear EFT approaches discussed above is the extended particle content. The additional flexibility, of course, comes at the price of an increased number of parameters.

Examples of such models for Higgs physics include an extended Higgs sector with an additional singlet and a doublet, which offers great flexibility to tune the Higgs couplings [178]. The authors of Reference [182] develop a model with an additional singlet and vector-like quarks. Finally, References [156, 183] discuss additional scalar singlets supplemented with higher-dimensional operators.

Comparison

All of these approaches define parametrisations of the Higgs properties that can be used as interfaces between different measurements and between experiment and theory. In Table 2.5 we summarise and compare their different properties.

	κ framework	POs	Non-linear EFT	Linear EFT	Simplified models
Motivation	experiment: simplest Higgs parametrisation	experiment: amplitude decomposition for a given process	theory: complete low-energy effects of NP with singlet h	theory: complete low-energy effects of NP with doublet ϕ	exp. / theory: new light particles
Input	SM Higgs couplings	process amplitudes, pole expansion, NP expansion $(1/\Lambda)$	SM particles (h), symmetries, counting scheme (loops)	SM particles (ϕ), symmetries, counting scheme ($1/\Lambda$)	new particles (masses, charges, interactions)
Parameters	coefficients of SM amplitude	coefficients of SM & NP amplitudes	Lagrangian parameters of consistent QFT	Lagrangian parameters of consistent QFT	depends
Validity conditions	SM-like NP	NP heavy, symmetries	NP heavy, symmetries	NP heavy, symmetries	single light new particles, other NP decouples
Shifted SM couplings	yes	yes	yes	yes	depends
Kinematic effects	no	yes	yes	yes	depends
New resonances, loop thresholds, invisible decays	no	no	no	no	yes
Correlations	no	no	some	many	depends

Table 2.5: Comparison between different parametrisations of Higgs properties. The upper part of the table focuses on the theoretical foundation, the lower on the phenomenology. Since ‘simplified models’ describe a rather general idea, many details depend on the specific realisation.

The different frameworks can be classified into consistent quantum field theories, which include the EFTs, and process-based parametrisations of amplitudes through form factors, such as the κ framework and pseudo-observables. Simplified models can fall into either category. Only the QFT formalism allows to link different processes and to incorporate any loop effects.

More important for practical purposes is the range of phenomena that can be described. The κ framework is limited to rescalings of the SM Higgs couplings and is not able to incorporate kinematic information. Pseudo-observables and the two EFT approaches are much more flexible and can describe a large number of kinematic features. However, they rely on new physics being substantially heavier than the experimentally probed energies around the weak scale. Features from light new particles, for instance resonances or loop thresholds, are only covered by appropriate simplified models. The dimension-six operators of linear Higgs EFT, and to a lesser extent the leading operators of the chiral EFT, also predict certain correlations between different couplings and measurements, whereas by definition the pseudo-observables are only valid for a given process.

To summarise, in the absence of new light particles, Higgs properties can be adequately parametrised by pseudo-observables, non-linear Higgs EFT, and linear Higgs EFT. The linear EFT approach is theoretically consistent, well-motivated, and phenomenologically powerful, and we focus on this framework during this thesis.

Chapter 3

Higgs effective theory at its limits

A HIERARCHY OF SCALES between the experimental momentum transfer and the new physics scale is the key premise behind the effective field theory paradigm described in the previous chapter. However, the limited precision of the LHC means that Higgs measurements are often only sensitive to models characterised by mass scales just above the electroweak scale. In this chapter we discuss if and when the EFT approach is nevertheless useful for Higgs physics, and how its validity can be improved.

In Section 3.1 we estimate the new physics scales probed by LHC Higgs measurements and formulate our strategy to test the dimension-six approach. The validity of the effective approach at the LHC depends on details of the matching procedure, which we discuss in Section 3.2. Section 3.3 contains the bulk of our results: the comparison of full models to their EFT approximations for a variety of scenarios. We go into more detail and analyse some practical questions in Section 3.4, and give our conclusions in Section 3.5.

Most of the work presented in this chapter was previously published in Reference [1], while the content of Section 3.4 was published in Reference [2]. A part of the content of this chapter was also included in Reference [3]. Nearly all of the results and most of their presentation in this chapter — including most plots and tables as well as a significant part of the text — are identical to that in these three publications.

3.1 Introduction

There is no doubt that effective field theories work extraordinarily well as long as there is a large separation between the experimentally probed energy and the new physics scale, $E \ll \Lambda$. On the other hand, one expects the EFT expansion to break down at $E \geq \Lambda$, where an infinite number of operators contribute at the same size and the effective model is neither predictive nor

renormalisable. The validity of the EFT in the intermediate region, $E \lesssim \Lambda$, is less obvious and will depend on the specific underlying model as well as on the observable studied.

In which of these categories do the LHC Higgs measurements fall? There is no immediately obvious answer, since Higgs production does not probe only a single experimental energy scale. While the momentum transfer is bounded from below by the Higgs mass m_h , selection criteria necessary to separate the signal from the QCD backgrounds often require a higher momentum transfer $E > m_h$. More importantly, most of the information on operators with derivatives comes from high-energy tails, as demonstrated in Section 2.3.3. During Run 1, significant event numbers have been recorded approximately within the range [26]

$$m_h \leq E \lesssim \mathcal{O}(400 \text{ GeV}) , \quad (3.1)$$

depending on the process, observable, amount of data collected, and analysis methods.

This has to be compared to the new physics scale Λ that LHC Higgs measurements are able to probe. Assuming a 10% precision on total Higgs rate measurements and no loop suppression of new physics effects, such a signature lies within the experimental reach of the LHC if

$$\left| \frac{\sigma \times \text{BR}}{(\sigma \times \text{BR})_{\text{SM}}} - 1 \right| \approx \frac{g^2 m_h^2}{\Lambda^2} \gtrsim 10\% \quad \Leftrightarrow \quad \Lambda \lesssim \frac{g m_h}{\sqrt{10\%}} \approx g \cdot 400 \text{ GeV}. \quad (3.2)$$

Here g is a typical coupling of the underlying theory and $\sigma \times \text{BR}$ the Higgs production cross section times branching ratio.

This simple estimate shows that the scale separation E/Λ is limited by the experimental precision and crucially depends on the size of the couplings of the underlying physics. For very weakly coupled theories, $g^2 \ll 1$, only new physics models with new particles at or below the electroweak scale can leave measurable signatures in Higgs observables, and the EFT approach is not justified. For truly strongly coupled theories, $1 < g \lesssim 4\pi$, new physics scenarios up to $\Lambda \lesssim 5 \text{ TeV}$ are relevant, and the EFT expansion converges flawlessly. In fact, the EFT approach to Higgs observables has largely been motivated by the desire to describe models based on a strongly interacting electroweak symmetry breaking [149]. For moderately weakly to moderately strongly coupled theories, $1/2 \lesssim g^2 \lesssim 2$, the LHC Higgs programme is sensitive to scales

$$280 \text{ GeV} \lesssim \Lambda \lesssim 560 \text{ GeV}. \quad (3.3)$$

This corresponds exactly to the intermediate region $E \lesssim \Lambda$ discussed at the beginning of this chapter. In this simple argument we ignored that new physics might also change distributions and especially affect the high-energy tails or off-shell regions.

A thorough global fit of Higgs results including kinematic information confirms the rough estimate given in Equation (3.3) [26]. Related to this is our work in Chapter 4, where we develop methods that let us calculate the maximum new physics scale that can be probed in a given process.

For moderately weakly coupled scenarios of new physics, the limited precision of LHC Higgs measurements therefore cannot guarantee a clear scale hierarchy, and the EFT expansion in $1/\Lambda$ does not converge fast. But this does not mean that an analysis of LHC data in terms of a truncated dimension-six Lagrangian cannot be useful. Instead, the applicability of the dimension-six model now depends on the nature of the underlying physics as well as on the process and observable, and has to be carefully checked for each situation.

From a practical perspective, the dimension-six operators work flawlessly as a framework to fit Higgs data including kinematic distributions [26]. Even if the LHC constraints do not induce a hierarchy of scales, and the EFT expansion does not converge, there appears to be no problem in using the truncated dimension-six Lagrangian as a phenomenological model. Translating limits on the dimension-six model to specific new-physics scenarios then induces model-dependent and process-dependent theory uncertainties [184].

In this chapter we analyse the usefulness of the dimension-six description of the Higgs sector with a comprehensive comparison between full models and their effective approximations. We select four specific models of new physics, map them onto dimension-six operators, and compare the predictions of the full and the effective model for a range of Higgs observables. In this way we analyse the convergence of the EFT expansion in $1/\Lambda$ by comparing the dimension-six operators not just to the dimension-eight terms, but to the infinite number of operators corresponding to the full model.

Our benchmark cases are moderately weakly interacting extensions of the Higgs sector of the Standard Model by a scalar singlet, a scalar doublet, coloured scalar top partners, and a massive vector triplet. For each of these models, we define a number of parameter points designed to highlight phenomenological features of the model and to be within the experimental reach of the LHC Higgs programme.

The corresponding EFT descriptions are constructed by integrating out the heavy fields and expanding the effective action to $\mathcal{O}(1/\Lambda^2)$. In other words, we match the theories to the dimension-six operators of the linear Higgs EFT introduced in Section 2.3.2. In the situation where the new physics scale is relatively close to the electroweak VEV, electroweak symmetry breaking can define additional scales and lead to ambiguities in the matching procedure. These subtleties can be crucial for Higgs signatures and will be discussed in detail in the next section.

For all of these scenarios, we calculate the Higgs couplings, and in a next step rates and distributions for selected Higgs production modes and decay channels. The key questions we aim to address are:

- Which observables are correctly described by the dimension-six model?
- Where does the EFT description break down, and does this pose a problem for LHC analyses?
- Can we improve the EFT performance with a refined matching procedure?

In this way, we analyse what problems the lack of a clear hierarchy of scales leads to in practice, and discuss how these might affect global fits. Turning the argument around, we ask whether and when the analysis of a UV-complete model offers an advantage compared to the effective theory.

After this broad survey of the applicability of dimension-six operators, we focus on the vector triplet scenario and Higgs production in weak boson fusion to discuss some practical aspects. First, we analyse which kinematic observables are particularly useful to characterise the validity of the EFT approach in WBF Higgs production. We then discuss whether the square of amplitudes from dimension-six operators should be included in calculations while dimension-eight operators are neglected. Both contribute to cross sections at $\mathcal{O}(1/\Lambda^4)$. Finally, we show how the EFT validity and its breakdown affect the limit-setting procedure when the EFT is used as an intermediate parametrisation.

In addition and partly simultaneously to our work, published in References [1, 2], the applicability of EFTs to Higgs physics at the LHC was studied in a range of different situations [3, 185–197]. The differences to our work lie in the considered new physics scenarios and observables. A great deal of attention has been focused on Higgs production in weak boson fusion and its sensitivity to UV physics [85, 86, 88, 89, 198]. Similar points were discussed for Higgs-strahlung [185], for the production of (potentially off-shell) Higgs bosons in gluon fusion [190, 194, 199–201], and for electroweak precision observables as well as Higgs decays to photons [197]. With the notable exception of Reference [197], these other studies generally do not discuss ambiguities in the matching procedure, a central aspect of the research presented here.

Validity issues from a lacking scale hierarchy are not unique to the EFT approach. As discussed at the end of Section 2.3.4, pseudo-observables rely on the same expansion in $1/\Lambda$, and the breakdown of this expansion has been studied in Reference [181].

Finally, similar concerns have fuelled an intense investigation in the context of dark matter searches [202–207]. In that field, EFT-based predictions are usually robust for early-universe and late-time annihilation rates and for dark matter-nucleon scattering, but the required hierarchy of scales often breaks down for dark matter signals at colliders.

3.2 Matching intricacies

3.2.1 Ambiguities

Before discussing the individual models and presenting our results, we have to define how we construct the effective theories. Matching the dimension-six Lagrangian to a full model is a three-step procedure. Its starting point is the definition of a heavy mass scale Λ . Second, we integrate out the degrees of freedom above Λ as described in Section 2.2.3, which leads to an

infinite tower of higher-dimensional operators. Finally, this effective action is truncated so that only the dimension-six terms, suppressed by $1/\Lambda^2$, remain.

The matching is not unambiguous: on the one hand, Λ is usually not uniquely defined. Consider a new physics scenario with only one heavy mass scale M in the Lagrangian, but also some mixing terms of the new fields with the SM Higgs doublet. In the unbroken electroweak phase the only new physics scale is then

$$\Lambda_1 = M. \quad (3.4)$$

But after electroweak symmetry breaking, the electroweak VEV v contributes through the mixing term to the actual physical masses m of the new particles. This defines additional scales of the form

$$\Lambda_2^2 = m^2 = M^2 \pm gv^2, \quad (3.5)$$

where g is a combination of couplings or mixing angles. Of course there can be many such scales.

Further ambiguities arise in the third step since we can choose which parameters to keep constant while expanding in $1/\Lambda$. For instance we can choose to express the Wilson coefficients in terms of Lagrangian couplings or in terms of mixing angles. Again, the first choice corresponds to the natural choice in the unbroken phase of the electroweak symmetry, while the latter is often only defined in the broken phase.

For both the cutoff scale and the Wilson coefficients, switching from one choice to another is equivalent to including additional contributions suppressed by more powers of v^2/Λ^2 to the Wilson coefficients of the dimension-six operators. In the first example,

$$\frac{f_i}{m^2} \mathcal{O}_x = \frac{f_i}{M^2 \pm gv^2} \mathcal{O}_i = \left(\frac{f_i}{M^2} \mp \frac{f_i g v^2}{M^4} \right) \mathcal{O}_i + \mathcal{O}(1/M^6). \quad (3.6)$$

It should be stressed that these choices affect observables at $\mathcal{O}(1/\Lambda^4)$, the same order in the EFT expansion as the leading effects from dimension-eight operators, which we always neglect. From a purely theoretical point of view these terms are subleading, and indeed in the obvious validity regime of the EFT they are irrelevant. However, as we discussed in the previous section, this is not the situation we find at the LHC. Here v^2/Λ^2 is not very small and these formally suppressed terms may be important in practice.

These ambiguities in the matching procedure therefore raise the question if we can improve the agreement between full model and dimension-six Lagrangian by incorporating effects of the non-zero electroweak VEV in the matching. To answer this question we now define two different matching prescriptions.

3.2.2 Default vs. v -improved matching

Our **default matching** follows a purely theoretical motivation and represents the conventional approach for the linear Higgs EFT. The dimension-six operators are formulated in terms of the doublet ϕ and based on the assumption $\Lambda \gg v$, so the EFT should be matched to the full theory in the unbroken phase of the electroweak symmetry. An obvious choice for the matching scale is then the mass scale of new particles in the limit of $v \rightarrow 0$, which, as in our simple example above, we denote

$$\Lambda_{\text{default}} = M . \quad (3.7)$$

For simplicity we assume there is only one such scale, i. e. that all new particles are mass-degenerate in the unbroken electroweak phase. Otherwise the new particles would have to be integrated out consecutively at different scales M_i . We then expand the effective action, expressed in parameters of the Lagrangian, and drop all terms of $\mathcal{O}(1/\Lambda^4)$.

Alternatively, we define a **v -improved matching** procedure that accounts for additional terms suppressed by v^2/Λ^2 in the Wilson coefficients of the dimension-six Lagrangian. This corresponds to matching the linear EFT in the broken electroweak phase. In the first matching step, we define Λ as the physical mass m of the new particles in the broken phase including contributions from v ,

$$\Lambda_{v\text{-improved}} = m . \quad (3.8)$$

Again, multiple particles with substantial mass splittings will require a multi-step matching procedure. The Wilson coefficients are expressed in terms of phenomenologically relevant quantities such as mixing angles and physical masses, again defined in the broken phase. This is a somewhat subjective criterion that depends on the model and process — the v -improved matching procedure is not uniquely defined, but rather a general guideline.

3.2.3 Making sense of v -improvement

Let us try to understand v -improved matching from a different perspective. Integrating out heavy particles generates an infinite number of operators with different mass dimensions. Some of the operators of dimension eight or higher are of the form

$$\mathcal{O}_i^{(d=6+2n)} = (\phi^\dagger \phi)^n \mathcal{O}_i^{(6)}, \quad (3.9)$$

where $\mathcal{O}_i^{(6)}$ is a dimension-six operator. The tower of higher-dimensional operators can be re-organised as

$$\begin{aligned}\mathcal{L}_{\text{EFT}} &\equiv \mathcal{L}_{\text{SM}} + \sum_i \frac{f_i^{(6)}}{\Lambda^2} \mathcal{O}_i^{(6)} + \sum_{d=8}^{\infty} \sum_j \frac{f_j^{(d)}}{\Lambda^{d-4}} \mathcal{O}_j^{(d)} \\ &= \mathcal{L}_{\text{SM}} + \sum_i \frac{f_i^{(6)}}{\Lambda^2} \mathcal{O}_i^{(6)} + \sum_i \sum_{n=1}^{\infty} \frac{f_i^{(6+2n)}}{\Lambda^{2+2n}} (\phi^\dagger \phi)^n \mathcal{O}_i^{(6)} + \sum_{d=8}^{\infty} \sum_k \frac{f_k^{(d)}}{\Lambda^{d-4}} \mathcal{O}_k^{(d)},\end{aligned}\quad (3.10)$$

where $\mathcal{O}_k^{(d)}$ are the dimension-eight and higher operators of a different form than Equation (3.9). A v -improved matching corresponds to replacing $\phi^\dagger \phi \rightarrow v^2/2$ in (part of) the second sum¹:

$$\mathcal{L}_{v\text{-improved dim-6}} = \mathcal{L}_{\text{SM}} + \underbrace{\sum_i \left[\frac{f_i^{(6)}}{\Lambda^2} + \sum_{n=1}^{\infty} \frac{f_i^{(6+2n)}}{\Lambda^{2+2n}} \left(\frac{v^2}{2} \right)^n \right] \mathcal{O}_i^{(6)}}_{(f_i^{(6)}/\Lambda^2)_{v\text{-improved}}}.\quad (3.11)$$

So from the perspective of the unbroken phase of the electroweak symmetry, v -improvement corresponds to a **partial resummation of dimension-eight and higher operators** into the Wilson coefficients of the dimension-six operators. The remaining parts of the operators in Equation (3.9) (the terms from $\phi^\dagger \phi \rightarrow vh + h^2/2$) and the higher-order operators of an entirely different type cannot be absorbed into the dimension-six Lagrangian in this way.

Let us illustrate this with the example of Section 3.2.1, where a heavy particle with mass scale M in the unbroken electroweak phase has a coupling g to Higgs doublets. Matching the theory in the unbroken phase, we find dimension-six operators of the form

$$\begin{array}{ccc} \text{Diagram: } & \text{Diagram: } & = \frac{f_i^{(6)}}{M^2} \mathcal{O}_i^{(6)}. \end{array} \quad (3.12)$$

The effect of the coupling g to the Higgs doublet only appears at dimension eight and higher, for instance as

$$\begin{array}{ccc} \text{Diagram: } & \text{Diagram: } & = \frac{g f_i^{(6)}}{M^4} \phi^\dagger \phi \mathcal{O}_i^{(6)}. \end{array} \quad (3.13)$$

¹The argument is slightly more complicated if additional powers of ϕ appear in $\mathcal{O}_i^{(6)}$. One can then also take into account terms where instances of ϕ in $\mathcal{O}_i^{(6)}$ are replaced by the VEV and fields in the prefactor are left alone. This effectively adds a combinatorial factor to the definition of the v -improved Wilson coefficient in Equation (3.11).

The v -improved matching replaces $M \rightarrow m$ as the suppression scale of the dimension-six operator,

$$\begin{array}{c}
 \text{Diagram: } \text{---} \times \text{---} = \text{---} \bullet \text{---} + \text{---} \bullet \text{---} \times \text{---} + \dots \\
 \text{Equation: } \frac{f_i^{(6)}}{m^2} \mathcal{O}_i^{(6)} = \frac{f_i^{(6)}}{M^2} \mathcal{O}_i^{(6)} + \frac{g f_i^{(6)}}{M^4} \frac{v^2}{2} \mathcal{O}_i^{(6)} + \dots
 \end{array} \quad (3.14)$$

equivalent to a partial absorption of the dimension-eight and higher operators with the replacement $\phi^\dagger \phi \rightarrow v^2/2$.

But such musings are not required to apply a v -improved matching in practice. In fact, from an experimental point of view (or in the broken electroweak phase), physical masses and mixing angles are simply a natural choice of parameters to describe a model. We thus expect that the v -improved matching procedure can improve the validity of the dimension-six model. To be precise, we have to distinguish between an expansion in v/Λ and E/Λ . We expect the v -improved matching prescription to lead to a better agreement with the full models in situations where the expansion in v/Λ is relevant, while it cannot help with the expansion in E/Λ , corresponding to genuine new dimension-eight operators not of the form in Equation (3.9). We come back to this difference in Section 3.3.5.

Again, the truncation of the EFT Lagrangian is formally justified as long as $v \ll \Lambda$ and we only probe energies $E \ll \Lambda$. In this limit the dimension-eight operators as well as the Λ -suppressed terms in the Wilson coefficients are negligible; our two matching procedures then give identical results. In the absence of a large enough scale separation, we can test if the v -improved matching enhances the validity of the dimension-six Lagrangian.

3.3 Full models vs. effective theory

The main aim of this chapter is to compare a comprehensive set of LHC predictions from specific new physics models to their corresponding effective field theory predictions. In this way we test the applicability of the dimension-six model for four different, more or less UV-complete, scenarios of underlying physics:

1. a scalar singlet extension, where the new scalar mixes with the SM-like Higgs;
2. a two-Higgs doublet model, adding a variable Yukawa structure;
3. scalar top partners, contributing to Higgs couplings at one loop; and

4. a vector triplet with gauge boson mixing.

This ensemble of models covers a wide range of CP -even new physics signatures in the Higgs sector.

After describing our technical setup, we analyse these four scenarios one by one. For each model we first define the theory and introduce the main phenomenological features at the LHC. We discuss the decoupling in the Higgs sector and derive the dimension-six setup. Finally, we define a number of benchmark points and give a detailed account of the full and dimension-six phenomenology at the LHC.

Effects in SM-like Higgs couplings will be parametrised with the relative shifts from the SM values

$$\Delta_x \equiv \frac{g_{hxx}}{g_{hxx}^{\text{SM}}} - 1, \quad (3.15)$$

as defined in Equation (2.65). Unlike in the published version [1], we express the effective Lagrangian in the HISZ basis with the ten dimension-six operators of Equation (2.45).

3.3.1 Setup

Our comparison covers the most relevant observables for LHC Higgs physics. Acceptance and background rejection cuts are kept to a minimum to be able to test the effective field theory approach over as much of the phase space as possible.

In the case of Higgs production through gluon fusion, we analyse the production process on its own and with a Higgs decay to four leptons or to photons,

$$\begin{aligned} gg &\rightarrow h \rightarrow 4\ell, \\ gg &\rightarrow h \rightarrow \gamma\gamma. \end{aligned} \quad (3.16)$$

For the photons we do not apply any cuts, while for $\ell = e, \mu$ we require²

$$m_{4\ell} > 100 \text{ GeV} \quad \text{and} \quad m_{\ell^+\ell^-}^{\text{same flavour}} > 10 \text{ GeV} \quad (3.17)$$

to avoid large contributions from the Z peak and from bremsstrahlung.

For Higgs production in weak boson fusion (WBF), we first evaluate the pure production process

$$ud \rightarrow h \bar{u}d, \quad (3.18)$$

which is the dominant partonic contribution at the LHC, without any cuts. We also consider WBF production with a decay

$$ud \rightarrow W^+ W^- \bar{u}d \rightarrow (\ell^+ \nu) (\ell^- \bar{\nu}) \bar{u}d, \quad (3.19)$$

²For a definition of all kinematic quantities, see Appendix A.2.

where we require typical WBF cuts

$$\begin{aligned} p_{T,j} > 20 \text{ GeV}, & \quad \Delta\eta_{jj} > 3.6, & \quad m_{jj} > 500 \text{ GeV}, \\ p_{T,\ell} > 10 \text{ GeV}, & \quad E_T^{\text{miss}} > 10 \text{ GeV}. \end{aligned} \quad (3.20)$$

The WBF kinematics can introduce new scales and a dependence on the UV structure of the model. This has been widely discussed in the context of perturbative unitarity [208–214]. Deviations from the SM Higgs-gauge couplings in the EFT may lead to an increasing rate at very large energies [215], well outside the EFT validity range $E/\Lambda \ll 1$. We demonstrate this signature in the high-energy tail of the distribution of the transverse mass

$$m_T^2 = (E_{T,\ell\ell} + E_{T,vv})^2 - (\mathbf{p}_{T,\ell\ell} + \mathbf{p}_T^{\text{miss}})^2 \quad (3.21)$$

with

$$E_{T,\ell\ell} = \sqrt{\mathbf{p}_{T,\ell\ell}^2 + m_{\ell\ell}^2} \quad \text{and} \quad E_{T,vv} = \sqrt{E_T^{\text{miss}}{}^2 + m_{\ell\ell}^2}. \quad (3.22)$$

As the last production mode of single Higgs bosons, we evaluate Higgs-strahlung,

$$q\bar{q} \rightarrow Vh \quad (3.23)$$

with $V = W^\pm, Z$. We do not simulate the Higgs and gauge boson decays, assuming that we can always reconstruct for example the full $Z h \rightarrow \ell^+ \ell^- b\bar{b}$ final state. No cuts are applied.

Finally, Higgs pair production,

$$gg \rightarrow hh, \quad (3.24)$$

is well known to be problematic when it comes to the effective theory description [92, 216, 217]. Again, neither Higgs decays nor kinematic cuts are expected to affect the questions we analyse, hence we leave them out.

We test all these channels for the singlet and doublet Higgs sector extensions. For the top partner and vector triplet models we focus on the WBF and Higgs-strahlung modes.

In the EFT simulations we always include the square of the dimension-six operator contributions. We discuss and justify this choice in Section 3.4.2. We restrict our analysis to the leading order in α_s and α_{ew} , which is sufficient given the size of new physics effects that the LHC is sensitive to. We always take into account interference terms between Higgs and gauge amplitudes.

For tree-level processes we generate event samples with MadGraph 5 [218], using our own model implementations in FeynRules [219, 220]. For the dimension-six predictions we resort to a modified version of the HEL model file [221].

The Higgs-gluon and Higgs-photon couplings are evaluated with the full one-loop form factors [222], including top, bottom, and W loops, as well as new particles present in the respective models. For Higgs pair production, we use a modified version of Reference [223], see also Reference [224].

Other loop effects are analysed using reweighting: we generate event samples using appropriate tree-level couplings. Next, we compute the one-loop matrix element for each phase space point and reweight the events with the ratio of the renormalised one-loop matrix element squared to the tree-level model. For the one-loop matrix elements we utilise FeynArts and FormCalc [225] with our own model files that include the necessary counterterms. The loop form factors are handled with dimensional regularisation in the 't Hooft-Veltman scheme, and written in terms of standard loop integrals. These are further reduced via Passarino-Veltman decomposition and evaluated with the help of LoopTools [226].

Generally we create event samples of at least 10^5 events per benchmark point and process for pp collisions at $\sqrt{s} = 13$ TeV. We use the CTEQ6L parton density function [227] and the default dynamical choices of the factorisation and renormalisation scale implemented in MadGraph 5. For this broad survey of EFT validity we limit ourselves to parton level and do not apply a detector simulation. The mass of the SM-like Higgs is fixed to $m_h = 125$ GeV [228], for the top mass we take $m_t = 173.2$ GeV [229, 230]. The Higgs width in each model is based on calculations with HDECAY [231], which we rescale with the appropriate coupling modifiers and complement with additional decay channels where applicable. Since we consider new physics scales close to the experimental energies, effects from the RG running of the Wilson coefficients are small, and we neglect them in line with the discussion in Section 2.3.2.

3.3.2 Singlet extension

Model setup

The simplest extension of the minimal Higgs sector of the Standard Model adds a real scalar singlet S [123, 232–237]. For the sake of simplicity we consider a minimal version of the singlet model, in which a discrete \mathbb{Z}_2 parity forbids additional terms in the potential. The theory is then given by

$$\mathcal{L}_{\text{singlet}} \supset (D_\mu \phi)^\dagger (D^\mu \phi) + \frac{1}{2} \partial_\mu S \partial^\mu S - V(\phi, S), \quad (3.25)$$

where the scalar potential has the form

$$V(\phi, S) = \mu_1^2 \phi^\dagger \phi + \lambda_1 (\phi^\dagger \phi)^2 + \mu_2^2 S^2 + \lambda_2 S^4 + \lambda_3 (\phi^\dagger \phi) S^2 \quad (3.26)$$

and the μ_i and λ_i are real parameters. The new scalar S can mix with the SM doublet ϕ if the singlet develops a VEV,

$$\langle S \rangle = \frac{v_s}{\sqrt{2}}, \quad (3.27)$$

leading to a mixing angle of

$$\tan(2\alpha) = \frac{\lambda_3 v v_s}{\lambda_2 v_s^2 - \lambda_1 v^2}. \quad (3.28)$$

Details on the parametrisation and Higgs mass spectrum are given in Appendix A.5.1.

Signatures and decoupling patterns

The additional scalar singlet affects Higgs physics in three ways. First, it mixes with the Higgs via the mixing angle α , which leads to a universal rescaling of all Higgs couplings to fermions and vectors. Second, it modifies the Higgs self-coupling. Finally, it introduces a new, heavy resonance H coupled to the Standard Model through mixing.

The key parameter is the portal interaction between the doublet and the singlet $\lambda_3(\phi^\dagger\phi)S^2$, which is responsible for the mixed mass eigenstates. The mixing reduces the couplings of the SM-like Higgs h to all other Standard Model particles universally,

$$\Delta_x = \cos \alpha - 1 \quad (3.29)$$

where $x = W, Z, t, b, \tau, g, \gamma, \dots$ includes all SM fermions and vectors. It also affects the self-coupling of the light Higgs, which takes on the form

$$g_{hhh} = 6 \cos^3 \alpha \lambda_1 v - 3 \cos^2 \alpha \sin \alpha \lambda_3 v_s + 3 \cos \alpha \sin^2 \alpha \lambda_3 v - 6 \sin^3 \alpha \lambda_2 v_s. \quad (3.30)$$

The parameter $\sin \alpha$ quantifies the departure from the SM limit $\alpha \rightarrow 0$. This limit can be attained in two ways: first, a small mixing angle can be caused by a weak portal interaction,

$$|\tan(2\alpha)| = \left| \frac{\lambda_3 v v_s}{\lambda_2 v_s^2 - \lambda_1 v^2} \right| \ll 1 \quad \text{if} \quad \lambda_3 \ll 1. \quad (3.31)$$

The Higgs couplings to SM particles approach their SM values, but there is no large mass scale associated with this limit. In the extreme case of $\lambda_2, \lambda_3 \ll \lambda_1$ we find a small $|\alpha| \approx |\lambda_3/\lambda_1| v_s/(2v)$ even for $v_s \lesssim v$. This situation mirrors the ‘alignment without decoupling’ scenario in the Two-Higgs-doublet model (2HDM) [238, 239] or the Minimal Supersymmetric Standard Model (MSSM) [240, 241]. It relies on a weak portal coupling and a small scale separation, which cannot be properly described by an effective field theory.

As a second possibility, the additional singlet can introduce a large mass scale $v_s \gg v$, giving us

$$\tan \alpha \approx \frac{\lambda_3}{2\lambda_2} \frac{v}{v_s} \ll 1 \quad \text{if} \quad v \ll v_s, \quad (3.32)$$

where $\lambda_3/(2\lambda_2)$ is an effective coupling of up to order one. In this limit the heavy Higgs mass is given by

$$m_H \approx \sqrt{2\lambda_2} v_s. \quad (3.33)$$

In terms of m_H , the Higgs couplings scale as

$$\Delta_x = -\frac{\alpha^2}{2} + \mathcal{O}(\alpha^3) \approx -\frac{\lambda_3^2}{4\lambda_2} \left(\frac{v}{m_H} \right)^2. \quad (3.34)$$

This shift is suppressed by two powers of a heavy mass scale, corresponding to the effect of a dimension-six operator. If we require effects large enough to be measurable at the LHC, $|\Delta_x| \gtrsim 10\%$, this implies

$$m_H \lesssim \frac{\lambda_3}{2\lambda_2 \sqrt{10\%}} v = \frac{\lambda_3}{\lambda_2} \cdot 390 \text{ GeV}. \quad (3.35)$$

If we assume that the two quartic couplings are perturbative and their ratio is around $\lambda_3/\lambda_2 \sim 1$, the LHC reach in the Higgs coupling analysis translates into heavy Higgs masses of up to 400 GeV, confirming our estimate in Equation (3.2).

Dimension-six description

In the EFT approach the singlet model only generates $\mathcal{O}_{\phi,2}$ at dimension six [192]. Before electroweak symmetry breaking, the only mass scale in the Lagrangian that describes the new physics is $\mu_2^2 < 0$. Defining the Wilson coefficients suppressed by this new physics scale gives clearly wrong results, as we show in the analogous case for the two-Higgs-doublet model in the next section. Instead we identify the leading contribution to the heavy Higgs mass as the new physics scale in our default matching, in agreement with the logic in Section 3.2. Following the discussion of decoupling patterns above this means

$$\Lambda_{\text{default}} = \sqrt{2\lambda_2} v_s \approx m_H. \quad (3.36)$$

The corresponding Wilson coefficient, expressed in terms of Lagrangian parameters, is

$$f_{\phi,2}^{\text{default}} = \frac{\lambda_3^2}{2\lambda_2}. \quad (3.37)$$

	Singlet				Default EFT			v -improved EFT		
	m_H	$\sin \alpha$	v_s/v	Δ_x	Λ	$f_{\phi,2}$	Δ_x	Λ	$f_{\phi,2}$	Δ_x
S1	500	0.2	10	-0.020	491	0.14	-0.018	500	0.15	-0.020
S2	350	0.3	10	-0.046	336	0.14	-0.037	350	0.16	-0.046
S3	200	0.4	10	-0.083	190	0.04	-0.031	200	0.06	-0.083
S4	1000	0.4	10	-0.083	918	2.60	-0.092	1000	3.13	-0.083
S5	500	0.6	10	-0.200	407	1.26	-0.231	500	1.24	-0.200

Table 3.1: Benchmarks for the singlet extension. In the left columns we show the model parameters and the universal coupling modification Δ_x for the complete model. We also give the cutoff scales Λ , the Wilson coefficients $f_{\phi,2}$, and the universal coupling shift in the corresponding EFT descriptions based on the default and on the v -improved matching schemes. All mass scales are given in GeV.

For the v -improved matching, we instead use the actual physical mass

$$\Lambda_{v\text{-improved}} = m_H. \quad (3.38)$$

In the broken phase the Higgs couplings are fully expressed through the mixing angle α as given in Equation (3.29). We define

$$f_{\phi,2}^{v\text{-improved}} = 2(1 - \cos \alpha) \frac{m_H^2}{v^2}, \quad (3.39)$$

which ensures that the Higgs couplings agree exactly between the full model and the v -improved dimension-six description.

Benchmark points

We start our numerical analysis by defining five singlet benchmark points in Table 3.1, with heavy Higgses ranging from 200 to 1000 GeV. The first three scenarios are in agreement with all experimental and theoretical constraints at the time of publication of Reference [1]. This includes direct mass bounds from heavy Higgs searches at colliders, Higgs coupling measurements, electroweak precision observables, perturbative unitarity and vacuum stability [234–236]. Note that for S4 and S5 the combination of large heavy Higgs masses together with large mixing angles is incompatible with perturbative unitarity, and electroweak precision constraints. We nevertheless keep these benchmarks for illustration purposes.

Higgs couplings and total production rates

Table 3.1 also shows the universal shift Δ_x of the light Higgs couplings, both for the full singlet model and its dimension-six approximations. For the default matching, we find reasonable agreement with the full model for the scenarios with a heavy additional Higgs, while large discrepancies appear when the new physics is lighter. In particular, note the difference between S₃ and S₄. Both describe the same coupling shift $\Delta_x = -0.083$. But while S₃ realises this with a weakly coupled light scalar, which the default EFT cannot describe, S₄ features a heavier and more strongly coupled new particle, and the EFT description works better. In all cases, the v -improved EFT by construction predicts the Higgs couplings correctly.

In Table 3.2 we show how well the effective models describe the total Higgs production cross sections in gluon fusion, WBF and Higgs-strahlung. These numbers confirm what we expect from the coupling modifications: while the default dimension-six model predicts qualitatively similar shifts in the total rates, there are rate deviations of up to 10%. In the v -improved EFT we find that the Higgs couplings and total rates agree exactly with the full model predictions. The dimension-six operators are sufficient to capture the coupling shifts, even though a significant part of their coefficients are formally of $\mathcal{O}(v^4/\Lambda^4)$.

Distributions

The most obvious source of discrepancy between the full model and the EFT is the heavy resonance H . It can for example be produced in gluon fusion and then observed as a peak in the $m_{4\ell}$ distribution. By construction, it will not be captured by the dimension-six model. We illustrate this in the upper left panel of Figure 3.1. For Higgs-strahlung production (Figure 3.1, upper right panel), where the novel H resonance does not appear in an intermediate Born-

	$\sigma_{\text{default EFT}}/\sigma_{\text{singlet}}$			$\sigma_{v\text{-improved EFT}}/\sigma_{\text{singlet}}$		
	ggF	WBF	Vh	ggF	WBF	Vh
S ₁	1.006	1.006	1.004	1.001	1.001	1.000
S ₂	1.019	1.021	1.019	1.000	1.001	1.000
S ₃	1.119	1.118	1.118	1.000	0.999	1.000
S ₄	0.982	0.982	0.982	0.999	0.999	1.000
S ₅	0.925	0.925	0.925	0.999	0.999	1.000

Table 3.2: Cross-section ratios of the dimension-six approximations to the full singlet model at the LHC. We show the leading Higgs production channels for all singlet benchmark points. The statistical uncertainties on these ratios are below 0.4%.

3 Higgs effective theory at its limits

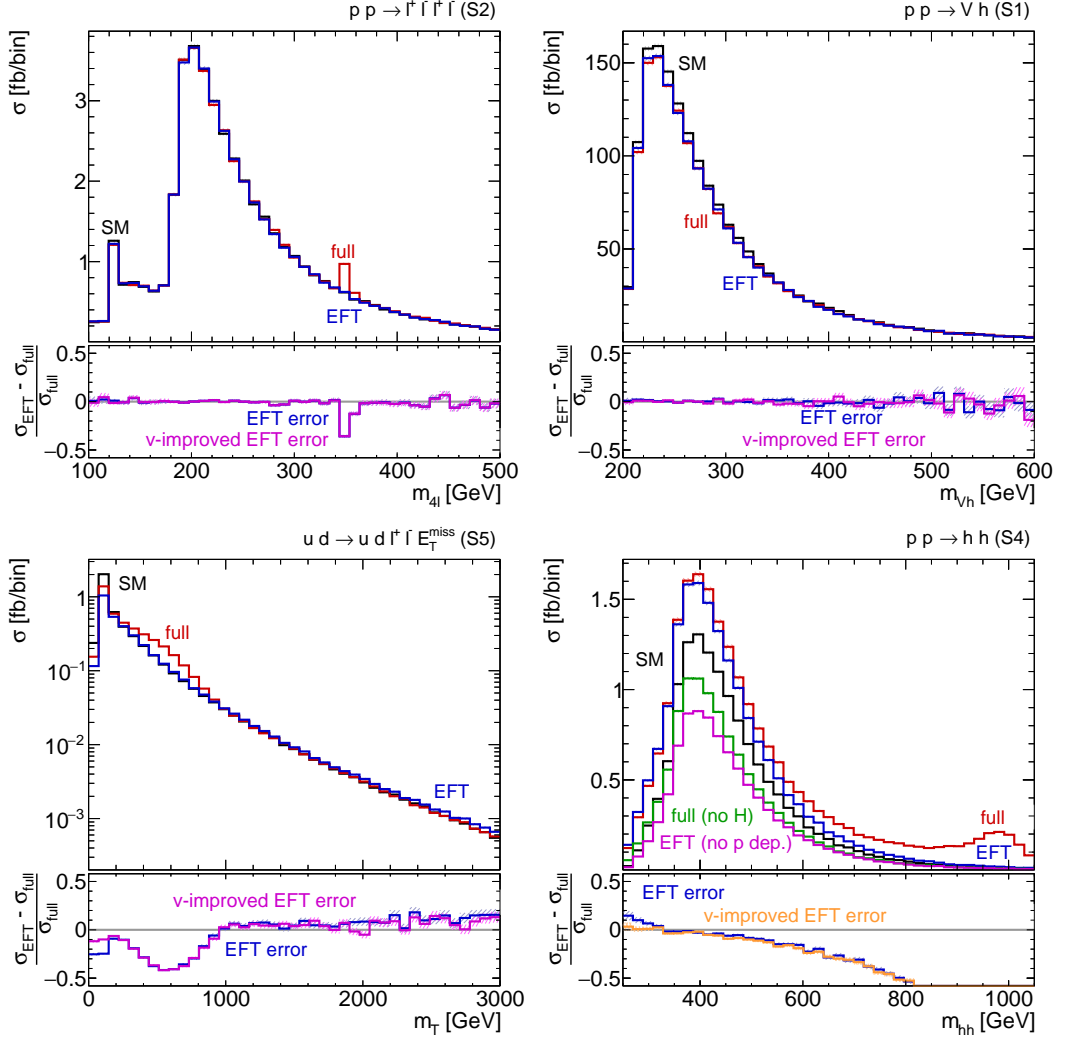


Figure 3.1: Selected kinematic distributions in the singlet model. The different curves show the SM, the full singlet model, and the dimension-six approximation with the default matching. In the bottom panels we give the relative EFT error, additionally including the v -improved dimension-six model. Top left: $m_{4\ell}$ distribution in the $gg \rightarrow h \rightarrow 4\ell$ channel for S2. Top right: m_{Vh} distribution in Vh production for S1. Bottom left: m_T distribution in the WBF $h \rightarrow \ell^+ \ell^- E_T^{\text{miss}}$ channel for S5. Bottom right: m_{hh} distribution in Higgs pair production for S4. In the m_{hh} plot we separate the different contributions in the full theory and the dimension-six approach. The shaded error bands give the statistical uncertainties.

level propagator and hence has no impact, we instead find excellent agreement between both descriptions over the entire phase space.

The second Higgs has an additional, more subtle effect. In the full model, both Higgs exchange diagrams are needed to unitarise WW scattering. Correspondingly, the EFT description breaks perturbative unitarity roughly at the scale [215]

$$m_{WW}^2 \sim \frac{16\pi}{\frac{f_{\phi,2}}{\Lambda^2} \left(1 - \frac{f_{\phi,2}v^2/\Lambda^2}{4(1+f_{\phi,2}v^2/\Lambda^2)}\right)} \approx \left(\frac{1.7 \text{ TeV}}{\sin \alpha}\right)^2. \quad (3.40)$$

In our benchmark point S5, this is around 2.8 TeV. The incomplete cancellation between Higgs and gauge amplitudes means that the dimension-six model tends to have a larger rate at energies already below this scale. This can be seen in the lower left panel of Figure 3.1, where we show the distribution of the transverse mass defined in Equation (3.21) in the process $ud \rightarrow W^+W^- ud \rightarrow (\ell^+\nu)(\ell^-\bar{\nu}) ud$, to which WBF production of both h and H contributes. We observe that the dimension-six model predicts a slightly higher rate at large m_T than both the full singlet model and the SM. Given the very mild signal, which results from the fast decrease in the parton densities and the small mixing angle for realistic scenarios, such an effect is likely of no relevance for LHC physics.

A more interesting channel to study in the singlet model is Higgs pair production. The Higgs self-coupling is the only Higgs coupling which gains a momentum dependence at tree level in the EFT. The approximate cancellation between the two leading SM amplitudes at threshold [91, 93] induces a second relevant scale and with it a sensitivity to small deviations in the Higgs couplings.

In the bottom right panel of Figure 3.1 we give the m_{hh} distribution in the full and dimension-six models. In addition, we show how the distributions would look in the full model without a H state, and in the EFT without the momentum-dependent (derivative) terms from $\mathcal{O}_{\phi,2}$. Already at threshold and far away from the H resonance, the interference of the SM-like terms with the H diagrams makes up a significant part of the amplitude. In the EFT the derivative terms are similarly relevant already at low energies. Close to threshold, the (v -improved) dimension-six model approximates the full theory well. But this agreement deteriorates already at moderately larger energies, with no significant difference between default and v -improved matching, and clearly breaks down towards the H pole.

Summary

If we limit ourselves to Higgs properties relevant for single Higgs production at the LHC, the modifications from a singlet extension are very simple: all Standard Model couplings acquire a common scaling factor, and no relevant new Lorentz structures appear at tree-level. The dimension-six setup reproduces this effect correctly: the reduced couplings to all SM fields alone do not require a large hierarchy of scales. A standard matching procedure that expands

the coefficients to leading order in v^2/Λ^2 may lead to sizeable deviations from the full model. However, a v -improved EFT construction that takes into account higher orders in v^2/Λ^2 yields perfect agreement with the full theory. In other words, all dimension-eight and higher operators relevant for single Higgs production that are generated from the singlet model are of the form $(\phi^\dagger \phi)^n \mathcal{O}_i^{(6)}$. After EWSB they can be resummed into the Wilson coefficients of the dimension-six operators as given by Equation (3.11).

Higgs pair production is different. There is a large contribution from off-shell H , while in the EFT the h self-coupling involves a derivative. These different structures lead to discrepancies between full and effective description that increase with momentum transfer, even for the v -improved matching.

3.3.3 Two-Higgs-doublet model

Model setup

The two-Higgs-doublet model (2HDM) [242, 243] adds a second scalar $SU(2)_L$ doublet ϕ_2 to the SM Higgs sector. The combined potential reads

$$V(\phi_1, \phi_2) = m_{11}^2 \phi_1^\dagger \phi_1 + m_{22}^2 \phi_2^\dagger \phi_2 + \frac{\lambda_1}{2} (\phi_1^\dagger \phi_1)^2 + \frac{\lambda_2}{2} (\phi_2^\dagger \phi_2)^2 + \lambda_3 (\phi_1^\dagger \phi_1)(\phi_2^\dagger \phi_2) + \lambda_4 |\phi_1^\dagger \phi_2|^2 + \left[-m_{12}^2 \phi_1^\dagger \phi_2 + \frac{\lambda_5}{2} (\phi_1^\dagger \phi_2)^2 + \text{h. c.} \right]. \quad (3.41)$$

The mass terms m_{ij}^2 and the dimensionless self-couplings λ_i are real parameters. The doublet VEVs $\langle \phi_j^0 \rangle = v_j/\sqrt{2}$ are parametrised by their ratio $\tan \beta = v_2/v_1$. For the Yukawa couplings, there are four possible scenarios that avoid tree-level flavour-changing neutral currents (FCNCs) [244]:

- type I, where all fermions couple to just one Higgs doublet ϕ_2 ;
- type II, where up-type (down-type) fermions couple exclusively to ϕ_2 (ϕ_1);
- lepton-specific, with a type-I quark sector and a type-II lepton sector; and
- flipped, with a type-II quark sector and a type-I lepton sector.

In all four cases, the absence of tree-level FCNCs is protected by a global \mathbb{Z}_2 discrete symmetry $\phi_i \rightarrow (-1)^i \phi_i$ (for $i = 1, 2$). This symmetry is softly broken by the mixed mass term m_{12} . For simplicity, we restrict our discussion to type I and type II.

The physical degrees of freedom are two neutral CP -even scalars h^0, H^0 , one neutral CP -odd scalar A^0 , and a set of charged scalars H^\pm , parametrised by the mixing angle between the CP -even scalars α . For a detailed account of the model setup, see Appendix A.5.2.

Signatures and decoupling patterns

The 2HDM predicts two types of LHC signatures: first, scalar and VEV mixing lead to modified light Higgs couplings. Unlike in the singlet extension, these coupling modifications are not universal, reflecting the more flexible flavour structure of the model. Second, there are three new heavy resonances H^0 , A^0 , and H^\pm , which should have near-degenerate masses to avoid custodial symmetry breaking.

The couplings of the light Higgs to weak bosons $V = W, Z$ scale with the mixing angles α and β as

$$\Delta_V = \sin(\beta - \alpha) - 1 = -\frac{\cos^2(\beta - \alpha)}{2} + \mathcal{O}(\cos^4(\beta - \alpha)). \quad (3.42)$$

We can insert the leading contribution of a mass-degenerate heavy Higgs sector and find [178]

$$\Delta_V \approx \frac{\sin^2(2\beta)}{8} \left(\frac{v}{m_{A^0}} \right)^4. \quad (3.43)$$

While in the singlet model the light Higgs coupling to gauge bosons is shifted at $\mathcal{O}(v^2/m_H^2)$, see Equation (3.34), the same coupling is now affected at $\mathcal{O}(v^4/m_{A^0}^4)$, corresponding to a dimension-eight effect.

The couplings to the fermions on the other hand are modified at $\mathcal{O}(v^2/m_{A_0}^2)$ [178]. For up-type quarks, we find

$$1 + \Delta_t = \frac{\cos \alpha}{\sin \beta}. \quad (3.44)$$

The couplings to down-type quarks and leptons are

$$1 + \Delta_b = 1 + \Delta_\tau = \frac{\cos \alpha}{\sin \beta} \quad (3.45)$$

in a type-I model and

$$1 + \Delta_b = 1 + \Delta_\tau = -\frac{\sin \alpha}{\cos \beta} \quad (3.46)$$

in a type-II 2HDM.

Finally, a H^\pm loop contributes to the Higgs-photon coupling. The expression for this coupling shift is given in Equation (A.62) in Appendix A.5.2.

Two aspects complicate the decoupling in the 2HDM: first, ‘delayed decoupling’ effects appear after electroweak symmetry breaking [245]. For example, in type-II models we find [178]

$$\Delta_b \approx -\tan \beta \frac{\sin(2\beta)}{2} \left(\frac{v}{m_{A^0}} \right)^2. \quad (3.47)$$

This correction to the bottom Yukawa coupling corresponds to a dimension-six effect, but can be enhanced by large values of $\tan \beta$, thus delaying the decoupling of the heavy 2HDM states in the Yukawa sector.

Second, unlike in the MSSM, the Higgs self-couplings λ_i and m_{12} are not bounded from above. Terms of the form $\lambda_i v^2$, potentially enhanced with factors of $\tan \beta$, contribute to the masses of the heavy Higgs bosons and to the interactions of the SM-like Higgs state, effectively inducing new energy scales.

Such additional mass scales driven by v lead to problems with any EFT derived from and matched to the full theory assuming only one new physics scale. While this should not be viewed as a problem of the EFT approach in general, it will require a v -improved matching procedure.

Dimension-six description

We first follow our default procedure and match the effective theory to the 2HDM in the unbroken electroweak phase. To this end, we first rotate ϕ_1 and ϕ_2 into the so-called Higgs basis, where only one Higgs doublet obtains a vacuum expectation value, $\langle \phi_l \rangle = v/\sqrt{2}$, $\langle \phi_h \rangle = 0$ [244, 246]. This doublet ϕ_l is then identified with the SM-like Higgs doublet, while the other doublet ϕ_h is integrated out. Its decoupling is described by the mass scale

$$\Lambda_{\text{default}}^2 = m_{11}^2 \sin^2 \beta + m_{22}^2 \cos^2 \beta + m_{12}^2 \sin(2\beta). \quad (3.48)$$

At tree level, the 2HDM generates a number of dimension-six operators, whose Wilson coefficients depend on the flavour structure. While the up-type Yukawa coupling is always modified in the same way, the down-type and lepton couplings are different for type-I and type-II. With the definition

$$\bar{\lambda} \equiv \frac{\sin(2\beta)}{2} \left[\frac{\lambda_1}{2} - \frac{\lambda_2}{2} + \left(\frac{\lambda_1}{2} + \frac{\lambda_2}{2} - \lambda_3 - \lambda_4 - \lambda_5 \right) \cos(2\beta) \right] \quad (3.49)$$

we find

$$\begin{aligned} f_t &= -\frac{\bar{\lambda} y_t}{\tan \beta}, \\ f_b &= \begin{cases} -\frac{\bar{\lambda} y_b}{\tan \beta} & \text{type I,} \\ \bar{\lambda} y_b \tan \beta & \text{type II,} \end{cases} \\ f_\tau &= \begin{cases} -\frac{\bar{\lambda} y_\tau}{\tan \beta} & \text{type I,} \\ \bar{\lambda} y_\tau \tan \beta & \text{type II.} \end{cases} \end{aligned} \quad (3.50)$$

Here y_t , y_b , y_τ refer to the SM values of the respective Yukawa couplings, $y_f = \sqrt{2}m_f/v$.

The contribution of the H^\pm loop to the Higgs-photon coupling is mapped onto \mathcal{O}_{BB} with a Wilson coefficient

$$f_{BB} = \frac{(\tan \beta + \cot \beta)}{3072 \pi^2} \left[\left(\lambda_1 + \lambda_2 - 2\lambda_3 + 6\lambda_4 + 6\lambda_5 - 8 \frac{m_{h^0}^2}{v^2} \right) \sin(2\beta) + 2(\lambda_1 - \lambda_2) \sin(4\beta) + (\lambda_1 + \lambda_2 - 2\lambda_3 - 2\lambda_4 - 2\lambda_5) \sin(6\beta) \right]. \quad (3.51)$$

In the effective Lagrangian there are no non-decoupling terms of $\mathcal{O}(\Lambda^0)$, because the charged Higgs loop decouples in the limit $m_{A^0} \rightarrow \infty$ with finite λ_i . If instead we keep m_{12} fixed and let one of the couplings λ_i grow with m_{A^0} , the charged Higgs does not decouple. We derive these results in Appendix A.5.2.

Upon electroweak symmetry breaking, the physical heavy Higgs masses m_{H^0} , m_{A^0} , and m_{H^\pm} acquire contributions $\sim \lambda_i v^2$ from the electroweak VEV in addition to the heavy scale Λ_{default} defined above. We therefore again consider an alternative v -improved matching where the matching scale is

$$\Lambda_{v\text{-improved}} = m_{A^0}. \quad (3.52)$$

In this setup, the Wilson coefficients in Equations (3.50) and (3.51) remain unchanged.³ The two matching schemes can exhibit significant differences in the 2HDM since the pseudoscalar mass $m_{A^0}^2 = m_{12}^2 / (\sin \beta \cos \beta) - \lambda_5 v^2$ does not coincide with Λ_{default} over large parts of the parameter space.

Benchmark points

In Table 3.3 we define four benchmark points for the 2HDM. They are in agreement with all constraints at the time of publication of Reference [1], implemented with the help of 2HDMC [247], HiggsBounds [248, 249], SuperIso [250], and HiggsSignals [251]. To better illustrate certain model features, in some scenarios we tolerate deviations between 1σ and 2σ in the Higgs couplings measurements.

The key physics properties of the different 2HDM scenarios can be summarised as follows:

- D1 **Moderate decoupling:** emphasises large Higgs coupling shifts, with up to 2σ deviations from the LHC constraints. Additional Higgs masses around $250 \dots 350$ GeV can leave visible imprints.

³An alternative definition of the v -improved Wilson coefficients could be based on the physical mixing angles α and β . Similar to the singlet model, in this way we could ensure that the tree-level Higgs-fermion couplings agree exactly between the full and the effective model. Here we refrain from such a fine-tuned matching prescription to demonstrate how a simple redefinition of Λ can improve the performance of the dimension-six model.

2HDM							
	Type	$\tan \beta$	α/π	m_{12}	m_{H^0}	m_{A^0}	m_{H^\pm}
D1	I	1.5	-0.086	45	230	300	350
D2	II	15.0	-0.023	116	449	450	457
D3	II	10.0	0.032	157	500	500	500
D4	I	20.0	0.000	45	200	500	500

Table 3.3: Benchmarks for the 2HDM. All masses are given in GeV.

Default EFT					
	$ \Lambda $ [GeV]	f_t	f_b	f_τ	f_{BB}
D1	100	0.12	0.003	0.001	0.009
D2	448	0.00	-0.006	-0.002	-0.001
D3	99	-0.07	0.206	0.077	-0.016
D4	142	0.00	0.000	0.000	-0.023

Table 3.4: Matching scales and Wilson coefficients for the effective theory matched to the 2HDM, based on the default matching in the unbroken electroweak phase.

v -improved EFT					
	Λ [GeV]	f_t	f_b	f_τ	f_{BB}
D1	300	-0.12	-0.003	-0.001	-0.009
D2	450	0.00	-0.006	-0.002	-0.001
D3	500	-0.07	0.206	0.077	-0.016
D4	500	0.00	0.000	0.000	-0.023

 Table 3.5: Matching scales and Wilson coefficients for the effective theory matched to the 2HDM, based on the v -improved matching with $\Lambda = m_{A^0}$.

	Δ_V		Δ_t			$\Delta_b = \Delta_\tau$		
	2HDM	EFT	2HDM	dEFT	v EFT	2HDM	dEFT	v EFT
D1	-0.05	0.00	0.16	-0.74	0.08	0.16	-0.74	0.08
D2	0.00	0.00	0.00	0.00	0.00	0.07	0.07	0.07
D3	-0.02	0.00	0.00	0.46	0.02	-2.02	-46.5	-1.84
D4	0.00	0.00	0.00	0.00	0.00	0.00	0.00	0.00

Table 3.6: Tree-level coupling shifts of the light Higgs in our 2HDM benchmarks. We compare the full 2HDM model to the EFT based on the default matching ('dEFT') and to the EFT based on v -improved matching (' v EFT').

- D₂ **Supersymmetric:** reproduces the characteristic mass splittings and Higgs self-couplings of the MSSM with light stops [252].
- D₃ **Sign-flipped bottom Yukawa:** this is possible in type-II models at large $\tan\beta$, as shown in Equation (3.47) [253]. This can be viewed as a manifestation of a delayed decoupling [245].
- D₄ **Fermiophobic heavy Higgs:** possible only in type-I models for $\sin\alpha = 0$. The heavy Higgs H^0 is relatively light, but essentially impossible to observe at the LHC [224].

In Tables 3.4 and 3.5 we show the heavy scales Λ and the Wilson coefficients for the EFT in the two matching schemes. With the exception of benchmark D₂, the suppression scales are drastically different. The matching in the unbroken phase is particularly pathological in benchmark D₁, where $\Lambda_{\text{default}}^2$ is negative and the signs of the Wilson coefficients are switched compared to the v -improved matching.

Higgs couplings and total production rates

Table 3.6 shows the tree-level coupling shifts of the light Higgs in the three models. The results confirm that the default matching defined in the unbroken phase does not reproduce the coupling patterns of the full model. We conclude that an EFT matched to the 2HDM in the unbroken electroweak phase is essentially useless, and we have to rely on v -improved matching. For simplicity, we will from now on leave out the results based on the default matching, which only confirm these initial results.

The v -improved matching captures most of the coupling shifts. It still fails to describe shifts in the couplings to weak bosons, which correspond to a dimension-eight operator as discussed above.⁴ Unlike in the singlet model, the v -improved EFT also struggles with scenarios of very

⁴Note that the operator \mathcal{O}_{BB} does contribute to the $h^0 VV$ coupling, representing the effect of a charged Higgs loop. But as our results show, this effect is negligible.

	Δ_g		Δ_γ		$\Delta_\gamma^{\text{direct}}$	
	2HDM	v EFT	2HDM	v EFT	2HDM	v EFT
D1	$0.16 + 0.00i$	0.08	-0.16	-0.10	-0.05	-0.07
D2	$0.00 + 0.00i$	0.00	0.00	0.00	0.00	0.00
D3	$0.07 - 0.09i$	0.02	-0.08	-0.05	-0.05	-0.05
D4	$0.00 + 0.00i$	0.00	-0.05	-0.05	-0.05	-0.05

Table 3.7: Coupling shifts of the light Higgs to gluons and photons in the 2HDM benchmarks and in the corresponding v -improved EFT (v EFT). In the full model, the bottom loop leads to small imaginary parts of Δ_g and Δ_γ . For the Higgs-photon coupling, these imaginary parts are always smaller than 1% of the real part of the amplitude and neglected here. The coupling shift $\Delta_\gamma^{\text{direct}}$ in the last two columns ignores the indirect effects from modified Higgs-fermion couplings, allowing us to analyse separately how well the H^\pm loop is captured by \mathcal{O}_{BB} .

light new physics such as D1. Still, all in all it performs well in situations with a modest scale hierarchy such as benchmark D2.

A particularly interesting scenario is described by benchmark D3. In the full model, the bottom Yukawa is exactly sign-flipped, a signature hardly visible at the LHC. Generating such a signature from higher-dimensional operators requires their contributions at $\mathcal{O}(v^2/\Lambda^2)$ to be twice as large as the SM Yukawa coupling. The EFT fails to capture this coupling shift fully, leading to a significantly different prediction for the Higgs decay into bottom quarks.

In Table 3.7 we repeat this analysis for the loop-induced couplings of an on-shell Higgs to gluons and photons. A large part of these coupling shifts stems from the modified Higgs-top and Higgs- W couplings. This means that in scenarios where the effective theory describes these tree-level couplings accurately, we also find good agreement between full and effective model for the loop-induced couplings. Separating the H^\pm contribution to the Higgs-photon coupling from these indirect effects, we find that \mathcal{O}_{BB} captures its effect very well.

Table 3.8 compares total production rates at the LHC. Depending on the benchmark, the dimension-six truncation leads to up to 10% deviations, in agreement with the results for the coupling shifts.

Distributions

As for the singlet model, the indirect signatures from the 2HDM are mostly reflected in the coupling patterns discussed above, and new kinematic effects do not play a significant role. In the left panel of Figure 3.2 we illustrate the coupling deviations in gluon-fusion Higgs production

with a decay $h \rightarrow \tau^+ \tau^-$, showing how the full 2HDM and the (v -improved) EFT give substantially different predictions for the size of the Higgs signal.

While on-shell Higgs decays to photons are generally well described by the EFT, this changes for off-shell Higgs production. At $m_{\gamma\gamma} \gtrsim 2m_{H^\pm}$, the H^\pm in the loop can resolve the charged Higgs, enhancing the size of its contribution significantly. This effect is not captured by the effective operator and leads to a different behaviour of the amplitude $gg \rightarrow h^0 \rightarrow \gamma\gamma$ between the full and the effective model, as shown in the right panel of Figure 3.2. However, the tiny rate and the large combinatorial background mean that this discrepancy will be irrelevant for LHC phenomenology. Similar threshold effects have been computed for the top-induced Higgs-gluon coupling and appear to be similarly irrelevant in practice [254].

The situation in Higgs pair production resembles the observations in the singlet model [224, 255, 256]. The agreement can be even worse already at threshold if Higgs-top coupling shifts are not correctly captured by the effective model.

Summary

The 2HDM discussion leads us to a similar conclusion as the singlet model: as long as the mixing is small and Higgs-gauge coupling shifts are negligible, all that the LHC probes in single Higgs production is a set of three coupling modifications Δ_t , Δ_b , Δ_τ , and the charged Higgs loop contribution to the Higgs-photon coupling. These aspects of Higgs phenomenology are generally well captured by an appropriately defined EFT. Problems arise in scenarios with very light new Higgs bosons, when the Higgs-W and Higgs-Z couplings are modified, and in the special case of Higgs pair production.

A naive construction of the EFT by matching the effective dimension-six Lagrangian to the 2HDM in the gauge-symmetric phase clearly fails to describe the modified Higgs boson dynamics in typical 2HDM scenarios; a v -improved matching procedure is more suitable.

	$\sigma_{v\text{-improved EFT}}/\sigma_{2\text{HDM}}$		
	ggF	WBF	Vh
D1	0.872	1.109	1.108
D2	1.001	1.000	1.000
D3	1.022	1.042	1.042
D4	1.001	1.001	1.003

Table 3.8: Cross-section ratios of the v -improved dimension-six approximation to the full 2HDM at the LHC. The statistical uncertainties on these ratios are below 0.4%.

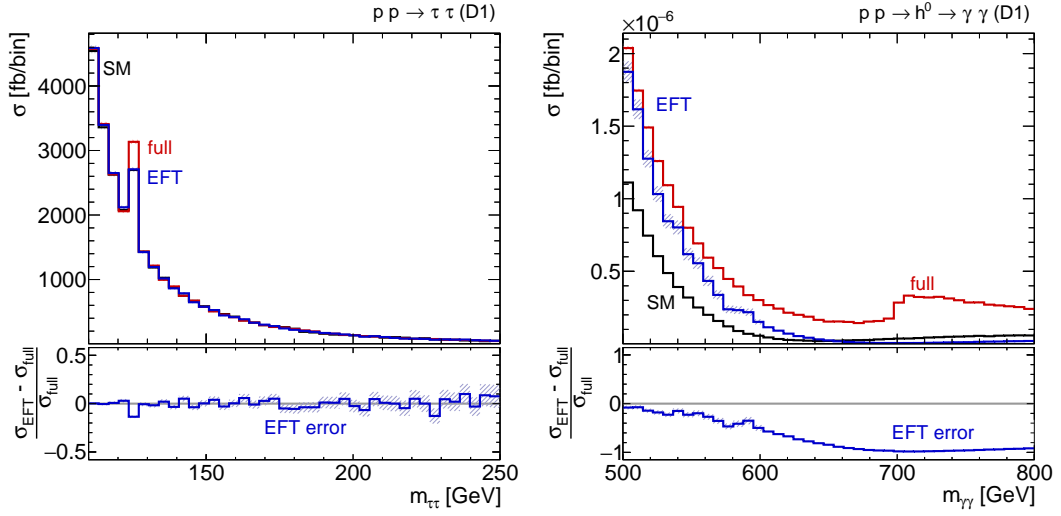


Figure 3.2: Selected kinematic distributions in 2HDM benchmark D1, comparing the full model to the EFT based on v -improved matching. Left: $m_{\tau\tau}$ distribution in the $gg \rightarrow \tau^+ \tau^-$ channel. Right: off-shell behaviour of the process $gg \rightarrow h^0 \rightarrow \gamma\gamma$, only taking into account the Higgs diagrams. At $m_{\gamma\gamma} \gtrsim 2m_{H^\pm} = 700$ GeV, the charged Higgs threshold is visible. The shaded error bands give the statistical uncertainties.

3.3.4 Scalar top partners

Model setup

New coloured scalar particles are, strictly speaking, not an extension of the SM Higgs sector, but they can lead to interesting modifications of the LHC observables. We consider a scalar top partner sector mimicking the stop and sbottom sector of the MSSM. Its Lagrangian has the form

$$\begin{aligned} \mathcal{L}_{\text{top partners}} \supset & (D_\mu \tilde{Q})^\dagger D^\mu \tilde{Q} + (D_\mu \tilde{t}_R)^* D^\mu \tilde{t}_R - M^2 \tilde{Q}^\dagger \tilde{Q} - M^2 \tilde{t}_R^* \tilde{t}_R \\ & - \kappa_{LL} (\phi \cdot \tilde{Q})^\dagger (\phi \cdot \tilde{Q}) - \kappa_{RR} (\tilde{t}_R^* \tilde{t}_R) (\phi^\dagger \phi) \\ & - [\kappa_{LR} M \tilde{t}_R^* (\phi \cdot \tilde{Q}) + \text{h. c.}] . \end{aligned} \quad (3.53)$$

Here, \tilde{Q} and \tilde{t}_R are the additional isospin doublet and singlet in the fundamental representation of $SU(3)_C$. Their mass terms can be different, but for the sake of simplicity we unify them to a single heavy mass scale M . The singlet state \tilde{b}_R is assumed to be heavier and integrated out.

This leaves us with three physical degrees of freedom, the scalars \tilde{t}_1 , \tilde{t}_2 and $\tilde{b}_2 = \tilde{b}_L$. The

eigenvalues of the stop mass matrix

$$\mathcal{M}_{\tilde{t}} = \begin{pmatrix} M^2 + \kappa_{LL} \frac{v^2}{2} & \kappa_{LR} \frac{Mv}{\sqrt{2}} \\ \kappa_{LR} \frac{Mv}{\sqrt{2}} & M^2 + \kappa_{RR} \frac{v^2}{2} \end{pmatrix} \quad (3.54)$$

define two masses $m_{\tilde{t}_1} < m_{\tilde{t}_2}$ and a mixing angle $\theta_{\tilde{t}}$. We provide a detailed description of the model setup in Appendix A.5.3.

Signatures and decoupling patterns

The main new physics effects in the Higgs sector are loop-induced modifications of the Higgs interactions, most notably to Δ_g , Δ_y , Δ_W , and Δ_Z , possibly including new Lorentz structures. The Yukawa couplings do not change at one-loop level because we do not include gauge boson partners. As a side remark, the 2HDM described in Section 3.3.3 combined with the scalar top partners given here corresponds to an effective description of the MSSM in the limit of infinitely heavy gauginos, sleptons, and light-flavour squarks.

In the limit of small $\theta_{\tilde{t}}$, the leading correction to the hVV coupling scales as

$$\Delta_V \approx \frac{\kappa_{LL}^2}{16\pi^2} \left(\frac{v}{m_{\tilde{t}_1}} \right)^2. \quad (3.55)$$

This shift can be sizeable only for relatively low stop and sbottom masses combined with large couplings κ_{ij} to the Higgs sector.

As already noted for the 2HDM, the decoupling of the heavy scalars becomes non-trivial in the presence of a Higgs VEV. Following Equation (3.54), the masses of the heavy scalars $m_{\tilde{t}_1}$, $m_{\tilde{t}_2}$ are not only controlled by the mass scale in the symmetric phase of the electroweak symmetry M , but they receive additional contributions of the type $\kappa_{LR} vM$, $\kappa_{LL} v^2$, or $\kappa_{RR} v^2$ after electroweak symmetry breaking. This leads to a mass splitting of order v between masses of order M , which is increased by large values of the couplings κ_i .

Dimension-six description

This motivates us to again define two different matching schemes. First, we stick to our default prescription and carry out the matching of the linear EFT Lagrangian to the full model in the unbroken phase. The matching scale is then dictated by the intrinsic mass scale of the heavy fields,

$$\Lambda_{\text{default}} = M, \quad (3.56)$$

Scalar top partner model							
	M	κ_{LL}	κ_{RR}	κ_{LR}	$m_{\tilde{t}_1}$	$m_{\tilde{t}_2}$	$\theta_{\tilde{t}}$
P1	500	-1.16	2.85	0.147	500	580	-0.15
P2	350	-3.16	-2.82	0.017	173	200	-0.10
P3	500	-7.51	-7.17	0.012	173	200	-0.10

Table 3.9: Benchmarks for the scalar top partner scenario. We show Lagrangian parameters (left) and physical parameters (right). All masses are given in GeV.

	Default EFT				v -improved EFT			
	Λ	$f_{\phi,2}$	f_{WW}	f_W	Λ	$f_{\phi,2}$	f_{WW}	f_W
P1	500	0.026	0.000	0.000	500	0.026	0.000	0.000
P2	350	0.023	0.005	0.000	173	0.023	0.005	0.000
P3	500	0.152	0.115	-0.207	173	0.152	0.115	-0.207

Table 3.10: Matching scales (in GeV) and selected Wilson coefficients for the top partner benchmarks, both for default and v -improved matching.

and is completely oblivious to contributions to the masses from the electroweak VEV. The suppression scale of loop effects in the complete model and this matching scale in the EFT only agree in the limit $M - m_{\tilde{t}_1} \sim v \ll M$.

The stop loops generate a number of operators [139, 145, 194],

$$\begin{aligned}
 f_{\phi,1} &= -\frac{1}{2(4\pi)^2} \left[\kappa_{LL}^2 - \frac{\kappa_{LL}\kappa_{LR}^2}{2} + \frac{\kappa_{LR}^4}{10} \right], \\
 f_{\phi,2} &= \frac{1}{4(4\pi)^2} \left[2\kappa_{RR}^2 - \kappa_{RR}\kappa_{LR}^2 + \frac{\kappa_{LR}^4}{5} \right], \\
 f_{GG} &= \frac{g_s^2}{24(4\pi)^2} \left[\kappa_{LL} + \kappa_{RR} - \kappa_{LR}^2 \right], \\
 f_{BB} &= -\frac{1}{36(4\pi)^2} \left[\kappa_{LL} + 16\kappa_{RR} - \frac{67}{10}\kappa_{LR}^2 \right], \\
 f_{WW} &= -\frac{1}{4(4\pi)^2} \left[\kappa_{LL} - \frac{3}{10}\kappa_{LR}^2 \right], \\
 f_{BW} &= \frac{1}{12(4\pi)^2} \left[2\kappa_{LL} - \frac{11}{5}\kappa_{LR}^2 \right], \\
 f_B &= \frac{1}{20(4\pi)^2} \kappa_{LR}^2, \quad \text{and}
 \end{aligned}$$

$$f_W = \frac{1}{20(4\pi)^2} \kappa_{LR}^2. \quad (3.57)$$

Unlike the tree-level effects in the previous two models, the top partner loops do not only induce modifications to the SM Higgs couplings, but induce new Lorentz structures. Note that some of these operators are tightly constrained from electroweak precision data, see Section 2.3.2. We will ignore these constraints for our discussion of Higgs physics.

In addition, we define a v -improved matching. As in the 2HDM, we pick the matching scale as a physical mass in the broken phase,

$$\Lambda = m_{\tilde{t}_1}. \quad (3.58)$$

The Wilson coefficients f_i are the same as in Equation (3.57).

Benchmark points

As Equation (3.55) suggests, sizeable loop corrections to the hVV coupling require light top partners with unrealistically strong couplings to the Higgs sector [257]. In Table 3.9 we define a set of benchmark points with this aim in mind. The corresponding Wilson coefficients in our two matching schemes are given in Table 3.10.

Higgs production rates and distributions

The contributions from scalar top partners to Higgs production in gluon fusion are well known [258–262] and the validity of the EFT approach for this process has been thoroughly scrutinised [190, 194]. We therefore focus on corrections to the hVV coupling in WBF and Higgs-strahlung.

The total Higgs production rates in these channels are given in Table 3.11. In benchmark P1 the WBF cross section is reduced by about 0.6% compared to the Standard Model, with good

	$\sigma_{\text{dEFT}}/\sigma_{\text{top partners}}$		$\sigma_{v\text{EFT}}/\sigma_{\text{top partners}}$	
	WBF	Vh	WBF	Vh
P1	1.000	0.999	1.000	0.999
P2	1.095	1.100	1.074	1.049
P3	2.081	1.904	1.749	1.363

Table 3.11: Cross-section ratios of the dimension-six approximation to the full top partner model at the LHC. We give the results both for the default matching scheme with matching scale $\Lambda = M$ ('dEFT') as well as for the v -improved matching with $\Lambda = m_{\tilde{t}_1}$ (' v EFT'). The statistical uncertainties on these ratios are below 0.4%.

3 Higgs effective theory at its limits

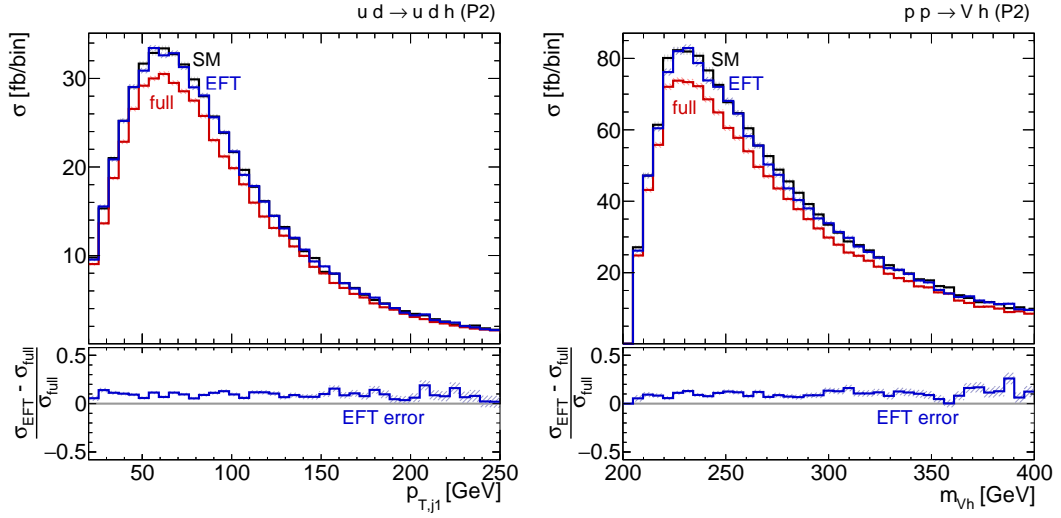


Figure 3.3: Kinematic distributions for the top partner model in benchmark P2. Left: tagging jet properties in WBF Higgs production. Right: m_{Vh} distribution in Higgs-strahlung. The shaded error bands give the statistical uncertainties.

agreement between effective and full description. Clearly, such a scenario is not relevant for LHC measurements in the foreseeable future. In more extreme corners of the parameter space, the loop effects in the full model grow, higher-dimensional terms in the EFT become larger, the validity of the dimension-six model worsens, and discrepancies between both increase. In benchmarks P2 and P3 the WBF rate is reduced by 9.1% and 43.5% with respect to the Standard Model. By construction, the EFT based on the default matching captures only the formally leading term at $\mathcal{O}(v^2/\Lambda^2)$, leading to a reduction of only 0.5% and 2.0%. The corresponding difference is, again, independent of kinematic variables, for example of the tagging jet's transverse momentum. With the v -improved matching, the cross section is reduced by 2.4% and 17.7%, still far from the result of the full model.

The results for Higgs-strahlung look similar: in the moderate benchmark P1 the predictions of the full model and the dimension-six Lagrangian agree within 0.1%, but in this scenario the overall deviation from the Standard Model is negligible. In scenarios with larger loop effects, the dimension-six prediction fails to capture most of the full top partner loops, with numerical results similar to those given for WBF Higgs production. Again switching to the v -improved matching does not improve the EFT approximation significantly.

In Figure 3.3 we finally show that these changes in the total rates do not have a dramatic effect on the kinematic distributions. This is not surprising, since the largest Wilson coefficient generated in our benchmark points is consistently that of $\mathcal{O}_{\phi,2}$, which corresponds to a universal

rescaling of the SM Higgs couplings.

Summary

Scalar top partners generate a large set of dimension-six operators through electroweak loops. However, in realistic scenarios with a large scale separation, the loop corrections for instance to the hVV vertex are tiny. Pushing for loop effects that are large enough to leave a visible imprint in WBF and Higgs-strahlung requires breaking the scale separation between the observed Higgs scalar and the top partners dramatically. In that case the EFT fails already for the total rates, kinematic distributions hardly add to this discrepancy.

3.3.5 Vector triplet

Model setup

Heavy vector bosons appear in many new physics scenarios, for instance when a larger gauge group is spontaneously broken down to the SM gauge group at higher energies. Such particles are often connected to the gauge-Higgs sector of the SM, predicting signatures in Higgs measurements [185, 263, 264]. As an example, we study a massive vector field⁵ V_μ^a which is a triplet under $SU(2)_L$ and uncharged under $SU(3)_c$ and $U(1)_Y$. This allows it to mix with the W bosons of the Standard Model and to couple to Higgs and fermion currents [185, 264]. For simplicity, we assume CP invariance and a flavour-universal coupling to the fermion current. Following the conventions of Reference [264], the Lagrangian then reads

$$\begin{aligned} \mathcal{L}_{\text{vector triplet}} \supset & -\frac{1}{4} V_{\mu\nu}^a V^{\mu\nu a} + \frac{M_V^2}{2} V_\mu^a V^{\mu a} \\ & + i \frac{g_V}{2} c_H V_\mu^a [\phi^\dagger \sigma^a \tilde{D}^\mu \phi] + \frac{g_W^2}{2g_V} V_\mu^a \sum_f c_F \bar{f}_L \gamma^\mu \sigma^a f_L \\ & + g_V^2 c_{VVHH} V_\mu^a V^{\mu a} \phi^\dagger \phi \\ & + \frac{g_V}{2} c_{VVV} \epsilon_{abc} V_\mu^a V_v^b D^{[\mu} V^{v]}_c - \frac{g_W}{2} c_{VWW} \epsilon_{abc} W^{\mu\nu} V_\mu^b V_v^c \end{aligned} \quad (3.59)$$

with the field strength $V_{\mu\nu}^a = D_\mu V_\nu^a - D_\nu V_\mu^a$ and where $D_\mu V_\nu^a = \partial_\mu V_\nu^a + g_V \epsilon^{abc} V_\mu^b V_v^c$.

The coupling g_V characterises the interactions of the heavy vector, while g_W is the $SU(2)_L$ coupling constant. After mixing, the original fields V^a and W^a combine to the mass eigenstates W^\pm , ξ^\pm , and ξ^0 , while a combination of the couplings g_W and g_V becomes the observed weak gauge coupling g . The parameters c_{VWW} and c_{VVV} are irrelevant for Higgs phenomenology at the LHC. For more details, see Appendix A.5.4.

⁵Note that such a model is not UV-complete: theories with massive vector bosons are not renormalisable [141].

However, such a mass can easily be generated from a consistent gauge theory with a Higgs mechanism at a higher scale [264]. The details of such an embedding do not matter here.

Signatures and decoupling patterns

In addition to the new heavy resonances ξ^0 and ξ^\pm , the signature feature of the vector triplet is that the mixing of the new states with the W and Z bosons affects the properties of the electroweak gauge bosons at tree level. In particular, the shift from the Lagrangian parameter g_W to the observable weak coupling g combined with the direct heavy vector coupling to the Higgs doublet modifies the Higgs couplings as

$$\begin{aligned}\Delta_V &\approx \frac{g^2 c_F c_H}{4} \left(\frac{v}{M_V} \right)^2 - \frac{3 g_V^2 c_H^2}{8} \left(\frac{v}{M_V} \right)^2, \\ \Delta_f &\approx \frac{g^2 c_F c_H}{4} \left(\frac{v}{M_V} \right)^2 - \frac{g_V^2 c_H^2}{8} \left(\frac{v}{M_V} \right)^2.\end{aligned}\quad (3.60)$$

In addition, contributions from virtual heavy states ξ modify the phase-space behaviour of Higgs signals in many ways.

Just as for the 2HDM and the top partners, the mass matrix for the massive vectors contains both the intrinsic mass scale M_V and terms proportional to some power of v multiplied by a combination of couplings. The new vector states have degenerate masses

$$m_\xi^2 \approx M_V^2 \left(1 + g_V^2 c_{VVHH} \frac{v^2}{M_V^2} + \frac{g_V^2 c_H^2}{4} \frac{v^2}{M_V^2} + \mathcal{O}\left(\frac{v^4}{M_V^4}\right) \right). \quad (3.61)$$

Even if there appears to be a clear scale separation $M_V \gg v$, large values of g_V , c_{VVHH} , or c_H can change m_ξ significantly and thus induce a second mass scale.

Dimension-six description

The obvious choice of the matching scale in the unbroken electroweak phase is the heavy mass scale in the Lagrangian

$$\Lambda_{\text{default}} = M_V, \quad (3.62)$$

which we use for our default matching scheme.

Integrating out the heavy vector triplet at tree level generates a number of operators with Wilson coefficients

$$\begin{aligned}f_{WW} &= c_F c_H, & f_{\phi,2} &= \frac{3}{4} c_H (c_H g_V^2 - 2 c_F g^2), \\ f_{BB} &= c_F c_H, & f_{\phi,3} &= -3 \lambda c_H (c_H g_V^2 - 2 c_F g^2), \\ f_{BW} &= c_F c_H, & f_f &= -\frac{1}{4} y_f c_H (c_H g_V^2 - 2 c_F g^2), \\ f_W &= -2 c_F c_H.\end{aligned}\quad (3.63)$$

	Triplet model					
	M_V	g_V	c_H	c_F	c_{VVHH}	m_ξ
T ₁	591	3.0	-0.47	-5.0	2.00	1200
T ₂	946	3.0	-0.47	-5.0	1.00	1200
T ₃	941	3.0	-0.28	3.0	1.00	1200
T ₄	1246	3.0	-0.50	3.0	-0.20	1200
T ₅	846	1.0	-0.56	-1.32	0.08	849

Table 3.12: Benchmark points for the vector triplet model. The masses are given in GeV.

Additional four-fermion contributions are irrelevant for Higgs physics. Loop-induced contributions are further suppressed and we neglect them here.

Once again, we compare this default matching to an alternative v -improved matching, where as a cutoff we now use the physical mass

$$\Lambda_{v\text{-improved}} = m_\xi. \quad (3.64)$$

The coefficients in Equation (3.63) remain unchanged.⁶

Unlike the previous models, the vector triplet generates \mathcal{O}_W , \mathcal{O}_{WW} , and \mathcal{O}_{BB} at tree level. As discussed in Section 2.3.3, these induce new kinematic structures in the hWW and hZZ couplings.

Benchmark points

We study a set of benchmark points defined in Table 3.12 and Table 3.13. Unlike additional scalars, light new vector triplets with masses just above the electroweak scale are unrealistic given the constraints from electroweak precision measurements and direct searches. We therefore focus on new vector bosons around the TeV scale. The different setups are motivated phenomenologically, from experimental constraints, or based on specific UV completions:

T₁₋₂ Higgs-gauge dynamics: designed for large momentum-dependent effects in the hVV couplings. \mathcal{O}_W and \mathcal{O}_{WW} receive large Wilson coefficients, while $\mathcal{O}_{\phi,2}$, $\mathcal{O}_{\phi,3}$, and \mathcal{O}_f vanish along the line

$$\frac{c_H}{c_F} = 2 \frac{g^2}{g_V^2}. \quad (3.65)$$

The large couplings also imply a large difference between M_V and m_ξ .

⁶In the spirit of v -improvement we could alternatively parametrise the Wilson coefficients with the physical mixing angles between the W , Z and V bosons, but this does not significantly change the results.

	Default EFT					v -improved EFT				
	Λ	$f_{\phi,2}$	f_{WW}	f_W	f_t	Λ	$f_{\phi,2}$	f_{WW}	f_W	f_t
T ₁	591	0.00	2.45	-4.90	0.00	1200	0.00	2.45	-4.90	0.00
T ₂	946	0.00	2.35	-4.71	0.00	1200	0.00	2.35	-4.71	0.00
T ₃	941	1.09	-0.82	1.64	-0.36	1200	1.09	-0.82	1.64	-0.36
T ₄	1246	2.64	-1.56	3.12	-0.87	1200	2.64	-1.56	3.12	-0.87
T ₅	846	-0.24	0.78	-1.55	0.08	849	-0.24	0.78	-1.55	0.08

Table 3.13: Matching scales (in GeV) and selected Wilson coefficients for the effective theory matched to the vector triplet model. We give these results for both the default EFT matching in the unbroken phase and for a v -improved matching with $\Lambda = m_\xi$.

- T₃ **Interference patterns:** the sign of c_W and of the Wilson coefficients are flipped compared to T₁ and T₂. This allows us to compare constructive and destructive interference patterns between SM amplitudes and new physics contributions.
- T₄ **Realistic:** the vector triplet couplings and masses satisfy the leading constraints from direct collider searches at the time of publication of Reference [1]. The most stringent bounds come from di-lepton and di-boson channels [264, 265].
- T₅ **UV completion:** typical coupling patterns from a weakly coupled UV completion based on the extended gauge group $SU(3) \times SU(2) \times SU(2) \times U(1)$ [266]. Such a scenario could for instance arise from deconstructed extra dimensions [267]. The vector triplet phenomenology is effectively described by the parameter $\alpha = g_V/\sqrt{g_V^2 - g_W^2}$ together with the symmetry breaking scale f [264], with the couplings

$$\begin{aligned} M_V^2 &= \alpha^2 g_V^2 f^2, & c_H &= -\alpha \frac{g_W^2}{g_V^2}, & c_{VVHH} &= \alpha^2 \left[\frac{g_W^4}{4g_V^4} \right], \\ c_F &= -\alpha, & c_{VWV} &= 1, & c_{VVV} &= -\frac{\alpha^3}{g_V} \left[1 - \frac{3g_W^2}{g_V^2} + \frac{2g_W^2}{g_V^4} \right]. \end{aligned} \quad (3.66)$$

The benchmarks T₁ to T₃ are meant to emphasise the phenomenological possibilities of the vector triplet model and ignore experimental constraints or parameter correlations from an underlying UV completion.

Higgs production rates and distributions

As shown in Figure 3.4, virtual heavy vector bosons contribute as intermediate t -channel mediators to WBF Higgs production and in the s -channel to Higgs-strahlung, promising non-trivial kinematic features in these production modes. In the EFT these effects are mapped onto large

Wilson coefficients for \mathcal{O}_W and \mathcal{O}_{WW} , adding a momentum dependence to the hVV couplings. Therefore our analysis focuses on these electroweak Higgs production modes.

Table 3.14 shows the agreement between EFT and full model for the total Higgs production rates in WBF Higgs production and Higgs-strahlung. The default dimension-six model matched in the unbroken phase, oblivious to the difference between the Lagrangian mass term M_V and the actual physical mass m_ξ , struggles with the first three benchmark points, in which this splitting is large. The discrepancies to the full model are particularly evident in Vh production.

The v -improved EFT, on the other hand, performs better and describes the rate accurately in most of the scenarios. Only in Higgs-strahlung in the extreme scenarios T1 and T2 we find significant deviations.

To better understand these differences, we have to look at kinematic distributions. Figure 3.5 shows different properties of the tagging jets in WBF Higgs production. In addition to the predictions of the full vector triplet model and the default and v -improved EFT, we show distributions of the vector triplet model where we have artificially removed all contributions from virtual ξ propagators.

We find that the vector triplet significantly modifies the WBF rate with respect to the Standard Model. Its effect increases with momentum transfer, measured as transverse jet momentum. This modification can be traced to contributions from ξ fusion and mixed W - ξ fusion diagrams as given in Figure 3.4. These contributions from ξ propagators can become relevant already at energy scales well below m_ξ , and increase further with the energy flow. In addition to the high-energy tails of the transverse momenta, large effects are visible in the azimuthal angle between the tagging jets, as shown in the bottom left panel of Figure 3.5. This angular correlation is well known to be sensitive to the modified Lorentz structure of the hWW vertex [82–89].

The EFT approach qualitatively captures these features of the full model, now parametrised by momentum-dependent operators such as \mathcal{O}_W and \mathcal{O}_{WW} . The signs of the Wilson coefficients in benchmarks T1 and T2 yield a non-linear increase of the cross section with energy. Conversely, the switched signs in T3 reduce the rate with energy, eventually driving the combined amplitude through zero.

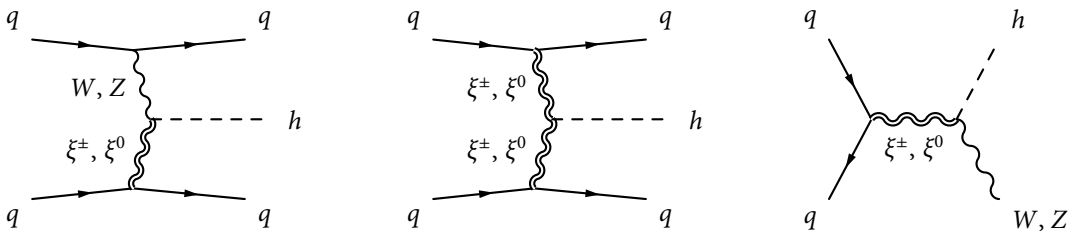


Figure 3.4: Example Feynman diagrams showing contributions from virtual heavy vector bosons ξ to Higgs production in weak boson fusion (left, middle) or Higgs-strahlung (right).

Comparing full and effective model for the more realistic benchmark points T₄ and T₅, we find good agreement in the bulk of the distribution. The deviations from the Standard Model are entirely captured by the dimension-six operators, including the momentum dependence coming from the ξ diagrams. Only at very large momentum transfer, most likely beyond the sensitivity of the LHC, the validity of the EFT breaks down.

In the more strongly coupled benchmark points T₁ to T₃, the full model predicts shifts in the jet distributions that are large enough to be relevant for the upcoming LHC run. We find good agreement between the full model and the default EFT only at low momentum transfer, where the effects of new physics are small. This naive dimension-six model fails to reproduce the full model results already at energy scales $p_{T,j} \gtrsim 80$ GeV, a phase space region highly relevant for constraints on new physics [26]. Perhaps counter-intuitively, this discrepancy does not signal a breakdown of the E/Λ expansion, but is linked to the difference between the physical mass m_ξ , which suppresses the ξ fusion diagrams, and the matching scale $\Lambda_{\text{default}} = M_V$, which suppresses the dimension-six operators. This can be seen by comparing the results to those based on v -improved matching, where the EFT cutoff scale matches the physical mass. Here the agreement is significantly better, and the dimension-six description successfully describes the momentum dependence up to large momentum transfer. Only at very high energies, $p_{T,j1} \gtrsim 300$ GeV, even the v -improved EFT breaks down.

The situation is similar in Higgs-strahlung. As shown in Figure 3.6, the dominant new physics effect is the interference with ξ -mediated diagrams rather than the modified hWW interaction. Not only does this lead to a significant change of the rate, it also introduces a strong dependence on the momentum transfer, probed by either the invariant mass of the gauge-Higgs system or the transverse momentum of the final vector boson. The relative sign of the interference between ξ amplitudes and SM-like diagrams is opposite to that in WBF: in T₃ and T₄ we find a non-linear

	$\sigma_{\text{default EFT}}/\sigma_{\text{triplet}}$		$\sigma_{v\text{-improved EFT}}/\sigma_{\text{triplet}}$	
	WBF	Vh	WBF	Vh
T ₁	1.299	0.299	0.977	0.794
T ₂	1.045	0.737	0.992	0.907
T ₃	0.921	1.066	0.966	1.024
T ₄	1.026	0.970	1.012	0.978
T ₅	1.001	1.043	1.002	1.043

Table 3.14: Cross-section ratios of the dimension-six approximation to the full vector triplet model at the LHC. To avoid large contributions from the ξ resonance in the Vh channel, we only take into account the region $m_{Vh} < 600$ GeV. The statistical uncertainties on these ratios are below 0.4%.

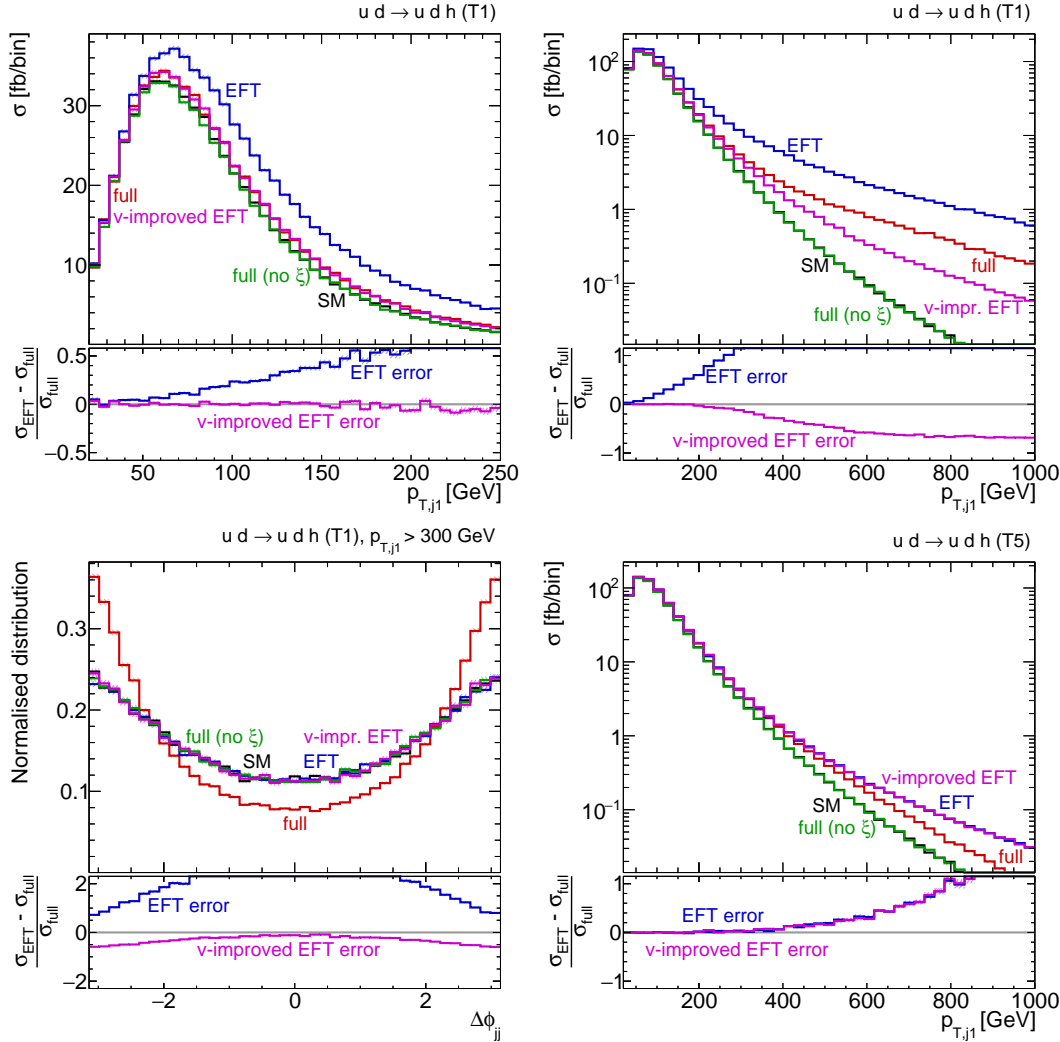


Figure 3.5: Tagging jet distributions in WBF Higgs production in the vector triplet model. Top: $p_{T,j1}$ distribution in benchmark T1, focusing on the low (left) and high (right) transverse momentum regions. Bottom left: $\Delta\phi_{jj}$ distribution above a certain $p_{T,j1}$ threshold for T1. Bottom right: $p_{T,j1}$ distribution for scenario T5. The shaded error bands give the statistical uncertainties.

3 Higgs effective theory at its limits

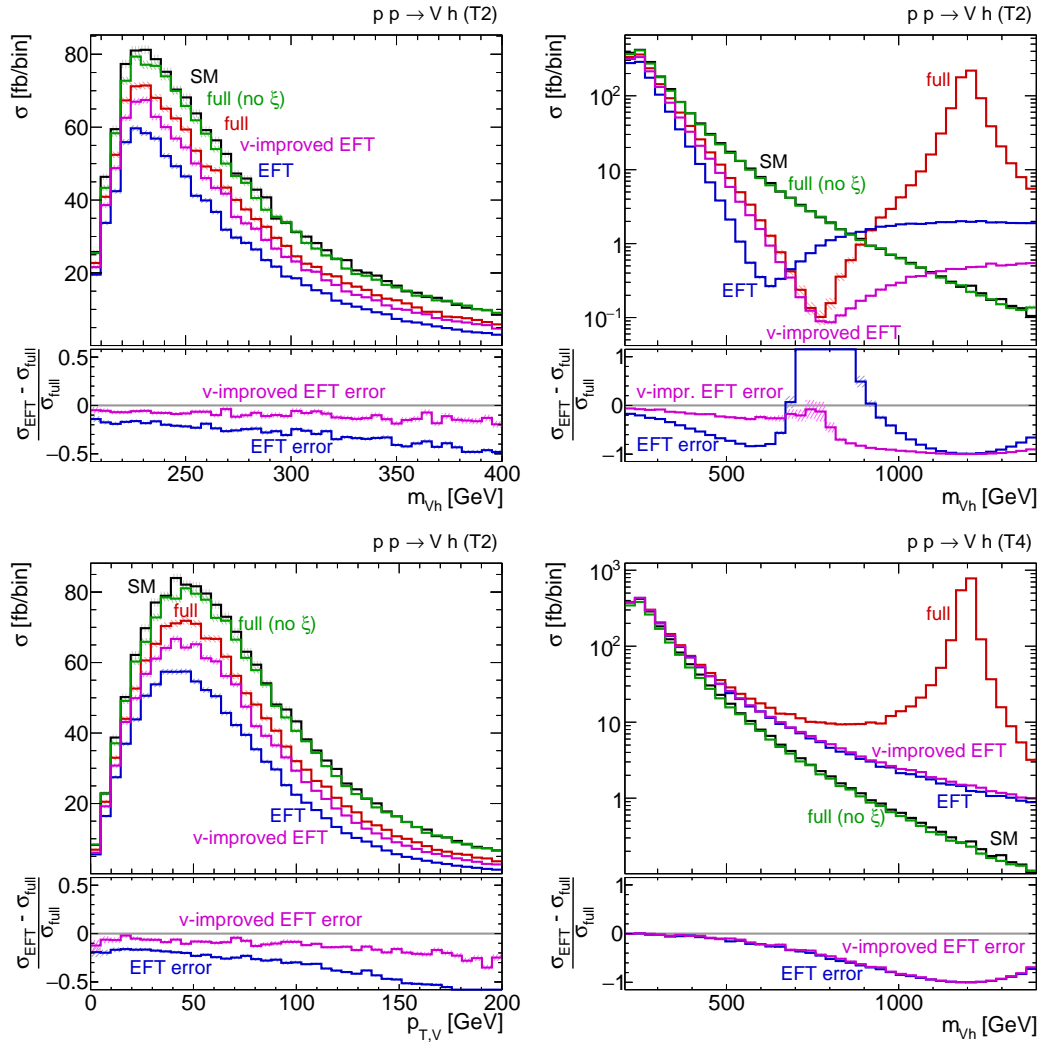


Figure 3.6: Higgs-strahlung distributions in the vector triplet model. Top: m_{Vh} distribution for benchmark T2, focusing on the low (left) and high (right) invariant mass regions. Bottom left: $p_{T,V}$ distribution for the same benchmark. Bottom right: m_{Vh} distribution for T4. The shaded error bands give the statistical uncertainties.

increase of the cross section with the energy scale. The other benchmarks predict a decrease of the amplitude with energy, eventually including a sign flip when the amplitude is driven through zero.

In the more weakly coupled benchmarks T₄ and T₅, the full and effective models agree well over most of the phase space, and the dimension-six operators successfully capture how the ξ contributions affect the Higgs-strahlung kinematics. At larger momentum transfer, higher-order terms in the EFT expansion become important, and dimension-six operators alone can no longer describe the kinematics accurately. Ultimately, the ξ resonance in the full model marks the obvious failure of the effective theory.

For benchmarks T₁ to T₃, the default EFT has a more limited validity range. The large couplings lead to a failure of this dimension-six model already at low energies $m_{Vh} \gtrsim 220$ GeV, even though the actual ξ resonances only appear at $m_\xi = 1.2$ TeV. The EFT approximation can again be significantly improved by switching to the v -improved matching. But even then, there is a pronounced mismatch between full and effective model. This EFT error is larger in Higgs-strahlung than in WBF, showing how ξ contributions play a larger role in this *s*-channel process than in the *t*-channel WBF diagrams.

Summary

Heavy vector bosons can induce large kinematic effects in Higgs-gauge interactions, providing a perfect test case for the EFT approach. For realistic scenarios, the EFT works up to large momentum transfer. Operators such as \mathcal{O}_W and \mathcal{O}_{WW} successfully capture the effects from virtual ξ contributions to WBF Higgs production, including non-trivial momentum dependencies. In Higgs-strahlung, *s*-channel ξ contributions prove more renitent to be mapped onto effective operators, but we still find good agreement for most of the phase space for realistic parameter choices.

Again, this remarkable performance of the dimension-six model requires particular care in the matching to the full theory. When the mixing with the SM gauge bosons is large, a naive matching procedure defined in the unbroken electroweak phase can lead to substantial errors already in the bulk of the WBF distributions. A v -improved dimension-six description, however, improves the EFT accuracy such that large deviations only occur in the high-energy tails of distributions.

3.4 Practical questions

We now focus on the example of WBF Higgs production in the vector triplet model to discuss some practical aspects. The first is the question which observables are most sensitive to the momentum transfer in this production mode, and therefore provide a handle on the validity

regions of the EFT. In Section 3.4.2 we then discuss the role of squared dimension-six terms in the differential cross section. Finally, Section 3.4.3 illustrates how constraints on the vector triplet model can be determined directly in the full model or indirectly via EFT measurements, and how this is affected by the breakdown of the EFT description.

In the previous section we established that a v -improved matching, defined in Equations (3.63) and (3.64), improves the agreement between effective model and full theory, hence from now on we use it exclusively.

3.4.1 Weak boson fusion observables

We have repeatedly argued that the validity of the effective field theory depends on the energy scale or momentum flow in a process. In a $2 \rightarrow 2$ process where all final-state particles can be measured precisely, the momentum transfer can easily be calculated, for instance with the Mandelstam variables s , t , and u . For WBF Higgs production, both the definition and the measurement of the momentum transfer are more involved. We have to take into account that this is a $2 \rightarrow 3$ process even without adding a Higgs decay, and that the charges of the initial and final partons cannot be determined experimentally.

To define the momentum transfer in weak boson fusion, we first note that W -mediated and Z -mediated diagrams contribute to this process. Quark-vector splittings are more likely to happen in the collinear direction [71], and the direction of the final-state quarks is typically only slightly deflected from that of the corresponding initial partons. The W -mediated and Z -mediated diagrams thus dominate in very different regions of phase space and their interference is negligible. This allows us to distinguish ‘ W -like’ and ‘ Z -like’ phase-space regions and to assign four-momenta p_{V1} and p_{V2} to the intermediate vector bosons [181]. For the dominant amplitude $ud \rightarrow u'd' h$, we define

$$\begin{aligned} p_{V1} &= p_{u'} - p_d, & p_{V2} &= p_{d'} - p_u && \text{for } W\text{-like phase-space points,} \\ p_{V1} &= p_{u'} - p_u, & p_{V2} &= p_{d'} - p_d && \text{for } Z\text{-like phase-space points.} \end{aligned} \quad (3.67)$$

The validity of the EFT is limited by the largest momentum flow in the process. We therefore define the relevant momentum transfer q as the maximum virtuality of the intermediate bosons,

$$q = \sqrt{\max(p_{V1}^2, p_{V2}^2)}. \quad (3.68)$$

Experimentally we can neither distinguish between the jets from up-type and down-type quarks, nor can we determine the charges of the initial-state partons. The true momentum transfer q therefore cannot be calculated and we have to resort to an experimentally accessible proxy. The transverse momenta of the two tagging jets, $p_{T,j1}$ and $p_{T,j2}$, are two good candidates. As can be seen from the Feynman diagram in Figure 2.1, these two jets directly recoil against

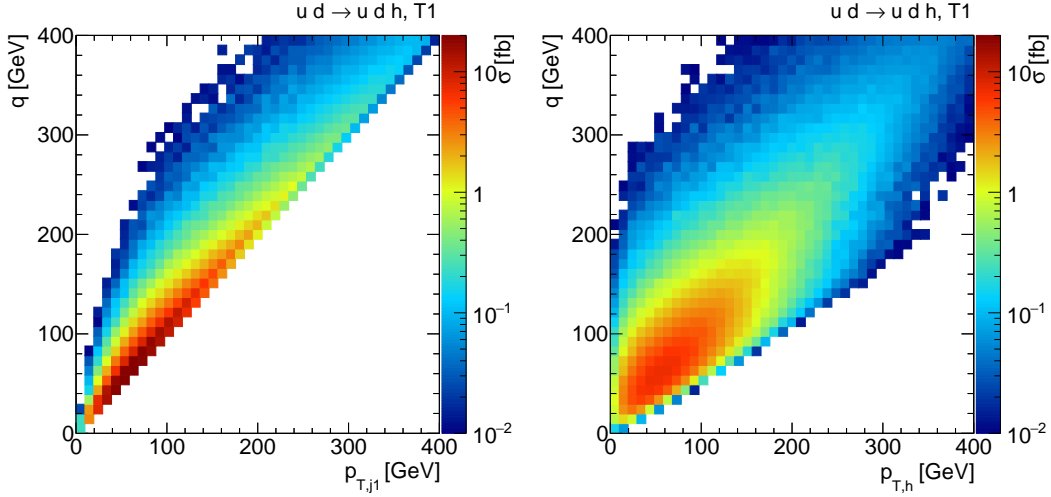


Figure 3.7: Correlations between the WBF momentum transfer q , defined in Equation (3.68), and the observable transverse momenta p_{T,j_1} (left) and $p_{T,h}$ (right). The shaded error bands give the statistical uncertainties.

the intermediate vector bosons, so $p_{T,j_i} = p_{T,V,i}$. We order them such that $p_{T,j_1} > p_{T,j_2}$. As an alternative to the two jets, we can consider the transverse momentum of the Higgs, $p_{T,h}$, which can be reconstructed even if the Higgs decay involves neutrinos.

Figure 3.7 shows the correlations of the virtuality q with the transverse momentum of the leading tagging jet and with the transverse momentum of the Higgs boson. Both observables are visibly correlated with the momentum transfer, but the correspondence is particularly clear for the jet p_T .

From the previous section we know that an EFT analysis of kinematic distributions faces a trade-off: on the one hand, new physics signatures often grow with the energy scale. On the other hand, the validity of the effective field theory is on a more secure footing at lower energy scales. However, we have never defined the ‘energy scale’ in these statements quantitatively. We now discuss this choice for WBF Higgs production. More precisely, we ask which observable x

1. can isolate phase-space regions with interesting NP signatures with a cut $x > x_{\min}$, and simultaneously
2. ensures the EFT validity with a cut $x < x_{\max}$.

We compare the observables

$$x \in \{q, p_{T,j_1}, p_{T,j_2}, p_{T,h}\} . \quad (3.69)$$

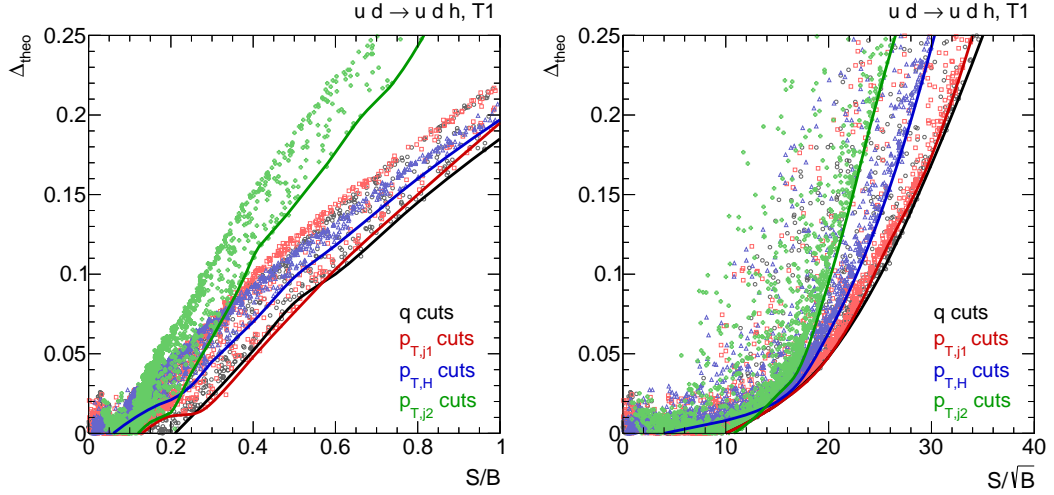


Figure 3.8: Trade-off between sensitivity to new physics signatures and EFT validity in different WBF distributions. We plot the significance of expected vector triplet signals (left: S/B , right: S/\sqrt{B}) against the theoretical uncertainty Δ_{theo} representing the EFT error. Each point corresponds to a selection window $x_{\min} < x < x_{\max}$ in one of the four momentum observables $x \in \{q, p_{T,j_1}, p_{T,j_2}, p_{T,h}\}$. The lines guide the eye to the best-performing cut windows on these variables.

As discussed above, they all provide probes of the momentum transfer through the intermediate vector bosons.

For each observable x we scan over values of x_{\min} and x_{\max} . For each window (x_{\min}, x_{\max}) we calculate the predictions for the parton-level WBF process defined in Equation (3.18) for the SM, the vector triplet benchmark point T1, and the corresponding v -improved EFT description. We reject windows that only leave a signal cross section of less than 20 fb before Higgs decays. We then estimate the significance of the vector triplet signal over the SM background, disregarding non-Higgs backgrounds or detector effects for our toy study. In a measurement limited by systematic uncertainties, the relevant quantity is

$$\frac{S}{B}(x_{\min}, x_{\max}) = \left| \frac{\sigma_{\text{vector triplet}} - \sigma_{\text{SM}}}{\sigma_{\text{SM}}} \right|, \quad (3.70)$$

while for a statistics-limited analysis we have to consider

$$\frac{S}{\sqrt{B}}(x_{\min}, x_{\max}) = \sqrt{L} \left| \frac{\sigma_{\text{vector triplet}} - \sigma_{\text{SM}}}{\sqrt{\sigma_{\text{SM}}}} \right|. \quad (3.71)$$

For our simple illustration we pick an integrated luminosity times Higgs branching ratio times efficiencies of $L \times \text{BR} \times \varepsilon = 30 \text{ fb}^{-1}$. For each window (x_{\min}, x_{\max}) we also calculate the theory

uncertainty that quantifies the EFT error in this kinematic region as

$$\Delta_{\text{theo}}(x_{\min}, x_{\max}) = \left| \frac{\sigma_{\text{EFT}} - \sigma_{\text{vector triplet}}}{\sigma_{\text{vector triplet}}} \right|. \quad (3.72)$$

The question is for which observable x we expect significant new physics signatures, i. e. large values of S/B and S/\sqrt{B} , while keeping the EFT error Δ_{theo} small. We show the results of our scan in Figure 3.8. The momentum transfer q as well as the leading tagging jet's p_T define kinematic regions with the highest significance for a given theoretical uncertainty Δ_{theo} . This indicates that as long as q is not directly accessible, the transverse momentum of the leading tagging jet indeed provides the best probe of the momentum flow through the WBF process, and justifies our choice of observables in the previous section.

3.4.2 To square or not to square

Differential cross sections are proportional to the squared matrix element. In our EFT approach, we have

$$|\mathcal{M}_{\text{EFT}}|^2 = \underbrace{|\mathcal{M}_4|^2}_{\mathcal{O}(1)} + \underbrace{2 \operatorname{Re} \mathcal{M}_4^* \mathcal{M}_6}_{\mathcal{O}(1/\Lambda^2)} + \underbrace{|\mathcal{M}_6|^2 + 2 \operatorname{Re} \mathcal{M}_4^* \mathcal{M}_8}_{\mathcal{O}(1/\Lambda^4)} + \mathcal{O}(1/\Lambda^6), \quad (3.73)$$

where the subscripts in \mathcal{M}_d denote the dimension of the operators in the amplitude, i. e. \mathcal{M}_4 is the SM amplitude and \mathcal{M}_6 contains one dimension-six interaction. The squared amplitudes from dimension-six operators contribute at the same order in the EFT expansion in $1/\Lambda$ as the leading contributions from dimension-eight operators. This raises the question whether these squared terms should be included in calculations when dimension-eight operators are ignored [181, 184, 195, 196, 268–270].

In a top-down perspective, i. e. when the underlying physics is known, the answer depends on the typical coupling strengths of the underlying physics. At least for tree-level effects, the Wilson coefficients of both dimension-six and dimension-eight operators will generally contain two couplings of the heavy field, $f_i \sim g_{UV}^2$, and we have to compare the terms

$$|\mathcal{M}_6|^2 \sim \frac{g_{UV}^4}{\Lambda^4} \quad \text{vs.} \quad 2 \operatorname{Re} \mathcal{M}_4^* \mathcal{M}_8 \sim \frac{g_{SM}^2 g_{UV}^2}{\Lambda^4}, \quad (3.74)$$

where g_{SM} denotes a typical SM coupling. In strongly coupled scenarios with $g_{UV} > g_{SM}$, we therefore expect the squared dimension-six terms to dominate over the dimension-eight contributions; it is then perfectly justified to include the squared dimension-six term, but no dimension-eight operators. In more weakly coupled models with $g_{UV} \sim g_{SM}$, the two should approximately contribute equally. The size of the squared dimension-six terms can then be seen

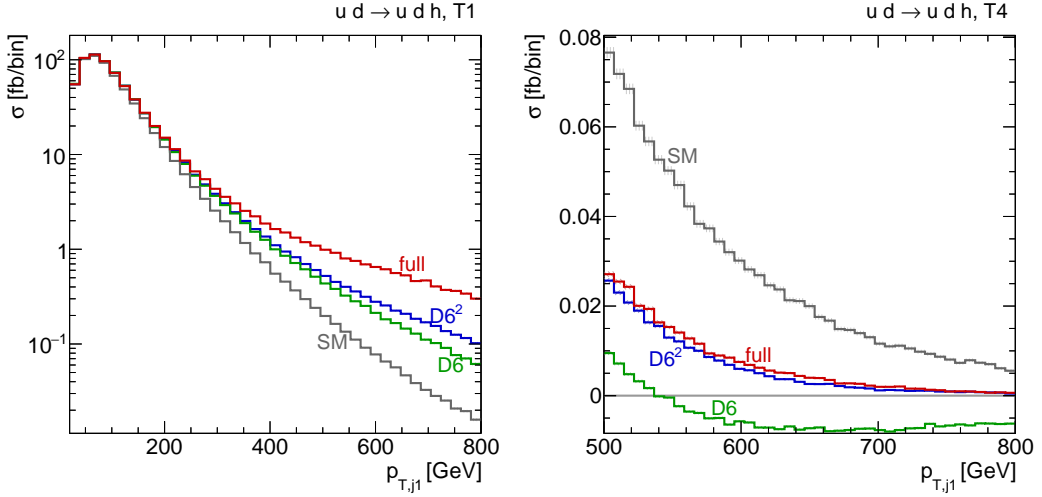


Figure 3.9: WBF distributions with ('D6²') and without ('D6') the squared amplitudes from dimension-six operators in benchmarks T1 (left) and T4 (right). The right panel zooms in on the region where leaving out the squared dimension-six terms leads to a negative cross section. The shaded error bands give the statistical uncertainties.

as an estimate for the size of the missing higher orders in the EFT expansion, and therefore as an indicator for the validity of the EFT approach [195].

Of course, in practice we do not know the coupling strength of UV physics. Generally discarding the squared dimension-six terms will degrade the EFT performance at least for strongly coupled scenarios. Similarly, using the size of the squared dimension-six amplitude as a universal theory error in global fits introduces an unnecessary theory dependence in the results.

Note also that the argument around Equation (3.74) relies on the assumption that — except for the typical couplings and the suppression scale Λ — all amplitudes have approximately the same size. But in phase-space regions where the dimension-four contribution is suppressed, the dimension-six squared term can easily be larger than the interference between the SM and the dimension-eight amplitude, even if the EFT expansion in v/Λ holds and higher-dimensional operators are negligible. One example is Higgs pair production with its accidental cancellation between the two SM contributions, as discussed in Section 2.1.2 and demonstrated in Section 3.3.2.

If we consider the dimension-six Lagrangian not as the leading term of a consistent effective field theory, but rather as a phenomenological parametrisation describing a vast range of LHC Higgs signatures, the counting argument becomes irrelevant and the square of dimension-six terms should always be included.

Finally, from a technical perspective the squared dimension-six terms are necessary to guaran-

tee positive cross sections. Without them, the expected rate can become negative in high-energy tails or in other regions of the phase space where the SM predictions are small.

Figure 3.9 demonstrates these considerations, again with the example of WBF Higgs production in the vector triplet model. The squared dimension-six terms improve the agreement with the full model, and can be necessary to avoid negative rates at high jet p_T .

To conclude, a simple expansion in $1/\Lambda$ suggests that the square of dimension-six amplitudes should not be taken into account in calculations within the dimension-six framework. But this argument is only valid if the underlying physics is weakly coupled and in phase-space regions with sizeable contributions from the SM. In these situations no harm is done by including the squared dimension-six terms. Since their inclusion can improve the EFT validity in many other scenarios and is necessary to guarantee positive cross sections, we recommend to include these terms in most situations.

3.4.3 Limit setting

An important purpose of the dimension-six Lagrangian is to act as an intermediate parametrisation in the process of using Higgs measurements to set exclusion limits on the parameter space of specific models. We now test explicitly if limits derived in this way agree with constraints directly calculated in the full model.

We follow a simplified limit setting procedure. Expected exclusion limits on the vector triplet in the absence of a signal are calculated, either directly based on the full model, or first on the dimension-six Wilson coefficients and then translated onto the full model. Motivated by the discussion in the previous section, we also calculate limits on the dimension-six Wilson coefficients without taking into account the squared dimension-six contributions, and again translate the results to the vector triplet parameters. As a process we consider WBF Higgs production as given in Equation (3.18) and multiply the total Higgs production cross sections with a branching ratio $\text{BR}(h \rightarrow 2\ell 2\nu) \approx 0.01$. We disregard non-Higgs backgrounds as well as parton-shower or detector effects. Our limits are based on expected event counts in two high-energy bins of the p_{T,j_1} distributions. We define a parameter point as excluded if $S/\sqrt{S+B} > 2$. While this statistical analysis is not designed to be realistic, it illustrates how the validity of our dimension-six approach affects possible limits.

We consider a two-dimensional plane in the parameter space of the vector triplet model. It is spanned by the mass m_ξ and a universal coupling rescaling c , and we choose the couplings as

$$g_V = 1, \quad c_H = c, \quad c_F = \frac{g_V^2}{2g^2} c, \quad \text{and} \quad c_{HHVV} = c^2, \quad (3.75)$$

such that the Wilson coefficients $f_{\phi,2}$, $f_{\phi,3}$, and f_t vanish,

$$f_{WW} = f_{BW} = \frac{c^2}{2g^2}, \quad \text{and} \quad f_W = -\frac{c^2}{g^2}. \quad (3.76)$$

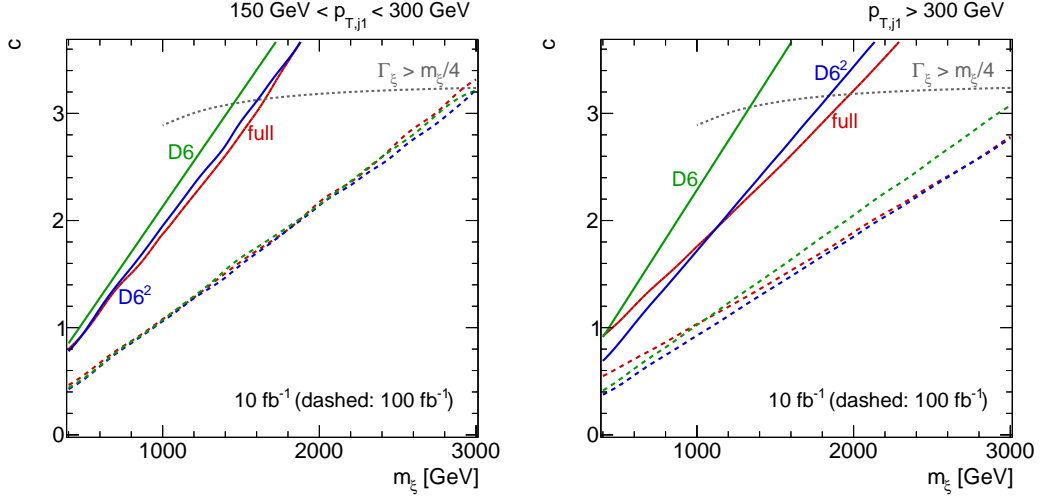


Figure 3.10: Toy limits on the two-dimensional slice of the vector triplet parameter space defined in Equation (3.75). We show the analysis based on the event numbers in $150 \text{ GeV} < p_{T,j1} < 300 \text{ GeV}$ (left) and based on the tail $p_{T,j1} > 300 \text{ GeV}$ (right).

In this parameter plane, all amplitudes from dimension-six operators scale with c^2/m_ξ^2 . Our perturbative calculation does not make sense for very strongly interacting systems, so we limit our analysis to $\Gamma_\xi/m_\xi < 1/4$.

The resulting toy limits are shown in Figure 3.10. Based on event numbers in the range $150 \text{ GeV} < p_{T,j1} < 300 \text{ GeV}$, constraints calculated directly in the full model and EFT limits translated to the vector triplet agree very well. The inclusion of the dimension-six squared terms, however, can be important for this agreement. With more statistics, the differences between the various procedures become smaller, and ultimately the question of whether the squared dimension-six amplitudes should be taken into account is rendered irrelevant.

Larger differences appear when we use the information from the high-energy tail $p_{T,j1} > 300 \text{ GeV}$ to constrain vector bosons with masses down to $m_\xi \gtrsim 500 \text{ GeV}$. This lack of a scale hierarchy does not improve with more statistics. The high-energy tail is also more sensitive to the square of dimension-six terms.

3.5 Conclusions

The dimension-six operators of linear Higgs effective field theory provide a theoretically well-defined, largely model-independent, and phenomenologically powerful framework to parametrise deviations from the Standard Model. However, the validity of the EFT approach relies on a gap between the experimental momentum transfer and the mass scales of the probed models of

new physics. The limited precision of the LHC Higgs measurements can guarantee such a clear scale hierarchy only under the additional assumption that the underlying physics is strongly coupled. For moderately weakly to moderately strongly coupled models, these analyses are sensitive to new physics scales ranging from the electroweak scale to approximately one TeV, casting doubt on the validity of the EFT approximation.

In this chapter we have studied the usefulness of the effective theory for LHC Higgs measurements by comparing different complete models of new physics to their descriptions in terms of dimension-six operators. Our comparison included a singlet extension of the Higgs sector, a two-Higgs doublet model, scalar top partners, and a heavy vector triplet, focusing on parameter ranges relevant for the LHC. We analysed Higgs couplings, total production rates, and kinematic distributions for the main Higgs production modes and representative decay channels.

A naive construction of the dimension-six model, where the effective theory is matched to the full model in the unbroken phase of the electroweak symmetry, confirms the concerns based on an estimate of the energy scales: such a dimension-six approximation does not describe the phenomenology of many models adequately. In Higgs couplings and total production rates, the discrepancies between the full model and its effective counterpart are of the order of v^2/Λ^2 , where Λ is the new physics scale. In the high-energy tails of distributions, the EFT error even scales with E^2/Λ^2 . For many weakly coupled scenarios relevant for LHC Higgs measurements, this implies an unacceptably large error.

But this is not the end of the story. As we discussed at length in Section 3.2, matching the dimension-six model to the full theory is not unambiguous. First, instead of setting the matching scale Λ to the intrinsic new physics scale in the Lagrangian, we can use the actual physical masses after electroweak symmetry breaking, including contributions from the electroweak VEV. Second, we can express the Wilson coefficients of the dimension-six operators in terms of physical quantities such as mixing angles instead of Lagrangian parameters. These alternative choices, which we collectively call ‘ v -improved matching’, amount to matching the EFT in the broken phase of the electroweak symmetry.

While a v -improved EFT construction may be unconventional from a purely theoretical perspective, expressing quantities in physical masses and mixing angles is a natural choice from a practical point of view. It can be interpreted as a partial absorption of the dimension-eight and higher operators of the form $(\phi^\dagger \phi)^n \mathcal{O}_i$ into the Wilson coefficients of dimension-six operators with the replacement $\phi^\dagger \phi \rightarrow v^2/2$. In this way, it can improve the effective description where the expansion in v/Λ converges slowly for the default matching; it cannot help in high-energy tails where E/Λ becomes large. Note that v -improvement does not change the form of the effective operators, nor does it affect their phenomenology, or the way that experimental collaborations should set limits on operators. It purely affects the interpretation of Wilson coefficients in terms of model parameters.

We find that with a v -improved matching procedure the dimension-six operators provide an

Model	Process	EFT failure		
		rates	kinematics	matching
singlet	on-shell ggF, WBF, Vh			x
	off-shell WBF		(x)	x
	hh	x	x	x
2HDM	on-shell ggF, WBF, Vh	(x)		x
	off-shell $h \rightarrow \gamma\gamma$		(x)	x
	hh	x	x	x
top partners	WBF, Vh	(x)		(x)
vector triplet	WBF		(x)	x
	Vh		(x)	x

Table 3.15: Possible sources of failure of the dimension-six Lagrangian in Higgs observables. In addition, new light resonances contributing to the same final states present an obvious breakdown of the effective description. We use parentheses where deviations appear, but are unlikely to be observed in realistic scenarios.

adequate description in almost all scenarios. The exceptions that confirm the rule are summarised in Table 3.15. The singlet and doublet extensions of the Higgs sector lead to simple shifts of the SM Higgs couplings, effects mostly well captured by the corresponding dimension-six operators. The effective description struggles with shifts of the Higgs-gauge couplings in the 2HDM, which only appear at dimension eight in the EFT. A more dramatic breakdown occurs in Higgs pair production, where two types of SM diagrams approximately cancel and off-shell contributions from new resonances have a large impact. With the scalar top partners, we illustrate that loop effects in Higgs-gauge couplings are either too small to be relevant for the LHC, or require light new particles and large couplings, in which case the effective description clearly breaks down. The vector triplet model generates interesting kinematic effects in Vh and WBF Higgs production at tree level. A v -improved dimension-six model can describe these effects over a large part of the phase space for realistic scenarios, breaking down only in the high-energy tails of certain kinematic distributions. Finally, the effective theory fails to describe new light resonances. Such a signature at the LHC would be an obvious signal to switch to an appropriate simplified model.

Focusing on Higgs production in weak boson fusion in the vector triplet model, we proceeded with a set of practical questions. First, we studied how the momentum transfer in weak boson fusion can be defined and measured, confirming the established notion that the transverse momenta of the tagging jets provide the most useful probe of the energy flow. We discussed the role of squared dimension-six amplitudes, which contribute to cross sections at the same

order in the EFT expansion as the leading effects from the neglected dimension-eight operators. Nevertheless, these squared terms can improve the performance of the dimension-six model in many cases and should in general be included in calculations from a bottom-up perspective.

We concluded our discussion of the vector triplet model with a brief demonstration of how the validity of the dimension-six model affects the setting of exclusion limits in practice. The effective theory is less reliable when very high-energy events are taken into account. This suggests that experiments should constrain Wilson coefficients not only with the full event samples, but also with additional upper bounds on the momentum transfer; alternatively, momentum-dependent theory uncertainties can be assigned to the events [271].

With the limited precision of the LHC, the EFT approach is not guaranteed to describe all potential signatures of new physics in Higgs measurements accurately. Nevertheless, we have demonstrated that the dimension-six model works remarkably well for a wide range of models, parameter choices, and observables in single Higgs production. Key to this good performance is a suitable matching procedure which takes into account subleading contributions from the Higgs VEV. This does not present a complication for an experimental fit of dimension-six operators to LHC Higgs data, it is purely a theoretical aspect for the interpretation of the results.

Chapter 4

Better Higgs measurements through information geometry

WITH THE RESULTS OF THE LAST CHAPTER, we rest assured that many potential signatures of new physics in Higgs observables can be parametrised by dimension-six operators. The next question is how the corresponding Wilson coefficients can be measured as precisely as possible. In this chapter we develop statistical tools based on information geometry that can help to optimise such measurements.

After an introduction in Section 4.1, in Section 4.2 we summarise the statistics of the measurement process, define the Fisher information, and discuss what constitutes an optimal measurement. In Section 4.3 we apply these general ideas to LHC physics and develop an algorithm to calculate the Fisher information in particle physics processes. We also discuss some aspects of information geometry particular to effective field theories. In Section 4.4 we use our formalism to understand how dimension-six operators can be optimally measured in a range of Higgs channels. We demonstrate how our approach can be extended to describe systematic uncertainties and link it to other statistical tools in Section 4.5. Finally, we give our conclusions in Section 4.6.

The majority of the research presented in this chapter was previously published in Reference [4]. Most of the results and their presentation, including many plots and tables as well as part of the text, are identical to the content of that article. They are supplemented with a few unpublished results.

4.1 Introduction

Having established that the dimension-six operators of the linear Higgs effective theory capture the indirect signatures of many scenarios of new physics, we now analyse how the Higgs

properties (in the EFT the Wilson coefficients f_i/Λ^2) can be measured most efficiently at the LHC. This is a highly non-trivial problem for two reasons: first, the Higgs properties form a high-dimensional parameter space. In Section 2.3.2 we showed that, even after removing redundant operators and generously neglecting those with tight limits from electroweak precision measurements or flavour constraints, we are left with 13 dimension-six operators relevant for Higgs physics. The Higgs-gauge interactions, for instance, are affected by seven of these operators, equivalent to a range of different kinematic structures or forms of momentum dependence. The second challenge is due to the complicated kinematics of some of the Higgs production channels and decay modes. For example, Higgs production in weak boson fusion with a decay $h \rightarrow W^+ W^- \rightarrow (\ell^+ \nu)(\ell^- \bar{\nu})$ is a $2 \rightarrow 6$ process even at parton level, made even more complicated by additional QCD radiation. Such a high-dimensional phase space defines a large number of kinematic observables, and it is often not obvious which of them carry information on the theory parameters of interest. The relation between the high-dimensional parameter space and the potentially high-dimensional phase space is (at parton level) encoded in the scattering amplitudes or Feynman diagrams, of which there can easily be hundreds for a given process.

Analyses of collider signatures with **traditional methods** typically begin with simple selection cuts on standard kinematic observables such as energies, momenta, angles, or invariant masses. Background contributions are estimated with simulational or data-driven methods. The final statistical analysis often relies on total event counts or on histograms of kinematic observables. These techniques are motivated by physical arguments, all their steps are transparent, and they are relatively easy to reproduce, even for theorists. They work well for simple signatures, such as a resonance peak on top of a smooth background, as in the discovery of the $gg \rightarrow h \rightarrow \gamma\gamma$ signal [17, 18]. This approach requires a careful tailoring to each problem, and does not scale well with the complexity of the theory questions or of the kinematics of the processes.

At the other end of the spectrum, the LHC collaborations increasingly rely on measurement strategies based on high-level statistical tools [272]. Some of them are based on the structure of the **matrix elements** contributing to the process. In the matrix element method [50–59], the differential cross section expected from a given model hypothesis at a specific phase-space point, or the ratio of two such expected rates, is directly used as an observable. The detector response is estimated by convoluting this expression with suitable transfer functions. Shower deconstruction [60, 61] and event deconstruction [62] extend this concept to the parton shower to take into account the information encoded in the jet substructure. The method of optimal observables [63–65] applies the same idea to the measurement of a small theory parameter. All of these tools intrinsically make full use of the information encoded in the underlying field theories, but rely on an approximate description of the detector systems. Large final-state multiplicities require integrating over a high-dimensional phase space and are computationally expensive. Finally, matrix-element-based tools generally either rely on the comparison of two discrete hypotheses or are designed for the measurement of one direction in theory space. Applying

these methods to high-dimensional theory spaces, such as Higgs effective field theory, often requires a discretisation of the theory space, which can be computationally expensive. In addition, care has to be taken to avoid dependencies on EFT basis choices.

A second class of complex statistical tools belongs to the category of **likelihood-free inference** [272]. These techniques are mostly based on (supervised) machine learning: flexible nonlinear functions, for example boosted decision trees or deep neural networks, are ‘trained’ to describe patterns in a set of training samples. This approach is agnostic about the amplitudes describing a process. The methods with which the input samples are generated are irrelevant. Unlike simple likelihood-based methods, these samples can be based on data or on full-fledged Monte-Carlo simulations with a parton shower and a detailed detector simulation. New ideas are developed at an impressive pace [28–32]. These tools are applied to problems at all steps of the analysis process, ranging from tracking [33, 273] to the analysis of jet substructure [34–42], to the discrimination between signal and background hypotheses [43–46], and finally to the statistical testing of model hypotheses [47–49]. For complicated problems, multivariate tools often outperform traditional approaches. However, their inner structure is often convoluted and not necessarily intuitive, and it is not always clear which physical structures these ‘black boxes’ are sensitive to.

With these wide range capabilities, it is increasingly important that we can understand and characterise the information contained in particle physics processes. An efficient estimation of the sensitivity of measurements to new physics signatures that does not require a full simulation of the analysis chain can help plan experiments. Moreover, the design of event selections and analysis strategies requires clearly defined guidelines.

We present a novel approach to tackle these problems based on information geometry [66–68]. It is intrinsically designed for continuous parameter spaces of arbitrary dimensionality, independent of basis choices, and without the need for any discretisation of the model hypothesis. These properties are particularly convenient for measurements of Higgs properties in terms of a large number of effective operators.

The central object in our approach is the **Fisher information** matrix. According to the Cramér-Rao bound [69, 70], it quantifies the maximum knowledge on theory parameters that we can derive in a measurement, independent of the analysis strategy. This allows us to calculate the best possible precision with which theory parameters can be measured with any multivariate black-box analysis. Also, the Fisher information defines a metric in the space of theory parameters. This provides an intuitive geometric interpretation for the discrimination power of an experiment. From a practical perspective, it gives us a handle on the linearisation of observables in terms of new physics parameters, as we demonstrate in the next section.

Two objects are particularly interesting for LHC physics. First, the distribution of the differential information over phase space defines the relevance of different phase-space regions for an analysis and should motivate the design of event selections. Second, we can calculate the

information contained in individual kinematic observables and compare it to the full Fisher information. This determines the most important observables and allows us to compare the power of traditional histogram-based analyses to that of modern multivariate tools.

We develop an algorithm, MadFisher, that can calculate the Fisher information for arbitrary perturbative particle physics processes based on Monte-Carlo methods. We can calculate the quantities outlined above, and use them to answer practical questions:

- What is the maximum precision with which continuous model parameters can be measured in a process?
- How is the information on model parameters distributed over phase space?
- How well can we measure model parameters based on individual kinematic observables, rather than on the information in the full high-dimensional phase space?
- Which role do non-linear effects in the theory parameters play?

As a first application, we calculate the information on CP -even dimension-six operators in WBF Higgs production with a decay into tau pairs, focusing on the kinematic structures defined by the tagging jets and their sensitivity to the Higgs-gauge coupling structure. We then examine WBF Higgs production in the four-lepton mode to see how much additional information is contained in the decay kinematics. The last channel we analyse is Higgs production in association with a single top. Finally, we demonstrate how systematic uncertainties can be treated in our approach, and compare the Fisher information to other statistical tools, including the log-likelihood ratio.

The Fisher information is commonly used in various fields, for instance in cosmology [274–277], but only rarely in particle physics [278]. To the best of our knowledge, most of the tools presented in Reference [4] and in this chapter are innovative at least for this field. Since the publication of Reference [4], these and similar ideas have received more attention [279, 280].

4.2 Essential statistics

4.2.1 Fisher information and Cramér-Rao bound

Any measurement uses experimental data \mathbf{x} to calculate an estimator $\hat{\boldsymbol{\theta}}(\mathbf{x})$ of the unknown true value of some parameters $\boldsymbol{\theta}$. The outcome of the experiment is described by the probability distribution $f(\mathbf{x}|\boldsymbol{\theta}_0)$ that depends on the true value $\boldsymbol{\theta}_0$, and thus the outcome of the estimator also follows a probability distribution

$$f(\hat{\boldsymbol{\theta}}|\boldsymbol{\theta}_0) = \int d\mathbf{x} f(\mathbf{x}|\boldsymbol{\theta}_0) \delta(\hat{\boldsymbol{\theta}} - \hat{\boldsymbol{\theta}}(\mathbf{x})). \quad (4.1)$$

Two key properties of this distribution characterise the measurement. First, the bias of an estimator is given by the difference between the expectation value

$$\bar{\theta} \equiv E[\hat{\theta}|\theta_0] = \int d\hat{\theta} \hat{\theta} f(\hat{\theta}|\theta_0) \quad (4.2)$$

and the true value θ_0 . An estimator is unbiased if the expectation value is always equal to the true value,

$$\bar{\theta} = \theta_0. \quad (4.3)$$

Second, the variance

$$\text{var}[\hat{\theta}|\theta_0] \equiv E[(\hat{\theta} - \bar{\theta})^2|\theta_0], \quad (4.4)$$

or for more than one parameter the covariance matrix

$$\text{cov}[\hat{\theta}|\theta_0]_{ij} \equiv E[(\hat{\theta}_i - \bar{\theta}_i)(\hat{\theta}_j - \bar{\theta}_j)|\theta_0], \quad (4.5)$$

provides a measure of the precision.

But how good can an estimator be? Clearly, any given experiment does not allow the measurement of parameters with arbitrary precision. We can make this statement more quantitatively. If the parameters θ_i are continuous, $f(\mathbf{x}|\boldsymbol{\theta})$ is twice differentiable in them, and if we can exchange this differentiation with the integration over \mathbf{x} , we can calculate the **Fisher information**

$$I_{ij}(\boldsymbol{\theta}) = E\left[\frac{\partial \log f(\mathbf{x}|\boldsymbol{\theta})}{\partial \theta_i} \frac{\partial \log f(\mathbf{x}|\boldsymbol{\theta})}{\partial \theta_j}\right] = -E\left[\frac{\partial^2 \log f(\mathbf{x}|\boldsymbol{\theta})}{\partial \theta_i \partial \theta_j}\right]. \quad (4.6)$$

The **Cramér-Rao bound** [69, 70] then states that the covariance matrix of any estimator $\hat{\theta}$ is bounded from below by the inverse Fisher information¹:

$$\text{cov}[\hat{\theta}|\theta_0]_{ab} \geq \frac{\partial \bar{\theta}_a}{\partial \theta_i}(\theta_0) I^{-1}_{ij}(\theta_0) \frac{\partial \bar{\theta}_b}{\partial \theta_j}(\theta_0), \quad (4.7)$$

where we implicitly sum over repeated indices i, j . For an unbiased estimator, i. e. for $\bar{\theta} = \theta_0$, the Cramér-Rao bound takes on the simple form

$$\text{cov}[\hat{\theta}|\theta_0]_{ij} \geq I^{-1}_{ij}(\theta_0). \quad (4.8)$$

In the one-dimensional case, this corresponds to a typical measurement error of

$$\Delta\theta \equiv \sqrt{\text{var}[\hat{\theta}|\theta_0]} \geq 1/\sqrt{I(\theta_0)}. \quad (4.9)$$

¹After removing blind directions, i. e. eigenvectors of the Fisher information with eigenvalue zero, the Fisher information is positive definite and therefore invertible.

We sketch the proof for the Cramér-Rao bound in Appendix A.6.1.

An unbiased estimator is called ‘efficient’ if it reaches the lower bound given by Equation (4.8) for any value of θ_0 ; that is, if its covariance matrix is equal to the inverse Fisher information. This is what we define as an optimal measurement. The Fisher information matrix I_{ij} hence encodes the maximal precision with which parameters can be measured at an experiment. Large entries in this matrix correspond to directions that can be measured particularly precisely. On the other hand, an eigenvector of the information matrix with corresponding eigenvalue zero is a blind direction that can never be probed by the experiment.

There is a subtlety to this statement. For some problems no efficient estimators exist. The textbook example is the estimation of the variance parameter of the normal distribution: here the sample variance is an unbiased estimator with minimum variance, but it does not reach the lower bound given by Equation (4.8). Even if an efficient estimator exists, just from the Fisher information we do not know how to construct its form $\hat{\theta}(\mathbf{x})$. However, it can be shown that under certain regularity assumptions², the **maximum-likelihood estimator** defined by

$$\hat{\theta}_{\text{MLE}}(\mathbf{x}) = \arg \max_{\theta} f(\mathbf{x}|\theta) \quad (4.10)$$

is asymptotically unbiased and efficient, i. e. in the limit of large sample size it leads to the minimum covariance matrix defined by the inverse Fisher information [281]. Such an estimator always exists for the problems discussed in the following, hence the upper bound on the precision defined by the Fisher information is achievable at least in the asymptotic limit. We therefore expect that the best achievable precision in a measurement can only be significantly worse than given by the Fisher information for problems with small event numbers.

The Fisher information has several useful properties. Unlike many other statistical tools, it summarises the sensitivity to **all** directions in theory space in one matrix, making it particularly useful for high-dimensional parameter spaces. It is additive between different measurements or between different phase-space regions in the same experiment. Furthermore, a description of experiments in terms of the Fisher information does not depend on arbitrary basis choices: it is independent of the parametrisation of the observables \mathbf{x} , and transforms covariantly under a reparametrisation of the theory parameters $\theta \rightarrow \Theta(\theta)$,

$$I_{ab}(\Theta) = \frac{\partial \theta_i}{\partial \Theta_a} I_{ij}(\theta) \frac{\partial \theta_j}{\partial \Theta_b}. \quad (4.11)$$

²One condition for this statement is the identifiability of the model: two different model parameters $\theta_a \neq \theta_b$ must always correspond to two distinct probability distribution $f(\mathbf{x}|\theta_a) \neq f(\mathbf{x}|\theta_b)$. This means that blind directions and physically identical parameter choices have to be removed before the maximum-likelihood estimator is guaranteed to saturate the Cramér-Rao bound. This can for instance become important when new physics effects can flip the sign of couplings, leading to the same predictions for cross sections as the SM. But these considerations are irrelevant for the analysis of small deformations from the SM with effective operators in this thesis.

In Appendix A.6.2 we explicitly show how the Fisher information can be calculated in a simple example, and how the results can be interpreted.

4.2.2 Information geometry

As a symmetric and positive definite rank-two tensor, the Fisher information defines a Riemannian metric³ on the manifold given by the theory space. This is the underpinning of information geometry [66–68]. In this field, methods from differential geometry are used to analyse the structure of the probability distributions, or the relation between experiment and models. Interpreted as a metric, the Fisher information defines infinitesimal distances

$$ds^2 = I_{ij}(\theta) d\theta_i d\theta_j. \quad (4.12)$$

Different from the conventions in differential geometry, we use lower indices for vectors and sum over repeated lower indices.

First, the metric defines a **local distance** in the tangent space at some point θ_a . We usually consider the distance between θ_a itself and some other point θ_b in this tangent space,

$$d_{\text{local}}(\theta_b; \theta_a) \equiv \sqrt{I_{ij}(\theta_a)(\theta_b - \theta_a)_i(\theta_b - \theta_a)_j}. \quad (4.13)$$

Contours of local distances $d_{\text{local}}(\theta_b; \theta_a) = d$ are directly related to the optimal error contours of a measurement according to the Cramér-Rao bound. Since these distances are based on the Fisher information at θ_a , they describe how unlikely it is to measure $\hat{\theta} = \theta_b$ if $\theta_0 = \theta_a$ is the true value. More precisely, if an unbiased estimator $\hat{\theta}$ with minimal variance (i. e. an optimal measurement) is distributed according to a Gaussian, $d_{\text{local}}(\theta_b; \theta_a)$ expresses how unlikely it is to measure $\hat{\theta} = \theta_b$ if the true value is $\theta_0 = \theta_a$, expressed in standard deviations or ‘sigmas’. In other words, in this Gaussian approximation the distance measure is equivalent to the maximal expected significance with which θ_a can be excluded if θ_b is true.

Going beyond the tangent space, **global distances** between two points on the model manifold can be defined along geodesics,

$$d(\theta_a, \theta_b) = \min_{\theta(s)} \int_{s_a}^{s_b} ds \sqrt{I_{ij}(\theta(s)) \frac{d\theta_i(s)}{ds} \frac{d\theta_j(s)}{ds}} \quad (4.14)$$

with $\theta(s_a) = \theta_a$ and $\theta(s_b) = \theta_b$. The shortest path $\theta(s)$ satisfies the geodesic equation

$$\frac{d^2\theta^i}{ds^2} = -\Gamma_{jk}^i \frac{d\theta^j}{ds} \frac{d\theta^k}{ds} \quad (4.15)$$

³This is only true after removing blind directions. Otherwise, the information matrix is positive semidefinite and defines a pseudometric.

where we, for once, distinguish upper and lower indices; indices are raised and lowered with the metric I_{ij} . Dots denote derivatives $\dot{\theta} \equiv d\theta(s)/ds$ and the Christoffel symbols are defined as

$$\Gamma_{ijk} \equiv \frac{1}{2} \left[\frac{\partial I_{ij}}{\partial \theta^k} + \frac{\partial I_{ik}}{\partial \theta^j} - \frac{\partial I_{jk}}{\partial \theta^i} \right]. \quad (4.16)$$

This distance measure is symmetric, $d(\boldsymbol{\theta}_a, \boldsymbol{\theta}_b) = d(\boldsymbol{\theta}_b, \boldsymbol{\theta}_a)$, and provides a more general notion of discrimination power between two parameter points that does not require choosing one of them to evaluate the Fisher information. Unlike local distances, global distances are sensitive to how the Fisher information changes over model space, i. e. they take into account the curvature of the geometry. From a practical perspective, this makes global distances a useful tool to track the effect of higher powers in the theory parameters, as we show in Section 4.3.6.

4.3 Tools for the LHC

The key method with which we analyse LHC channels is the calculation of the Fisher information with Monte-Carlo methods. We compare three different types of measurements: total cross sections, individual distributions of kinematic observables, and the full high-dimensional kinematics of a process. After deriving the information content in these measurements, we introduce the differential Fisher information and the information matrix profiled over nuisance parameters, sketch the structure of our algorithms, and discuss the application to effective field theories.

4.3.1 Information in total rates

The simplest LHC measurement is an event count in some fiducial region described by Poisson statistics. As explicitly calculated in Appendix A.6.2, the Fisher information for the measurement of theory parameters $\boldsymbol{\theta}$ in such an experiment reads

$$I_{ij}^{\text{xsec}}(\boldsymbol{\theta}) = L \frac{\partial \sigma(\boldsymbol{\theta})}{\partial \theta_i} \frac{1}{\sigma(\boldsymbol{\theta})} \frac{\partial \sigma(\boldsymbol{\theta})}{\partial \theta_j}. \quad (4.17)$$

Here L is the integrated luminosity and $\sigma(\boldsymbol{\theta})$ the total cross section as a function of the theory parameters.

4.3.2 Information in distributions

The most straightforward way to add kinematic features is to measure a differential cross section or histogram of a kinematic observable v , for instance a transverse momentum, energy, invariant mass, or angle. Leaving aside systematic uncertainties, such a histogram is just a set of statistically

independent counting experiments, each with a different Poisson mean that depends on the theory parameters in some way. The Fisher information is hence given by

$$I_{ij}^{\text{distribution}}(\boldsymbol{\theta}) = L \sum_{\text{bins } b} \frac{\partial \sigma_b(\boldsymbol{\theta})}{\partial \theta_i} \frac{1}{\sigma_b(\boldsymbol{\theta})} \frac{\partial \sigma_b(\boldsymbol{\theta})}{\partial \theta_j}. \quad (4.18)$$

Each bin b corresponds to a set of cuts $v_{\min} \leq v < v_{\max}$. In the limit of many small bins that span the entire kinematically allowed range for v , we call Equation (4.18) the information in the distribution of v .

This can be trivially extended from a one-dimensional histogram of a single observable v to a multi-dimensional histogram of many observables \mathbf{v} . Equation (4.18) still applies, with the bins now spanning a multi-dimensional space of observables.

Instead of correlating two observables in a two-dimensional histogram, we can also combine the information in two one-dimensional histograms. Assuming that the distributions of the two observables are independent except for the total rate, we can simply calculate the combined information as

$$I_{ij}^{\text{combined}}(\boldsymbol{\theta}) = I_{ij}^{\text{distribution 1}}(\boldsymbol{\theta}) + I_{ij}^{\text{distribution 2}}(\boldsymbol{\theta}) - I_{ij}^{\text{xsec}}(\boldsymbol{\theta}). \quad (4.19)$$

This can be trivially extended to more than two histograms. For correlated observables, for instance the transverse momenta of two different particles that recoil against each other, such a straightforward combination is not possible. In reality, most pairs of observables have some degree of correlation, and this naive combination procedure is of limited use.

Comparing the information in different distributions to each other defines which kinematic observables provide probes of which directions in theory space. In practice, this can be used as a guideline for which distributions to measure and publish.

4.3.3 Information in full kinematics

To describe the full high-dimensional kinematics of LHC processes including all correlations and without relying on a choice of observables or binning, we use an **extended likelihood** ansatz, also known as marked Poisson process. The observables in LHC physics consist of a total number of events n , each of which has some high-dimensional kinematic properties \mathbf{x}_i . The probability distribution is given by

$$f(\mathbf{x}|\boldsymbol{\theta}) = \text{Pois}(n|L\sigma(\boldsymbol{\theta})) \prod_{i=1}^n f^{(1)}(\mathbf{x}_i|\boldsymbol{\theta}), \quad (4.20)$$

where $f^{(1)}(\mathbf{x}_i|\boldsymbol{\theta})$ is the probability distribution function for a single event.

Calculating the Fisher information for this ansatz, we find

$$I_{ij}^{\text{full}}(\boldsymbol{\theta}) = L \frac{\partial \sigma(\boldsymbol{\theta})}{\partial \theta_i} \frac{1}{\sigma(\boldsymbol{\theta})} \frac{\partial \sigma(\boldsymbol{\theta})}{\partial \theta_j} + L \sigma(\boldsymbol{\theta}) E \left[\frac{\partial \log f^{(1)}(\mathbf{x}|\boldsymbol{\theta})}{\partial \theta_i} \frac{\partial \log f^{(1)}(\mathbf{x}|\boldsymbol{\theta})}{\partial \theta_j} \middle| \boldsymbol{\theta} \right], \quad (4.21)$$

adding a distribution term to the Poisson part. Typically, the single-event likelihood functions $f^{(1)}(x|\boldsymbol{\theta})$ are complex expressions given by a sum of intricate amplitudes. Instead of calculating their derivatives analytically, we rely on a Monte-Carlo approach, approximating the phase-space integral with a sum over events:⁴

$$\int dx f^{(1)}(x) \rightarrow \sum_{\text{events } k} \frac{\Delta\sigma_k}{\sigma}. \quad (4.22)$$

This turns the Fisher information into the familiar form of a sum of Poisson terms for the individual events,

$$I_{ij}^{\text{full}}(\boldsymbol{\theta}) = L \sum_{\text{events } k} \frac{\partial\Delta\sigma_k(\boldsymbol{\theta})}{\partial\theta_i} \frac{1}{\Delta\sigma_k(\boldsymbol{\theta})} \frac{\partial\Delta\sigma_k(\boldsymbol{\theta})}{\partial\theta_j}. \quad (4.23)$$

Calculating the Fisher information thus only requires the event weights and their derivatives with respect to the theory parameters as input, and can be implemented with standard Monte-Carlo tools as we explain in Section 4.3.7.

The total Fisher information in Equation (4.23) defines the maximum precision with which theory parameters can be constrained — independent of the analysis strategy. By comparing this matrix to the Fisher information in kinematic distributions as defined in 4.3.2, we can calculate how much discrimination power is lost in a traditional histogram-based analysis compared to a hypothetical ideal multivariate analysis.

4.3.4 Distribution of differential information

From Equation (4.23) it is obvious that the Fisher information is additive between different phase-space regions. By restricting the sum to those events passing a certain selection requirement, we can calculate the Fisher information after different cuts. In particular, we can calculate the Fisher information contained in different bins of a kinematic observable v . In the limit of many small bins this defines the differential Fisher information dI_{ij}^{full}/dv . Here I_{ij}^{full} uses the full, high-dimensional kinematics of the event, but we are able to study how it is distributed with respect to v . Integrating this differential information over v , or summing over the bins, restores the total Fisher information defined in Equation (4.23).

The distribution of the differential information defines the important phase-space region for measurements and should drive the design of event selections: it allows us to calculate the information loss from kinematic cuts, and to quantify the trade-off between signal purity and maximal information.

⁴In its simplest form, this step implicitly assumes that we can experimentally distinguish between all phase-space points. Resolution effects and undetected particles can be taken into account with suitable transfer functions [282–284] or with a simple smearing as discussed in Section 4.3.7.

Note the difference between the information in a kinematic distribution discussed in Section 4.3.2, and the distribution of the full information over phase space discussed here. The former answers the question of how well we can constrain theory parameters by measuring the distribution of one kinematic variable instead of the full kinematics. The latter describes how well we can constrain theory parameters using the full, high-dimensional kinematics of the event, but only taking into account the events in a certain slice of the phase space.

4.3.5 Nuisance parameters and profiled information matrix

So far our approach was based on the assumption that event numbers are described by Poisson statistics, where the mean as a function of the theory parameters is known exactly. We now extend it to include systematic and theory uncertainties. The parameter space then consists of nuisance parameters ν_i in addition to the theory parameters θ_i . For concreteness, we assume that $\nu = \mathbf{0}$ corresponds to the best estimate of the nuisance parameters. The knowledge on the nuisance parameters is encoded in constraint terms added to the likelihood, which subsequently appear in the Fisher information. If, for instance, the k th parameter is a nuisance parameter with a Gaussian constraint term with width σ_k , the additional term in the Fisher information reads

$$I_{ij}(\boldsymbol{\theta}, \nu) = \dots + \frac{\delta_{ik}\delta_{jk}}{\sigma_k^2} \quad (4.24)$$

without sum over k . Local and global information distances now refer to the combined space of theory and nuisance parameters $(\boldsymbol{\theta}, \nu)$.

In practice we are interested in the sensitivity of an experiment on some parameters of interest, for instance the theory parameters, without explicit dependence on the nuisance parameters. In a Bayesian approach, one can assign a prior probability distribution to the nuisance parameters and integrate ('marginalise') over them. Instead, we follow a conservative method that is consistent with a frequentist definition of statistics and does not require the choice of a prior. Loosely speaking, we calculate the minimum sensitivity to theory parameters for any value of the nuisance parameters within their constraints (i. e. for nuisance parameters that are 'allowed to float'). This concept of 'profiling' over nuisance parameters is well established for instance for hypothesis tests based on the likelihood ratio [285].

Applying this idea to the geometric picture, we define a profiled local distance between two points $\boldsymbol{\theta}_a$ and $\boldsymbol{\theta}_b$ as

$$d_{\text{profiled}}(\boldsymbol{\theta}_b, \boldsymbol{\theta}_a) = \min_{\nu} d_{\text{local}}((\boldsymbol{\theta}_b, \nu); (\boldsymbol{\theta}_a, \mathbf{0})). \quad (4.25)$$

The contours of the local distance $(\boldsymbol{\theta}_a, \mathbf{0})$ define an ellipsoid around this point. The contours of the profiled distance are just the parallel projection of this ellipsoid onto the subspace spanned by the theory parameters (but not the nuisance parameters).

Since the parallel projection of an ellipsoid is again a (less-dimensional) ellipsoid, the profiled distances can be described by a metric in the physical subspace. Instead of minimising the distance itself, we can therefore absorb the minimisation procedure into the metric and define a **profiled Fisher information** matrix. For simplicity, we assume the last of n parameters to be the only nuisance parameter. The Fisher information including this nuisance parameter then has the form

$$I_{ij} = \begin{pmatrix} I^{\text{theory}} & \mathbf{m} \\ \mathbf{m}^T & s \end{pmatrix}, \quad (4.26)$$

where I^{theory} is the information matrix restricted to the $n - 1$ theory parameters, the vector \mathbf{m} describes the effect of the nuisance parameters on the sensitivity to the theory parameters, and s reflects the constraints on the nuisance parameter.

To calculate the profiled Fisher information, we start from the ellipsoid

$$\boldsymbol{\theta}_i I_{ij} \boldsymbol{\theta}_j = d. \quad (4.27)$$

The projection is described by a set of tangents

$$\boldsymbol{\theta} = \begin{pmatrix} \boldsymbol{\theta}^{\text{theory}} \\ t \end{pmatrix}, \quad (4.28)$$

where $\boldsymbol{\theta}^{\text{theory}}$ defines the coordinates in the parameters of interest and t parametrises the tangent along the nuisance direction. The tangents on the ellipsoid have to satisfy Equation (4.27) with exactly one solution for t (if there are two solutions, they intersect the ellipsoid; if there is none, they never touch it). This is the case if the discriminant describing this quadratic equation is zero. After a brief calculation, this can be brought to the form

$$\boldsymbol{\theta}_a^{\text{theory}} \left(I_{ab}^{\text{theory}} - \frac{m_a m_b}{s} \right) \boldsymbol{\theta}_b^{\text{theory}} = d. \quad (4.29)$$

The Fisher information in Equation (4.26) profiled over the nuisance parameter is therefore given by the $(n - 1) \times (n - 1)$ matrix

$$I_{ab}^{\text{profiled}} = I_{ab}^{\text{theory}} - \frac{m_a m_b}{s}. \quad (4.30)$$

This can be easily generalised to multiple nuisance parameters. For a Fisher information matrix of the block form

$$I_{ij} = \begin{pmatrix} I^{\text{theory}} & (I^{\text{mix}})^T \\ I^{\text{mix}} & I^{\text{nuisance}} \end{pmatrix}, \quad (4.31)$$

the profiled Fisher information matrix reads [280]

$$I^{\text{profiled}} = I^{\text{theory}} - (I^{\text{mix}})^T (I^{\text{nuisance}})^{-1} I^{\text{mix}}. \quad (4.32)$$

In addition to the geometric explanation given above, this result can be understood from the Cramér-Rao bound: the upper left block of the inverse of Equation (4.31) is equal to the inverse of Equation (4.32).

The most obvious applications for this tool are systematic and theory uncertainties; we demonstrate this in Section 4.5.1. The profiled Fisher information can also be used to quantify the sensitivity on one parameter when other theory parameters are of no interest. It allows us for instance to quantify how well genuine CP -violating effects [286, 287] can be measured by profiling over all relevant sources of CP -even new physics.

4.3.6 Geometry of effective field theories

We calculate the Fisher information in terms of the dimension-six operators of linear Higgs effective field theory. As theory parameters we pick a dimensionless rescaling of the Wilson coefficients,

$$\theta_i = \frac{f_i}{\Lambda^2} v^2, \quad (4.33)$$

such that the SM corresponds to the origin $\boldsymbol{\theta} = \mathbf{0}$.

Through the Cramér-Rao bound in Equation (4.9), the Fisher information in a given direction in theory space I defines a maximal precision $\Delta\theta_{\min} = 1/\sqrt{I}$ with which this direction can be measured. For an EFT this can directly be translated into a **new physics reach**

$$\frac{\Lambda}{\sqrt{f}} = \frac{v}{\sqrt{\Delta\theta_{\min}}} = v I^{1/4}. \quad (4.34)$$

The maximal probed energy scale Λ depends on the size of the Wilson coefficients f and thus on the typical couplings of the underlying theory, in agreement with the discussion in Section 3.1.

Local and global geometry have an interesting and useful interpretation when applied to EFTs. Recall that squared amplitudes from dimension-six operators contribute to the cross section at the same order as the leading effects from the neglected dimension-eight operators. In Section 3.4.2 we argued that under the assumptions that the new physics couplings are of the same size as the relevant SM couplings and that the dimension-four amplitudes are not accidentally suppressed, the size of the dimension-six squared term can be used as an estimate for the error of the EFT approximation. In general, the dimension-six squared terms can be larger than the dimension-eight effects, and they are necessary from a technical point of view to guarantee positive cross sections.

As can be seen from Equation (4.23), the Fisher information at the SM $I_{ij}(\mathbf{0})$ only measures the $\mathcal{O}(\boldsymbol{\theta})$ terms in the differential cross sections and is insensitive to higher orders. In other words, information distances in the tangent space at the SM only take into account the leading dimension-six operator effects at $\mathcal{O}(1/\Lambda^2)$. On the other hand, the dimension-six squared contributions do appear in the Fisher information away from the SM and therefore in global distances as given in Equation (4.14). The difference between linearised distances based on the SM Fisher information metric and global distances measured along geodesics, related to the curvature of the theory manifold, therefore provides an intuitive measure of the role of $\mathcal{O}(1/\Lambda^4)$ contributions.

Different bases for effective operators are physically equivalent, and the directions in theory space defined by the basis operators \mathcal{O}_i do not have a special meaning. Any statistical tool that singles out individual directions or parameter points in the model space can introduce a bias towards a specific operator base. In the worst case, it can be blind to effects on diagonal directions, e. g. along $\mathcal{O}_i + \mathcal{O}_j$. Our approach, based on a geometric description of the model space, does not suffer from these problems.

In particular, the Fisher information transforms covariantly under basis transformations, see Equation (4.11). Eigenvalues, traces, and determinants of the Fisher information are invariant under basis rotations $\mathcal{O}_i \rightarrow R_{ij}\mathcal{O}_j$ with $R \in O(n)$. Rescalings $\mathcal{O}_i \rightarrow \alpha\mathcal{O}_i$ change the eigenvalues of individual information matrices. However, in our analysis we will usually compare the information in different approaches relative to each other, with ratios such as $\det I_1 / \det I_2$ remaining invariant even then.

4.3.7 The MadFisher algorithm

The Fisher information matrices discussed above are calculated with a combination of existing Monte-Carlo generators and our own algorithm, which we name MadFisher. Our setup consists of three steps:

1. Monte-Carlo tools are used to generate event samples, i. e. sets of phase-space points \mathbf{x} with the corresponding differential rates $\Delta\sigma(\mathbf{x}|\boldsymbol{\theta}_n)$, for a set of basis parameter points $\boldsymbol{\theta}_n$.
2. With a morphing technique [288] we calculate the differential rates $\Delta\sigma(\boldsymbol{\theta})$ for arbitrary parameter points $\boldsymbol{\theta}$.
3. We calculate the Fisher information matrices as derived in the previous sections.

First, for the event generation we use MadMax [289, 290]. This add-on to MadGraph 5 [218] allows us to simultaneously calculate the differential rates $\Delta\sigma(\mathbf{x}|\boldsymbol{\theta}_n)$ for different parameter points $\boldsymbol{\theta}_n$ using the same phase-space grid.⁵

⁵An alternative tool for this step, which supports a variety of transfer functions to describe the detector response, is MadWeight [282–284].

We simulate the effective dimension-six model with our own FeynRules [219] model file, which does not truncate operator effects at $\mathcal{O}(1/\Lambda^2)$. MadMax requires fixed renormalisation and factorisation scales, which we set following Reference [3]. To keep the calculation times manageable, we restrict some processes to the dominant sub-processes, for instance to initial-state u and d quarks in the WBF case. We then normalise the Higgs rates to the recommendations of the LHC Higgs Cross Section Working Group for the total cross sections [3], calculating the effect of the different acceptance regions with MadGraph 5. Background processes are simply rescaled to MadGraph predictions.

For this first proof of concept, we restrict our simulation to the parton level. The phenomenologically most drastic effect of the detector response is the smearing of narrow resonance peaks in invariant mass distributions. This is taken into account with the procedure outlined in References [289, 291]: we replace the propagator of the corresponding s -channel particle with the square root of a smearing function, for instance a Gaussian or double Gaussian with parameters fitted to ATLAS and CMS results. Other detector effects are not included in the first studies presented here. However, a more realistic description of the experimental resolution can easily be achieved by including a complete set of transfer functions, similar to the usual approach for the matrix element method [282–284].

The second step is based on the fact that the differential cross section can be decomposed into a finite set of components, representing the different squared amplitudes and interference terms:

$$\begin{aligned} \Delta\sigma(\mathbf{x}|\boldsymbol{\theta}) &\propto \sum_p \left| \sum_i \tilde{w}_{p,i}(\boldsymbol{\theta}) \mathcal{M}_{p,i} \right|^2 \\ &= \sum_p \sum_{i,j} \tilde{w}_{p,i}^*(\boldsymbol{\theta}) \tilde{w}_{p,j}(\boldsymbol{\theta}) (\mathcal{M}_{p,i}^\dagger \mathcal{M}_{p,j})(\mathbf{x}) \\ &\propto \sum_c w_c(\boldsymbol{\theta}) \Delta\sigma_c(\mathbf{x}). \end{aligned} \quad (4.35)$$

Here p labels different sub-processes (which do not interfere with each other), while i, j denote the different amplitudes contributing to a sub-process. In the last step we collect the various terms into components c .

If the model parameters $\boldsymbol{\theta}$ contribute additively and multiplicatively to vertices, as is often the case for effective field theories as discussed in Section 2.3.3, the functions w_c are polynomials in the different θ_i . As a simple example, consider a process with just one vertex, with known coupling g in the SM and new physics amplitude proportional to the parameter θ . The differential

cross section is then proportional to

$$\begin{aligned}
 \Delta\sigma(\mathbf{x}|\theta) &\propto |g\mathcal{M}_{\text{SM}} + \theta\mathcal{M}_{\text{NP}}|^2 \\
 &= g^2 |\mathcal{M}_{\text{SM}}|^2 + 2g\theta \operatorname{Re}\mathcal{M}_{\text{SM}}^\dagger\mathcal{M}_{\text{NP}} + \theta^2 |\mathcal{M}_{\text{NP}}|^2 \\
 &\propto \underbrace{g^2}_{w_1(\theta)} \underbrace{\Delta\sigma_{\text{SM}}(\mathbf{x})}_{\Delta\sigma_1(\mathbf{x})} + \underbrace{2g\theta}_{w_2(\theta)} \underbrace{\Delta\sigma_{\text{interference}}(\mathbf{x})}_{\Delta\sigma_2(\mathbf{x})} + \underbrace{\theta^2}_{w_3(\theta)} \underbrace{\Delta\sigma_{\text{NP}}(\mathbf{x})}_{\Delta\sigma_3(\mathbf{x})}.
 \end{aligned} \tag{4.36}$$

In the EFT language, the different contributions correspond to different powers of the suppression factor $1/\Lambda$. For more contributing couplings, or if more than one vertex is affected by these couplings, the number of components increases as shown in Table 4.1. One noteworthy exception to the polynomial form of w_c is the dimension-six operator $\mathcal{O}_{\phi,2}$. As discussed in Section 2.3.3, it rescales all Higgs interactions non-linearly with $1/\sqrt{1+f_{\phi,2}v^2/\Lambda^2}$ and does not respect the counting in terms of $1/\Lambda$ given in Table 4.1. In any case, the weights $w_c(\theta)$ are known analytical functions of the model parameters.

In Equation (4.35) the contributions from the different components $\Delta\sigma_c(\mathbf{x})$ are still unknown. To calculate them, note that for a set of basis parameter points θ_n one can read Equation (4.35) as a matrix multiplication:

$$\Delta\sigma_n(\mathbf{x}) = W_{nc} \Delta\sigma_c(\mathbf{x}) \tag{4.37}$$

with $\Delta\sigma_n(\mathbf{x}) \equiv \Delta\sigma(\mathbf{x}|\theta_n)$ and the matrix

$$W_{nc} \equiv w_c(\theta_n). \tag{4.38}$$

For a suitable choice of basis parameters, we can invert this equation to

$$\Delta\sigma_c(\mathbf{x}) = W_{cn}^{-1} \Delta\sigma_n(\mathbf{x}). \tag{4.39}$$

Vertices	Components	Components at EFT orders				
		$\mathcal{O}(\Lambda^0)$	$\mathcal{O}(1/\Lambda^2)$	$\mathcal{O}(1/\Lambda^4)$	$\mathcal{O}(1/\Lambda^6)$	$\mathcal{O}(1/\Lambda^8)$
1	$\frac{(n+1)(n+2)}{2}$	1	n	$\frac{n(n+1)}{2}$		
2	$\binom{n+4}{4}$	1	n	$\frac{n(n+1)}{2}$	$\binom{n+2}{3}$	$\binom{n+3}{4}$

Table 4.1: Number of components contributing to different processes, depending on the number of model parameters n and on the number of modified vertices. Two affected vertices correspond, for instance, to a Higgs process where all n model parameters affect both Higgs production and decay. We also give the number of components for each order in $1/\Lambda$ in the EFT case.

Plugging this into Equation (4.35), we have

$$\Delta\sigma(\mathbf{x}|\boldsymbol{\theta}) = \sum_{c,n} w_c(\boldsymbol{\theta}) W_{cn}^{-1} \Delta\sigma_n(\mathbf{x}). \quad (4.40)$$

So with the pre-calculated matrix W that depends on the basis parameter points, the analytically known weight functions $w_c(\boldsymbol{\theta})$, and the event samples for the basis parameters $\Delta\sigma_n(\mathbf{x})$, we can exactly calculate the differential rates $\Delta\sigma(\mathbf{x}|\boldsymbol{\theta})$ for arbitrary values of $\boldsymbol{\theta}$, without having to rerun the Monte-Carlo simulation.

Derivatives with respect to the theory parameters can easily be calculated numerically,

$$\frac{\partial \Delta\sigma(\boldsymbol{\theta})}{\partial \theta_i} \approx \frac{\Delta\sigma(\boldsymbol{\theta} + \boldsymbol{\varepsilon}_i) - \Delta\sigma(\boldsymbol{\theta} - \boldsymbol{\varepsilon}_i)}{2|\boldsymbol{\varepsilon}_i|} \quad (4.41)$$

with a small vector $\boldsymbol{\varepsilon}_i$ in i -direction.

With Equations (4.40) and (4.41) it is straightforward to calculate the Fisher information matrices. For the total Fisher information, we calculate the information in each event with Equation (4.23) and then sum the results. For the information in total rates and in individual distributions, we first sum the weights to get the total cross sections, and calculate the Fisher information with Equations (4.17) and (4.18).

Finally, we calculate local and global distances in theory space as given in Equations (4.13) and (4.14). The latter are calculated in analogy to free fall in general relativity: a starting point and a set of directions in parameter space define the initial conditions, from which we numerically calculate distances along curves defined by the geodesic equation.

To summarise, based on a single run of a Monte-Carlo simulation with MadMax, our MadFisher algorithm can calculate the Fisher information matrices $I_{ij}(\boldsymbol{\theta})$ for arbitrary values of the theory parameters $\boldsymbol{\theta}$. One can choose to determine the information in the total rate, in individual kinematic distributions, or in the full process kinematics of arbitrary dimensionality. It can be calculated based on the full phase space, after selection cuts, or differentially in kinematic variables.

4.4 Higgs measurements

We now apply these tools to calculate the information on dimension-six operators in Higgs measurements. Three processes are considered: Higgs production in weak boson fusion with a decay into tau pairs or four leptons, and Higgs production with a single top.

For this first demonstration we neglect both systematic and theory uncertainties; we later show how these can be added in Section 4.5.1. The maximum precision on Wilson coefficients calculated in this section is therefore optimistic. Our main focus here is the relative comparison

of the information in different phase-space regions or in different distributions. These are not affected by systematic uncertainties that dominantly concern the overall rate.

4.4.1 Weak-boson-fusion Higgs to taus

The first question we tackle with our information geometry approach is what can be learned about higher-dimensional operators from the non-trivial kinematics of weak-boson-fusion production. As a decay we include a simple fermionic two-body decay $h \rightarrow \tau\tau$ [79, 292], see Figure 4.1. For our proof of concept we stick to a parton-level analysis at leading order. The dominant irreducible backgrounds are QCD Zjj production and electroweak Zjj production, both with the decay $Z \rightarrow \tau\tau$, and Higgs production in gluon fusion with $h \rightarrow \tau\tau$.

We do not simulate tau decays, but multiply the rates with the branching ratios for the semi-leptonic di-tau mode $\tau\tau \rightarrow (\ell\nu\nu)(j\nu\nu)$, and assume that the di-tau system can be reconstructed with a reasonable resolution for $m_{\tau\tau}$, for instance with the collinear approximation [71, 79, 292]. We take the experimental mass resolution into account by smearing the $m_{\tau\tau}$ distributions. The smearing functions and their parameters are estimated from Figure 1a of Reference [293] and are described in Section A.6.3. Otherwise, no detector effects are included. We require only loose acceptance cuts

$$\begin{aligned} p_{T,j} > 20 \text{ GeV}, & \quad |\eta_j| < 5.0, & \quad \Delta\eta_{jj} > 2.0, \\ p_{T,\tau} > 10 \text{ GeV}, & \quad |\eta_\tau| < 2.5, & \end{aligned} \quad (4.42)$$

to include as much of the phase space as possible.

The different QCD radiation patterns of the Higgs signal and the electroweak and QCD background processes are a key feature to separate the signal from the background [75–81]. We take this into account through approximate central jet veto (CJV) survival probabilities taken

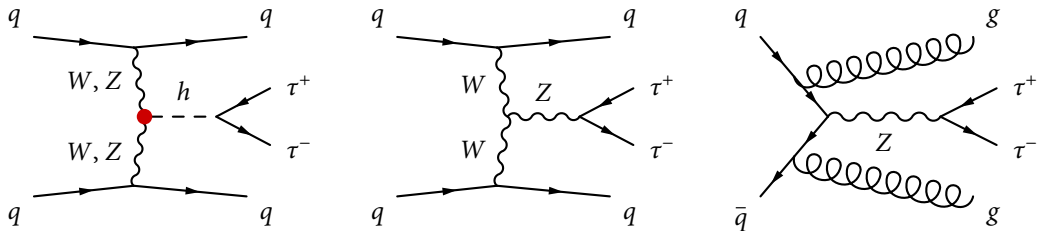


Figure 4.1: Left: Feynman diagram for WBF Higgs production in the $\tau\tau$ mode. The red dot shows the Higgs-gauge interactions affected by the dimension-six operators of our analysis; in addition $\mathcal{O}_{\phi,2}$ also rescales the decay vertex. Middle and right: example diagrams for the electroweak and QCD Zjj backgrounds.

from Reference [79],

$$\varepsilon_{\text{WBF } H}^{\text{CJV}} = 0.71, \quad \varepsilon_{\text{EW } Z}^{\text{CJV}} = 0.48, \quad \varepsilon_{\text{QCD } Z}^{\text{CJV}} = 0.14, \quad \varepsilon_{\text{ggF } H}^{\text{CJV}} = 0.14, \quad (4.43)$$

neglecting the dependence of the veto efficiency on the phase space. All other particle identification and trigger efficiencies are absorbed into a single universal efficiency factor ε . We calculate the Fisher information for pp collisions at $\sqrt{s} = 13$ TeV for an integrated luminosity times universal efficiencies of

$$L \cdot \varepsilon = 30 \text{ fb}^{-1}. \quad (4.44)$$

After the event selection given in Equation (4.42) and the CJV efficiencies, the WBF Higgs signal of 53 fb in the SM faces a dominant QCD Z background of 2.7 pb, corresponding to 1600 vs. 81 000 expected events.

Following the construction of the effective operators in Section 2.3.2, five CP -even dimension-six operators in the HISZ basis affect Higgs production in weak boson fusion. \mathcal{O}_B , \mathcal{O}_W , \mathcal{O}_{BB} , and \mathcal{O}_{WW} introduce new Lorentz structures into Higgs-gauge interactions as given in Equation (2.57). In addition, $\mathcal{O}_{\phi,2}$ leads to a universal rescaling of all Higgs couplings. The relevant model space is therefore spanned by five dimensionless parameters

$$\boldsymbol{\theta} = \frac{v^2}{\Lambda^2} \begin{pmatrix} f_{\phi,2} \\ f_W \\ f_{WW} \\ f_B \\ f_{BB} \end{pmatrix}. \quad (4.45)$$

In our analysis we neglect the effects from \mathcal{O}_W and \mathcal{O}_B on the subleading electroweak Zjj background, but take into account how $\mathcal{O}_{\phi,2}$ rescales the gluon-fusion Higgs contribution.

Our analysis focuses on the Fisher information around the SM point $\boldsymbol{\theta} = \mathbf{0}$ as well as on the two-dimensional planes in parameter space where all but two operators are zero. All in all, we calculate Fisher information matrices at approximately 6000 parameter points.

Total Fisher information

With the combination of MadGraph 5 [218], MadMax [289, 290], and our own MadFisher algorithm described in Section 4.3.7, we first calculate the total Fisher information. At the SM point we find

$$I_{ij}(\mathbf{0}) = \begin{pmatrix} 3202.1 & -625.3 & -7.2 & -34.8 & 0.3 \\ -625.3 & 451.0 & -109.5 & 23.3 & -1.5 \\ -7.2 & -109.5 & 243.7 & -5.5 & 2.8 \\ -34.8 & 23.3 & -5.5 & 4.1 & -0.3 \\ 0.3 & -1.5 & 2.8 & -0.3 & 0.1 \end{pmatrix}. \quad (4.46)$$

The eigenvectors and eigenvalues of this matrix are

$$\begin{aligned}
 \boldsymbol{\theta}_1 = \begin{pmatrix} 0.98 \\ -0.21 \\ 0.01 \\ -0.01 \\ 0.00 \end{pmatrix} : \quad I_1 = 3338 \quad \leftrightarrow \quad \left(\frac{\Lambda}{\sqrt{f}} \right)_1 = 1870 \text{ GeV}, \\
 \boldsymbol{\theta}_2 = \begin{pmatrix} -0.18 \\ -0.79 \\ 0.58 \\ -0.04 \\ 0.01 \end{pmatrix} : \quad I_2 = 395 \quad \leftrightarrow \quad \left(\frac{\Lambda}{\sqrt{f}} \right)_2 = 1097 \text{ GeV}, \\
 \boldsymbol{\theta}_3 = \begin{pmatrix} 0.12 \\ 0.57 \\ 0.81 \\ 0.03 \\ 0.01 \end{pmatrix} : \quad I_3 = 165 \quad \leftrightarrow \quad \left(\frac{\Lambda}{\sqrt{f}} \right)_3 = 881 \text{ GeV}, \\
 \boldsymbol{\theta}_4 = \begin{pmatrix} 0.00 \\ -0.05 \\ 0.00 \\ 1.00 \\ -0.07 \end{pmatrix} : \quad I_4 = 2.9 \quad \leftrightarrow \quad \left(\frac{\Lambda}{\sqrt{f}} \right)_4 = 321 \text{ GeV}, \\
 \boldsymbol{\theta}_5 = \begin{pmatrix} 0.00 \\ 0.00 \\ -0.01 \\ 0.07 \\ 1.00 \end{pmatrix} : \quad I_5 = 0.1 \quad \leftrightarrow \quad \left(\frac{\Lambda}{\sqrt{f}} \right)_5 = 138 \text{ GeV}. \tag{4.47}
 \end{aligned}$$

Here Λ/\sqrt{f} is the maximal new physics reach corresponding to the eigenvalue as defined in Equation (4.34).

These results show that the WBF process has quite different sensitivities to the five operators: $\mathcal{O}_{\phi,2}$, which is the only one that affects the decay vertex in addition to the production process, can be most strongly constrained and is weakly correlated with \mathcal{O}_W . An ideal measurement can probe this operator with a precision of $\Delta\theta \approx 0.02$, translating into a maximal new physics reach $\Lambda/\sqrt{f_{\phi,2}} \approx 1.9$ TeV. The sensitivity to the strongly correlated \mathcal{O}_W - \mathcal{O}_{WW} plane is also quite large: these directions can be probed at the $\Delta\theta \approx 0.05$ or $\Lambda/\sqrt{f_{W/WW}} \approx 1$ TeV level. Finally, \mathcal{O}_B and \mathcal{O}_{BB} only play a role in subleading Z -mediated production diagrams. Their Wilson coefficients cannot be measured very well in this process, and do not affect the measurement of the other

operators through correlations.

In Figure 4.2 we visualise the sensitivity to the three operators $\mathcal{O}_{\phi,2}$, \mathcal{O}_W , and \mathcal{O}_{WW} as contours of the local information distances from the SM as defined in Equation (4.13). Such an error ellipsoid shows the maximum precision that can be attained in a measurement in this process in the absence of new physics.

Moving away from the SM, the Fisher information and with it the sensitivity to the different operators changes. The largest effects are visible towards large positive (large negative) values of $f_{\phi,2}$, where the expected cross section is much smaller (larger) and theory parameters can be measured with smaller (larger) precision. Following Equation (4.14), we integrate infinitesimal distances along geodesics in theory space to define global distances in the model parameter space. Unlike the local distances, these take into account the curvature of the manifold, i. e. how the Fisher information changes with the theory parameters. Figure 4.3 shows the resulting distances for a number of two-dimensional slices in parameter space, confirming the large sensitivity to $\mathcal{O}_{\phi,2}$, \mathcal{O}_W , and \mathcal{O}_{WW} .

In Figure 4.4 we compare the global distances to the local distances defined in Equation (4.13). This provides some insight into the role of $\mathcal{O}(1/\Lambda^4)$ effects, as discussed in Section 4.3.6. At $d = 1, 2$ the differences are small, signalling that an optimal measurement will be dominated by the linearised dimension-six amplitudes. On the other hand, analyses based on less luminosity or requiring more stringent exclusion criteria (translating into larger distances) will only probe

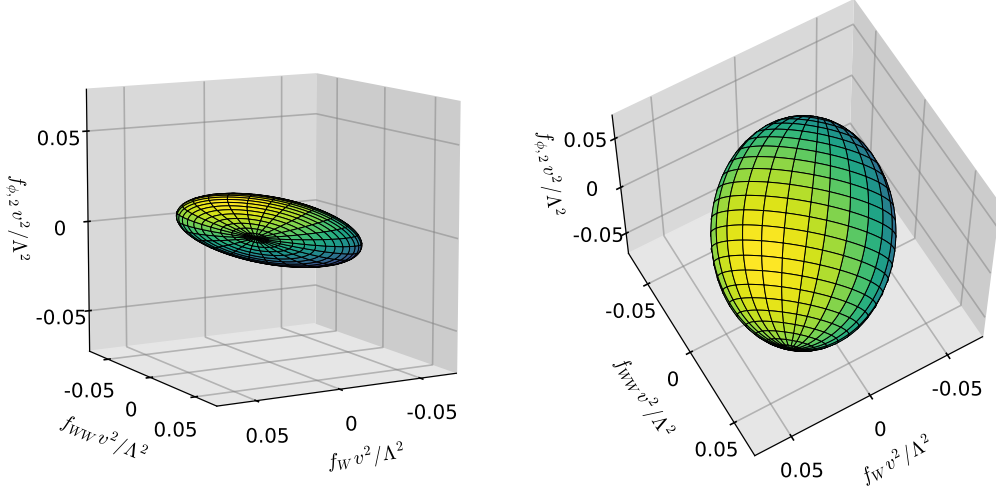


Figure 4.2: Error ellipsoid defined by the Fisher information in the WBF $h \rightarrow \tau\tau$ channel through the contour $d_{\text{local}}(\theta; \mathbf{0}) = 1$. The θ_i not shown are set to zero. The two panels show different views of the same ellipsoid.

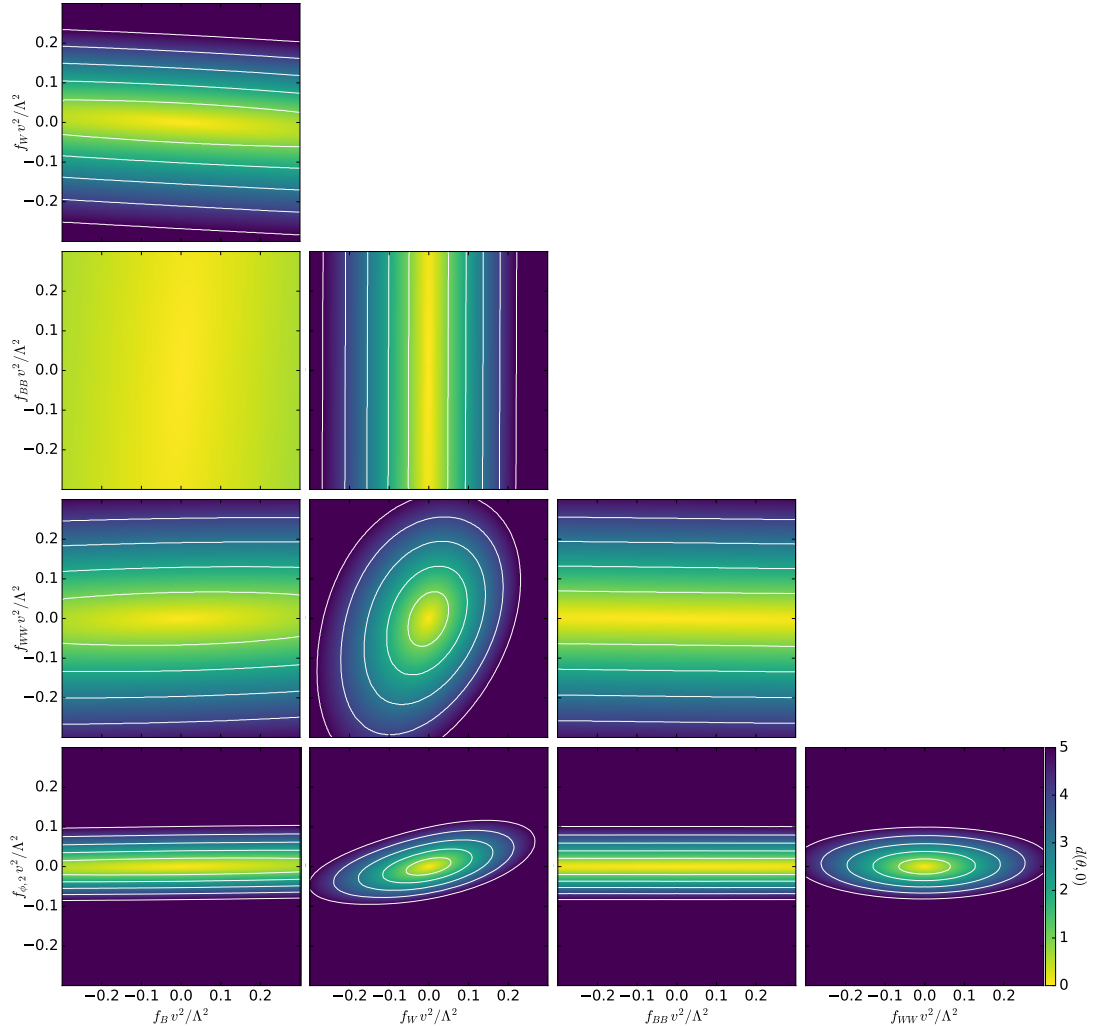


Figure 4.3: Error ellipses defined by the Fisher information in the WBF $h \rightarrow \tau\tau$ channel. We show global distances from the SM $d(\theta, \mathbf{0})$, where in each panel the θ_i not shown are set to zero. The white contours show distances of $d = 1, 2, 3, 4, 5$.

new physics scales closer to the electroweak scale, in which case the squared dimension-six terms will have a larger effect.

Differential information

In a next step, we calculate the distribution of this information, evaluated at the SM point $\theta = \mathbf{0}$, over phase space. Following Section 4.3.4, we calculate the Fisher information in bins of kinematic variables. This set of information matrices can be condensed into a single real-valued function of the phase-space variables by calculating the determinants. The resulting distributions of differential information over typical kinematic variables are shown in Figures 4.5 and 4.6 and compared to the differential cross sections of the signal and the dominant background process.

Clearly, the signal-to-background ratio improves for large invariant masses of the tagging jets and towards $m_{\tau\tau}$ values around the Higgs mass. The information on all directions in model space is larger in these phase-space regions. On the other hand, most of our dimension-six operators include derivatives, leading to an amplitude increasing with the momentum transfer through the gauge-Higgs vertex. This momentum flow is not observable, but the transverse momenta of the tagging jets and the Higgs boson are strongly correlated with it, as shown in Section 3.4.1. Indeed most of the information on higher-dimensional operators comes from the high-energy tail of the transverse momenta of the tagging jets or the $\tau\tau$ system, confirming what we demonstrated for specific model setups in the previous chapter.

In the rapidity difference between the tagging jets we can see a trade-off between these two effects: on the one hand, at larger rapidity distances the signal-to-background ratio clearly improves [75–81]. On the other hand, the largest effects from dimension-six operators appear

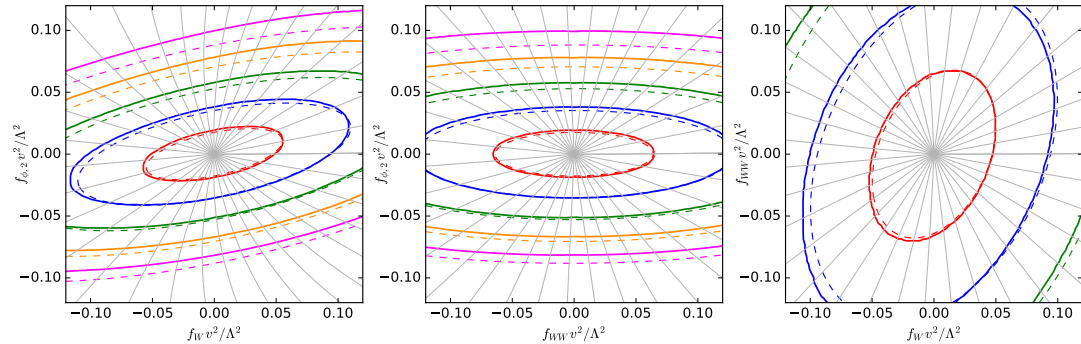


Figure 4.4: Error ellipses defined by the Fisher information in the WBF $h \rightarrow \tau\tau$ channel. We show contours of local distance $d_{\text{local}}(\theta; \mathbf{0})$ (dashed) and global distance $d(\theta; \mathbf{0})$ (solid). The coloured contours indicate distances of $d = 1, 2, 3, 4, 5$. In grey we show example geodesics. The θ_i not shown are set to zero.

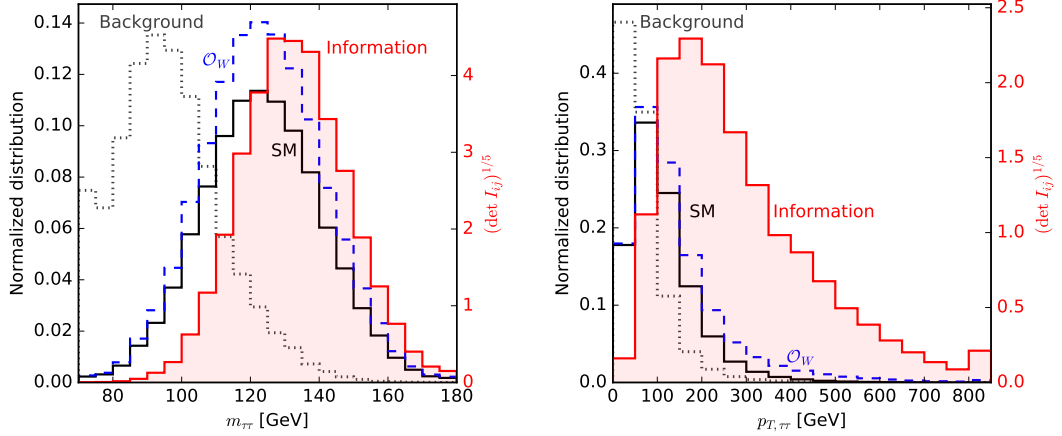


Figure 4.5: Distribution of the differential Fisher information in the WBF $h \rightarrow \tau\tau$ channel (shaded red) with respect to the invariant mass of the $\tau\tau$ system (left) and its transverse momentum (right). We also show the normalised rates for the SM signal (solid black) and the QCD Zjj background (dotted grey). The dashed blue lines show the effect of an exaggerated new physics benchmark $f_W v^2/\Lambda^2 = 0.5$ on the WBF signal. The last bin is an overflow bin.

at smaller $\Delta\eta_{jj}$, again driven by the larger momentum transfer [2]. In the bottom left panel of Figure 4.6 we see that most of the information on these operators comes from $\Delta\eta_{jj} = 3 \dots 7$. Tight cuts with the aim to remove backgrounds thus discard a sizeable fraction of the information on dimension-six operators.

In practice, the distribution of the differential information can be a useful tool to guide the design of event selections. As an example, we consider a class of typical WBF cuts

$$105 \text{ GeV} < m_{\tau\tau} < 165 \text{ GeV}, \quad p_{T,j_1} > 50 \text{ GeV}, \quad \Delta\eta_{jj} > \Delta\eta_{jj}^{\min}, \quad \text{and} \quad m_{jj} > m_{jj}^{\min}. \quad (4.48)$$

In Figure 4.7 we show how the signal purity and the Fisher information depend on the choice of $\Delta\eta_{jj}^{\min}$ and m_{jj}^{\min} . For a given signal-to-background ratio we can pick cuts that maximise the Fisher information, or vice versa, as demonstrated in the left panel of Figure 4.8. This is somewhat reminiscent of ‘receiver operating characteristic’ (ROC) curves that compare the efficiency for the SM Higgs signal to the background rejection rate, as shown in the right panel of Figure 4.8. The information-based analysis, however, takes into account the sensitivity of signal events in different phase-space regions to new physics effects, which the ROC curve is blind to by design.

The distribution of the differential Fisher information also provides us with another perspective on the EFT validity discussed in the previous chapter. There we demonstrated that the effective

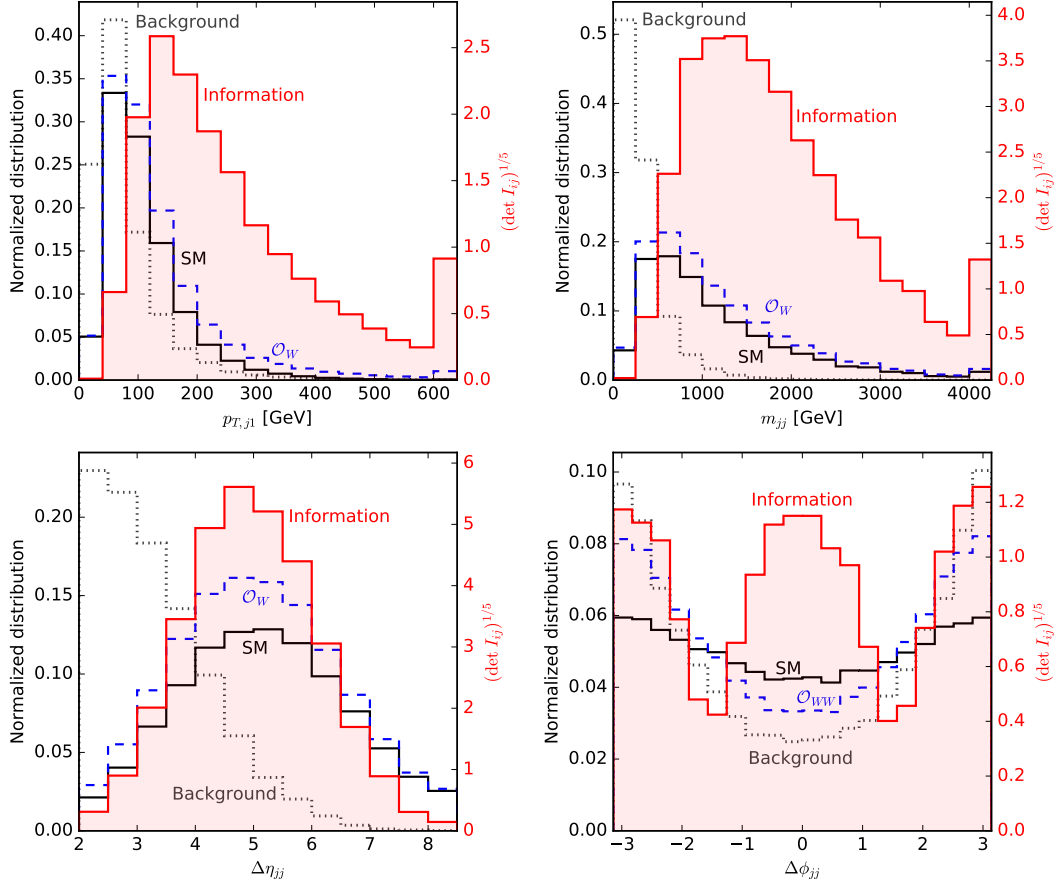


Figure 4.6: Distribution of the differential Fisher information in the WBF $h \rightarrow \tau\tau$ channel (shaded red) with respect to the transverse momentum of the leading jet (top left), the dijet mass (top right), the separation in pseudorapidity between the two jets (bottom left), and their difference in the azimuthal angle (bottom right). We also show the normalised rates for the SM signal (solid black) and the QCD Zjj background (dotted grey). The dashed blue lines show the effect of $f_W v^2/\Lambda^2 = 0.5$ on the WBF signal, except in the bottom right panel, where we show $f_{WW} v^2/\Lambda^2 = 0.5$. The last bin is an overflow bin.

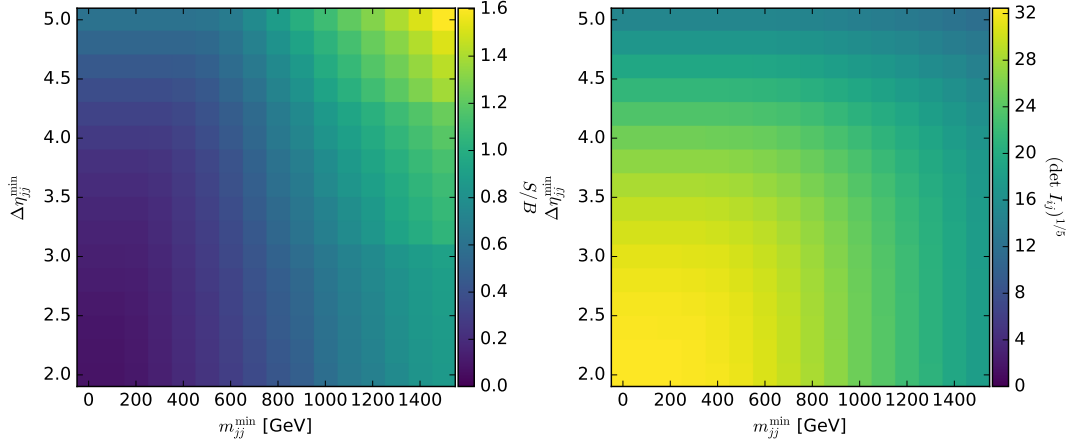


Figure 4.7: SM signal-to-background ratio (left) and determinant of the Fisher information (right) in the WBF $h \rightarrow \tau\tau$ channel as a function of the WBF cuts $\Delta\eta_{jj} > \Delta\eta_{jj}^{\min}$ and $m_{jj} > m_{jj}^{\min}$.

model can break down in the high-energy tail of distributions, and concluded that an additional analysis with cuts that impose a maximum momentum transfer can improve the applicability of the EFT. For weak boson fusion, this means requiring

$$p_{T,j} < p_{T,j}^{\max}, \quad (4.49)$$

as shown in Section 3.4.1.

Our tools let us calculate the Fisher information in the WBF $h \rightarrow \tau\tau$ channel for different cuts of the form of Equation (4.49). For simplicity, we focus on the operators \mathcal{O}_W and \mathcal{O}_{WW} and calculate the determinant of the Fisher information in this plane in model space. Following Equation (4.34), we translate it into a typical new physics reach

$$\frac{\Lambda}{\sqrt{f}} = v \sqrt{\det I_{ij}(\mathbf{0})}^{1/4} \quad (4.50)$$

of an optimal measurement. For universal Wilson coefficients $f_W = f_{WW} \equiv f$, we can calculate the new physics reach Λ and compare it to the maximum momentum transfer $p_{T,j}^{\max}$.

Figure 4.9 shows that for strongly coupled physics we can probe new physics scales significantly above the experimental momentum transfer, at least in our simple setup that neglects systematic and theory uncertainties. Such a scenario does not require any validity cuts for the EFT to work. However, for smaller Wilson coefficients $0.25 \lesssim f \lesssim 1$, the scale hierarchy is less clear, confirming the discussion in Section 3.1. Our results show that imposing a maximum momentum transfer of a few hundred GeV can increase the separation between the experimental energy scale and the probed new physics scales, and thus the usefulness of the effective theory.

Information in distributions

While this total Fisher information based on the full kinematics provides us with optimal experimental results, it remains to be shown that we can access it in practice. Matrix-element-based methods [50–65] and recent proposals using machine learning for high-dimensional likelihood fits [28, 31] aim to tackle exactly this problem. Still, a relevant question is how much of this maximum information is retained in simple one-dimensional or two-dimensional distributions of standard kinematic observables \mathbf{v} . On the one hand, this lets us assess the potential of traditional histogram-based analysis methods and compare it to the optimal results discussed before. On the other hand, the information in kinematic distributions provides a ranking of the most useful observables that experimentalists should measure and publish, for instance to be used in recasted analyses or in global fits by theorists [26, 27].

In the presence of backgrounds, a histogram-based analysis requires a stringent event selection, either based on traditional kinematic cuts or on a multivariate classifier. First, we choose the WBF cuts

$$105 \text{ GeV} < m_{\tau\tau} < 165 \text{ GeV}, \quad p_{T,j1} > 50 \text{ GeV}, \quad m_{jj} > 1 \text{ TeV}, \quad \Delta\eta_{jj} > 3.6. \quad (4.51)$$

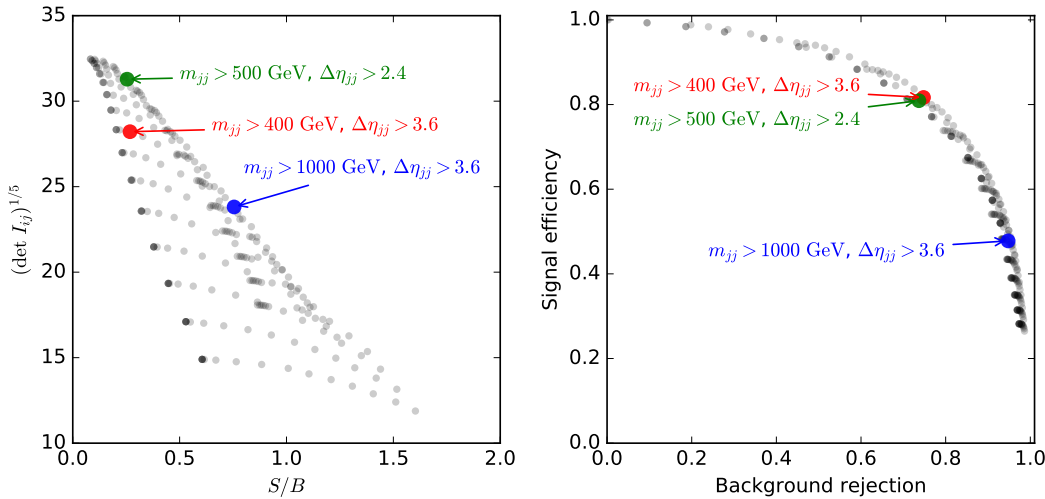


Figure 4.8: Trade-off between signal purity and information in the WBF $h \rightarrow \tau\tau$ channel for different WBF cuts. Left: determinant of the Fisher information vs. signal-to-background ratio. Right: signal efficiency vs. background rejection, calculated after the common cuts $105 \text{ GeV} < m_{\tau\tau} < 165 \text{ GeV}$ and $p_{T,j1} > 50 \text{ GeV}$. The coloured dots show three example selections.

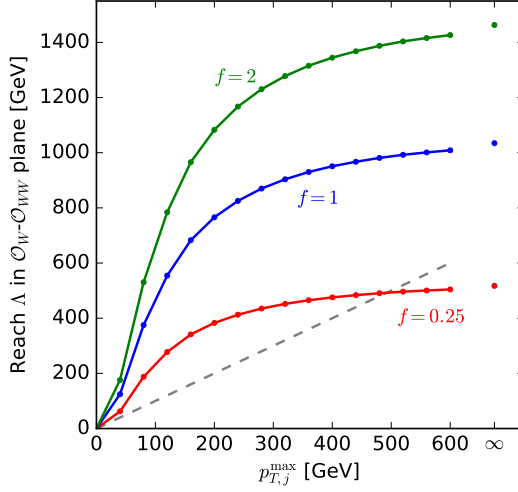


Figure 4.9: Maximal new physics reach of the WBF $h \rightarrow \tau\tau$ channel in the \mathcal{O}_W - \mathcal{O}_{WW} plane as a function of an upper cut of the transverse jet momenta $p_{T,j}^{\max}$. The green, blue, and red curves show the new physics reach for different values of the Wilson coefficients $f_W = f_{WW} \equiv f$, as defined in Equation (4.50). To roughly assess the EFT validity, these should be compared to the maximum jet p_T in these events (dashed grey).

As shown in Figure 4.8, this improves the signal-to-background ratio to nearly unity, though at the cost of losing discrimination power. An analysis would profit from an optimisation of these cuts, but this goes beyond the scope of our demonstration. Based on this selection, we analyse the distributions of the following standard observables:

- the transverse momentum of the leading τ , p_{T,τ_1} , with bin size 25 GeV up to 500 GeV and an overflow bin;
- the invariant mass of the $\tau\tau$ system, $m_{\tau\tau}$, with bin size 5 GeV in the allowed range of 105 GeV < $m_{\tau\tau}$ < 165 GeV;
- the transverse momentum of the $\tau\tau$ system, $p_{T,\tau\tau}$, with bin size 50 GeV up to 800 GeV and an overflow bin;
- the transverse momentum of the leading jet, p_{T,j_1} , with bin size 50 GeV up to 800 GeV and an overflow bin;
- the invariant mass of the dijet system, m_{jj} , with bin size 250 GeV up to 4 TeV and an overflow bin;
- the separation in pseudorapidity between the two jets, $\Delta\eta_{jj}$, with bin size 0.5 up to 8.0 and an overflow bin;

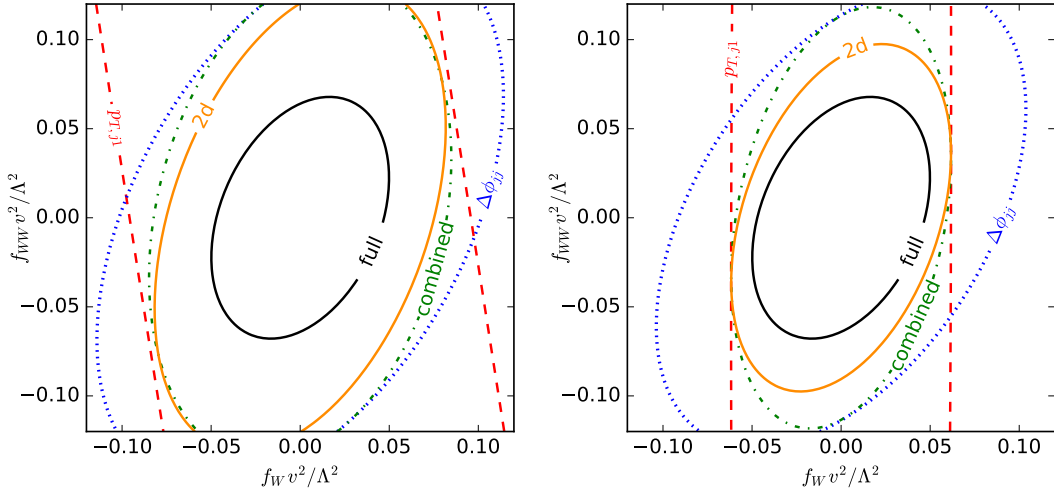


Figure 4.10: Information in distributions in the WBF $h \rightarrow \tau\tau$ channel, shown as contours $d_{\text{local}}(\boldsymbol{\theta}; \mathbf{0}) = 1$. We show the total information in the full kinematics (black), the information in the distributions of $p_{T,j1}$ (red) and $\Delta\phi_{jj}$ (blue), their naive combination assuming no mutual information (green), and their two-dimensional histogram (yellow). The θ_i not shown are set to zero. Left: based on the kinematic WBF cuts in Equation (4.51). Right: based on the matrix-element-based selection in Equation (4.52).

- the separation in azimuthal angle between the two jets, now defined in a signed version [294] $\Delta\phi_{jj} = \phi_{j_{\eta < 0}} - \phi_{j_{\eta > 0}}$, with bin size $2\pi/20$;
- the separation in pseudorapidity between the $\tau\tau$ system and the leading jet, $\Delta\eta_{\tau\tau,j1}$, with bin size 0.5 up to 8.0 and an overflow bin; and
- the separation in azimuthal angle between the $\tau\tau$ system and the leading jet, $\Delta\phi_{\tau\tau,j1}$, with bin size $\pi/10$.

In the left panel of Figure 4.10, we compare the error ellipses expected from the analysis of a few of these distributions. Measures of the momentum transfer such as the transverse momentum of the leading tagging jet mostly constrain \mathcal{O}_W , while angular correlations between the jets are more sensitive to \mathcal{O}_{WW} . Stringent constraints on the full operator space can be achieved by combining the information in these distributions. A fully correlated two-dimensional histogram carries slightly more information than a combination of the one-dimensional histograms following Equation (4.19).

Finally, we compare the information in all of the above distributions in Figure 4.11. The top panel shows the eigenvalues of the individual information matrices, and the colours indicate

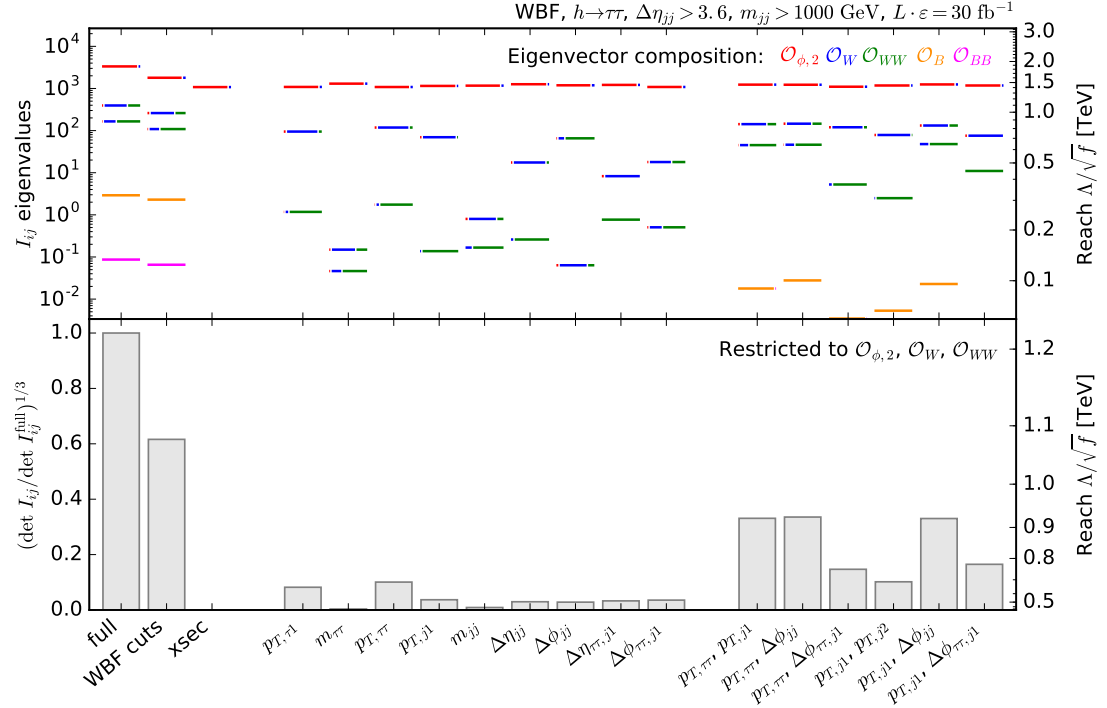


Figure 4.11: Fisher information in different distributions in the WBF $h \rightarrow \tau\tau$ channel, based on a tight kinematic selection. We compare the total Fisher information based on the full kinematics ('full'), the Fisher information after the cuts in Equation (4.51) ('WBF cuts'), the rate-only information after these cuts ('xsec'), and the information in several one-dimensional and two-dimensional distributions after this selection. The top panel shows the eigenvalues of these information matrices, the colours denote the composition of the corresponding eigenvectors. The right axis translates the eigenvalues into a new physics reach for the corresponding combination of Wilson coefficients. In the bottom panel we show the determinants of the three-dimensional Fisher information restricted to $\mathcal{O}_{\phi,2}$, \mathcal{O}_W , and \mathcal{O}_{WW} , normalised to the full information. Again, the right axis translates them into a new physics reach.

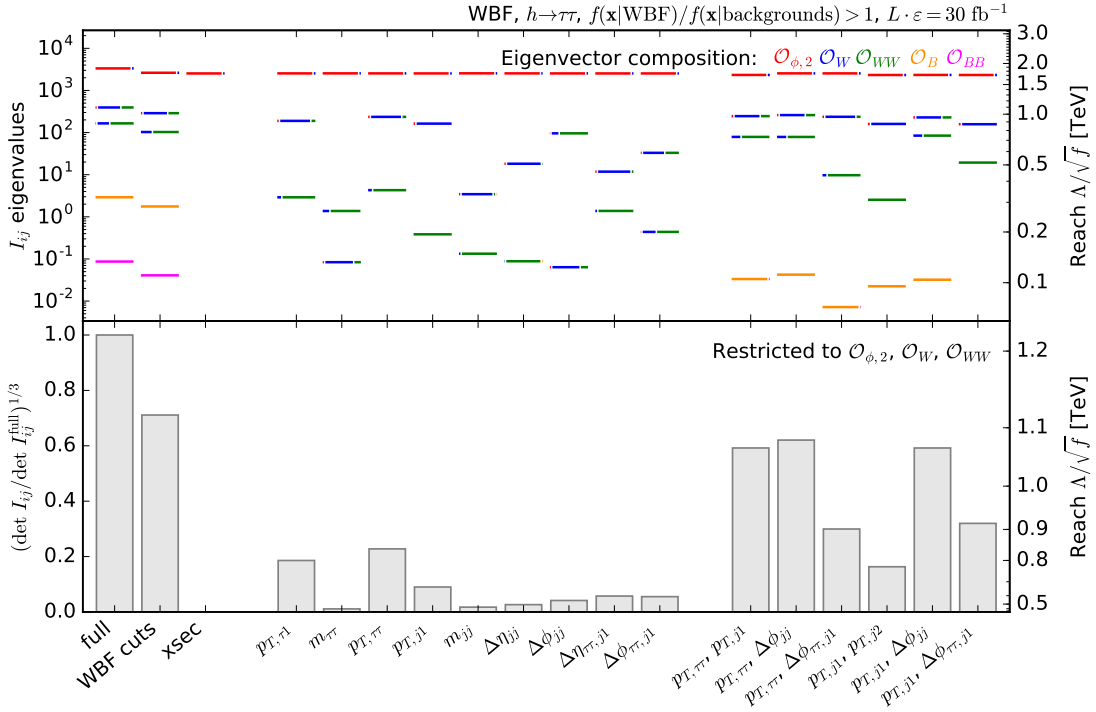


Figure 4.12: Fisher information in different distributions in the WBF $h \rightarrow \tau\tau$ channel, based on a matrix-element-based selection. We compare the total Fisher information based on the full kinematics ('full'), the Fisher information after the multivariate event selection in Equation (4.52) ('WBF cuts'), the rate-only information after this selection ('xsec'), and the information in several one-dimensional and two-dimensional distributions after this selection. Except for the event selection, the plot is analogous to Figure 4.11.

which operators the corresponding eigenvectors are composed of. This allows us to see which distributions measure which directions in theory space well, and where blind directions arise.

The lower panel shows the determinants of the Fisher information matrices. We restrict this analysis to the space spanned by the three operators $\mathcal{O}_{\phi,2}$, \mathcal{O}_W , and \mathcal{O}_{WW} to avoid results that strongly depend on the other two operators, which cannot be measured reliably in this process anyway. These determinants provide a straightforward measure of the information in the distributions that is independent of EFT basis rotations, see Section 4.3.6.

In general, one-dimensional histograms of single observables probe individual directions in phase space well, but always suffer from basically blind directions. To maximise the constraining power on all operators, we need to combine measures of momentum transfer such as the jet

or $\tau\tau$ transverse momenta on the one hand with jet angular correlations on the other hand. Even then there is a substantial difference to the maximum information in the process: the combined analysis of jet transverse momenta and $\Delta\phi_{jj}$ has a new physics reach Λ/\sqrt{f} in the $\mathcal{O}_{\phi,2}\text{-}\mathcal{O}_W\text{-}\mathcal{O}_{WW}$ space of 0.9 TeV, compared to 1.2 TeV for the full kinematics. Under our simplistic assumptions this corresponds to roughly three times as much data. Half of this loss in constraining power is due to information in background-rich regions discarded by the WBF cuts, the other half is due to non-trivial kinematics not captured by the double differential distributions.

In the light of the large loss of information due to the WBF cuts in Equation (4.51), we repeat this comparison with an alternative matrix-element-based event selection. Instead of cutting on standard kinematic observables, we select all events in ‘signal-like’ phase-space regions, defined as those with a larger expected SM WBF rate than the combined expected background rates,

$$\frac{\sigma_{\text{SM WBF}} f^{(1)}(\mathbf{x}|\text{SM WBF})}{\sigma_{\text{backgrounds}} f^{(1)}(\mathbf{x}|\text{backgrounds})} = \frac{\Delta\sigma_{\text{SM WBF}}(\mathbf{x})}{\Delta\sigma_{\text{backgrounds}}(\mathbf{x})} > 1. \quad (4.52)$$

We then calculate the information in the same distributions as before.

As shown in the right panel of Figure 4.10 and in Figure 4.12, the cut in Equation (4.52) defines a sample with little background contamination without sacrificing much discrimination power. One-dimensional and two-dimensional distributions can extract information on the operators more reliably than after the kinematic event selection in Equation (4.51). A combined measurement of the jet transverse momenta and $\Delta\phi_{jj}$ is now able to probe new physics scales of up to 1.1 TeV compared to 1.2 TeV for the fully multivariate approach, corresponding to 70% more data.

4.4.2 Weak-boson-fusion Higgs to four leptons

With a thorough understanding of the WBF production process, we now ask how much information a non-trivial decay mode $h \rightarrow ZZ^* \rightarrow 4\ell$ with $\ell = e, \mu$ adds. For this particularly clean channel, shown in Figure 4.13, the backgrounds are not the limiting factor, so we omit them for our toy study: a calculation with MadGraph 5 shows that in the relevant phase-space region the cross section of the dominant irreducible $ZZ^* jj$ background is more than one order of magnitude smaller than the SM Higgs signal. This also allows us to avoid smearing the $m_{4\ell}$ distribution. Again, we restrict our initial study to the parton level and leading order.

Requiring only minimal acceptance cuts

$$p_{T,j} > 20 \text{ GeV}, \quad |\eta_j| < 5.0, \quad p_{T,\ell} > 10 \text{ GeV}, \quad \text{and} \quad |\eta_\ell| < 2.5, \quad (4.53)$$

we calculate the Fisher information for pp collision at $\sqrt{s} = 13$ TeV. We now assume an increased integrated luminosity of

$$L \cdot \varepsilon = 100 \text{ fb}^{-1}, \quad (4.54)$$

where ε again refers to the combined particle identification and trigger efficiencies. The SM cross section after our selection cuts is 0.36 fb, corresponding to 36 expected events.

The relevant dimension-six operators are the same as in the $\tau\tau$ channel, and we again parametrise the model space with Equation (4.45). All other details follow the setup in the previous section.

Total Fisher information

The full Fisher information at the SM for this process is

$$I_{ij}(\mathbf{0}) = \begin{pmatrix} 144.3 & -27.3 & -11.5 & -1.6 & -0.7 \\ -27.3 & 50.9 & -9.1 & 6.7 & -0.2 \\ -11.5 & -9.1 & 36.9 & -1.2 & 1.0 \\ -1.6 & 6.7 & -1.2 & 1.9 & -0.1 \\ -0.7 & -0.2 & 1.0 & -0.1 & 0.1 \end{pmatrix}, \quad (4.55)$$

with the eigenvectors, eigenvalues, and corresponding new physics reach

$$\theta_1 = \begin{pmatrix} 0.96 \\ -0.25 \\ -0.08 \\ -0.02 \\ 0.00 \end{pmatrix} : \quad I_1 = 152.4 \quad \leftrightarrow \quad \left(\frac{\Lambda}{\sqrt{f}} \right)_1 = 864 \text{ GeV},$$

$$\theta_2 = \begin{pmatrix} -0.16 \\ -0.79 \\ 0.58 \\ -0.11 \\ 0.02 \end{pmatrix} : \quad I_2 = 52.8 \quad \leftrightarrow \quad \left(\frac{\Lambda}{\sqrt{f}} \right)_2 = 663 \text{ GeV},$$

$$\theta_3 = \begin{pmatrix} 0.21 \\ 0.54 \\ 0.81 \\ 0.09 \\ 0.02 \end{pmatrix} : \quad I_3 = 27.8 \quad \leftrightarrow \quad \left(\frac{\Lambda}{\sqrt{f}} \right)_3 = 565 \text{ GeV},$$

$$\theta_4 = \begin{pmatrix} 0.02 \\ 0.14 \\ 0.01 \\ -0.99 \\ 0.04 \end{pmatrix} : I_4 = 1.0 \leftrightarrow \left(\frac{\Lambda}{\sqrt{f}} \right)_4 = 246 \text{ GeV},$$

$$\theta_5 = \begin{pmatrix} 0.00 \\ 0.00 \\ -0.03 \\ 0.04 \\ 1.00 \end{pmatrix} : I_5 = 0.0 \leftrightarrow \left(\frac{\Lambda}{\sqrt{f}} \right)_5 = 114 \text{ GeV}. \quad (4.56)$$

The Fisher information approach allows us to directly compare this outcome to the information in the $h \rightarrow \tau\tau$ channel in Equation (4.46), or to calculate the combined information in these two channels by simply adding their Fisher information matrices after rescaling them to the same luminosity. Clearly, the $\tau\tau$ channel contains significantly more information on all operators. The decay $h \rightarrow 4\ell$ does not even increase the sensitivity to \mathcal{O}_B or \mathcal{O}_{BB} , both are still basically blind directions.

Again we calculate global distances between theory points along geodesics and show them in Figure 4.14. Local and global distances are compared in Figure 4.15, with larger differences than in the $h \rightarrow \tau\tau$ channel. This is because the tiny $h \rightarrow 4\ell$ branching fraction decreases the new physics reach and with it the hierarchy of scales in our effective Lagrangian, making the squared dimension-six amplitudes numerically more relevant.

The distribution of the differential information over phase space is essentially identical to the results for the WBF $h \rightarrow \tau\tau$ mode given in Figures 4.5 and 4.6, with the obvious replacement of the reconstructed $\tau\tau$ system by the 4ℓ system.

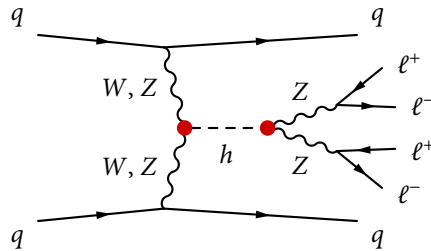


Figure 4.13: Feynman diagram for WBF Higgs production in the 4ℓ mode. The red dots show the Higgs-gauge interactions affected by the dimension-six operators of our analysis.

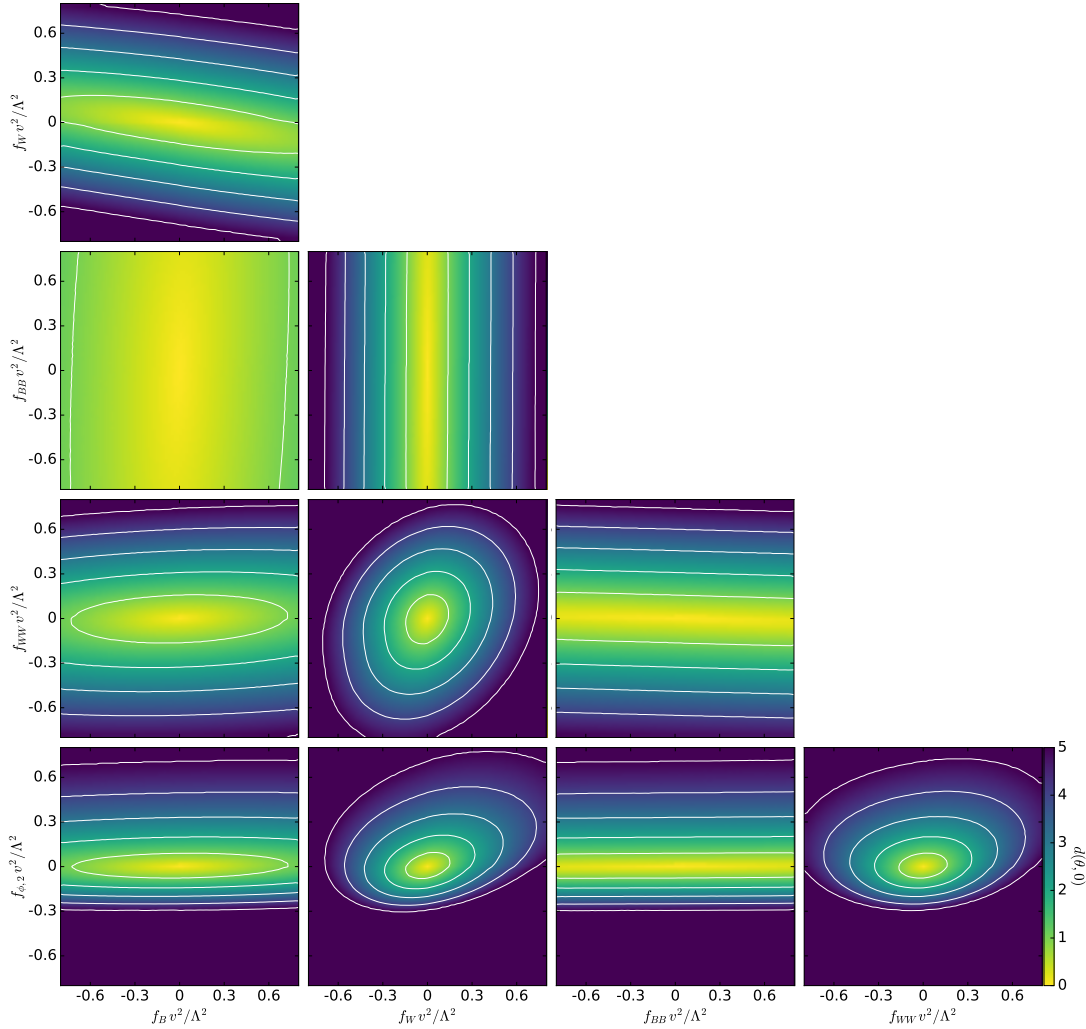


Figure 4.14: Error ellipses defined by the Fisher information in the WBF $h \rightarrow 4\ell$ channel. We show global distances from the SM $d(\theta, 0)$, where in each panel the θ_i not shown are set to zero. The white contours show distances of $d = 1, 2, 3, 4, 5$.

Production vs. decay kinematics

The key question for the WBF $h \rightarrow 4\ell$ mode is how the rich decay kinematics can improve the sensitivity to the dimension-six operators. In Figure 4.16, we separately study the effects of the effective operators on the production vertex (fixing the decay vertex to the SM value) and on the decay vertex (where the production is fixed to the SM structure). We find that only the sensitivity to $\mathcal{O}_{\phi,2}$ profits from effects in the decay vertex. Since this operator rescales all Higgs couplings in the same way, this also applies to any other Higgs decay mode. The sensitivity on the momentum-dependent operators \mathcal{O}_W , \mathcal{O}_{WW} , \mathcal{O}_B , and \mathcal{O}_{BB} , on the other hand, comes almost entirely from effects on the Higgs production.

This is not surprising: the momentum flow through the intermediate W or Z bosons can be very large at the LHC, enhancing production-side effects by sizeable factors of E^2/Λ^2 . The momentum flow through the decay vertices, on the other hand, is bounded by the Higgs mass (neglecting off-shell Higgs decays), and E^2/Λ^2 is small. Our results show that this is not compensated by the complex $h \rightarrow 4\ell$ kinematics.

To overcome this disadvantage, momentum-dependent signatures in Higgs decays require a large production cross section. Gluon-fusion production with $h \rightarrow 4\ell$ has a rate that is approximately 13 times larger than the WBF process [3]. Since the decay kinematics is the same as in the process studied here and the Fisher information scales linearly with the number of events, we can provide a rough estimate of the information in this process by scaling the decay-only Fisher information with this factor 13. We find that even with the increased rate from production in gluon fusion, the $h \rightarrow 4\ell$ channel is not as sensitive to Higgs-gauge operators as the WBF production process. Of course, this simple estimate ignores any differences in the backgrounds, efficiencies, systematic

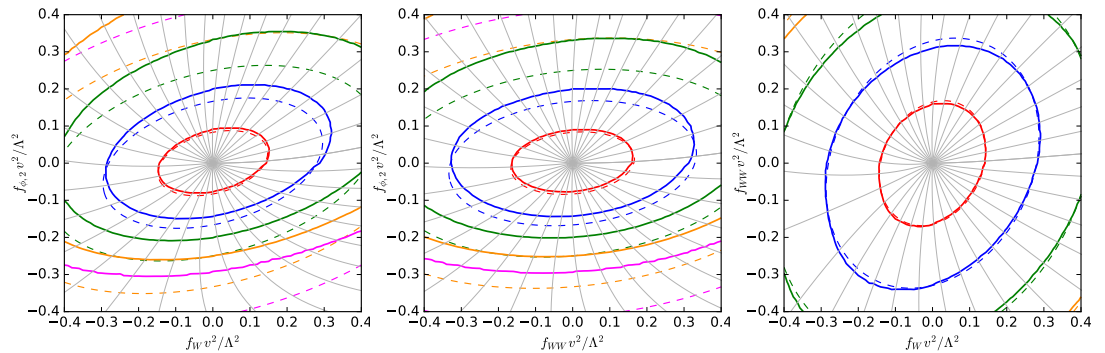


Figure 4.15: Error ellipses defined by the Fisher information in the WBF $h \rightarrow 4\ell$ channel. We show contours of local distance $d_{\text{local}}(\theta; \mathbf{0})$ (dashed) and global distance $d(\theta, \mathbf{0})$ (solid). The coloured contours indicate distances of $d = 1, 2, 3, 4, 5$. In grey we show example geodesics. The θ_i not shown are set to zero.

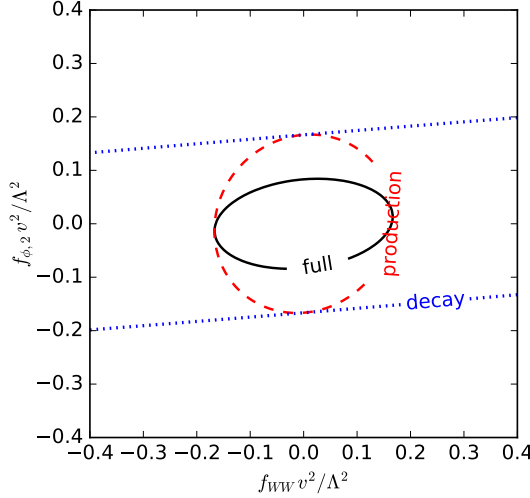


Figure 4.16: Information in the WBF $h \rightarrow 4\ell$ channel separated into production effects and decay effects. We show the contours $d_{\text{local}}(\boldsymbol{\theta}; \mathbf{0}) = 1$ based on calculations where dimension-six operators are taken into account only in the production vertex (red), only in the decay vertex (blue), and in both vertices (black). The θ_i not shown are set to zero.

or theory uncertainties, and Higgs kinematics between the two production processes.

Information in distributions

The question of production and decay effects can also be tackled by comparing the information in different observables: the properties of the tagging jets are linked to the production process, while the decay products of the Higgs are mostly sensitive to the decay vertex. We define the jet observables in complete analogy to the $\tau\tau$ channel in Section 4.4.1. These are complemented by observables characterising the decay kinematics [86, 295]:

- the transverse momentum of the leading lepton, p_{T,ℓ_1} ;
- the transverse momentum of the four-lepton system, $p_{T,4\ell}$, which is equal to the Higgs p_T ;
- the smaller invariant mass of the reconstructed $\ell^+ \ell^-$, m_{Z_2} ;
- the angle $\cos \theta_1 = \hat{p}_{\ell_1^-} \cdot \hat{p}_{Z_2}|_{Z_1}$ with spatial unit vectors \hat{p} defined in the Z_1 system;
- analogously $\cos \theta_2$; and
- the angle $\cos \Phi = (\hat{p}_{\ell_1^-} \times \hat{p}_{\ell_1^+}) \cdot (\hat{p}_{\ell_2^-} \times \hat{p}_{\ell_2^+})|_{4\ell}$, defined in the 4ℓ rest frame.

In all cases we use at least ten bins and include underflow and overflow bins where applicable.

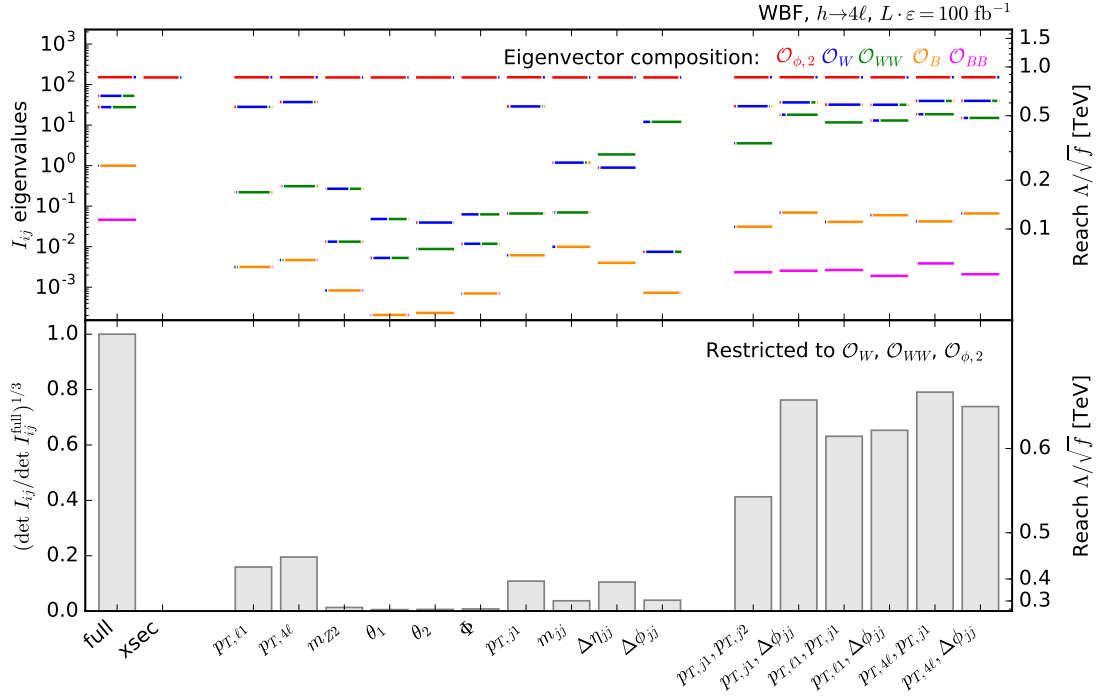


Figure 4.17: Fisher information in different distributions in the WBF $h \rightarrow 4\ell$ channel. We compare the total Fisher information based on the full kinematics ('full'), the information in the total rate ('xsec'), and the information in several one-dimensional and two-dimensional distributions. The top panel shows the eigenvalues of these information matrices, the colours denote the composition of the corresponding eigenvectors. The right axis translates the eigenvalues into a new physics reach for the corresponding combination of Wilson coefficients. In the bottom panel we show the determinants of the three-dimensional Fisher information restricted to $\mathcal{O}_{\phi,2}$, \mathcal{O}_W , and \mathcal{O}_{WW} , normalised to the full information. Again, the right axis translates them into a new physics reach.

The comparison in Figure 4.17 reveals similar patterns as the $\tau\tau$ mode. The key observables are again transverse momenta and jet angular correlations. Without the necessity of removing backgrounds efficiently, the combined analysis of these variables comes close to the maximum information: a two-dimensional histogram of jet transverse momenta and $\Delta\phi_{jj}$ probes new physics scales up to 650 GeV, while for a fully differential analysis the maximum probed new physics scale is close to 700 GeV. This difference roughly corresponds to 25% more data. The observables characterising the decay kinematics, in particular the angular correlations, carry very little information, in agreement with our previous results. This shows again how the sensitivity of the decay vertices to dimension-six operators is limited by the restriction of the momentum flow through the decay vertex to the Higgs mass.

4.4.3 Higgs plus single top

Our final example process is Higgs production with a single top in the t -channel. We focus on the $h \rightarrow \gamma\gamma$ mode and a hadronic top decay $t \rightarrow bjj$. As shown in Figure 4.18, diagrams where the Higgs is radiated off a W boson interfere destructively with diagrams with a top-Higgs coupling, making this channel a direct probe of the sign of the top Yukawa coupling [90]. Our analysis focuses on the question which of the phase-space distributions provide access to this interesting amplitude structure. We stick to a parton-level analysis at leading order in the five-flavour scheme. For our toy example we include only one of the dominant backgrounds, single top production with two photons, and in particular ignore the multi-jet background. The subleading $t\bar{t}\gamma\gamma$ background populates qualitatively different phase-space regions from the single-top signal and can be suppressed with an appropriate event selection [296].

To simulate the experimental mass resolution, we smear the $m_{\gamma\gamma}$ distribution of the signal process with the smearing function of Reference [290], described in Section A.6.3. We do not

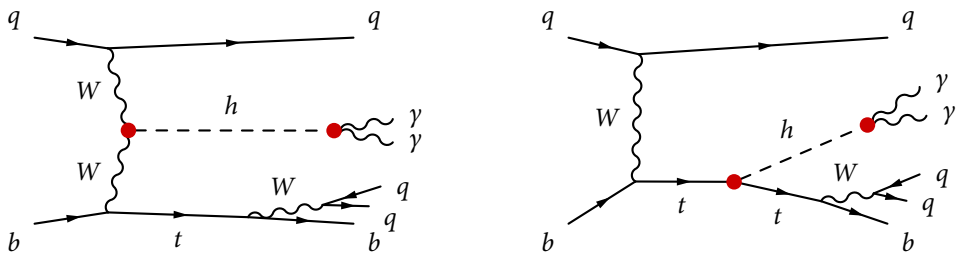


Figure 4.18: Feynman diagrams for t -channel Higgs plus single top production with $h \rightarrow \gamma\gamma$ and a hadronic top decay. The red dots show the Higgs interactions modified by the dimension-six operators considered in our analysis.

include any other detector effects. Our basic event selection requires

$$\begin{aligned} p_{T,j} > 20 \text{ GeV}, \quad |\eta_j| < 5.0, \quad \Delta R_{jj} > 0.4, \quad 152 \text{ GeV} < m_{bjj} < 192 \text{ GeV}, \\ p_{T,\gamma} > 10 \text{ GeV}, \quad |\eta_\gamma| < 2.5, \quad \Delta R_{\gamma j}, \Delta R_{\gamma\gamma} > 0.4, \quad 120 \text{ GeV} < m_{\gamma\gamma} < 130 \text{ GeV}, \end{aligned} \quad (4.57)$$

after which the SM signal of 0.10 fb faces a background of 0.22 fb. We calculate the Fisher information for pp collisions at $\sqrt{s} = 13$ TeV with a large amount of collected data,

$$L \cdot \varepsilon = 300 \text{ fb}^{-1}. \quad (4.58)$$

Again, ε denotes the combined particle identification and trigger efficiencies. This is equivalent to 30 expected signal events and 66 expected background events.

Out of the CP -even dimension-six operators discussed in Section 2.3.2, \mathcal{O}_W and \mathcal{O}_{WW} modify the Higgs- W coupling structure, while \mathcal{O}_t changes the value of the Higgs-top coupling. $\mathcal{O}_{\phi,2}$ rescales both contributions universally. While all these operators affect the $h \rightarrow \gamma\gamma$ decay as well, the largest effect is expected from \mathcal{O}_{WW} , which contributes to this coupling at tree level and can easily compete with the loop-suppressed SM term. Since we are mainly interested in the production kinematics, we neglect the subleading effects from \mathcal{O}_W and \mathcal{O}_t on the Higgs-photon coupling. Our model space is therefore parametrised by the dimensionless parameters

$$\boldsymbol{\theta} = \frac{v^2}{\Lambda^2} \begin{pmatrix} f_{\phi,2} \\ f_W \\ f_{WW} \\ f_t \end{pmatrix}. \quad (4.59)$$

As in the previous processes, we focus on the Fisher information in the vicinity of the SM, $\boldsymbol{\theta} = \mathbf{0}$, and in the two-dimensional planes in the parameter space where all but two operators are set to zero. Using the setup described in Section 4.3.7, we calculate the Fisher information for approximately 2500 parameter points.

Total Fisher information

For the total Fisher information at the SM, we find

$$I_{ij}(\mathbf{0}) = \begin{pmatrix} 80.1 & -18.7 & -957.0 & 13.2 \\ -18.7 & 32.6 & 221.7 & 27.0 \\ -957.0 & 221.7 & 11446.1 & -146.0 \\ 13.2 & 27.0 & -146.0 & 150.3 \end{pmatrix}. \quad (4.60)$$

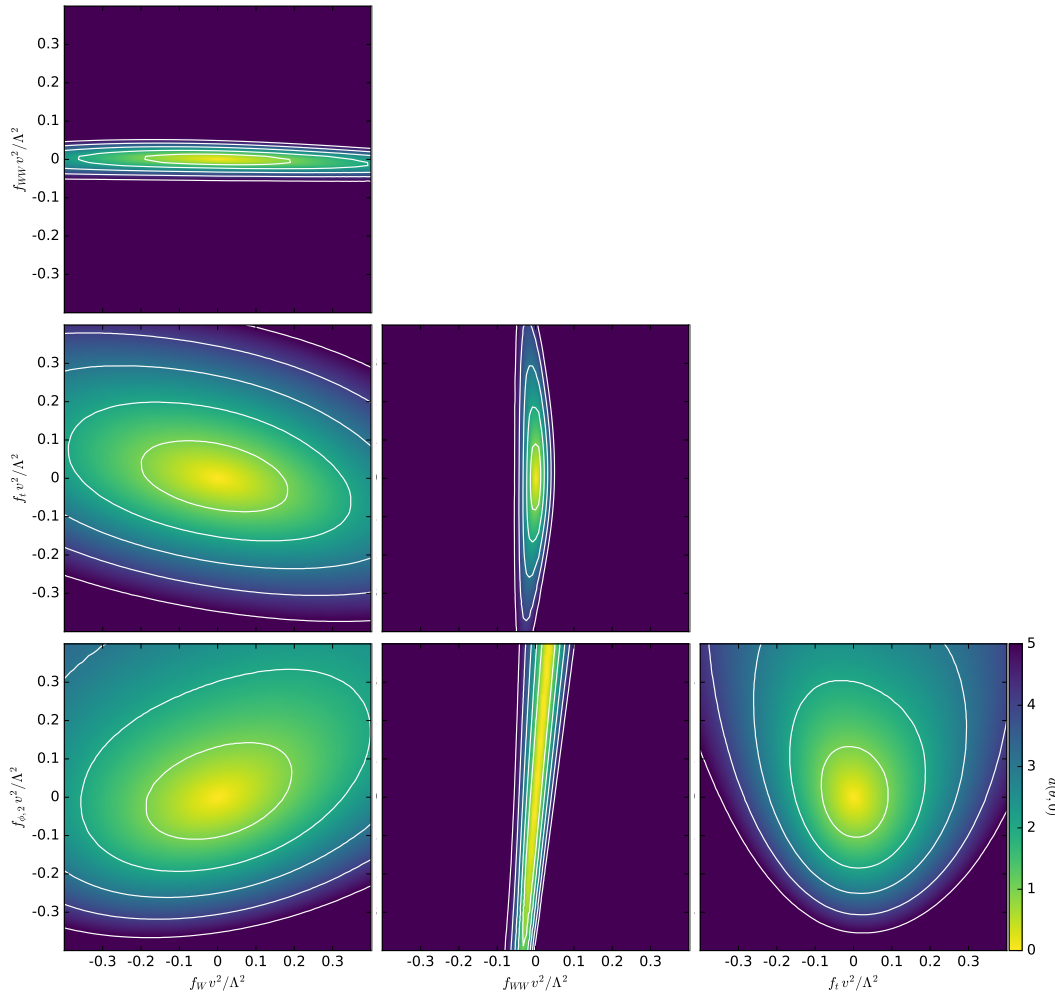


Figure 4.19: Error ellipses defined by the Fisher information in Higgs plus single top production. We show global distances from the SM $d(\boldsymbol{\theta}, \mathbf{0})$, where in each panel the θ_i not shown are set to zero. The white contours show distances of $d = 1, 2, 3, 4, 5$.

Composing this into eigenvectors and eigenvalues (and the corresponding new physics reach, see Equation (4.34)), we find

$$\begin{aligned}
 \boldsymbol{\theta}_1 &= \begin{pmatrix} 0.08 \\ -0.02 \\ -1.00 \\ 0.01 \end{pmatrix} : \quad I_1 = 11532 \quad \leftrightarrow \quad \left(\frac{\Lambda}{\sqrt{f}} \right)_1 = 2550 \text{ GeV}, \\
 \boldsymbol{\theta}_2 &= \begin{pmatrix} 0.00 \\ -0.23 \\ -0.01 \\ -0.97 \end{pmatrix} : \quad I_2 = 155 \quad \leftrightarrow \quad \left(\frac{\Lambda}{\sqrt{f}} \right)_2 = 868 \text{ GeV}, \\
 \boldsymbol{\theta}_3 &= \begin{pmatrix} -0.02 \\ 0.97 \\ -0.02 \\ -0.23 \end{pmatrix} : \quad I_3 = 21.3 \quad \leftrightarrow \quad \left(\frac{\Lambda}{\sqrt{f}} \right)_3 = 528 \text{ GeV}, \\
 \boldsymbol{\theta}_4 &= \begin{pmatrix} 1.00 \\ 0.02 \\ 0.08 \\ -0.01 \end{pmatrix} : \quad I_4 = 0.1 \quad \leftrightarrow \quad \left(\frac{\Lambda}{\sqrt{f}} \right)_4 = 138 \text{ GeV}. \tag{4.61}
 \end{aligned}$$

The large sensitivity to \mathcal{O}_{WW} comes from the large effect of this operator on the $h \rightarrow \gamma\gamma$ decay in addition to production effects, which will already be tightly constrained once a $t\bar{h}$ measurement is feasible. The orthogonal direction in the $\mathcal{O}_{\phi,2}\text{-}\mathcal{O}_{WW}$ plane is for all practical

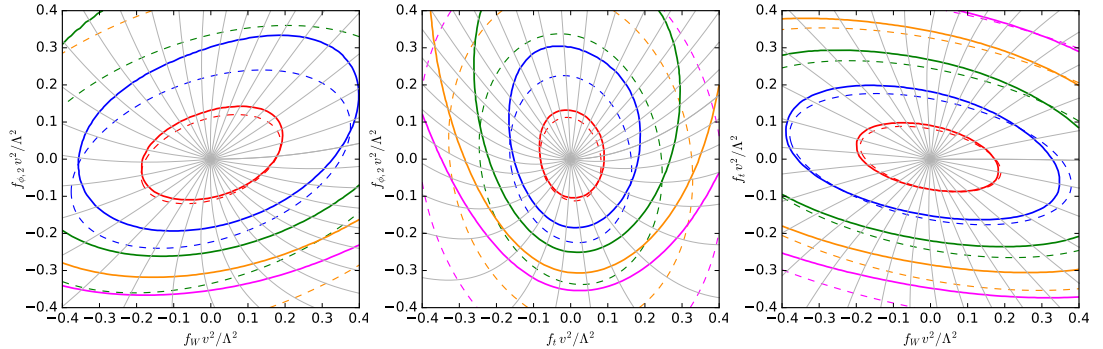


Figure 4.20: Error ellipses defined by the Fisher information in Higgs plus single top production. We show contours of local distance $d_{\text{local}}(\boldsymbol{\theta}; \mathbf{0})$ (dashed) and global distance $d(\boldsymbol{\theta}, \mathbf{0})$ (solid). The coloured contours indicate distances of $d = 1, 2, 3, 4, 5$. In grey we show example geodesics. The θ_i not shown are set to zero.

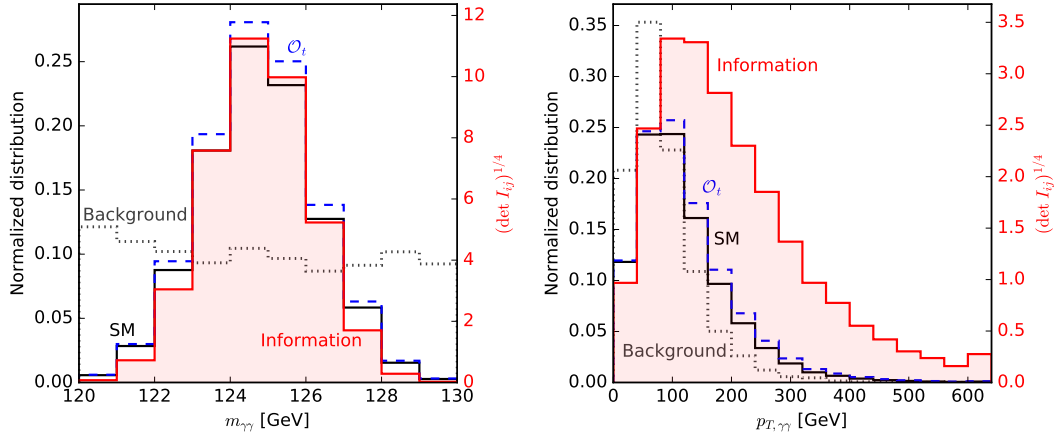


Figure 4.21: Distribution of the differential SM Fisher information in the Higgs plus single top channel (shaded red) with respect to the mass (left) and transverse momentum (right) of the diphoton system. We also show the normalised rates for the SM signal (solid black) and the single-top background (dotted grey). The dashed blue lines show the effect of $f_t v^2 / \Lambda^2 = 0.2$ on the \mathcal{O}_t signal. In the right panel, the last bin is an overflow bin.

purposes blind. Even with the large amount of integrated luminosity that this calculation is based on, the sensitivity to \mathcal{O}_W and \mathcal{O}_t is limited, with some mixing between the two operators.

Going beyond the local information geometry, we calculate global information distances in the model space and show them in Figure 4.19. These results confirm the small sensitivity of this process to all operators except \mathcal{O}_{WW} . Local and global distances are compared in Figure 4.20. Large differences are visible at the $d = 2$ level, implying that a measurement of this channel will always be sensitive to the squared dimension-six terms.

Differential information

In Figures 4.21 and 4.22 we show the distribution of this information over phase space. As expected, the discrimination power is concentrated in the $m_{\gamma\gamma} \sim m_H$ peak and in the high-energy tails of the transverse momenta of jets or photons. Studying angular correlations between the diphoton system and the top decay products, we find that the region $\Delta\eta_{\gamma\gamma,bjj} \lesssim 3$ contains a lot of information.

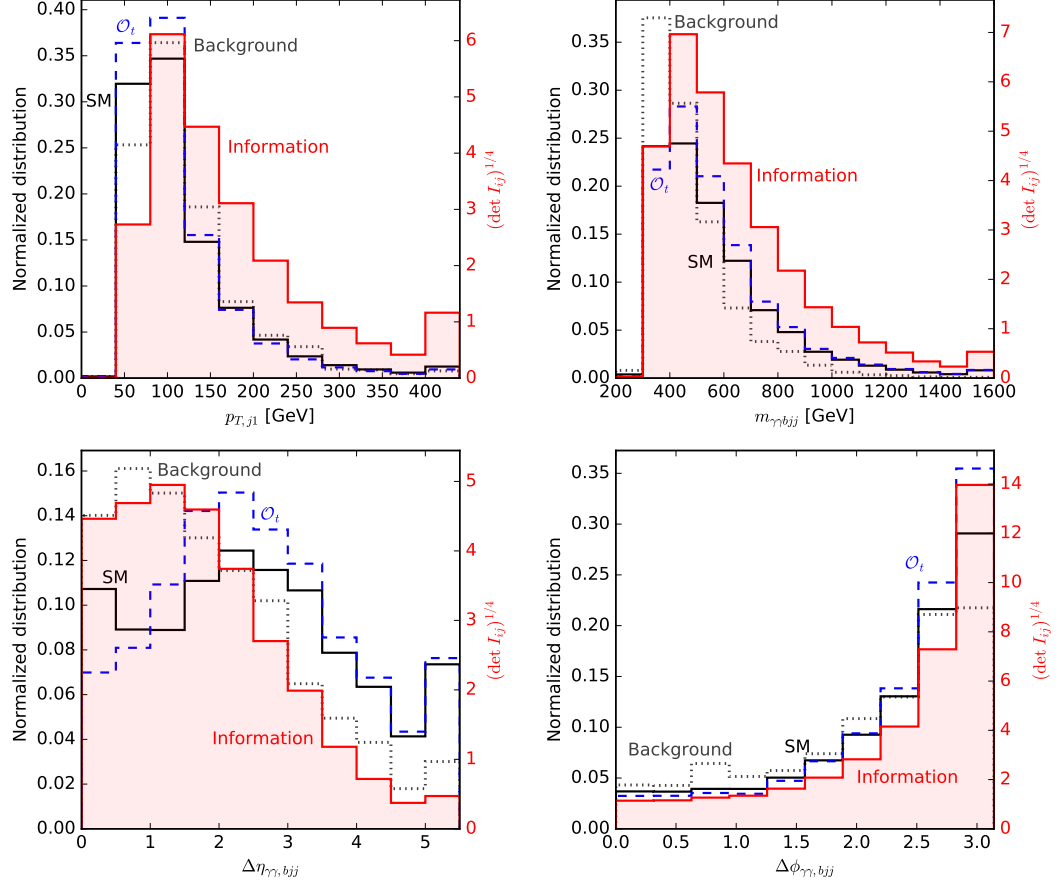


Figure 4.22: Distribution of the differential SM Fisher information in the Higgs plus single top channel (shaded red) with respect to the transverse momentum of the leading jet (top left), the invariant mass of the $t\bar{t}$ system (top right), and the differences in pseudorapidity and azimuthal angle between the diphoton system and the top decay products (bottom). We also show the normalised rates for the SM signal (solid black) and the single-top background (dotted grey). The dashed blue lines show the effect of $f_t v^2 / \Lambda^2 = 0.2$ on the $t\bar{t}$ signal. The last bins are overflow bins where applicable.

Information in distributions

The next question is again how much of this maximal information is contained in various kinematic distributions. A histogram-based analysis is only feasible with a reasonable signal-to-background ratio, so we require

$$p_{T,j_1} > 50 \text{ GeV}, \quad p_{T,\gamma} > 50, 30 \text{ GeV}, \quad \text{and} \quad 122 \text{ GeV} < m_{\gamma\gamma} < 128 \text{ GeV}. \quad (4.62)$$

This reduces the single-top background to the level of the signal. Based on this selection, we analyse the information in the following distributions:

- the transverse momentum of the leading photon, p_{T,γ_1} , with bin size 25 GeV up to 400 GeV and an overflow bin;
- the invariant mass of the diphoton system, $m_{\gamma\gamma}$, with bin size 1 GeV in the allowed range of 123 ... 127 GeV;
- the transverse momentum of the diphoton system, $p_{T,\gamma\gamma}$, with bin size 40 GeV up to 600 GeV and an overflow bin;
- the separation in azimuthal angle between the two photons, $\Delta\phi_{\gamma\gamma}$, with bin size $\pi/10$;
- the transverse momentum of the leading light (i. e. non- b) jet, p_{T,j_1} , with bin size 40 GeV up to 400 GeV and an overflow bin;
- the transverse momentum of the b jet, $p_{T,b}$, with bin size 40 GeV up to 400 GeV and an overflow bin;
- the transverse momentum of the reconstructed t momentum, $p_{T,bjj}$, with bin size 40 GeV up to 600 GeV and an overflow bin;
- the separation in azimuthal angle between the diphoton system and the b jet, $\Delta\phi_{\gamma\gamma,b}$, with bin size $\pi/10$;
- the separation in pseudorapidity between the diphoton system and the b jet, $\Delta\eta_{\gamma\gamma,b}$, with bin size 0.5 up to 5.0 and an overflow bin;
- the invariant mass of the full th system, $m_{\gamma\gamma bjj}$, with bin size 100 GeV up to 1500 GeV and an overflow bin;
- the transverse momentum of the full th system, $p_{T,\gamma\gamma bjj}$ with bin size 40 GeV up to 400 GeV and an overflow bin;
- the separation in azimuthal angle between the diphoton system and the reconstructed t momentum, $\Delta\phi_{\gamma\gamma,bjj}$, with bin size $\pi/10$; and
- the separation in pseudorapidity between the diphoton system and the reconstructed t momentum, $\Delta\eta_{\gamma\gamma,bjj}$, with bin size 0.5 up to 5.0 and an overflow bin.

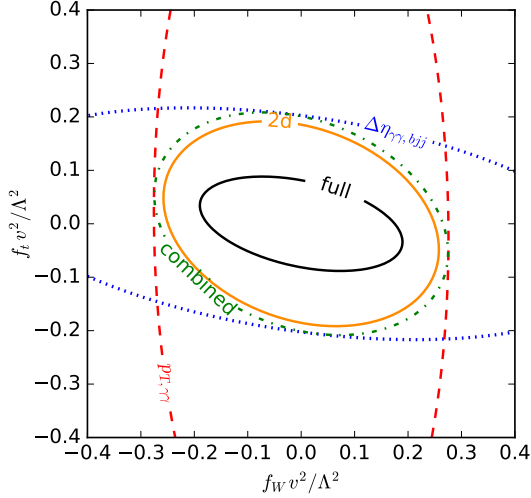


Figure 4.23: Information in distributions in the Higgs plus single top channel, shown as contours $d_{\text{local}}(\boldsymbol{\theta}; \mathbf{0}) = 1$. We show the total information in the full kinematics (black), the information in the distributions of $p_{T,\gamma\gamma}$ (red) and $\Delta\eta_{\gamma\gamma,bjj}$ (blue), their naive combination assuming no mutual information (green), and their two-dimensional histogram (yellow). The θ_i not shown are set to zero.

As in the WBF case, different observables probe different Wilson operators. In Figure 4.23 we demonstrate that the diphoton transverse momentum constrains mostly the \mathcal{O}_W direction, while the rapidity separation between the Higgs and top systems is more sensitive to \mathcal{O}_t .

In Figure 4.24 we compare the eigenvalues, eigenvectors, and determinants of the information matrices in all of the above distributions, in analogy to Figure 4.11. We confirm that the photon observables mostly probe changes in the Higgs-gauge coupling from \mathcal{O}_W , while a rescaled top Yukawa will be visible in the properties of the top decay products. Distributions of the properties of the b jet consistently contain significantly less information than the corresponding distributions for the reconstructed top system. The rapidity difference between the $\gamma\gamma$ system and the reconstructed top provides a particularly good probe of this operator. Combining this variable with the transverse momentum of the $\gamma\gamma$ system, we can probe new physics scales in the $\mathcal{O}_{\phi,2}\text{-}\mathcal{O}_W\text{-}\mathcal{O}_t$ space of around $\Lambda/\sqrt{f} \sim 550$ GeV, compared to 700 GeV based on the full high-dimensional kinematics. This corresponds to almost three times as much data. Of course, the histogram-based analysis would profit from an optimisation of the selection cuts in Equation (4.62), which goes beyond the scope of this demonstration.

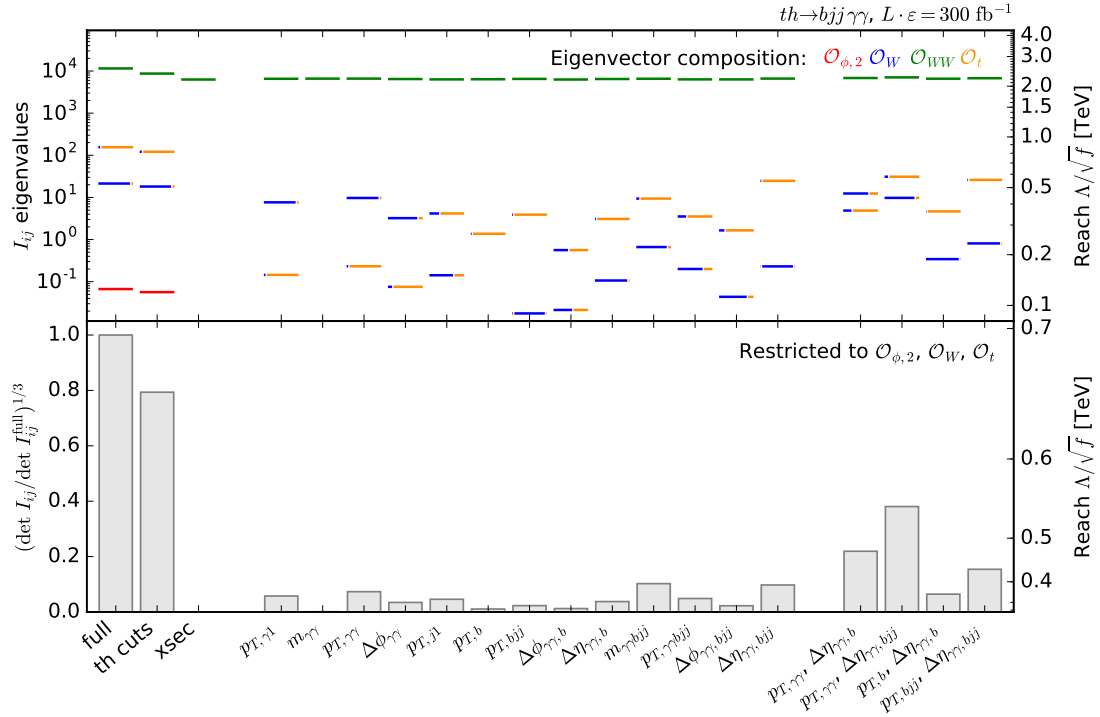


Figure 4.24: Fisher information in different distributions for the Higgs plus single top channel.

We compare the total Fisher information based on the full kinematics ('full'), the Fisher information after the cuts in Equation (4.62) ('th cuts'), the rate-only information after these cuts ('xsec'), and the information in several one-dimensional and two-dimensional distributions after this selection. The top panel shows the eigenvalues of these information matrices, the colours denote the composition of the corresponding eigenvectors. The right axis translates the eigenvalues into a new physics reach for the corresponding combination of Wilson coefficients. In the bottom panel we show the determinants of the three-dimensional Fisher information restricted to $\mathcal{O}_{\phi,2}$, \mathcal{O}_W , and \mathcal{O}_t , normalised to the full information. Again, the right axis translates them into a new physics reach.

4.5 Extensions

The applications of information geometry in the previous sections were based on a number of simplifying assumptions. Most importantly, we only considered statistical sources of uncertainty and neglected systematic and theory uncertainties on the signal and background predictions. In Section 4.5.1 we demonstrate how such effects change our results. Section 4.5.2 finally compares the Fisher information to two other statistical tools, the well-known log-likelihood ratio and the ambient information geometry.

4.5.1 Systematic uncertainties

The precision of most Higgs measurements at the LHC are ultimately limited by systematic and theory uncertainties [3, 74]. The expected differential signal and background cross sections are not exactly known, but depend on nuisance parameters ν . In Section 4.3.5 we showed how these can be incorporated in our approach, and defined a profiled Fisher information.

We now demonstrate this tool for the information on CP -even dimension-six operators in WBF Higgs production with $h \rightarrow \tau\tau$. Our setup is the same as in Section 4.4.1, except that we assign a 5% or 10% Gaussian uncertainty on the overall signal rate, representing for instance

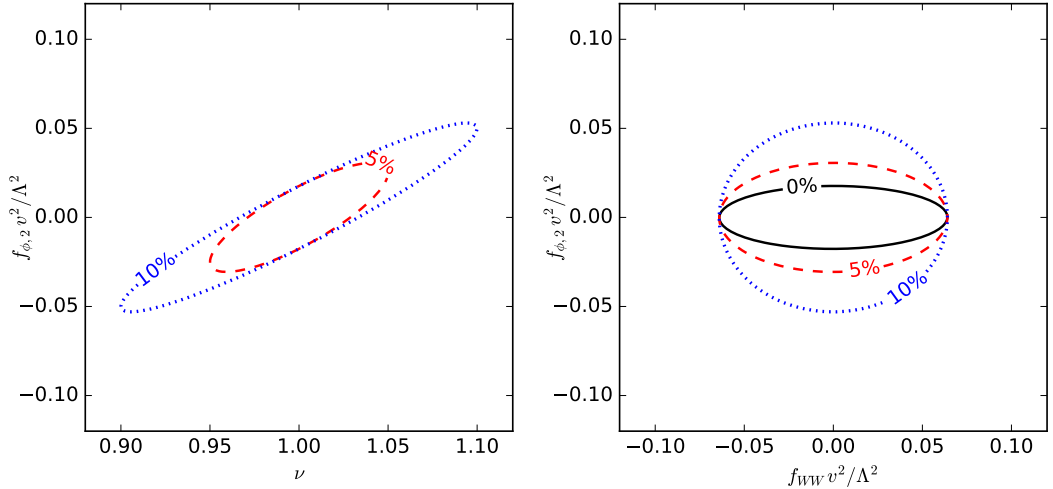


Figure 4.25: Error ellipses in the presence of nuisance parameters. We consider Gaussian uncertainties of 5% and 10% on the total signal rate in the WBF $h \rightarrow \tau\tau$ channel. Left: contour $d_{\text{local}}((\theta, \nu); (0, 1)) = 1$ in the plane spanned by a physical parameter θ and the nuisance parameter ν rescaling the signal rate. Right: contour $d_{\text{profiled}}(\theta; \mathbf{0}) = 1$ after profiling over this systematic uncertainty. The θ_i not shown are set to zero.

missing higher orders, parton density function uncertainties, or errors on the efficiencies. Figure 4.25 demonstrates how profiling over these nuisance parameters significantly reduces the information on $\mathcal{O}_{\phi,2}$, which only rescales the total signal rate. The other operators are mostly constrained from kinematic shapes and much less sensitive to such a systematic uncertainty on the overall normalisation.

In Figure 4.26 we show how the information in various distributions is affected by such a systematic error, in complete analogy to Figure 4.11. The new physics reach in the $\mathcal{O}_{\phi,2}$ direction is reduced by 800 GeV.

This treatment of systematic uncertainties on total rates can easily be extended to phase-space-dependent effects, for instance representing how the accuracy of the parton shower or the size of missing higher-order corrections depend on the energy scale. This requires parametrised smearing functions and an interpolation of the differential cross sections between different benchmark values of the nuisance parameters.

4.5.2 Comparison with other tools

Likelihood ratio

There is a certain ambiguity in what constitutes an optimal measurement. The aim of our approach is to minimise the covariance matrix of estimators, which the Cramér-Rao bound links to the Fisher information. Alternatively one can maximise the power of hypothesis tests at a given significance level. According to the Neyman-Pearson lemma, the best test statistic is the likelihood ratio between the two hypotheses. These two objects are designed for different questions: the likelihood ratio compares two discrete hypotheses, while the Fisher information describes continuous parameter spaces of arbitrary dimensionality. Nevertheless, it is instructive to compare these tools.

We consider the expected log likelihood ratio

$$q(\boldsymbol{\theta}_b; \boldsymbol{\theta}_a) \equiv -2 E \left[\log \frac{f(\mathbf{x}|\boldsymbol{\theta}_b)}{f(\mathbf{x}|\boldsymbol{\theta}_a)} \middle| \boldsymbol{\theta}_a \right]. \quad (4.63)$$

For the extended likelihood ansatz of Equation (4.20), a brief calculation gives the likelihood ratio as

$$\begin{aligned} q(\boldsymbol{\theta}_b; \boldsymbol{\theta}_a) = & -2 \sigma(\boldsymbol{\theta}_a) L \left(1 - \frac{\sigma(\boldsymbol{\theta}_b)}{\sigma(\boldsymbol{\theta}_a)} + \log \frac{\sigma(\boldsymbol{\theta}_b)}{\sigma(\boldsymbol{\theta}_a)} \right) \\ & - 2 \sigma(\boldsymbol{\theta}_a) L E \left[\log \frac{f^{(1)}(\mathbf{x}|\boldsymbol{\theta}_b)}{f^{(1)}(\mathbf{x}|\boldsymbol{\theta}_a)} \middle| \boldsymbol{\theta}_a \right]. \end{aligned} \quad (4.64)$$



Figure 4.26: Fisher information in different distributions in the WBF $h \rightarrow \tau\tau$ channel profiled over a 10% signal rate uncertainty. We compare the total Fisher information based on the full kinematics ('full'), the Fisher information after the cuts in Equation (4.51) ('WBF cuts'), the rate-only information after these cuts ('xsec'), and the information in several one-dimensional and two-dimensional distributions after this selection. The top panel shows the eigenvalues of these information matrices, the colours denote the composition of the corresponding eigenvectors. The right axis translates the eigenvalues into a new physics reach for the corresponding combination of Wilson coefficients. In the bottom panel we show the determinants of the three-dimensional Fisher information restricted to $\mathcal{O}_{\phi,2}$, \mathcal{O}_W , and \mathcal{O}_{WW} , normalised to the full information. Again, the right axis translates them into a new physics reach.

This can be calculated with Monte-Carlo integration as given in Equation (4.22), finally leading to

$$q(\boldsymbol{\theta}_b; \boldsymbol{\theta}_a) = -2 L \sum_{\text{events}} \Delta\sigma(\boldsymbol{\theta}_a) \log \frac{\Delta\sigma(\boldsymbol{\theta}_b)}{\Delta\sigma(\boldsymbol{\theta}_a)}. \quad (4.65)$$

With this result we can compare the log likelihood ratio to the distances defined by information geometry. For WBF Higgs production in the $\tau\tau$ mode as described in Section 4.4.1, we sample parameter points $\boldsymbol{\theta}$ in the \mathcal{O}_W - \mathcal{O}_{WW} plane. For each of these points we calculate the local and global distance from the SM point defined by the Fisher information, as well as the expected log likelihood ratio to the SM.

As shown in Figure 4.27, the local and especially the global distances are almost exactly equal to the square root of the expected likelihood ratio, with small differences only becoming visible around the 3σ level. This demonstrates that different statistical tools probe the same physics and can be chosen based on practical considerations. In particular, the conclusions from an information-based analysis, utilising the convenient properties of the Fisher information for high-dimensional theory spaces, also apply to exclusion limits based on the log likelihood ratio.

Ambient Fisher information

Information geometry, as introduced in Section 4.2, assigns a structure to the parameter space of a theory. It is, interestingly, also possible to define a distance measure in the space of **all** distributions, without relying on any model structure. One such approach is the **ambient Fisher information** [297, 298]. It defines the distance between two distributions $f_a(\mathbf{x})$ and $f_b(\mathbf{x})$ as

$$d_{\text{ambient}}(f_a, f_b) = \arccos \int d\mathbf{x} \sqrt{f_a(\mathbf{x}) f_b(\mathbf{x})}. \quad (4.66)$$

This measure does not require an integration along model parameters. As long as the distributions f_a and f_b are similar or the distances small, it approaches the usual global distance of information geometry [298]:

$$2 d_{\text{ambient}}(f(\mathbf{x}|\boldsymbol{\theta}_a), f(\mathbf{x}|\boldsymbol{\theta}_b)) \sim d(\boldsymbol{\theta}_a, \boldsymbol{\theta}_b). \quad (4.67)$$

For this reason, distances based on the ambient Fisher information have been suggested as a computationally less expensive approximation for information distances [298].

In Figure 4.28 we compare this tool to our global distance measure. Again, we use the WBF $h \rightarrow \tau\tau$ channel as described in Section 4.4.1 and sample parameter points in the \mathcal{O}_W - \mathcal{O}_{WW} plane. Equation (4.67) holds at distances up to $d \lesssim 2$, beyond which the two measures diverge, and the ambient distance is ultimately limited from above at $\pi/2$.



Figure 4.27: Comparison of the local (left) and global (right) distances defined by the Fisher information with the expected log likelihood ratio defined in Equation (4.65). We use WBF Higgs production in the $h \rightarrow \tau\tau$ channel and sample parameter points in the \mathcal{O}_W - \mathcal{O}_{WW} plane.

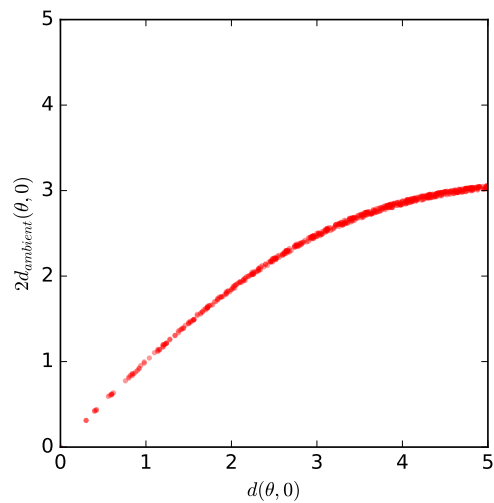


Figure 4.28: Comparison of the usual global distance defined by the Fisher information with the distance defined by the ambient Fisher information, see Equation (4.66). We use WBF Higgs production in the $h \rightarrow \tau\tau$ channel and sample parameter points in the \mathcal{O}_W - \mathcal{O}_{WW} plane.

4.6 Conclusions

Information geometry can be used to optimise measurements of any set of continuous theory parameters at the LHC. Following the Cramér-Rao bound, the Fisher information matrix defines the maximum precision with which model parameters can be estimated. This object is well-suited to high-dimensional parameter spaces since it requires no discretisation of the tested hypotheses, does not depend on arbitrary basis choices, and can simultaneously encode the maximum sensitivity to all directions in model space in a single matrix. These properties make information geometry particularly useful for the analysis of effective field theories. Moreover, the Fisher information is additive between different measurements and between different phase-space regions within the same process, making it trivial to discuss the combination of different channels. Understood as a metric on the theory space, it provides an intuitive geometric interpretation of discrimination power.

We developed an algorithm that can calculate the Fisher information in arbitrary high-energy physics processes based on Monte-Carlo simulations. We can calculate the total information based on the full high-dimensional phase space with all correlations. This defines the maximal precision with which the parameters can be probed; applied to effective field theories this gives us the maximal new physics reach of any process.

The Fisher information can also be calculated differentially to understand how the discriminating power is distributed over phase space, helping define optimal event selection. Alternatively, we can calculate the information in individual distributions of kinematic observables rather than the full high-dimensional kinematics. This defines the most powerful observables, and lets us compare the power of simple histogram-based analyses to methods based on the matrix elements or machine-learning techniques. All of these instruments can be useful to improve measurement strategies.

An interesting feature of the geometric interpretation is that the curvature of the Riemannian manifold defined by the Fisher information provides a handle on the square of dimension-six contributions. As discussed in Section 3.4.2, under certain assumptions this lets us analyse the convergence of the EFT expansion in $1/\Lambda$.

With these novel tools we analysed how well effective dimension-six operators can be measured in three different Higgs channels. First, we studied the kinematics of Higgs production in weak boson fusion with a decay into tau pairs. As expected, a large fraction of the constraining power in this process comes from few events with large momentum transfer. Care has to be taken with tight cuts on the rapidity separation of the tagging jets, which throw away a large amount of discrimination power. Different kinematic observables probe different directions in theory space: transverse momenta of the final-state particles, for instance the tagging jets, generally probe \mathcal{O}_W , while the only standard observable with a large sensitivity to \mathcal{O}_{WW} is the azimuthal angle between the tagging jets. To facilitate the most powerful and flexible interpretation of their

results, the experimental collaborations should ideally measure and publish the fully correlated two-dimensional histogram between these two quantities. Under idealised conditions, the analysis of such a two-dimensional histogram can probe new physics scales around 1.1 TeV in the \mathcal{O}_W - \mathcal{O}_{WW} - $\mathcal{O}_{\phi,2}$ space in the early phase of Run 2. Fully multivariate analyses have the potential to further enhance the sensitivity and probe new physics scales of up to 1.2 TeV.

Our next example process was Higgs production with a $h \rightarrow 4\ell$ decay, a very clean signature with rich kinematics. We used it to compare the sensitivity to dimension-six physics in the decay and production vertices within the same process. Our results are unambiguous: the decay kinematics is much less sensitive to momentum-dependent operators than the production-side probes provided by the tagging jets. This reflects the E^2/Λ^2 dependency of such dimension-six effects, which can be large in the production vertex, while the momentum flow through the decay vertex is limited to the Higgs mass.

Higgs production in association with a single top has an interesting amplitude structure where diagrams with Higgs-gauge interactions interfere destructively with diagrams depending on the top Yukawa coupling. Small changes to these interactions can in principle change the total production rate and the kinematics drastically. We showed that kinematic properties of the Higgs decay products and observables related to the top system provide orthogonal information on the theory space; in particular the diphoton transverse momentum as well as the rapidity separation of the $\gamma\gamma$ and the bjj system provide useful information. Unfortunately, the tiny cross section of this process strongly limits the constraining power on dimension-six operators. Even with HL-LHC data and under idealised conditions, these distributions are only sensitive to new physics scales around 550 GeV, while an optimal multivariate analysis may be able to probe scales up to 700 GeV according to the Cramér-Rao bound.

These initial studies do not include systematic and theory uncertainties, and detector effects are taken into account only with rudimentary smearing functions. Our results for the maximum precision are therefore optimistic. We showed how our approach can be extended to include systematic effects, and introduced a profiling procedure for the Fisher information. These tools define many directions for future research. First, the Higgs signatures discussed here can be re-examined with a proper treatment of shower and detector effects as well as systematic and theory uncertainties. Second, we can analyse the detection of CP violation in the Higgs sector. Using the profiling procedure for the Fisher information, we can pay particular attention to the question which signatures of CP violation are genuine, i. e. cannot be caused by any CP -conserving new physics. Finally, while we focused on Higgs physics in terms of effective field theories in this thesis, these tools can be applied to any other measurement of continuous parameters in perturbative LHC processes.

Chapter 5

Conclusions

MEASURING THE PROPERTIES of the Higgs boson is one of the most important missions for Run 2 of the LHC and may help us understand some of the open questions of fundamental physics. The efficient combination of different experimental channels and their interpretation in the many theories of physics beyond the Standard Model benefit from a universal parametrisation of these properties. The dimension-six operators of linear Higgs effective field theory provide such a framework that is theoretically well-motivated, largely independent of model assumptions, and phenomenologically powerful.

In this thesis we discussed two aspects of this approach, both of immediate practical relevance: we analysed whether these effective operators accurately capture the relevant signatures of specific scenarios of new physics, and we developed statistical tools that can help to design efficient measurements of the Higgs properties.

In the first part we argued that the validity of the dimension-six model for LHC Higgs physics is not at all obvious. The effective field theory approach is based on the assumption that the typical mass scale of new physics is significantly larger than the experimentally probed energy scale. But the limited precision of Higgs measurements at the LHC cannot guarantee such a scale separation: signatures of weakly coupled new physics can only have a relevant size if the new physics scale is close to the electroweak scale, and the effective theory may not be valid in general.

We studied whether the dimension-six model is nevertheless useful for Higgs signatures by comparing the phenomenology of different scenarios of physics beyond the Standard Model to the corresponding effective theories. For extended Higgs sectors with an additional scalar singlet or doublet, scalar top partners, and heavy vector bosons, we analysed total rates and kinematic distributions in the most important Higgs production and decay channels.

Our results show that the agreement between the full models and their dimension-six approx-

imations crucially depends on the matching procedure, i. e. the construction of the effective theory from a full model. Standard procedures for the matching, defined in the unbroken phase of the electroweak symmetry, lead to large errors of the effective field theory description already for total rates, which only deteriorate in kinematic distributions.

This does not mean, though, that the dimension-six model is not useful for Higgs physics. We introduced v -improved matching, a procedure that improves the performance of the dimension-six model by resumming certain terms that arise during electroweak symmetry breaking. While formally of subleading order in the EFT expansion, these effects can be large under LHC conditions. With such a matching, the dimension-six model provides a good description even in many scenarios where the EFT validity is not self-evident, and typically only breaks down at new resonances or in the far high-energy tails of certain distributions.

In addition, we discussed the role of squared amplitudes from dimension-six operators. Even though they appear at the same order in the EFT expansion as the leading effects from the neglected dimension-eight operators, we argued that it is often preferable to include them in calculations. In a detailed study of Higgs production in weak boson fusion, we finally showed that the transverse momenta of the tagging jets provide the best measure of the unobservable momentum transfer.

Our research was motivated by the question which parametrisation of Higgs properties to use during Run 2 of the LHC. With these results we conclude that despite the unclear scale separation, the dimension-six operators of linear Higgs effective field theory capture a wide range of new physics signatures accurately. Subtleties in the matching procedure are not a problem for an experimental fit of dimension-six operators at the LHC, but have to be taken into account when interpreting the results in specific models.

Having established that Higgs EFT works well as a largely model-independent language for Higgs physics at the LHC, we turned to the question of how its parameters can be measured most efficiently. The high-dimensional theory space defined by the Higgs properties and the intricate kinematics of some Higgs channels present challenges for traditional analysis methods based on cuts and kinematic distributions, while modern multivariate methods can be non-transparent and difficult to reproduce.

We showed that information geometry allows us to understand the information contained in LHC signatures and can help optimise measurement strategies. This formalism is based on the Fisher information matrix, which according to the Cramér-Rao bound quantifies the maximal precision with which continuous model parameters can be measured in an experiment. It can be interpreted geometrically, and its properties are well-suited to high-dimensional parameter spaces such as that of Higgs effective field theory.

We developed a novel algorithm to calculate the Fisher information in LHC processes, taking into account the full kinematics including all correlations. In addition to the total Fisher information, we also showed how to calculate the distribution of the differential information over phase

space, and the information in individual kinematic distributions. These tools define the important phase-space regions and observables for an analysis and let us compare the discrimination power of traditional histogram-based analyses to that of modern multivariate ones.

Applying these techniques to Higgs production in weak boson fusion with decays into tau pairs or four leptons, we demonstrated that the kinematics of the tagging jets is significantly more sensitive to new physics in the form of dimension-six operators than observables that characterise the Higgs decay. The transverse momenta of these jets and their angular correlations are particularly powerful observables. Still, a multivariate analysis with matrix-element-based methods or machine-learning tools can potentially extract significantly more information. Finally, we analysed the structure of Higgs production with a single top. Higgs decay products and angular distributions between the Higgs and top daughters are sensitive to different operators, but overall the sensitivity of this process to dimension-six physics is limited.

While there is no shortage of statistical tools in the field, these new methods can help to plan and optimise measurements of high-dimensional, continuous parameter spaces in an intuitive way. We demonstrated this approach in different Higgs channels for dimension-six operators, showing how it aids efficient measurements of the Higgs properties and thus contributes to the second major question raised in the introduction. Our tools can easily be translated to other processes and models.

To summarise, effective dimension-six operators provide a powerful framework to measure and understand the properties of the Higgs boson. We analysed the validity of this approach at the LHC and showed how it can be improved with a suitable matching procedure. In a next step, we developed statistical tools based on information geometry to guide the design of efficient measurements. These new ideas can contribute to a better understanding of the nature of the Higgs boson, which may ultimately point us to what lies beyond the Standard Model.

Acknowledgements

For the three fun years my PhD turned out to be, I first want to thank my advisor Tilman Plehn: for taking me on as a student, for working with me on interesting physics, and for disagreeing with me on countless questions over coffee. But most of all, I am sincerely grateful to him for always having my back. This includes him coming into the office on a Sunday morning to get me a backup laptop when mine broke down days before a deadline.

I would like to thank Björn Malte Schäfer for reading and refereeing this thesis, and Monica Dunford and Peter Bachert for completing my examination committee.

The Research Training Group ‘Particle physics at the LHC’ (DFG GRK 1940) paid my salary and, together with the Heidelberg Graduate School of Fundamental Physics, my travels. I am grateful for their support.

I had the great pleasure to collaborate with a number of extraordinary scientists. Ayres Freitas and David López-Val saw me off to a great start and taught me a lot. Anke Biekötter joined us a little later, giving fresh impetus to our research. Chasing the diboson ambulance with JoAnne Hewett, Joachim Kopp, Tom Rizzo, and Jamie Tattersall was a wild and fun ride. But one of the best ideas during my PhD was to grab a beer with Kyle Cranmer in Café Botanik. Working with him was inspiring, and was even more fun once Felix Kling joined our team.

The work presented in this thesis benefited greatly from discussions with others. In particular I would like to express my gratitude to Anja Butter for keeping me on track with sharp questions, Juan González Fraile for teaching me one thing or two about effective field theories, Torben Schell for being an unwavering source of physics knowledge as well as a saviour in the hour of incomprehensible linker errors, and Peter Schichtel for helping me set up MadMax.

From Marstall lunches to Pheno ‘class trips’, with nut cakes, PhD hats, and the eternal coffee list, I thoroughly enjoyed being part of the Heidelberg pheno group. I would like to thank Martin Bauer, Elias Bernreuther, Anke Biekötter, Katja Böhnke, Anja Butter, Daniel Camargo, Nishita Desai, Karin Firnkes, Josua Göcking, Juan González Fraile, Jamil Hetzel, Sebastian Hoof, Jan Horak, Thomas Hugle, Jörg Jäckel, Martin Jankowiak, Florian Jetter, Martin Klassen, Lara Kuhn, Rabea Link, Viraf Mehta, Luminita Mihaila, Rhea Moutafis, Tilman Plehn, Peter Reimitz,

Acknowledgements

Michael Russel, Torben Schell, Sebastian Schenk, Peter Schichtel, Linda Shen, Beatriz Tapia Oregui, Jamie Tattersall, Valentin Tenorth, Jennifer Thompson, Susanne Westhoff, and Nikolai Zerf. I am grateful to Anke Biekötter, Patrick Foldenauer, and Sebastian Schenk for wine and cheese. Most of all, I would like to thank Anja Butter and Torben Schell, who shared nearly the entire PhD journey with me. Without the two, these three years would not have been half as much fun.

Further away from the Philosophenweg, I would like to thank the friends whose company I enjoyed during the last years, and in particular give a shout out to the Dossenheim gang — Marcel Gutsche, Clemens Hassel, and Julia Velte — and to Christina Eilers. I want to thank Astrid Hiller Blin for jump-starting many of my days over coffee and arXiv, and for unfailingly cheering me up (and on). A big thank you goes to my marvellous parents Antje and Andreas Brehmer. And then there is Merle Reinhart, who I cannot thank enough and who in just about any circumstances makes life better.

If this thesis is legible, it is largely due to the trustworthy proof readers. I am grateful to Martin Bauer, Anke Biekötter, Anja Butter, Patrick Foldenauer, Juan González Fraile, Eric Miller, and Sebastian Schenk. In particular, I am indebted to Astrid Hiller Blin, Antje Brehmer, and Merle Reinhart, who were crazy enough to read the whole thing front to back.

Appendices

For completeness and reproducibility, we here collect our conventions, some technical details, and additional examples. We begin in Appendix A.1 with our conventions for the Standard Model. Appendix A.2 defines standard kinematic quantities and units. Section A.3 provides explicit examples for the manipulation of effective Lagrangians with field redefinitions and for matching with functional methods. In Appendix A.4 we define an alternative basis for dimension-six operators and link it to the HISZ basis used in this thesis. Appendix A.5 contains some additional details on the models considered in Chapter 3. Finally, in Appendix A.6 we collect some auxiliary results related to Chapter 4.

Large parts of this appendix have been published previously, as part of the same articles that contained much of the main body of this thesis. In particular, Appendices A.4 and A.5 were part of References [1, 2], while Appendix A.6 contains material published in Reference [4].

A.1 Standard model conventions

We begin with our conventions for the Standard Model, which also apply to all models of new physics. The Standard Model is a renormalisable and local quantum field theory. It is invariant under global proper orthochronous Poincaré transformations (which include translations, rotations, and boosts), and a local $SU(3)_C \times SU(2)_L \times U(1)_Y$ gauge group. Its Lagrangian is given by

$$\begin{aligned} \mathcal{L}_{\text{SM}} = & -\frac{1}{4}G_{\mu\nu}^a G^{a\mu\nu} - \frac{1}{4}W_{\mu\nu}^a W^{a\mu\nu} - \frac{1}{4}B_{\mu\nu} B^{\mu\nu} + \frac{\theta_{QCD}}{32\pi^2} G_{\mu\nu}^a \tilde{G}^{a\mu\nu} + \sum_f \bar{f} i \not{D} f \\ & + (D_\mu \phi)^\dagger (D^\mu \phi) - \mu^2 \phi^\dagger \phi - \lambda (\phi^\dagger \phi)^2 \\ & - \sum_{\text{generations}} \left(y_u \left(\frac{\bar{u}}{d} \right)_L \tilde{\phi} u_R + y_d \left(\frac{\bar{u}}{d} \right)_L \phi d_R + y_\ell \left(\frac{\bar{\nu}}{\ell} \right)_L \phi \ell_R + \text{h. c.} \right). \end{aligned} \quad (\text{A.1})$$

Appendices

Fermions	Representation		
	$SU(3)_C$	$SU(2)_L$	$U(1)_Y$
LH quarks	$\begin{pmatrix} u \\ d \end{pmatrix}_L$	$\begin{pmatrix} c \\ s \end{pmatrix}_L$	$\begin{pmatrix} t \\ b \end{pmatrix}_L$
RH up-type quarks	u_R	c_R	t_R
RH down-type quarks	d_R	s_R	b_R
LH leptons	$\begin{pmatrix} \nu_e \\ e^- \end{pmatrix}_L$	$\begin{pmatrix} \nu_\mu \\ \mu^- \end{pmatrix}_L$	$\begin{pmatrix} \nu_\tau \\ \tau^- \end{pmatrix}_L$
RH leptons	e_R^-	μ_R^-	τ_R^-

Table A.1: SM fermions and their charges under the SM gauge group.

As civilised high-energy physicists, we use natural units with

$$\hbar = c = 1 , \quad (\text{A.2})$$

sum over repeated indices, and use the Minkowski metric

$$g_{\mu\nu} = \text{diag}(1, -1, -1, -1) . \quad (\text{A.3})$$

The fields in this Lagrangian are a scalar ϕ transforming as the $(\mathbf{1}, \mathbf{2}, 1/2)$ representation of the SM gauge group; the gauge bosons G_μ^a , W_μ^a , and B_μ ; and the fermions given in Table A.1. We usually leave out generation (flavour) indices and simply denote up-type quarks, down-type quarks, charged leptons, and neutrinos with u , d , ℓ , ν , respectively, and the doublets of left-handed quarks and leptons with Q and L . Equation (A.1) includes the field strength tensors

$$G_{\mu\nu}^a = \partial_\mu G_\nu^a - \partial_\nu G_\mu^a + g_s f^{abc} G_\mu^b G_\nu^c , \quad (\text{A.4})$$

$$W_{\mu\nu}^a = \partial_\mu W_\nu^a - \partial_\nu W_\mu^a + g \epsilon^{abc} W_\mu^b W_\nu^c , \quad (\text{A.5})$$

$$B_{\mu\nu} = \partial_\mu B_\nu - \partial_\nu B_\mu \quad (\text{A.6})$$

and the dual field strength tensor

$$\tilde{G}_{\mu\nu}^a = \frac{1}{2} \epsilon_{\mu\nu\rho\sigma} G^{a\mu\nu} \quad (\text{A.7})$$

with the totally antisymmetric tensor $\epsilon_{\mu\nu\rho\sigma}$. The covariant derivatives are defined according to

the gauge charges and with a conventional minus sign in front of the gauge term, for instance

$$D_\mu \phi = \left(\partial_\mu - i g \frac{\sigma^a}{2} W_\mu^a - i g' \frac{1}{2} B_\mu \right) \phi, \\ D_\mu \begin{pmatrix} u \\ d \end{pmatrix}_L = \left(\partial_\mu - i g_s \frac{\lambda^a}{2} G_\mu^a - i g \frac{\sigma^a}{2} W_\mu^a - i g' \frac{1}{6} B_\mu \right) \begin{pmatrix} u \\ d \end{pmatrix}_L. \quad (\text{A.8})$$

These expressions contain the structure constants f^{abc} and ϵ^{abc} of $SU(3)$ and $SU(2)$, as well as the Pauli matrices σ^a and the Gell-Mann matrices λ^a .

The Standard Model has 19 free parameters. In the form of Equation (A.1), they are:

- the coupling constants corresponding to the three components of its gauge group, g_s , g , and g' ;
- the real parameter θ_{QCD} ;
- the two real parameters μ^2 and λ of the Higgs potential; and
- the Yukawa couplings y_f . These are unitary, complex-valued matrices in flavour space, and their components correspond to 13 physical parameters.

For $\mu^2 < 0$, the potential for ϕ has a minimum at the non-zero vacuum expectation value (VEV)

$$v^2 \equiv 2 |\langle \phi \rangle|^2 = -\frac{\mu^2}{\lambda}. \quad (\text{A.9})$$

Using some of the gauge freedom, we can choose that the vacuum expectation value of ϕ points into the lower component of the doublet. Expanding the four physical degrees of freedom w^a and h around this minimum, we have

$$\phi = \frac{1}{\sqrt{2}} \begin{pmatrix} -w^2 - i w^1 \\ v + h + i w^3 \end{pmatrix}. \quad (\text{A.10})$$

Plugging this into Equation (A.1), and diagonalising the mass matrices, one sees that the gauge bosons W^a and B combine with the Goldstone bosons w^a to the mass eigenstates

$$W_\mu^\pm = \frac{1}{\sqrt{2}} \left(\left(W_\mu^1 - \frac{1}{gv} \partial_\mu w^1 \right) \pm i \left(W_\mu^2 - \frac{1}{gv} \partial_\mu w^2 \right) \right), \quad (\text{A.11})$$

$$Z_\mu = c_W \left(W_\mu^3 - \frac{1}{gv} \partial_\mu w^3 \right) - s_W B_\mu, \quad (\text{A.12})$$

$$A_\mu = s_W W_\mu^3 + c_W B_\mu \quad (\text{A.13})$$

with weak mixing angle (or Weinberg angle)

$$c_W \equiv \cos \theta_W = \frac{g}{\sqrt{g^2 + g'^2}}, \quad s_W \equiv \sin \theta_W = \frac{g'}{\sqrt{g^2 + g'^2}} \quad (\text{A.14})$$

Appendices

and masses

$$m_W = \frac{gv}{2} \quad \text{and} \quad m_Z = \frac{gv}{2c_W}. \quad (\text{A.15})$$

The remaining degree of freedom from ϕ is the physical Higgs boson h with a mass

$$m_h^2 = -2\mu^2 = 2\lambda v^2. \quad (\text{A.16})$$

Inserting Equation (2.5) into the Yukawa couplings also yields fermion masses

$$m_f = \frac{y_f v}{\sqrt{2}}. \quad (\text{A.17})$$

Since the Yukawa couplings are not flavour-diagonal, these mass matrices have to be diagonalised in flavour space, ultimately leading to the CKM matrix. But this does not affect the Higgs couplings, and in this thesis we can safely assume flavour-diagonal Yukawa couplings.

With respect to the remaining gauge group $U(1)_Q$ with the gauge boson A_μ and the gauge coupling

$$e = \frac{gg'}{\sqrt{g^2 + g'^2}} = gs_W = g'c_W, \quad (\text{A.18})$$

the fermions carry the electromagnetic charge

$$q = y + \frac{\sigma_3}{2}, \quad (\text{A.19})$$

where the second term is shorthand for its eigenvalue in the case of $SU(2)_L$ doublets and zero for the singlets. More important for this thesis, the terms that lead to mass terms for the weak gauge bosons and fermions also yield couplings between the Higgs boson and these particles. Expressed in terms of the masses, these couplings read

$$g_{hff} = -\frac{m_f}{v} \quad (\text{A.20})$$

for the fermions and

$$g_{hW^+W^-} = \frac{2m_W^2}{v}, \quad g_{hZZ} = \frac{m_Z^2}{v} \quad (\text{A.21})$$

for the vector bosons.

A.2 Phenomenology glossary

Most of this thesis discusses interactions in proton-proton collisions at the LHC. Here we define kinematical quantities and units commonly used to describe such processes.

With the metric in Equation (A.3), the norm of any four-momentum p_μ is the invariant mass

$$p^2 = E^2 - \mathbf{p}^2 \quad (\text{A.22})$$

with energy $E = p_0$ and three-momentum \mathbf{p} . We use the symbol m for invariant masses of systems of two or more particles, for instance $m_{ij}^2 \equiv (p_i + p_j)^2$. For a single particle i , m_i instead denotes the mass parameter, and $p_i^2 = m_i^2$ only for on-shell particles.

We use a standard coordinate system where the component p_3 (also called longitudinal momentum p_L) points into the direction of the proton beam. The other two spatial components make up the transverse momentum \mathbf{p}_T . Often we use its magnitude

$$p_T \equiv \sqrt{p_x^2 + p_y^2}. \quad (\text{A.23})$$

The missing transverse momentum or missing transverse energy is given by

$$\mathbf{p}_T^{\text{miss}} \equiv - \sum_{\text{visible}} \mathbf{p}_T, \quad E_T^{\text{miss}} \equiv |\mathbf{p}_T^{\text{miss}}|, \quad (\text{A.24})$$

where the sum goes over all particles that can be experimentally detected.

The particle direction is usually characterised in a spherical coordinate system: ϕ is the azimuthal angle in the transverse plane and θ the polar angle between the spatial momentum and the beam axis. The latter is conventionally expressed in the pseudo-rapidity

$$\eta \equiv -\log\left(\tan\frac{\theta}{2}\right), \quad (\text{A.25})$$

such that $\eta \rightarrow \pm\infty$ corresponds to the beam directions and $\eta = 0$ to the orthogonal plane. Small values $|\eta| \lesssim 2.5$ correspond to the central regions of typical general-purpose particle detectors such as ATLAS and CMS, larger values $2.5 \lesssim |\eta| \lesssim 5$ to the ‘forward regions’. We often analyse angular correlations between particles, in particular the difference in pseudorapidity $\Delta\eta_{ij} \equiv |\eta_i - \eta_j|$ and the difference in azimuthal angle $\Delta\phi_{ij} \equiv |\phi_i - \phi_j|$.

Energies, momenta, and masses are expressed in GeV or TeV, with

$$1 \text{ GeV} = 1.60 \cdot 10^{-10} \text{ J} = 1.78 \cdot 10^{-27} \text{ kg} = 5.34 \cdot 10^{-19} \text{ kg m/s}. \quad (\text{A.26})$$

Cross sections are given in fb or pb, integrated luminosities in fb^{-1} , where

$$1 \text{ fb} = 10^{-43} \text{ m}^2 = 2.57 \cdot 10^{-12} \text{ GeV}^{-2}. \quad (\text{A.27})$$

A.3 EFT fundamentals

A.3.1 Nonlinear field redefinitions

In Section 2.2.2 we stated that non-linear field redefinitions of the form given in Equation (2.12) leave the S -matrix elements and thus all observable physics invariant, but change the form of the Lagrangian. According to Equation (2.13), the leading term of the change of the Lagrangian is given by the classical equations of motion. This defines an equivalence relation between some operators that can be used to remove redundant operators and define a minimal basis, as discussed in Section 2.3.2 for the Higgs EFT.

Here we illustrate this procedure by explicitly calculating the effect of such a non-linear field redefinition without truncating the Lagrangian at the leading order in the transformation parameter. We start with the CP -even $B\phi$ sector of the SM effective field theory, and add effective operators up to mass dimension six. Ordering the terms by mass dimension, it reads

$$\begin{aligned} \mathcal{L}_{\text{before}} = & -\mu^2 \phi^\dagger \phi \\ & - \frac{1}{4} B_{\mu\nu} B^{\mu\nu} + (D_\mu \phi)^\dagger (D^\mu \phi) - \lambda (\phi^\dagger \phi)^2 \\ & + \frac{f_{\phi,1}}{\Lambda^2} (D_\mu \phi)^\dagger \phi \phi^\dagger D^\mu \phi + \frac{f_{\phi,2}}{\Lambda^2} \frac{1}{2} \partial_\mu (\phi^\dagger \phi) \partial^\mu (\phi^\dagger \phi) + \frac{f_{\phi,3}}{\Lambda^2} \frac{1}{3} (\phi^\dagger \phi)^3 \\ & + \frac{f_{\phi,4}}{\Lambda^2} (\phi^\dagger \phi) (D_\mu \phi)^\dagger D^\mu \phi + \frac{f_B}{\Lambda^2} \frac{i g'}{2} (D^\mu \phi)^\dagger D^\nu \phi B_{\mu\nu} - \frac{f_{BB}}{\Lambda^2} \frac{g'^2}{4} (\phi^\dagger \phi) B_{\mu\nu} B^{\mu\nu} \\ & + \mathcal{O}(1/\Lambda^4). \end{aligned} \quad (\text{A.28})$$

The simplest non-linear field transformation is

$$\phi \rightarrow \phi + \frac{\varepsilon}{\Lambda^2} (\phi^\dagger \phi) \phi. \quad (\text{A.29})$$

It transforms this Lagrangian into

$$\mathcal{L}_{\text{after}} = \mathcal{L}_{\text{before}} + \delta \mathcal{L}_4 + \delta \mathcal{L}_6 + \delta \mathcal{L}_8 + \delta \mathcal{L}_{\geq 10} \quad (\text{A.30})$$

where the indices denote the mass dimension of the operators. The SM dimension-two term generates

$$\delta \mathcal{L}_4 = -2\mu^2 \frac{\varepsilon}{\Lambda^2} (\phi^\dagger \phi)^2. \quad (\text{A.31})$$

At the dimension-six level, we have

$$\delta \mathcal{L}_6 = \frac{\varepsilon}{\Lambda^2} [\partial_\mu (\phi^\dagger \phi) \partial^\mu (\phi^\dagger \phi) - 4\lambda (\phi^\dagger \phi)^3 + 2 (\phi^\dagger \phi) (D_\mu \phi)^\dagger D^\mu \phi] - \mu^2 \frac{\varepsilon^2}{\Lambda^4} (\phi^\dagger \phi)^3. \quad (\text{A.32})$$

The effects at dimension eight read

$$\begin{aligned}
\delta\mathcal{L}_8 = & \frac{\varepsilon}{\Lambda^4} \left[\frac{ig'f_B}{2} \partial_\mu(\phi^\dagger\phi) (\phi^\dagger \overleftrightarrow{D}_\nu\phi) B^{\mu\nu} + f_{\phi,4} (\phi^\dagger\phi) \partial_\mu(\phi^\dagger\phi) \partial^\mu(\phi^\dagger\phi) \right. \\
& + ig'f_B (\phi^\dagger\phi) (D_\mu\phi)^\dagger D_\nu\phi B^{\mu\nu} + 4f_{\phi,1} \phi^\dagger\phi (D_\mu\phi)^\dagger\phi \phi^\dagger D^\mu\phi \\
& + f_{\phi,1} \phi^\dagger\phi \partial_\mu(\phi^\dagger\phi) \partial^\mu(\phi^\dagger\phi) + 4f_{\phi,4} (\phi^\dagger\phi)^2 (D_\mu\phi)^\dagger D^\mu\phi \\
& \left. - \frac{1}{2} g'^2 f_{BB} (\phi^\dagger\phi)^2 B_{\mu\nu} B^{\mu\nu} + 2f_{\phi,3} (\phi^\dagger\phi)^4 \right] \\
& + \frac{\varepsilon^2}{\Lambda^4} \left[+2 \phi^\dagger\phi \partial_\mu(\phi^\dagger\phi) \partial^\mu(\phi^\dagger\phi) - 6\lambda (\phi^\dagger\phi)^4 + (\phi^\dagger\phi)^2 (D_\mu\phi)^\dagger D^\mu\phi \right], \quad (\text{A.33})
\end{aligned}$$

and so on for higher mass dimensions.

Setting the $\mathcal{O}(\varepsilon)$ terms in Equations (A.31) to (A.33) to zero corresponds exactly to the classical equations of motion for ϕ , as discussed in Section 2.2.2 and applied to the SM EFT in Equation (2.42). The higher orders in ε are missing in the equations of motion, but their inclusion does not affect our choice of redundant operators.

Similarly, a transformation

$$B_\mu \rightarrow B_\mu + \frac{\varepsilon}{\Lambda^2} \phi^\dagger\phi B_\mu \quad (\text{A.34})$$

corresponds to the classical equations of motion for B_μ plus $\mathcal{O}(\varepsilon^2)$ corrections.

A.3.2 Functional matching

In 2.2.3 we discussed the effective theory in a top-down approach, finally arriving at the expression for the effective action at one-loop level given in Equation (2.27).

We now show a simple example of how this object can be calculated with functional methods. We closely follow Reference [140], which contains a more detailed explanation of all symbols and methods. Our toy theory consists of two real scalar fields. The light field ϕ has mass m , the heavy field Φ with mass M is being integrated out. The underlying theory is given by

$$\begin{aligned}
S[\phi, \Phi] = & \int d^4x \left[\frac{1}{2} \partial_\mu\phi \partial^\mu\phi - \frac{m^2}{2} \phi^2 + \frac{1}{2} \partial_\mu\Phi \partial^\mu\Phi - \frac{M^2}{2} \Phi^2 \right. \\
& \left. - \frac{\lambda_0}{4!} \phi^4 - \frac{\lambda_2}{4} \phi^2 \Phi^2 - \frac{\lambda_4}{4!} \Phi^4 \right]. \quad (\text{A.35})
\end{aligned}$$

Odd interactions and a mixing term $\phi\Phi$ are forbidden with suitable \mathbb{Z}_2 symmetries.

The classical equation of motion for Φ is

$$\left(\partial^2 + M^2 + \frac{\lambda_2}{2}\phi^2 + \frac{\lambda_4}{3!}\Phi_c^2\right)\Phi_c = 0 \quad (\text{A.36})$$

with the trivial solution $\Phi_c = 0$.

The first term of the effective action in Equation (2.27) then just gives back ϕ^4 theory for the light field, without any new effective interactions:

$$S[\phi, \Phi_c] = \int d^4x \left[\frac{1}{2} \partial_\mu \phi \partial^\mu \phi - \frac{m^2}{2} \phi^2 - \frac{\lambda_0}{4!} \phi^4 \right]. \quad (\text{A.37})$$

The second term is

$$\begin{aligned} \frac{i}{2} \text{tr} \log \left(-\frac{\delta^2 S}{\delta \Phi^2} \Big|_{\Phi=\Phi_c} \right) &= \frac{i}{2} \text{tr} \log \left(\partial^2 + M^2 + \frac{\lambda_2}{2} \phi^2 \right) \\ &= \frac{i}{2} \text{tr} \log (\partial^2 + M^2) + \frac{i}{2} \text{tr} \log \left(1 + \frac{\lambda_2}{2} \frac{1}{\partial^2 + M^2 + i\varepsilon} \phi^2 \right), \end{aligned} \quad (\text{A.38})$$

where derivatives in the denominator are defined as Green's functions. Since $\text{tr} \log (\partial^2 + M^2)$ is just a constant that can be calculated for instance in dimensional regularisation, the first part does not give us any higher-dimensional operators of the light fields ϕ . Expanding the logarithm in the second term, we find

$$\begin{aligned} S_{\text{eff}} &\supset \frac{i\lambda_2}{4} \text{tr} \frac{1}{\partial^2 + M^2 - i\varepsilon} \phi^2 - \frac{i\lambda_2^2}{8} \text{tr} \left(\frac{1}{\partial^2 + M^2 - i\varepsilon} \phi^2 \right)^2 \\ &\quad + \frac{i\lambda_2^3}{12} \text{tr} \left(\frac{1}{\partial^2 + M^2 - i\varepsilon} \phi^2 \right)^3 + \mathcal{O}(\lambda_2^4). \end{aligned} \quad (\text{A.39})$$

The first of these terms renormalises the ϕ mass term, and the second contributes to the ϕ^4 interaction. This is important for RG running, but does not create the kind of new effective interactions we are interested in here. Instead, we focus on the last term and evaluate the functional trace with Equation (2.28) (for a detailed description of the formalism see for instance Reference [140]):

$$\begin{aligned} S_{\text{eff}} &\supset \frac{i\lambda_2^3}{12} \int \frac{d^4k}{(2\pi)^4} \langle k | \left(\frac{1}{\partial^2 + M^2 - i\varepsilon} \phi^2 \right)^3 | k \rangle \\ &\supset \frac{i\lambda_2^3}{12} \int d^4x \int d^4y \int d^4z \int \frac{d^4k}{(2\pi)^4} \int \frac{d^4p}{(2\pi)^4} \int \frac{d^4q}{(2\pi)^4} \int \frac{d^4q}{(2\pi)^4} \langle k | \frac{1}{\partial^2 + M^2 - i\varepsilon} | x \rangle \langle x | \phi^2 | p \rangle \\ &\quad \times \langle p | \frac{1}{\partial^2 + M^2 - i\varepsilon} | y \rangle \langle y | \phi^2 | q \rangle \langle q | \frac{1}{\partial^2 + M^2 - i\varepsilon} | z \rangle \langle z | \phi^2 | k \rangle. \end{aligned} \quad (\text{A.40})$$

Here we have used the definition of the functional trace in Equation (2.28) and inserted unity, $1 = \int d^4x |x\rangle\langle x| = \int d^4p/(2\pi)^4 |p\rangle\langle p|$. The states $|k\rangle, |p\rangle$, and $|q\rangle$ are eigenstates of the derivative operator ∂ , i. e. $\langle k| i\partial_\mu = \langle k| k_\mu$, while $|x\rangle, |y\rangle$, and $|z\rangle$ denote the eigenstates of local operators, $\langle x| \phi^2 = \langle x| \phi^2(x)$. Their inner product is $\langle x|k\rangle = e^{-ikx}$. Using these properties and shifting the integration variables, we get

$$\begin{aligned} S_{\text{eff}} &\supset \frac{i\lambda_2^3}{12} \int d^4x \int d^4y \int d^4z \int \frac{d^4k}{(2\pi)^4} \int \frac{d^4p}{(2\pi)^4} \int \frac{d^4q}{(2\pi)^4} \frac{1}{-k^2 + M^2 - i\varepsilon} e^{ikx} \phi(x)^2 e^{-ipx} \\ &\quad \times \frac{1}{-p^2 + M^2 - i\varepsilon} e^{ipy} \phi(y)^2 e^{-iqy} \frac{1}{-q^2 + M^2 - i\varepsilon} e^{iqz} \phi(z)^2 e^{-ikz} \\ &\supset -\frac{i\lambda_2^3}{12} \int d^4x \int d^4y \int d^4z \int \frac{d^4k}{(2\pi)^4} \int \frac{d^4p}{(2\pi)^4} \int \frac{d^4q}{(2\pi)^4} \phi(x)^2 \phi(y)^2 \phi(z)^2 \\ &\quad \times \frac{e^{ip(z-x)} e^{iq(z-y)}}{(k^2 - M^2 + i\varepsilon)((k+p)^2 - M^2 + i\varepsilon)((k+p+q)^2 - M^2 + i\varepsilon)}. \end{aligned} \quad (\text{A.41})$$

We can now perform the integral over the loop momentum k with Feynman parameters:

$$\begin{aligned} &\int \frac{d^4k}{(2\pi)^4} \frac{1}{(k^2 - M^2 + i\varepsilon)((k+p)^2 - M^2 + i\varepsilon)((k+p+q)^2 - M^2 + i\varepsilon)} \\ &= 2 \int_0^1 dx_1 \int_0^{1-x_1} dx_2 \int \frac{d^4k}{(2\pi)^4} \left[x_1(k^2 - M^2 + i\varepsilon) + x_2((k+p)^2 - M^2 + i\varepsilon) \right. \\ &\quad \left. + (1-x_1-x_2)((k+p+q)^2 - M^2 + i\varepsilon) \right]^{-3} \\ &= 2 \int_0^1 dx_1 \int_0^{1-x_1} dx_2 \int \frac{d^4k}{(2\pi)^4} \frac{1}{[(k+a)^2 - B + i\varepsilon]^3} \end{aligned} \quad (\text{A.42})$$

with $a = (1-x_1)p + (1-x_1-x_2)q$ and $B = M^2 - (1-x_1-x_2)(p+q)^2 - x_2 p^2 + a^2$. Shifting the loop momentum as $k \rightarrow k + a$, we finally arrive at

$$T_3(p, q) = 2 \int_0^1 dx_1 \int_0^{1-x_1} dx_2 \int \frac{d^4k}{(2\pi)^4} \frac{1}{[k^2 - B + i\varepsilon]^3}. \quad (\text{A.43})$$

To evaluate this, we first Wick-rotate $k^0 = ik_E^0$. Formally, this means shifting the integration path in the complex plane of k^0 from along the real axis to along the imaginary axis. The Cauchy theorem assures that this does not change the value of the integral as long as we choose the contour such that the poles are not caught between the two contours. Defining $k_E^2 = (k_E^0)^2 + \mathbf{k}^2 = -k^2$, we find

$$I_{0,3} \equiv \int \frac{d^4k}{(2\pi)^4} \frac{1}{[k^2 - B + i\varepsilon]^3} = i \int \frac{d^4k_E}{(2\pi)^4} \frac{1}{[-k_E^2 - B]^3}, \quad (\text{A.44})$$

where the $+i\epsilon$ is no longer necessary. With $\bar{k} = |k_E|$ we can finally calculate the integral:

$$I_{0,3} = \frac{2\pi^2}{(2\pi)^4} \int d\bar{k} \bar{k}^3 \frac{1}{[\bar{k}^2 + B]^3} = \frac{-i}{32\pi^2 B}. \quad (\text{A.45})$$

Collecting all the pieces, we have

$$\begin{aligned} S_{\text{eff}} \supset & -\frac{\lambda_2^3}{192\pi^2} \int d^4x \int d^4y \int d^4z \phi(x)^2 \phi(y)^2 \phi(z)^2 \\ & \times \int \frac{d^4p}{(2\pi)^4} \int \frac{d^4q}{(2\pi)^4} e^{ip(z-x)} e^{iq(z-y)} \int_0^1 dx_1 \int_0^{1-x_1} dx_2 \\ & \times [M^2 - (1-x_1-x_2)(p+q)^2 - x_2 p^2 + ((1-x_1)p + (1-x_1-x_2)q)^2]^{-1}. \end{aligned} \quad (\text{A.46})$$

At first glance, this is disappointing: this effective action looks non-local and involves highly non-trivial integrals. It turns out that these can in fact be calculated and give a finite result [299, 300]. The full expression is quite ugly, but fortunately, we do not need it. Instead, we expand the integrand in powers of $1/M^2$. We only calculate the leading term at $\mathcal{O}(1/M^2)$. Since it produces a finite result as well, the rest term at $\mathcal{O}(1/M^4)$ also has to be finite. In this way, we find the much simpler result

$$\begin{aligned} S_{\text{eff}} \supset & -\frac{\lambda_2^3}{192\pi^2 M^2} \int d^4x \int d^4y \int d^4z \phi(x)^2 \phi(y)^2 \phi(z)^2 \\ & \times \int \frac{d^4p}{(2\pi)^4} \int \frac{d^4q}{(2\pi)^4} e^{ip(z-x)} e^{iq(z-y)} + \mathcal{O}(1/M^4) \\ \supset & -\frac{\lambda_2^3}{192\pi^2 M^2} \int d^4x \int d^4y \int d^4z \phi(x)^2 \phi(y)^2 \phi(z)^2 \delta(z-x) \delta(z-y) \\ \supset & -\frac{\lambda_2^3}{192\pi^2 M^2} \int d^4x \phi(x)^6. \end{aligned} \quad (\text{A.47})$$

After the expansion in $1/M$, we have finally arrived at a local theory.

What about the higher terms in Equation (A.39)? Their calculation is analogous to that presented here and leads to operators of the form ϕ^8 and higher. They are suppressed at least with $1/M^4$ and are thus irrelevant for our dimension-six effective theory.

Combining Equation (A.37) and Equation (A.47), up to one loop and $\mathcal{O}(1/M^2)$ the effective action is given by

$$S_{\text{eff}}[\phi] = \int d^4x \left[\frac{1}{2} \partial_\mu \phi \partial^\mu \phi - \frac{m^2}{2} \phi^2 - \frac{\lambda_0}{4!} \phi^4 - \frac{\lambda_2^3}{12(4\pi)^2 M^2} \phi^6 \right]. \quad (\text{A.48})$$

As expected, the dimension-six operator is suppressed by two powers of the heavy scale $\Lambda \equiv M$, and the Wilson coefficient consists of the couplings λ_2^3 times a loop factor.

$\mathcal{O}_H^{\text{SILH}} = \partial^\mu (\phi^\dagger \phi) \partial_\mu (\phi^\dagger \phi)$	$\mathcal{O}_{HB}^{\text{SILH}} = (D^\mu \phi)^\dagger D^\nu \phi B_{\mu\nu}$
$\mathcal{O}_T^{\text{SILH}} = (\phi^\dagger \overleftrightarrow{D}^\mu \phi) (\phi^\dagger \overleftrightarrow{D}_\mu \phi)$	$\mathcal{O}_{HW}^{\text{SILH}} = (D^\mu \phi)^\dagger \sigma^k D^\nu \phi W_{\mu\nu}^k$
$\mathcal{O}_6^{\text{SILH}} = (\phi^\dagger \phi)^3$	$\mathcal{O}_B^{\text{SILH}} = (\phi^\dagger \overleftrightarrow{D}^\mu \phi) (\partial^\nu B_{\mu\nu})$
$\mathcal{O}_u^{\text{SILH}} = (\phi^\dagger \phi) (\phi^\dagger \cdot \bar{Q}_L) u_R + \text{h. c.}$	$\mathcal{O}_W^{\text{SILH}} = (\phi^\dagger \sigma^k \overleftrightarrow{D}^\mu \phi) (D^\nu W_{\mu\nu}^k)$
$\mathcal{O}_d^{\text{SILH}} = (\phi^\dagger \phi) (\phi \bar{Q}_L) d_R + \text{h. c.}$	$\mathcal{O}_g^{\text{SILH}} = (\phi^\dagger \phi) G_{\mu\nu}^a G^{\mu\nu a}$
$\mathcal{O}_\ell^{\text{SILH}} = (\phi^\dagger \phi) (\phi \bar{L}_L) l_R + \text{h. c.}$	$\mathcal{O}_\gamma^{\text{SILH}} = (\phi^\dagger \phi) B_{\mu\nu} B^{\mu\nu}$

Table A.2: Dimension-six operators in the SILH basis relevant for Higgs physics.

A.4 SILH basis

For the dimension-six operators of linear Higgs effective field theory, we closely follow the conventions of References [25, 153, 154], which are based on the Hagiwara-Ishihara-Szalapski-Zeppenfeld basis (HISZ) [151]. Our framework is defined in Section 2.3.2. The Lagrangian is given in Equation (2.36), and the operators are listed in Tables 2.1 to 2.4. We discuss the phenomenology of these operators in Section 2.3.3.

Another common basis for dimension-six operators was developed in References [149, 150] and is usually named ‘Strongly Interacting Light Higgs’ or ‘SILH’ after the title of Reference [149]. It is based on the Lagrangian

$$\begin{aligned} \mathcal{L}_{\text{SILH}} = & \mathcal{L}_{\text{SM}} + \frac{c_H}{2v^2} \mathcal{O}_H^{\text{SILH}} + \frac{c_T}{2v^2} \mathcal{O}_T^{\text{SILH}} - \frac{c_6 \lambda}{v^2} \mathcal{O}_6^{\text{SILH}} \\ & + \frac{ig c_W}{2m_W^2} \mathcal{O}_W^{\text{SILH}} + \frac{ig' c_B}{2m_W^2} \mathcal{O}_B^{\text{SILH}} + \frac{ig c_{HW}}{m_W^2} \mathcal{O}_{HW}^{\text{SILH}} + \frac{ig' c_{HB}}{m_W^2} \mathcal{O}_{HB}^{\text{SILH}} \\ & + \frac{g'^2 c_\gamma}{m_W^2} \mathcal{O}_\gamma^{\text{SILH}} + \frac{g_s^2 c_g}{m_W^2} \mathcal{O}_g^{\text{SILH}} - \sum_f \frac{c_f}{v^2} \gamma_f \mathcal{O}_f^{\text{SILH}} \end{aligned} \quad (\text{A.49})$$

with the Wilson coefficients c_i , and the operators $\mathcal{O}_i^{\text{SILH}}$ defined in Table A.2. Note that this Lagrangian is not of the form given in Equation (2.11): the dimension-six operators are suppressed by conventional powers of m_W or v instead of the cutoff scale Λ .

These operators can be translated to our conventions (the HISZ basis) with the following dictionary:

$$\mathcal{O}_H^{\text{SILH}} = 2\mathcal{O}_{\phi,2}, \quad \mathcal{O}_{HB}^{\text{SILH}} = -\frac{2i}{g'} \mathcal{O}_B,$$

$$\begin{aligned}
 \mathcal{O}_T^{\text{SILH}} &= 2\mathcal{O}_{\phi,2} - 4\mathcal{O}_{\phi,1}, & \mathcal{O}_{HW}^{\text{SILH}} &= -\frac{2i}{g}\mathcal{O}_W, \\
 \mathcal{O}_6^{\text{SILH}} &= 3\mathcal{O}_{\phi,3}, & \mathcal{O}_B^{\text{SILH}} &= \frac{2i}{g'}(\mathcal{O}_{BB} + \mathcal{O}_{BW} - 2\mathcal{O}_B), \\
 \mathcal{O}_u^{\text{SILH}} &= \mathcal{O}_u, & \mathcal{O}_g^{\text{SILH}} &= \mathcal{O}_{GG}, \\
 \mathcal{O}_d^{\text{SILH}} &= \mathcal{O}_d, & \mathcal{O}_W^{\text{SILH}} &= \frac{2i}{g}(\mathcal{O}_{WW} + \mathcal{O}_{BW} - 2\mathcal{O}_W), \\
 \mathcal{O}_\ell^{\text{SILH}} &= \mathcal{O}_\ell, & \mathcal{O}_\gamma^{\text{SILH}} &= -\frac{4}{g'^2}\mathcal{O}_{BB}. \tag{A.50}
 \end{aligned}$$

For the Wilson coefficients, we find

$$\begin{aligned}
 c_H &= \frac{v^2}{\Lambda^2} \left(\frac{1}{2}f_{\phi,1} + f_{\phi,2} \right), & c_{HB} &= \frac{v^2}{\Lambda^2} \frac{g^2}{8}(f_B + 2f_{BW} - 2f_{WW}), \\
 c_T &= -\frac{v^2}{\Lambda^2} \frac{1}{2}f_{\phi,1}, & c_{HW} &= \frac{v^2}{\Lambda^2} \frac{g^2}{8}(f_W + 2f_{WW}), \\
 c_6 &= -\frac{v^2}{\Lambda^2} \frac{1}{3\lambda}f_{\phi,3}, & c_B &= \frac{v^2}{\Lambda^2} \frac{g^2}{4}(f_{WW} - f_{BW}), \\
 c_u &= -\frac{v^2}{\Lambda^2} \frac{1}{y_u}f_u, & c_W &= -\frac{v^2}{\Lambda^2} \frac{g^2}{4}f_{WW}, \\
 c_d &= -\frac{v^2}{\Lambda^2} \frac{1}{y_d}f_d, & c_g &= \frac{v^2}{\Lambda^2} \frac{g^2}{4g_s^2}f_{GG}, \\
 c_\ell &= -\frac{v^2}{\Lambda^2} \frac{1}{y_\ell}f_\ell, & c_\gamma &= \frac{v^2}{\Lambda^2} \frac{g^2}{16}(f_{BW} - f_{BB} - f_{WW}). \tag{A.51}
 \end{aligned}$$

A.5 Model fine print

A.5.1 Singlet extension

The singlet model is defined in Equations (3.25) and (3.26) in Section 3.3.2. Ignoring the Goldstones, the scalar doublet and singlet fields can be expanded into components as

$$\begin{aligned}
 \phi &= \frac{1}{\sqrt{2}} \begin{pmatrix} 1 \\ v + \phi^0 \end{pmatrix}, \\
 S &= \frac{1}{\sqrt{2}}(v_s + s^0), \tag{A.52}
 \end{aligned}$$

where $v \equiv \sqrt{2}\langle\phi\rangle = 246$ GeV and $v_s \equiv \sqrt{2}\langle S\rangle$ denote their respective VEVs. The minimisation condition for this potential can be used to eliminate the parameters $\mu_{1,2}$ in favour of v and v_s .

The components ϕ^0 and s^0 mix to form a light (h) and a heavy (H) mass eigenstate,

$$\begin{aligned} h &= \phi^0 \cos \alpha - s^0 \sin \alpha, \\ H &= \phi^0 \sin \alpha + s^0 \cos \alpha, \end{aligned} \quad (\text{A.53})$$

where

$$\tan(2\alpha) = \frac{\lambda_3 v v_s}{\lambda_2 v_s^2 - \lambda_1 v^2}. \quad (\text{A.54})$$

Their masses are

$$m_{h,H}^2 = \lambda_1 v^2 + \lambda_2 v_s^2 \mp |\lambda_1 v^2 - \lambda_2 v_s^2| \sqrt{1 + \tan^2(2\alpha)} \quad (\text{A.55})$$

with $m_H^2 \approx 2\lambda_2 v_s^2 \gg m_h^2$ in the limit $v^2 \ll v_s^2$.

A.5.2 Two-Higgs-doublet model

Model setup

We analyse the most general gauge invariant, CP -even theory for two scalar fields with an additional \mathbb{Z}_2 symmetry, as defined in Equation (3.41) in Section 3.3.3. The scalar mass eigenstates follow from the set of rotations

$$\begin{pmatrix} H^0 \\ h^0 \end{pmatrix} = R(\alpha) \begin{pmatrix} h_1^0 \\ h_2^0 \end{pmatrix}, \quad \begin{pmatrix} w^0 \\ A^0 \end{pmatrix} = R(\beta) \begin{pmatrix} a_1^0 \\ a_2^0 \end{pmatrix}, \quad \begin{pmatrix} w^\pm \\ H^\pm \end{pmatrix} = R(\beta) \begin{pmatrix} h_1^\pm \\ h_2^\pm \end{pmatrix}, \quad (\text{A.56})$$

with

$$\phi_k = \begin{pmatrix} h_k^+ \\ \frac{1}{\sqrt{2}}(v_k + h_k^0 + ia_k) \end{pmatrix} \quad (\text{A.57})$$

and

$$R(\theta) = \begin{pmatrix} \cos \theta & \sin \theta \\ -\sin \theta & \cos \theta \end{pmatrix}. \quad (\text{A.58})$$

Since the two doublets contribute to giving masses to the weak gauge bosons, custodial symmetry will impose tight constraints on the viable mass spectrum of the model [301–309]. Analytic relations linking the different Higgs masses and mixing angles with the Lagrangian parameters in Equation (3.41) can be found for example in Appendix A of Reference [178]. The conventions

$$0 < \beta < \pi/2 \quad \text{and} \quad 0 \leq \beta - \alpha < \pi \quad (\text{A.59})$$

guarantee that the Higgs coupling to vector bosons has the same sign in the 2HDM and in the SM.

Couplings

The tree-level coupling shifts of the light Higgs directly follow from the rotations in Equation (A.56) and are given in Equations (3.42) to (3.46). The light Higgs coupling to a charged Higgs pair reads

$$\frac{g_{h^0 H^+ H^-}}{g_{hh}^{\text{SM}}} = \frac{1}{3m_{h^0}^2} \left[\sin(\beta - \alpha) (2m_{H^\pm}^2 - m_{h^0}^2) + \frac{\cos(\alpha + \beta)}{\sin(2\beta)} \left(2m_{h^0}^2 - \frac{2m_{12}^2}{\sin \beta \cos \beta} \right) \right], \quad (\text{A.60})$$

with $g_{hh}^{\text{SM}} = -3m_h^2/v$.

The loop-induced couplings are more involved, giving

$$1 + \Delta_g = \frac{1}{A_{gg}^{\text{SM}}} \left[\sum_{f=t,b} (1 + \Delta_f) A_f(\tau_f) \right], \quad (\text{A.61})$$

$$1 + \Delta_\gamma = \frac{1}{A_{\gamma\gamma}^{\text{SM}}} \left[\sum_{f=t,b} N_C Q_f^2 (1 + \Delta_f) A_f(\tau_f) + Q_\tau^2 (1 + \Delta_\tau) A_\tau(\tau_\tau) + (1 + \Delta_W) A_\nu(\tau_W) - g_{h^0 H^+ H^-} \frac{m_W s_w}{e m_{H^\pm}^2} A_s(\tau_{H^\pm}) \right], \quad (\text{A.62})$$

where A_{xx}^{SM} are the corresponding contributions in the SM. The conventional loop form factors read

$$\begin{aligned} A_s(\tau) &= -\frac{\tau}{2} [1 - \tau f(\tau)] &= 1/6 + \mathcal{O}(\tau^{-1}), \\ A_f(\tau) &= \tau [1 + (1 - \tau) f(\tau)] &= 2/3 + \mathcal{O}(\tau^{-1}), \\ A_V(\tau) &= -\frac{1}{2} [2 + 3\tau + 3(2\tau - \tau^2) f(\tau)] &= -7/2 + \mathcal{O}(\tau^{-1}), \end{aligned} \quad (\text{A.63})$$

where

$$f(\tau) = \begin{cases} -\frac{1}{4} \left[\log \frac{1+\sqrt{1-\tau}}{1-\sqrt{1-\tau}} - i\pi \right]^2 & \text{for } \tau < 1 \\ \left[\arcsin \frac{1}{\sqrt{\tau}} \right]^2 & \text{for } \tau \geq 1, \end{cases} \quad (\text{A.64})$$

and $\tau_x = 4m_x^2/m_{h^0}^2$.

Matching

The effect of the second doublet on the phenomenology of the light Higgs consists purely of shifted couplings Δ_x . This allows us to match the dimension-six model by equating the coupling shifts from the full model, given in Equations (3.42) to (3.46) and (A.62), to the corresponding couplings in the dimension-six Lagrangian, see Equation (2.58).

In a second step we then expand in $1/\Lambda$ and keep terms up to $\mathcal{O}(1/\Lambda^2)$. Λ is either defined in the unbroken phase for the default matching, or as the physical mass m_{A^0} in the v -improved matching, as described in Section 3.3.3.

This defines the effective model in a straightforward way. For more details see Appendix A.3 of Reference [1].

A.5.3 Scalar top partners

Model setup

The potential for the simplified scalar top partner model consists of three parts,

$$\begin{aligned} \mathcal{L}_{\text{top partners}} \supset & (D_\mu \tilde{Q})^\dagger D^\mu \tilde{Q} + (D_\mu \tilde{t}_R)^* D^\mu \tilde{t}_R - \underbrace{M^2 \tilde{Q}^\dagger \tilde{Q} - M^2 \tilde{t}_R^* \tilde{t}_R}_{\mathcal{L}_{\text{mass}}} \\ & - \underbrace{\kappa_{LL} (\phi \cdot \tilde{Q})^\dagger (\phi \cdot \tilde{Q}) - \kappa_{RR} (\tilde{t}_R^* \tilde{t}_R) (\phi^\dagger \phi)}_{\mathcal{L}_{\text{Higgs}}} - \underbrace{[\kappa_{LR} M \tilde{t}_R^* (\phi \cdot \tilde{Q}) + \text{h. c.}]}_{\mathcal{L}_{\text{mixing}}}. \end{aligned} \quad (\text{A.65})$$

We use the customary notation for the $SU(2)_L$ invariant product $\phi \cdot \tilde{Q} \equiv \epsilon_{ab} \phi^a \tilde{Q}^b$, with the help of the antisymmetric pseudo-tensor $\epsilon_{ij} \equiv i\sigma_{ij}^2$ such that $\epsilon_{12} = -\epsilon_{21} = 1$.

The term $\mathcal{L}_{\text{Higgs}}$ gives rise to scalar partner masses proportional to the Higgs VEV, mirroring the supersymmetric F -term contribution to the squark masses. By a similar token, the explicit mass terms $\mathcal{L}_{\text{mass}}$ are analogous to the squark soft-SUSY breaking mass terms. $\mathcal{L}_{\text{mixing}}$ is responsible for the mixing between the gauge eigenstates, reminiscent of the MSSM A -terms. In the absence of an underlying supersymmetry, the Lagrangian features no equivalent of the D -term contributions.

Collecting all bilinear terms from Equation (A.65), we get

$$\mathcal{L}_{\text{top partners}} \supset (\tilde{t}_L^* \tilde{t}_R^*) \mathcal{M}_{\tilde{t}} \begin{pmatrix} \tilde{t}_L \\ \tilde{t}_R \end{pmatrix}, \quad (\text{A.66})$$

with the mass matrix $\mathcal{M}_{\tilde{t}}$ given in Equation (3.54). Assuming all parameters in Equation (A.65) to be real, it can be diagonalised through the usual orthogonal transformation $R(\theta_{\tilde{t}})$ given in Equation (A.58). This rotates the gauge eigenstates $(\tilde{t}_L, \tilde{t}_R)$ into the mass basis $(\tilde{t}_1, \tilde{t}_2)$,

$$\begin{pmatrix} \tilde{t}_1 \\ \tilde{t}_2 \end{pmatrix} = R(\theta_{\tilde{t}}) \begin{pmatrix} \tilde{t}_L \\ \tilde{t}_R \end{pmatrix}. \quad (\text{A.67})$$

The physical scalar partner masses and the mixing angle are then given by

$$\begin{aligned} m_{\tilde{t}_1}^2 &= M_{LL}^2 \cos^2 \theta_{\tilde{t}} + M_{RR}^2 \sin^2 \theta_{\tilde{t}} + 2M_{LR}^2 \sin \theta_{\tilde{t}} \cos \theta_{\tilde{t}}, \\ m_{\tilde{t}_2}^2 &= M_{LL}^2 \sin^2 \theta_{\tilde{t}} + M_{RR}^2 \cos^2 \theta_{\tilde{t}} - 2M_{LR}^2 \sin \theta_{\tilde{t}} \cos \theta_{\tilde{t}}, \end{aligned} \quad (\text{A.68})$$

$$\tan(2\theta_{\tilde{t}}) = \frac{2M_{LR}^2}{M_{LL}^2 - M_{RR}^2}. \quad (\text{A.69})$$

As we assume the right-handed bottom partner \tilde{b}_R to be heavy and thus decoupled, the sbottom-like scalar eigenstate \tilde{b}_L undergoes no mixing and can be directly identified with the physical eigenstate.

Matching

We compute the effective action at one loop with the help of the covariant derivative expansion [139, 143], which is fully consistent with our mass degeneracy setup. Since the Lagrangian Equation (A.65) lacks any linear terms in the heavy scalar fields $\Psi \equiv (\tilde{Q}, \tilde{t}_R^*)$, the tree-level exchange of such heavy partners cannot generate any effective interaction at dimension six. Our results are in agreement with References [139, 145, 194] and given in Equation (3.57).

A.5.4 Vector triplet

Model setup

Our final example is the heavy vector triplet defined in Equation (3.59). This Lagrangian includes conventional factors of coupling constants, introduced for a convenient power counting in certain UV embeddings [264]: insertions of V and ϕ are weighted by one factor of g_V , while SM gauge bosons come with a factor of g_W . In addition, the coupling to fermions is weighted with an additional factor of g_W^2/g_V^2 . For simplicity, it is assumed that the fermion current in Equation (3.59) is universal.

We can add an explicit kinetic V - W mixing term

$$\mathcal{L} \supset c_{WV} \frac{g_W}{2g_V} D_{[\mu} V_{\nu]}^a W^{\mu\nu a} \quad (\text{A.70})$$

to the Lagrangian in Equation (3.59). As it turns out, this term is redundant and can be removed with field redefinitions, shifting its effects into the other model parameters [264, 310]. For more details, see Appendix A.5 of Reference [1].

In this model, seven gauge eigenstates W^a, B, V^a mix into mass eigenstates A, W^\pm, Z, ξ^\pm , and ξ^0 . The photon is as usual defined as the component that remains massless during EWSB,

$$A_\mu = c_w B_\mu + s_w W_\mu^3, \quad (\text{A.71})$$

where the Weinberg angle is linked to the gauge couplings through $e = g_W s_w = g' c_w$. For the remaining fields we have to diagonalise the neutral and charged mass matrices, giving the mass eigenstates

$$\begin{aligned} Z_\mu &= \cos \theta_N (-s_w B_\mu + c_w W_\mu^3) + \sin \theta_N V_\mu^3, \\ \xi_\mu^0 &= -\sin \theta_N (-s_w B_\mu + c_w W_\mu^3) + \cos \theta_N V_\mu^3, \\ W_\mu^\pm &= \cos \theta_C \frac{W_\mu^1 \mp W_\mu^2}{\sqrt{2}} + \sin \theta_C \frac{V_\mu^1 \mp V_\mu^2}{\sqrt{2}}, \\ \xi_\mu^\pm &= -\sin \theta_C \frac{W_\mu^1 \mp W_\mu^2}{\sqrt{2}} + \cos \theta_C \frac{V_\mu^1 \mp V_\mu^2}{\sqrt{2}}. \end{aligned} \quad (\text{A.72})$$

The corresponding mass eigenvalues read

$$\begin{aligned} m_{Z/\xi^0}^2 &= \frac{1}{2} \left[\hat{m}_V^2 + \hat{m}_Z^2 \mp \sqrt{\left(\hat{m}_Z^2 - \hat{m}_V^2 \right)^2 + c_H^2 g_V^2 \hat{m}_Z^2 \hat{v}^2} \right] \\ &= \begin{cases} \hat{m}_Z^2 \left(1 - \frac{c_H^2 g_V^2}{4} \frac{\hat{v}^2}{\hat{m}_V^2} + \mathcal{O}(\hat{v}^4/\hat{m}_V^4) \right) \\ \hat{m}_V^2 \left(1 + \frac{c_H^2 g_V^2}{4} \frac{\hat{v}^2}{\hat{m}_V^2} + \mathcal{O}(\hat{v}^4/\hat{m}_V^4) \right), \end{cases} \end{aligned} \quad (\text{A.73})$$

and

$$\begin{aligned} m_{W^\pm/\xi^\pm}^2 &= \frac{1}{2} \left[\hat{m}_V^2 + \hat{m}_W^2 \mp \sqrt{\left(\hat{m}_W^2 - \hat{m}_V^2 \right)^2 + c_H^2 g_V^2 \hat{m}_W^2 \hat{v}^2} \right] \\ &= \begin{cases} \hat{m}_W^2 \left(1 - \frac{c_H^2 g_V^2}{4} \frac{\hat{v}^2}{\hat{m}_V^2} + \mathcal{O}(\hat{v}^4/\hat{m}_V^4) \right) \\ \hat{m}_V^2 \left(1 + \frac{c_H^2 g_V^2}{4} \frac{\hat{v}^2}{\hat{m}_V^2} + \mathcal{O}(\hat{v}^4/\hat{m}_V^4) \right). \end{cases} \end{aligned} \quad (\text{A.74})$$

For the mixing angles, we find

$$\begin{aligned} \tan(2\theta_N) &= \frac{c_H g_V \hat{v} \hat{m}_Z}{\hat{m}_V^2 - \hat{m}_Z^2} = \frac{c_H g g_V}{2 c_w} \frac{\hat{v}^2}{\hat{m}_V^2} + \mathcal{O}(\hat{v}^4/\hat{m}_V^4), \\ \tan(2\theta_C) &= \frac{c_H g_V \hat{v} \hat{m}_W}{\hat{m}_V^2 - \hat{m}_W^2} = \frac{c_H g g_V}{2} \frac{\hat{v}^2}{\hat{m}_V^2} + \mathcal{O}(\hat{v}^4/\hat{m}_V^4), \end{aligned} \quad (\text{A.75})$$

or

$$\sin \theta_C = \frac{c_H g g_V}{4} \frac{\hat{v}^2}{M_V^2} + \mathcal{O}(\hat{v}^4/\hat{m}_V^4). \quad (\text{A.76})$$

Appendices

Here we use the definitions

$$\hat{m}_Z = \frac{g_W \hat{v}}{2 c_w}, \quad \hat{m}_W = \frac{g_W \hat{v}}{2}, \quad \hat{m}_V^2 = M_V^2 + g_V^2 c_{VVHH} \hat{v}^2, \quad (\text{A.77})$$

where \hat{v} is the actual VEV of ϕ , which does not necessarily have the SM value of $v = 2m_W/g = 246$ GeV.

This mixing affects the weak current interactions: instead of being simply governed by the $SU(2)_L$ coupling constant g_W , the physical Wff' couplings are now determined by

$$g = \cos \theta_C g_W - \sin \theta_C c_F \frac{g_W^2}{g_V} = g_W \left(1 - \frac{c_F c_H g_W^2}{4} \frac{v^2}{M_V^2} \right) + \mathcal{O}(v^4/M_V^4). \quad (\text{A.78})$$

The relation between \hat{v} and v can be read off from Equation (A.74):

$$\frac{\hat{v}}{v} = 1 + \frac{c_H^2 g_V^2}{8} \frac{v^2}{M_V^2} - \frac{c_F c_H g_W^2}{4} \frac{v^2}{M_V^2} + \mathcal{O}(v^4/M_V^4). \quad (\text{A.79})$$

Finally, note that to ensure compatibility with electroweak precision measurements, the neutral and charged states ξ^0 and ξ^\pm have to be nearly mass-degenerate,

$$m_{\xi^\pm} \approx m_{\xi^0} \equiv m_\xi. \quad (\text{A.80})$$

In practice, we set up our model in the m_W - g scheme, i. e. based on the input parameters g , m_W , α , m_{h^0} , α_s , the vector triplet couplings g_V and c_i , as well as the physical mass m_{ξ^\pm} . The remaining Lagrangian parameters, mixing angles, and couplings are calculated by solving Equations (A.73) and (A.74) iteratively.

Couplings

The mismatch between g and g_W as well as between v and \hat{v} leads to a shift of the Higgs couplings to fermions,

$$\begin{aligned} \Delta_f &= \frac{g_W}{g} \frac{v}{\hat{v}} - 1 = \frac{1}{\cos \theta_C - c_F \frac{g_W}{g_V} \sin \theta_C} \frac{v}{\hat{v}} - 1 \\ &= c_H^2 \frac{g_V^2 v^2}{8M_V^2} + c_F c_H \frac{g^2 v^2}{4M_V^2} + \mathcal{O}(M_V^{-4}), \end{aligned} \quad (\text{A.81})$$

and to (on-shell) W bosons,

$$\begin{aligned}\Delta_W &= \frac{1}{gm_W} \left(\frac{\cos^2 \theta_C g^2 \hat{v}}{2(\cos \theta_C - c_F \frac{g_W}{g_V} \sin \theta_C)^2} - c_H \frac{\sin \theta_C \cos \theta_C g g_V \hat{v}}{\cos \theta_C - c_F \frac{g_W}{g_V} \sin \theta_C} \right. \\ &\quad \left. + 2 c_{VVHH} \sin^2 \theta_C g_V^2 \hat{v} \right) - 1 \\ &= c_H^2 \frac{3g_V^2 v^2}{8M_V^2} + c_F c_H \frac{g^2 v^2}{4M_V^2} + \mathcal{O}(M_V^{-4}) .\end{aligned}\tag{A.82}$$

Matching

Since we are only interested in tree-level effects, we can construct the effective theory in our default matching procedure with the classical equation of motion for V_μ^a , corresponding to the first term in Equation (2.27). To simplify the notation, we define currents

$$J_F^{\mu,a} \equiv \bar{f}_L \gamma^\mu \sigma^a f_L, \quad J_H^{\mu,a} \equiv \phi^\dagger \sigma^a \overleftrightarrow{D}^\mu \phi .\tag{A.83}$$

This Euler-Lagrange equation then reads

$$[\partial^\mu \partial^\nu - g^{\mu\nu} \partial^2 - M_V^2] V_\nu^a = g_V c_H J_H^{\mu,a} + \frac{g_W^2}{2g_V} c_F \sum_F J_F^{\mu,a} + \mathcal{O}(V^2)\tag{A.84}$$

or

$$V^{\mu,a} = -\frac{1}{M_V^2} \left[g_V c_H J_H^{\mu,a} + \frac{g_W^2}{2g_V} c_F \sum_F J_F^{\mu,a} \right] + \mathcal{O}(p_V^2/\tilde{M}_V^4) + \mathcal{O}(V^2),\tag{A.85}$$

where we neglect higher powers of V that are irrelevant for our analysis.

Inserting this into the Lagrangian in Equation (3.59), we find the effective theory

$$\mathcal{L}_{\text{EFT}} \supset -\frac{g_W^4 c_F^2}{8g_V^2 M_V^2} J_F^{\mu,a} J_\mu^{F,a} - \frac{g_V^2 c_H^2}{2M_V^2} J_H^{\mu,a} J_\mu^{H,a} - \frac{g_W^2 c_F c_H}{2M_V^2} J_H^{\mu,a} J_\mu^{F,a} .\tag{A.86}$$

$J_F^{\mu,a} J_\mu^{F,a}$ only contains four-fermion operators irrelevant for our analysis. The remaining current products can be expressed in terms of dimension-six operators as

$$\begin{aligned}J_H^{\mu,a} J_\mu^{H,a} &= -\frac{1}{2} (\mathcal{O}_{\phi,2} - 2 \phi^\dagger \phi (D_\mu \phi)^2) \\ &= -\frac{1}{2} \left[3\mathcal{O}_{\phi,2} - 12\lambda \mathcal{O}_{\phi,3} - \sum_f y_f \mathcal{O}_f \right],\end{aligned}\tag{A.87}$$

$$\begin{aligned}J_F^{\mu,a} J_\mu^{H,a} &= \frac{1}{2} \mathcal{O}_{\phi F}^{(3)} \\ &= \frac{-2}{g_W^2} [\mathcal{O}_{WW} + \mathcal{O}_{BW} - 2\mathcal{O}_W] + 3\mathcal{O}_{\phi,2} - 12\lambda \mathcal{O}_{\phi,3} - \sum_f y_f \mathcal{O}_f .\end{aligned}\tag{A.88}$$

Here we used the equations of motion in Equations (2.39) to (2.41) to bring the operators to our HISZ basis.

Combining the pieces, we finally arrive at

$$\begin{aligned} \mathcal{L}_{\text{EFT}} \supset & \left(\frac{g_V^2 c_H^2}{4 M_V^2} - \frac{g_W^2 c_F c_H}{2 M_V^2} \right) \left[3\mathcal{O}_{\phi,2} - 12\lambda\mathcal{O}_{\phi,3} - \sum_f y_f \mathcal{O}_f \right] \\ & + \frac{c_F c_H}{M_V^2} [\mathcal{O}_{WW} + \mathcal{O}_{BW} - 2\mathcal{O}_W], \end{aligned} \quad (\text{A.89})$$

corresponding to the Wilson coefficients given in Equation (3.63).

A.6 Information geometry

A.6.1 Cramér-Rao bound

In Equation (4.7) in Section 4.2 we stated the Cramér-Rao bound [69, 70]: the covariance matrix of any estimator is bounded from below by the inverse Fisher information. Here we show the proof for one-dimensional unbiased estimators, closely following Reference [311].

An unbiased estimator $\hat{\theta}(\mathbf{x})$ based on data \mathbf{x} has an expectation value equal to the unknown true value θ ,

$$\theta = E[\hat{\theta}|\theta] = \int d\mathbf{x} \hat{\theta} f(\mathbf{x}|\theta). \quad (\text{A.90})$$

Like any probability distribution function, $f(\mathbf{x}|\theta)$ is normalised to one,

$$1 = \int d\mathbf{x} f(\mathbf{x}|\theta). \quad (\text{A.91})$$

We assume that these two equations are differentiable with respect to θ , and that we can exchange this derivative with the integral. Differentiating Equation (A.91) with respect to θ gives

$$\begin{aligned} 0 &= \int d\mathbf{x} \partial_\theta f(\mathbf{x}|\theta) \\ &= \int d\mathbf{x} \frac{\partial_\theta f(\mathbf{x}|\theta)}{f(\mathbf{x}|\theta)} f(\mathbf{x}|\theta) \\ &= E[\partial_\theta \log f(\mathbf{x}|\theta)|\theta]. \end{aligned} \quad (\text{A.92})$$

For Equation (A.90) we find in the same way

$$\begin{aligned} 1 &= \int d\mathbf{x} \hat{\theta} \partial_\theta f(\mathbf{x}|\theta) \\ &= E[\hat{\theta} \partial_\theta \log f(\mathbf{x}|\theta)|\theta]. \end{aligned} \quad (\text{A.93})$$

We can phrase this in terms of the covariance

$$\begin{aligned}\text{cov}[X, Y|\theta] &\equiv E[(X - E[X|\theta])(Y - E[Y|\theta])|\theta] \\ &= E[XY|\theta] - E[X|\theta]E[Y|\theta]\end{aligned}\quad (\text{A.94})$$

(which is closely related, but not identical, to the covariance matrix defined in Equation (4.5)). Using Equations (A.94) and (A.92), Equation (A.93) can be written as

$$1 = \text{cov}[\hat{\theta}, \partial_\theta \log f(\mathbf{x}|\theta)|\theta]. \quad (\text{A.95})$$

We can square this equation and apply the Cauchy-Schwartz identity¹

$$\text{cov}[X, Y]^2 \leq \text{var}[X] \text{ var}[Y], \quad (\text{A.96})$$

leading to

$$1 \leq \text{var}[\hat{\theta}|\theta] \text{ var}[\partial_\theta \log f(\mathbf{x}|\theta)|\theta] \quad (\text{A.97})$$

or

$$\text{var}[\hat{\theta}|\theta] \geq \frac{1}{\text{var}[\partial_\theta \log f(\mathbf{x}|\theta)|\theta]}. \quad (\text{A.98})$$

Invoking Equation (A.92) one more time, we finally arrive at the Cramér-Rao bound

$$\text{var}[\hat{\theta}|\theta] \geq \frac{1}{I(\theta)} \quad (\text{A.99})$$

with the Fisher information

$$I(\theta) = E[(\partial_\theta \log f(\mathbf{x}|\theta))^2|\theta]. \quad (\text{A.100})$$

A.6.2 A simple example

In Section 4.2 we introduced the Fisher information as the mathematical object that quantifies the maximal precision with which continuous theory parameters can be measured. As a simple example, we now calculate the Fisher information in a number of event counts n_c in different channels c . We assume that the channels are independent and follow Poisson distributions with mean values $\bar{n}_c = \nu_c$:

$$f(\mathbf{n}|\boldsymbol{\nu}) = \prod_c \text{Pois}(n_c|\nu_c) = \prod_c \frac{\nu_c^{n_c} e^{-\nu_c}}{n_c!}. \quad (\text{A.101})$$

¹This inequality is well-known in the form of the bounds on the Pearson correlation coefficient, $-1 \leq r \equiv \text{cov}[X, Y]/\sqrt{\text{var}[X] \text{ var}[Y]} \leq 1$.

Appendices

Following Equation (4.6), we can calculate the Fisher information in terms of the vector of Poisson means $\boldsymbol{\nu}$. With

$$\frac{\partial \log f}{\partial \nu_c} = \frac{\partial}{\partial \nu_c} [-\nu_c + n_c \log \nu_c - \log(n_c!)] = \frac{n_c}{\nu_c} - 1 \quad (\text{A.102})$$

and

$$\frac{\partial^2 \log f}{\partial \nu_c \partial \nu_{c'}} = -\frac{\delta_{cc'} n_c}{\nu_c^2} \quad (\text{A.103})$$

we find

$$I_{cc'}(\boldsymbol{\nu}) \equiv -E \left[\frac{\partial^2 \log f}{\partial \nu_c \partial \nu_{c'}} \middle| \boldsymbol{\nu} \right] = \frac{\delta_{cc'}}{\nu_c}. \quad (\text{A.104})$$

Equation (4.11) then allows us to calculate the Fisher information in terms of some theory parameters θ_i rather than the Poisson means ν_c :

$$I_{ij}(\boldsymbol{\theta}) = \sum_c \frac{\partial \nu_c}{\partial \theta_i} \frac{1}{\nu_c} \frac{\partial \nu_c}{\partial \theta_j}. \quad (\text{A.105})$$

At the LHC, the matrix $\partial \nu_c / \partial \theta_i$ is determined by the luminosity, the relevant cross sections and branching ratios, as well as acceptance and efficiency factors. For instance, in the κ framework for Higgs physics discussed in Section 2.3.4 it is trivial to calculate the matrix $\partial \nu_c / \partial g_i$ in closed form. For each channel this matrix is singular, which means that it measures one direction in parameter space and is blind to all orthogonal directions. At least as many channels as parameters are required to make the combined information in Equation (A.105) non-singular and to remove all blind directions (assuming the channels do not provide degenerate information, i. e. linearly dependent eigenvectors in the Fisher information).

For illustration, consider the case where we want to measure one coupling $\theta = g$ in one channel with the expected number of events

$$\nu = L(\sigma_S(g) + \sigma_B) = Lg^2\sigma_0 + L\sigma_B, \quad (\text{A.106})$$

where L , $\sigma_S(g) = g^2\sigma_0$, and σ_B stand for the integrated luminosity as well as the signal and background cross sections.

The Fisher information in terms of the coupling g is then

$$I(g) = 4L \frac{g^2 \sigma_0^2}{g^2 \sigma_0 + \sigma_B} = \frac{4L}{g^2} \frac{\sigma_0^2}{\sigma_S + \sigma_B}. \quad (\text{A.107})$$

The Cramér-Rao bound in Equation (4.8) then states that any unbiased estimator has a standard deviation of at least

$$\frac{\Delta \hat{g}}{g} \geq \frac{1}{g\sqrt{I}} = \frac{1}{2} \frac{1}{\sqrt{L}} \frac{\sqrt{\sigma_S + \sigma_B}}{\sigma_S}, \quad (\text{A.108})$$

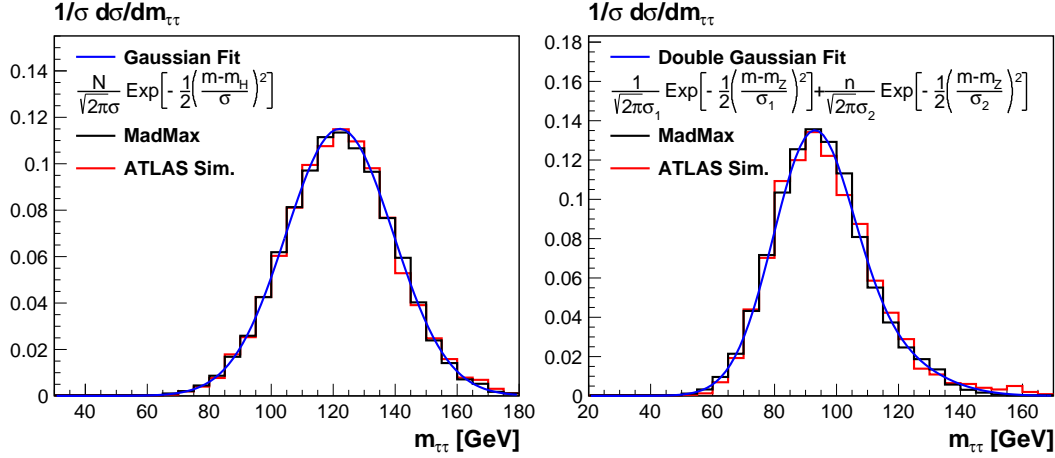


Figure A.1: Resolution effects in the invariant mass distribution in the WBF $h \rightarrow \tau\tau$ channel for the Higgs contributions (left) and the Zjj backgrounds (right). We show the ATLAS results from Figure 1a of Reference [293] (black), the fitted response function (blue), and our final MadMax output including the smearing function.

independent of how the data are analysed. The three terms show how the sensitivity to g profits from the square in the cross section, the square-root dependence on the statistics, and the dependence on the signal-to-background ratio.

A.6.3 Detector response

In Section 4.4 we described the calculation of the Fisher information in terms of dimension-six operators for a range of LHC Higgs channels. We include an idealised treatment of the detector response in which the invariant mass distributions from narrow resonance peaks are smeared according to the experimental resolution, following the procedure developed in References [289, 291] and described in Section 4.3.7. Other detector effects are not included.

For Higgs production in weak boson fusion with a decay into tau pairs, we model the smearing of the signal and background processes according to Figure 1a of Reference [293]. For the Higgs processes we use a Gaussian with width 17 GeV. For the Z backgrounds we rely on a double Gaussian, in which the dominant component has a width of 13 GeV, and the second, wider component ensures an accurate description of the high-mass tail of the Z peak around $m_{\tau\tau} \sim m_H$. The ATLAS data, our fitted smearing function, and the final MadMax output are shown in Figure A.1. We check that other distributions are not affected by the smearing.

In the 4ℓ channel, the backgrounds are negligible around $m_{4\ell} \approx m_h$, hence we do not have to include a smearing to estimate the discrimination power. For Higgs production with a single

Appendices

top in the $h \rightarrow \gamma\gamma$ mode, we follow Reference [290] and smear the $m_{\gamma\gamma}$ distribution of the signal process with a Gaussian of width 1.52 GeV. This resolution is based on Figure 6b of Reference [312].

References

- [1] J. Brehmer, A. Freitas, D. Lopez-Val, and T. Plehn: ‘Pushing Higgs effective theory to its limits’. *Phys. Rev.* D93 (7), p. 075014, 2016. arXiv:1510.03443.
- [2] A. Biekötter, J. Brehmer, and T. Plehn: ‘Extending the limits of Higgs effective theory’. *Phys. Rev.* D94 (5), p. 055032, 2016. arXiv:1602.05202.
- [3] D. de Florian et al. (LHC Higgs Cross Section Working Group): ‘Handbook of LHC Higgs Cross Sections: 4. Deciphering the Nature of the Higgs Sector’, 2016. arXiv:1610.07922.
- [4] J. Brehmer, K. Cranmer, F. Kling, and T. Plehn: ‘Better Higgs boson measurements through information geometry’. *Phys. Rev.* D95 (7), p. 073002, 2017. arXiv:1612.05261.
- [5] J. Brehmer: ‘Higgs Effective Field Theory’, 2016. Student lecture, research training group ‘Particle Physics Beyond the Standard Model’. URL http://www.thphys.uni-heidelberg.de/~gk_ppbsm/lib/exe/fetch.php?media=students:lectures:student_lecture_eft.pdf.
- [6] J. Brehmer, J. Hewett, J. Kopp, T. Rizzo, and J. Tattersall: ‘Symmetry Restored in Dibosons at the LHC?’ *JHEP* 10, p. 182, 2015. arXiv:1507.00013.
- [7] J. Brehmer et al.: ‘The Diboson Excess: Experimental Situation and Classification of Explanations; A Les Houches Pre-Proceeding’, 2015. arXiv:1512.04357.
- [8] G. Brooijmans et al.: ‘Les Houches 2015: Physics at TeV colliders - new physics working group report’, 2016. arXiv:1605.02684.
- [9] P. W. Higgs: ‘Broken symmetries, massless particles and gauge fields’. *Phys. Lett.* 12, p. 132, 1964.
- [10] P. W. Higgs: ‘Broken Symmetries and the Masses of Gauge Bosons’. *Phys. Rev. Lett.* 13, p. 508, 1964.
- [11] F. Englert and R. Brout: ‘Broken Symmetry and the Mass of Gauge Vector Mesons’. *Phys. Rev. Lett.* 13, p. 321, 1964.
- [12] G. S. Guralnik, C. R. Hagen, and T. W. B. Kibble: ‘Global Conservation Laws and Massless Particles’. *Phys. Rev. Lett.* 13, p. 585, 1964.

References

- [13] P. W. Higgs: ‘Spontaneous Symmetry Breakdown without Massless Bosons’. *Phys. Rev.* **145**, p. 1156, 1966.
- [14] S. L. Glashow: ‘Partial Symmetries of Weak Interactions’. *Nucl. Phys.* **22**, p. 579, 1961.
- [15] S. Weinberg: ‘A Model of Leptons’. *Phys. Rev. Lett.* **19**, p. 1264, 1967.
- [16] A. Salam: ‘Weak and Electromagnetic Interactions’. *Conf. Proc. C680519*, p. 367, 1968.
- [17] G. Aad et al. (ATLAS): ‘Observation of a new particle in the search for the Standard Model Higgs boson with the ATLAS detector at the LHC’. *Phys. Lett. B716*, p. 1, 2012. arXiv:1207.7214.
- [18] S. Chatrchyan et al. (CMS): ‘Observation of a new boson at a mass of 125 GeV with the CMS experiment at the LHC’. *Phys. Lett. B716*, p. 30, 2012. arXiv:1207.7235.
- [19] S. R. Coleman, J. Wess, and B. Zumino: ‘Structure of phenomenological Lagrangians. 1.’ *Phys. Rev.* **177**, p. 2239, 1969.
- [20] C. G. Callan, Jr., S. R. Coleman, J. Wess, and B. Zumino: ‘Structure of phenomenological Lagrangians. 2.’ *Phys. Rev.* **177**, p. 2247, 1969.
- [21] S. Weinberg: ‘Effective Gauge Theories’. *Phys. Lett. B91*, p. 51, 1980.
- [22] C. J. C. Burges and H. J. Schnitzer: ‘Virtual Effects of Excited Quarks as Probes of a Possible New Hadronic Mass Scale’. *Nucl. Phys. B228*, p. 464, 1983.
- [23] C. N. Leung, S. T. Love, and S. Rao: ‘Low-Energy Manifestations of a New Interaction Scale: Operator Analysis’. *Z. Phys. C31*, p. 433, 1986.
- [24] W. Buchmuller and D. Wyler: ‘Effective Lagrangian Analysis of New Interactions and Flavor Conservation’. *Nucl. Phys. B268*, p. 621, 1986.
- [25] T. Corbett, O. J. P. Eboli, J. Gonzalez-Fraile, and M. C. Gonzalez-Garcia: ‘Robust Determination of the Higgs Couplings: Power to the Data’. *Phys. Rev. D87*, p. 015022, 2013. arXiv:1211.4580.
- [26] T. Corbett, O. J. P. Eboli, D. Goncalves, J. Gonzalez-Fraile, T. Plehn, and M. Rauch: ‘The Higgs Legacy of the LHC Run I’. *JHEP* **08**, p. 156, 2015. arXiv:1505.05516.
- [27] A. Butter, O. J. P. Éboli, J. Gonzalez-Fraile, M. C. Gonzalez-Garcia, T. Plehn, and M. Rauch: ‘The Gauge-Higgs Legacy of the LHC Run I’. *JHEP* **07**, p. 152, 2016. arXiv:1604.03105.
- [28] K. Cranmer, J. Pavez, and G. Louppe: ‘Approximating Likelihood Ratios with Calibrated Discriminative Classifiers’, 2015. arXiv:1506.02169.
- [29] G. Louppe, M. Kagan, and K. Cranmer: ‘Learning to Pivot with Adversarial Networks’, 2016. arXiv:1611.01046.
- [30] G. Louppe, K. Cranmer, and J. Pavez: ‘carl: a likelihood-free inference toolbox’. *J. Open Source Softw.*, 2016.

- [31] K. Cranmer and G. Louppe: ‘Unifying generative models and exact likelihood-free inference with conditional bijections’. *J. Brief Ideas* , 2016.
- [32] P. Baldi, K. Cranmer, T. Faucett, P. Sadowski, and D. Whiteson: ‘Parameterized neural networks for high-energy physics’. *Eur. Phys. J. C*76 (5), p. 235, 2016. arXiv:1601.07913.
- [33] J. Brehmer, J. Albrecht, and P. Seyfert (LHCb): ‘Ghost Probability: An Efficient Tool to Remove Background Tracks’, 2012. Internal note LHCb-INT-2012-025.
- [34] J. Cogan, M. Kagan, E. Strauss, and A. Schwartzman: ‘Jet-Images: Computer Vision Inspired Techniques for Jet Tagging’ *JHEP* 02, p. 118, 2015. arXiv:1407.5675.
- [35] P. Baldi, P. Sadowski, and D. Whiteson: ‘Enhanced Higgs Boson to $\tau^+ \tau^-$ Search with Deep Learning’. *Phys. Rev. Lett.* 114 (11), p. 111801, 2015. arXiv:1410.3469.
- [36] L. de Oliveira, M. Kagan, L. Mackey, B. Nachman, and A. Schwartzman: ‘Jet-images - deep learning edition’. *JHEP* 07, p. 069, 2016. arXiv:1511.05190.
- [37] L. G. Almeida, M. Backovic, M. Cliche, S. J. Lee, and M. Perelstein: ‘Playing Tag with ANN: Boosted Top Identification with Pattern Recognition’. *JHEP* 07, p. 086, 2015. arXiv:1501.05968.
- [38] P. Baldi, K. Bauer, C. Eng, P. Sadowski, and D. Whiteson: ‘Jet Substructure Classification in High-Energy Physics with Deep Neural Networks’. *Phys. Rev. D*93 (9), p. 094034, 2016. arXiv:1603.09349.
- [39] D. Guest, J. Collado, P. Baldi, S.-C. Hsu, G. Urban, and D. Whiteson: ‘Jet Flavor Classification in High-Energy Physics with Deep Neural Networks’. *Phys. Rev. D*94 (11), p. 112002, 2016. arXiv:1607.08633.
- [40] P. T. Komiske, E. M. Metodiev, and M. D. Schwartz: ‘Deep learning in color: towards automated quark/gluon jet discrimination’. *JHEP* 01, p. 110, 2017. arXiv:1612.01551.
- [41] G. Kasieczka, T. Plehn, M. Russell, and T. Schell: ‘Deep-learning Top Taggers or The End of QCD?’, 2017. arXiv:1701.08784.
- [42] G. Louppe, K. Cho, C. Becot, and K. Cranmer: ‘QCD-Aware Recursive Neural Networks for Jet Physics’, 2017. arXiv:1702.00748.
- [43] P. Baldi, P. Sadowski, and D. Whiteson: ‘Searching for Exotic Particles in High-Energy Physics with Deep Learning’. *Nature Commun.* 5, p. 4308, 2014. arXiv:1402.4735.
- [44] J. Searcy, L. Huang, M.-A. Pleier, and J. Zhu: ‘Determination of the WW polarization fractions in $pp \rightarrow W^\pm W^\pm jj$ using a deep machine learning technique’. *Phys. Rev. D*93 (9), p. 094033, 2016. arXiv:1510.01691.
- [45] R. Santos, J. Webster, S. Ryu, J. Adelman, S. Chekanov, and J. Zhou: ‘Machine learning techniques in searches for $t\bar{t}h$ in the $h \rightarrow b\bar{b}$ decay channel’, 2016. arXiv:1610.03088.
- [46] A. Alves: ‘Stacking machine learning classifiers to identify Higgs bosons at the LHC’, 2016. arXiv:1612.07725.

References

- [47] A. Buckley, A. Shilton, and M. J. White: ‘Fast supersymmetry phenomenology at the Large Hadron Collider using machine learning techniques’, 2012. arXiv:1106.4613.
- [48] N. Bornhauser and M. Drees: ‘Determination of the CMSSM Parameters using Neural Networks’. Phys. Rev. D88, p. 075016, 2013. arXiv:1307.3383.
- [49] P. Bechtle, S. Belkner, D. Dercks, et al.: ‘SCYNet: Testing supersymmetric models at the LHC with neural networks’, 2017. arXiv:1703.01309.
- [50] K. Kondo: ‘Dynamical Likelihood Method for Reconstruction of Events With Missing Momentum. 1: Method and Toy Models’ J. Phys. Soc. Jap. 57, p. 4126, 1988.
- [51] V. M. Abazov et al. (Do): ‘A precision measurement of the mass of the top quark’. Nature 429, p. 638, 2004. arXiv:hep-ex/0406031.
- [52] Y. Gao, A. V. Gritsan, Z. Guo, K. Melnikov, M. Schulze, and N. V. Tran: ‘Spin determination of single-produced resonances at hadron colliders’. Phys. Rev. D81, p. 075022, 2010. arXiv:1001.3396.
- [53] J. Alwall, A. Freitas, and O. Mattelaer: ‘The Matrix Element Method and QCD Radiation’. Phys. Rev. D83, p. 074010, 2011. arXiv:1010.2263.
- [54] P. Avery et al.: ‘Precision studies of the Higgs boson decay channel $H \rightarrow ZZ \rightarrow 4l$ with MEKD’. Phys. Rev. D87 (5), p. 055006, 2013. arXiv:1210.0896.
- [55] J. R. Andersen, C. Englert, and M. Spannowsky: ‘Extracting precise Higgs couplings by using the matrix element method’. Phys. Rev. D87 (1), p. 015019, 2013. arXiv:1211.3011.
- [56] J. M. Campbell, R. K. Ellis, W. T. Giele, and C. Williams: ‘Finding the Higgs boson in decays to $Z\gamma$ using the matrix element method at Next-to-Leading Order’. Phys. Rev. D87 (7), p. 073005, 2013. arXiv:1301.7086.
- [57] P. Artoisenet, P. de Aquino, F. Maltoni, and O. Mattelaer: ‘Unravelling $t\bar{t}h$ via the Matrix Element Method’. Phys. Rev. Lett. 111 (9), p. 091802, 2013. arXiv:1304.6414.
- [58] T. Martini and P. Uwer: ‘Extending the Matrix Element Method beyond the Born approximation: Calculating event weights at next-to-leading order accuracy’. JHEP 09, p. 083, 2015. arXiv:1506.08798.
- [59] A. V. Gritsan, R. Röntsch, M. Schulze, and M. Xiao: ‘Constraining anomalous Higgs boson couplings to the heavy flavor fermions using matrix element techniques’. Phys. Rev. D94 (5), p. 055023, 2016. arXiv:1606.03107.
- [60] D. E. Soper and M. Spannowsky: ‘Finding physics signals with shower deconstruction’. Phys. Rev. D84, p. 074002, 2011. arXiv:1102.3480.
- [61] D. E. Soper and M. Spannowsky: ‘Finding top quarks with shower deconstruction’. Phys. Rev. D87, p. 054012, 2013. arXiv:1211.3140.

- [62] D. E. Soper and M. Spannowsky: ‘Finding physics signals with event deconstruction’. Phys. Rev. D89 (9), p. 094005, 2014. arXiv:1402.1189.
- [63] D. Atwood and A. Soni: ‘Analysis for magnetic moment and electric dipole moment form-factors of the top quark via $e^+ e^- \rightarrow t\bar{t}$ ’. Phys. Rev. D45, p. 2405, 1992.
- [64] M. Davier, L. Duflot, F. Le Diberder, and A. Rouge: ‘The Optimal method for the measurement of tau polarization’. Phys. Lett. B306, p. 411, 1993.
- [65] M. Diehl and O. Nachtmann: ‘Optimal observables for the measurement of three gauge boson couplings in $e^+ e^- \rightarrow W^+ W^-$ ’. Z. Phys. C62, p. 397, 1994.
- [66] B. Efron: ‘Defining the curvature of a statistical problem (with applications to second order efficiency)’. Ann. Statist. 3 (6), p. 1189, 1975.
- [67] S.-I. Amari: ‘Differential geometry of curved exponential families-curvatures and information loss’. Ann. Statist. 10 (2), p. 357, 1982.
- [68] S. Amari and H. Nagaoka: ‘Jōhō Kika No Hōhō’. Fields Institute Communications, American Mathematical Society, 2000, ISBN 9780821805312.
- [69] C. Radhakrishna Rao: ‘Information and the accuracy attainable in the estimation of statistical parameters’. Bull. Calcutta Math. Soc. 37, p. 81, 1945.
- [70] H. Cramér: ‘Mathematical Methods of Statistics’. Princeton University Press, 1946, ISBN 0691080046.
- [71] T. Plehn: ‘Lectures on LHC Physics’. Lect. Notes Phys. 844, p. 1, 2012. arXiv:0910.4182.
- [72] H. Georgi: ‘Effective field theory’. Ann. Rev. Nucl. Part. Sci. 43, p. 209, 1993.
- [73] D. B. Kaplan: ‘Five lectures on effective field theory’, 2005. arXiv:nucl-th/0510023.
- [74] G. Aad et al. (ATLAS, CMS): ‘Measurements of the Higgs boson production and decay rates and constraints on its couplings from a combined ATLAS and CMS analysis of the LHC pp collision data at $\sqrt{s} = 7$ and 8 TeV’. JHEP 08, p. 045, 2016. arXiv:1606.02266.
- [75] R. Kleiss and W. J. Stirling: ‘Tagging the Higgs’. Phys. Lett. B200, p. 193, 1988.
- [76] U. Baur and E. W. N. Glover: ‘Tagging the Higgs boson in $pp \rightarrow W^+ W^- jj$ ’. Phys. Lett. B252, p. 683, 1990.
- [77] V. D. Barger, K.-m. Cheung, T. Han, J. Ohnemus, and D. Zeppenfeld: ‘A Comparative study of the benefits of forward jet tagging in heavy Higgs production at the SSC’. Phys. Rev. D44, p. 1426, 1991.
- [78] D. L. Rainwater, R. Szalapski, and D. Zeppenfeld: ‘Probing color singlet exchange in $Z +$ two jet events at the CERN LHC’. Phys. Rev. D54, p. 6680, 1996. arXiv:hep-ph/9605444.

References

- [79] D. L. Rainwater, D. Zeppenfeld, and K. Hagiwara: ‘Searching for $H \rightarrow \tau^+ \tau^-$ in weak boson fusion at the CERN LHC’. *Phys. Rev.* **D59**, p. 014037, 1998. arXiv:hep-ph/9808468.
- [80] B. E. Cox, J. R. Forshaw, and A. D. Pilkington: ‘Extracting Higgs boson couplings using a jet veto’. *Phys. Lett.* **B696**, p. 87, 2011. arXiv:1006.0986.
- [81] E. Gerwick, T. Plehn, and S. Schumann: ‘Understanding Jet Scaling and Jet Veto in Higgs Searches’. *Phys. Rev. Lett.* **108**, p. 032003, 2012. arXiv:1108.3335.
- [82] O. J. P. Eboli and D. Zeppenfeld: ‘Observing an invisible Higgs boson’. *Phys. Lett.* **B495**, p. 147, 2000. arXiv:hep-ph/0009158.
- [83] T. Plehn, D. L. Rainwater, and D. Zeppenfeld: ‘Determining the structure of Higgs couplings at the LHC’. *Phys. Rev. Lett.* **88**, p. 051801, 2002. arXiv:hep-ph/0105325.
- [84] V. Hankele, G. Klamke, D. Zeppenfeld, and T. Figy: ‘Anomalous Higgs boson couplings in vector boson fusion at the CERN LHC’. *Phys. Rev. D74*, p. 095001, 2006. arXiv:hep-ph/0609075.
- [85] K. Hagiwara, Q. Li, and K. Mawatari: ‘Jet angular correlation in vector-boson fusion processes at hadron colliders’. *JHEP* **07**, p. 101, 2009. arXiv:0905.4314.
- [86] C. Englert, D. Goncalves-Netto, K. Mawatari, and T. Plehn: ‘Higgs Quantum Numbers in Weak Boson Fusion’. *JHEP* **01**, p. 148, 2013. arXiv:1212.0843.
- [87] M. R. Buckley, T. Plehn, and M. J. Ramsey-Musolf: ‘Top squark with mass close to the top quark’. *Phys. Rev.* **D90** (1), p. 014046, 2014. arXiv:1403.2726.
- [88] J. Brehmer, J. Jaeckel, and T. Plehn: ‘Polarized WW Scattering on the Higgs Pole’. *Phys. Rev.* **D90** (5), p. 054023, 2014. arXiv:1404.5951.
- [89] J. Brehmer: ‘Polarised WW Scattering at the LHC’. Master’s thesis, U. Heidelberg, 2014. URL http://www.thphys.uni-heidelberg.de/~plehn/includes/theses/brehmer_m.pdf.
- [90] F. Maltoni, K. Paul, T. Stelzer, and S. Willenbrock: ‘Associated production of Higgs and single top at hadron colliders’. *Phys. Rev.* **D64**, p. 094023, 2001. arXiv:hep-ph/0106293.
- [91] T. Plehn, M. Spira, and P. M. Zerwas: ‘Pair production of neutral Higgs particles in gluon-gluon collisions’. *Nucl. Phys.* **B479**, p. 46, 1996. [Erratum: *Nucl. Phys.* **B531**, p. 655, 1998]. arXiv:hep-ph/9603205.
- [92] U. Baur, T. Plehn, and D. L. Rainwater: ‘Measuring the Higgs boson self coupling at the LHC and finite top mass matrix elements’. *Phys. Rev. Lett.* **89**, p. 151801, 2002. arXiv:hep-ph/0206024.
- [93] X. Li and M. B. Voloshin: ‘Remarks on double Higgs boson production by gluon fusion at threshold’. *Phys. Rev.* **D89** (1), p. 013012, 2014. arXiv:1311.5156.
- [94] H. Murayama: ‘Supersymmetry phenomenology’. In ‘Proceedings, Summer School in Particle Physics, Trieste’, p. 296–335, 2000. arXiv:hep-ph/0002232.

- [95] S. Weinberg: ‘Anthropic Bound on the Cosmological Constant’. *Phys. Rev. Lett.* **59**, p. 2607, 1987.
- [96] J. D. Barrow and F. J. Tipler: ‘The Anthropic Cosmological Principle’. Oxford U. Pr., Oxford, 1988, ISBN 0192821474, 9780192821478.
- [97] V. Agrawal, S. M. Barr, J. F. Donoghue, and D. Seckel: ‘The Anthropic principle and the mass scale of the standard model’. *Phys. Rev. D* **57**, p. 5480, 1998. arXiv:hep-ph/9707380.
- [98] R. Harnik, G. D. Kribs, and G. Perez: ‘A Universe without weak interactions’. *Phys. Rev. D* **74**, p. 035006, 2006. arXiv:hep-ph/0604027.
- [99] L. Clavelli and R. E. White, III: ‘Problems in a weakless universe’, 2006. arXiv:hep-ph/0609050.
- [100] G. F. Giudice: ‘Naturally Speaking: The Naturalness Criterion and Physics at the LHC’, 2008. arXiv:0801.2562.
- [101] J. F. Donoghue, K. Dutta, A. Ross, and M. Tegmark: ‘Likely values of the Higgs vev’. *Phys. Rev. D* **81**, p. 073003, 2010. arXiv:0903.1024.
- [102] O. Gedalia, A. Jenkins, and G. Perez: ‘Why do we observe a weak force? The Hierarchy problem in the multiverse’. *Phys. Rev. D* **83**, p. 115020, 2011. arXiv:1010.2626.
- [103] F. C. Adams: ‘Constraints on Alternate Universes: Stars and habitable planets with different fundamental constants’. *JCAP* **1602** (02), p. 042, 2016. arXiv:1511.06958.
- [104] P. W. Graham, D. E. Kaplan, and S. Rajendran: ‘Cosmological Relaxation of the Electroweak Scale’. *Phys. Rev. Lett.* **115** (22), p. 221801, 2015. arXiv:1504.07551.
- [105] N. Arkani-Hamed, T. Cohen, R. T. D’Agnolo, A. Hook, H. D. Kim, and D. Pinner: ‘Solving the Hierarchy Problem at Reheating with a Large Number of Degrees of Freedom’. *Phys. Rev. Lett.* **117** (25), p. 251801, 2016. arXiv:1607.06821.
- [106] H. P. Nilles: ‘Supersymmetry, Supergravity and Particle Physics’. *Phys. Rept.* **110**, p. 1, 1984.
- [107] H. E. Haber and G. L. Kane: ‘The Search for Supersymmetry: Probing Physics Beyond the Standard Model’. *Phys. Rept.* **117**, p. 75, 1985.
- [108] S. P. Martin: ‘A Supersymmetry primer’, 1997. [Adv. Ser. Direct. High Energy Phys.18,1(1998)]. arXiv:hep-ph/9709356.
- [109] D. B. Kaplan and H. Georgi: ‘ $SU(2) \times U(1)$ Breaking by Vacuum Misalignment’. *Phys. Lett. B* **136**, p. 183, 1984.
- [110] D. B. Kaplan, H. Georgi, and S. Dimopoulos: ‘Composite Higgs Scalars’. *Phys. Lett. B* **136**, p. 187, 1984.
- [111] T. Banks: ‘Constraints on $SU(2) \times U(1)$ breaking by vacuum misalignment’. *Nucl. Phys. B* **243**, p. 125, 1984.

References

- [112] K. Agashe, R. Contino, and A. Pomarol: ‘The Minimal composite Higgs model’. *Nucl. Phys.* **B719**, p. 165, 2005. arXiv:hep-ph/0412089.
- [113] B. Gripaios, A. Pomarol, F. Riva, and J. Serra: ‘Beyond the Minimal Composite Higgs Model’. *JHEP* **04**, p. 070, 2009. arXiv:0902.1483.
- [114] W. A. Bardeen: ‘On naturalness in the standard model’. In ‘Ontake Summer Institute on Particle Physics’, , 1995. URL http://lss.fnal.gov/cgi-bin/find_paper.pl?conf=95-391.
- [115] N. Arkani-Hamed, S. Dimopoulos, and G. R. Dvali: ‘The Hierarchy problem and new dimensions at a millimeter’. *Phys. Lett.* **B429**, p. 263, 1998. arXiv:hep-ph/9803315.
- [116] N. Arkani-Hamed, S. Dimopoulos, and G. R. Dvali: ‘Phenomenology, astrophysics and cosmology of theories with submillimeter dimensions and TeV scale quantum gravity’. *Phys. Rev.* **D59**, p. 086004, 1999. arXiv:hep-ph/9807344.
- [117] L. Randall and R. Sundrum: ‘A Large mass hierarchy from a small extra dimension’. *Phys. Rev. Lett.* **83**, p. 3370, 1999. arXiv:hep-ph/9905221.
- [118] T. Appelquist, H.-C. Cheng, and B. A. Dobrescu: ‘Bounds on universal extra dimensions’. *Phys. Rev.* **D64**, p. 035002, 2001. arXiv:hep-ph/0012100.
- [119] C. D. Froggatt and H. B. Nielsen: ‘Hierarchy of Quark Masses, Cabibbo Angles and CP Violation’. *Nucl. Phys.* **B147**, p. 277, 1979.
- [120] G. Degrassi, S. Di Vita, J. Elias-Miro, et al.: ‘Higgs mass and vacuum stability in the Standard Model at NNLO’. *JHEP* **08**, p. 098, 2012. arXiv:1205.6497.
- [121] A. Eichhorn, H. Gies, J. Jaeckel, T. Plehn, M. M. Scherer, and R. Sondenheimer: ‘The Higgs Mass and the Scale of New Physics’. *JHEP* **04**, p. 022, 2015. arXiv:1501.02812.
- [122] T. Plehn: ‘Dark Matter from a Particle Theorist’s Perspective’, 2017. URL http://www.thphys.uni-heidelberg.de/~plehn/pics/dark_matter.pdf.
- [123] B. Patt and F. Wilczek: ‘Higgs-field portal into hidden sectors’, 2006. arXiv:hep-ph/0605188.
- [124] A. D. Sakharov: ‘Violation of CP Invariance, C Asymmetry, and Baryon Asymmetry of the Universe’. *Pisma Zh. Eksp. Teor. Fiz.* **5**, p. 32, 1967. [*Usp. Fiz. Nauk* **161**, 61(1991)].
- [125] M. Kobayashi and T. Maskawa: ‘CP Violation in the Renormalizable Theory of Weak Interaction’. *Prog. Theor. Phys.* **49**, p. 652, 1973.
- [126] V. A. Kuzmin, V. A. Rubakov, and M. E. Shaposhnikov: ‘On the Anomalous Electroweak Baryon Number Nonconservation in the Early Universe’. *Phys. Lett.* **B155**, p. 36, 1985.
- [127] K. Kajantie, M. Laine, K. Rummukainen, and M. E. Shaposhnikov: ‘Is there a hot electroweak phase transition at $m(H)$ larger or equal to $m(W)$?’. *Phys. Rev. Lett.* **77**, p. 2887, 1996. arXiv:hep-ph/9605288.

- [128] V. A. Rubakov and M. E. Shaposhnikov: ‘Electroweak baryon number nonconservation in the early universe and in high-energy collisions’. *Usp. Fiz. Nauk* 166, p. 493, 1996. [*Phys. Usp.* 39, 461(1996)]. arXiv:hep-ph/9603208.
- [129] L. D. McLerran, M. E. Shaposhnikov, N. Turok, and M. B. Voloshin: ‘Why the baryon asymmetry of the universe is approximately 10^{-10} ’. *Phys. Lett.* B256, p. 451, 1991.
- [130] N. Turok and J. Zadrozny: ‘Electroweak baryogenesis in the two doublet model’. *Nucl. Phys.* B358, p. 471, 1991.
- [131] A. G. Cohen, D. B. Kaplan, and A. E. Nelson: ‘Spontaneous baryogenesis at the weak phase transition’. *Phys. Lett.* B263, p. 86, 1991.
- [132] F. L. Bezrukov and M. Shaposhnikov: ‘The Standard Model Higgs boson as the inflaton’. *Phys. Lett.* B659, p. 703, 2008. arXiv:0710.3755.
- [133] J. Wudka: ‘Electroweak effective Lagrangians’. *Int. J. Mod. Phys.* A9, p. 2301, 1994. arXiv:hep-ph/9406205.
- [134] H. D. Politzer: ‘Power Corrections at Short Distances’. *Nucl. Phys.* B172, p. 349, 1980.
- [135] H. Georgi: ‘On-shell effective field theory’. *Nucl. Phys.* B361, p. 339, 1991.
- [136] C. Arzt: ‘Reduced effective Lagrangians’. *Phys. Lett.* B342, p. 189, 1995. arXiv:hep-ph/9304230.
- [137] H. Simma: ‘Equations of motion for effective Lagrangians and penguins in rare B decays’. *Z. Phys.* C61, p. 67, 1994. arXiv:hep-ph/9307274.
- [138] M. K. Gaillard: ‘Effective One Loop Scalar Actions in (Mostly) Four-Dimensions’. In ‘3rd Jerusalem Winter School for Theoretical Physics: Strings and Superstrings’, , 1986.
- [139] B. Henning, X. Lu, and H. Murayama: ‘How to use the Standard Model effective field theory’. *JHEP* 01, p. 023, 2016. arXiv:1412.1837.
- [140] B. Henning, X. Lu, and H. Murayama: ‘One-loop Matching and Running with Covariant Derivative Expansion’, 2016. arXiv:1604.01019.
- [141] M. Peskin and D. Schroeder: ‘An Introduction to Quantum Field Theory’. Avalon Publishing, 1995, ISBN 9780201503975.
- [142] M. Srednicki: ‘Quantum Field Theory’. Cambridge University Press, 2007, ISBN 9781139462761.
- [143] M. K. Gaillard: ‘The Effective One Loop Lagrangian With Derivative Couplings’. *Nucl. Phys.* B268, p. 669, 1986.
- [144] O. Cheyette: ‘Effective Action for the Standard Model With Large Higgs Mass’. *Nucl. Phys.* B297, p. 183, 1988.

References

- [145] A. Drozd, J. Ellis, J. Quevillon, and T. You: ‘The Universal One-Loop Effective Action’, 2015. arXiv:1512.03003.
- [146] C. Arzt, M. B. Einhorn, and J. Wudka: ‘Patterns of deviation from the standard model’. Nucl. Phys. B433, p. 41, 1995. arXiv:hep-ph/9405214.
- [147] B. Grzadkowski, M. Iskrzynski, M. Misiak, and J. Rosiek: ‘Dimension-Six Terms in the Standard Model Lagrangian’. JHEP 10, p. 085, 2010. arXiv:1008.4884.
- [148] B. Henning, X. Lu, T. Melia, and H. Murayama: ‘2, 84, 30, 993, 560, 15456, 11962, 261485, ...: Higher dimension operators in the SM EFT’, 2015. arXiv:1512.03433.
- [149] G. F. Giudice, C. Grojean, A. Pomarol, and R. Rattazzi: ‘The Strongly-Interacting Light Higgs’. JHEP 06, p. 045, 2007. arXiv:hep-ph/0703164.
- [150] R. Contino, M. Ghezzi, C. Grojean, M. Muhlleitner, and M. Spira: ‘Effective Lagrangian for a light Higgs-like scalar’. JHEP 07, p. 035, 2013. arXiv:1303.3876.
- [151] K. Hagiwara, S. Ishihara, R. Szalapski, and D. Zeppenfeld: ‘Low-energy effects of new interactions in the electroweak boson sector’. Phys. Rev. D48, p. 2182, 1993.
- [152] A. Falkowski, B. Fuks, K. Mawatari, K. Mimasu, F. Riva, and V. sanz: ‘Rosetta: an operator basis translator for Standard Model effective field theory’. Eur. Phys. J. C75 (12), p. 583, 2015. arXiv:1508.05895.
- [153] J. Gonzalez-Fraile: ‘On the origin of masses at the LHC’. Ph.D. thesis, Universitat de Barcelona, 2014.
- [154] T. Corbett: ‘Effective Lagrangians for Higgs Physics’. Ph.D. thesis, Stony Brook University, 2015.
- [155] T. Corbett, O. J. P. Eboli, D. Goncalves, J. Gonzalez-Fraile, T. Plehn, and M. Rauch: ‘The Non-Linear Higgs Legacy of the LHC Run I’, 2015. arXiv:1511.08188.
- [156] M. Bauer, A. Butter, J. Gonzalez-Fraile, T. Plehn, and M. Rauch: ‘Learning from the New Higgs-like Scalar before It Vanishes’, 2016. arXiv:1607.04562.
- [157] M. B. Gavela, J. Gonzalez-Fraile, M. C. Gonzalez-Garcia, L. Merlo, S. Rigolin, and J. Yepes: ‘CP violation with a dynamical Higgs’. JHEP 10, p. 044, 2014. arXiv:1406.6367.
- [158] E. E. Jenkins, A. V. Manohar, and M. Trott: ‘Renormalization Group Evolution of the Standard Model Dimension Six Operators I: Formalism and lambda Dependence’. JHEP 10, p. 087, 2013. arXiv:1308.2627.
- [159] E. E. Jenkins, A. V. Manohar, and M. Trott: ‘Renormalization Group Evolution of the Standard Model Dimension Six Operators II: Yukawa Dependence’. JHEP 01, p. 035, 2014. arXiv:1310.4838.
- [160] R. Alonso, E. E. Jenkins, A. V. Manohar, and M. Trott: ‘Renormalization Group Evolution of the Standard Model Dimension Six Operators III: Gauge Coupling Dependence and Phenomenology’. JHEP 04, p. 159, 2014. arXiv:1312.2014.

- [161] T. Appelquist and C. W. Bernard: ‘Strongly Interacting Higgs Bosons’. Phys. Rev. D22, p. 200, 1980.
- [162] A. C. Longhitano: ‘Heavy Higgs Bosons in the Weinberg-Salam Model’. Phys. Rev. D22, p. 1166, 1980.
- [163] T. Appelquist, M. J. Bowick, E. Cohler, and A. I. Hauser: ‘The Breaking of Isospin Symmetry in Theories With a Dynamical Higgs Mechanism’. Phys. Rev. D31, p. 1676, 1985.
- [164] B. Grinstein and M. Trott: ‘A Higgs-Higgs bound state due to new physics at a TeV’. Phys. Rev. D76, p. 073002, 2007. arXiv:0704.1505.
- [165] R. Alonso, M. B. Gavela, L. Merlo, S. Rigolin, and J. Yepes: ‘The Effective Chiral Lagrangian for a Light Dynamical “Higgs Particle”’. Phys. Lett. B722, p. 330, 2013. [Erratum: Phys. Lett. B726, p. 926, 2013]. arXiv:1212.3305.
- [166] G. Buchalla, O. Catà, and C. Krause: ‘Complete Electroweak Chiral Lagrangian with a Light Higgs at NLO’. Nucl. Phys. B880, p. 552, 2014. [Erratum: Nucl. Phys. B913, p. 475, 2016]. arXiv:1307.5017.
- [167] G. Buchalla, O. Catà, and C. Krause: ‘On the Power Counting in Effective Field Theories’. Phys. Lett. B731, p. 80, 2014. arXiv:1312.5624.
- [168] I. Brivio, T. Corbett, O. J. P. Éboli, et al.: ‘Disentangling a dynamical Higgs’. JHEP 03, p. 024, 2014. arXiv:1311.1823.
- [169] G. Buchalla, O. Catà, A. Celis, and C. Krause: ‘Note on Anomalous Higgs-Boson Couplings in Effective Field Theory’. Phys. Lett. B750, p. 298, 2015. arXiv:1504.01707.
- [170] I. Brivio, J. Gonzalez-Fraile, M. C. Gonzalez-Garcia, and L. Merlo: ‘The complete HEFT Lagrangian after the LHC Run I’. Eur. Phys. J. C76 (7), p. 416, 2016. arXiv:1604.06801.
- [171] S. Scherer: ‘Introduction to chiral perturbation theory’. Adv. Nucl. Phys. 27, p. 277, 2003. arXiv:hep-ph/0210398.
- [172] A. N. Hiller Blin: ‘Electromagnetic interactions of light hadrons in covariant chiral perturbation theory’. Ph.D. thesis, Valencia U., IFIC, 2016. URL <http://roderic.uv.es/bitstream/handle/10550/56957/Tesis.pdf>.
- [173] B. M. Gavela, E. E. Jenkins, A. V. Manohar, and L. Merlo: ‘Analysis of General Power Counting Rules in Effective Field Theory’. Eur. Phys. J. C76 (9), p. 485, 2016. arXiv:1601.07551.
- [174] C. G. Krause: ‘Higgs Effective Field Theories - Systematics and Applications’. Ph.D. thesis, Munich U., 2016. arXiv:1610.08537.
- [175] A. David, A. Denner, M. Duehrssen, et al. (LHC Higgs Cross Section Working Group): ‘LHC HXSWG interim recommendations to explore the coupling structure of a Higgs-like particle’, 2012. arXiv:1209.0040.
- [176] R. Lafaye, T. Plehn, M. Rauch, D. Zerwas, and M. Duhrssen: ‘Measuring the Higgs Sector’. JHEP 08, p. 009, 2009. arXiv:0904.3866.

References

- [177] G. Passarino: ‘NLO Inspired Effective Lagrangians for Higgs Physics’. *Nucl. Phys.* B868, p. 416, 2013. arXiv:1209.5538.
- [178] D. López-Val, T. Plehn, and M. Rauch: ‘Measuring extended Higgs sectors as a consistent free couplings model’. *JHEP* 10, p. 134, 2013. arXiv:1308.1979.
- [179] G. Isidori and M. Trott: ‘Higgs form factors in Associated Production’. *JHEP* 02, p. 082, 2014. arXiv:1307.4051.
- [180] M. Bordone, A. Greljo, G. Isidori, D. Marzocca, and A. Patti: ‘Higgs Pseudo Observables and Radiative Corrections’. *Eur. Phys. J.* C75 (8), p. 385, 2015. arXiv:1507.02555.
- [181] A. Greljo, G. Isidori, J. M. Lindert, and D. Marzocca: ‘Pseudo-observables in electroweak Higgs production’. *Eur. Phys. J.* C76 (3), p. 158, 2016. arXiv:1512.06135.
- [182] M. J. Dolan, J. L. Hewett, M. Krämer, and T. G. Rizzo: ‘Simplified Models for Higgs Physics: Singlet Scalar and Vector-like Quark Phenomenology’. *JHEP* 07, p. 039, 2016. arXiv:1601.07208.
- [183] B. Gripaios and D. Sutherland: ‘An operator basis for the Standard Model with an added scalar singlet’. *JHEP* 08, p. 103, 2016. arXiv:1604.07365.
- [184] L. Berthier and M. Trott: ‘Consistent constraints on the Standard Model Effective Field Theory’. *JHEP* 02, p. 069, 2016. arXiv:1508.05060.
- [185] A. Biekötter, A. Knochel, M. Krämer, D. Liu, and F. Riva: ‘Vices and virtues of Higgs effective field theories at large energy’. *Phys. Rev.* D91, p. 055029, 2015. arXiv:1406.7320.
- [186] C. Arnesen, I. Z. Rothstein, and J. Zupan: ‘Smoking Guns for On-Shell New Physics at the LHC’. *Phys. Rev. Lett.* 103, p. 151801, 2009. arXiv:0809.1429.
- [187] C. Englert and M. Spannowsky: ‘Effective Theories and Measurements at Colliders’. *Phys. Lett.* B740, p. 8, 2015. arXiv:1408.5147.
- [188] M. de Vries: ‘Four-quark effective operators at hadron colliders’. *JHEP* 03, p. 095, 2015. arXiv:1409.4657.
- [189] N. Craig, M. Farina, M. McCullough, and M. Perelstein: ‘Precision Higgsstrahlung as a Probe of New Physics’. *JHEP* 03, p. 146, 2015. arXiv:1411.0676.
- [190] S. Dawson, I. M. Lewis, and M. Zeng: ‘Usefulness of effective field theory for boosted Higgs production’. *Phys. Rev.* D91, p. 074012, 2015. arXiv:1501.04103.
- [191] R. Edezhath: ‘Dimension-6 Operator Constraints from Boosted VBF Higgs’, 2015. arXiv:1501.00992.
- [192] M. Gorbahn, J. M. No, and V. Sanz: ‘Benchmarks for Higgs Effective Theory: Extended Higgs Sectors’. *JHEP* 10, p. 036, 2015. arXiv:1502.07352.
- [193] L. Edelhäuser, A. Knochel, and T. Steeger: ‘Applying EFT to Higgs Pair Production in Universal Extra Dimensions’. *JHEP* 11, p. 062, 2015. arXiv:1503.05078.

- [194] A. Drozd, J. Ellis, J. Quevillon, and T. You: ‘Comparing EFT and Exact One-Loop Analyses of Non-Degenerate Stops’. *JHEP* 06, p. 028, 2015. arXiv:1504.02409.
- [195] C. Englert, R. Kogler, H. Schulz, and M. Spannowsky: ‘Higgs coupling measurements at the LHC’. *Eur. Phys. J.* C76 (7), p. 393, 2016. arXiv:1511.05170.
- [196] R. Contino, A. Falkowski, F. Goertz, C. Grojean, and F. Riva: ‘On the Validity of the Effective Field Theory Approach to SM Precision Tests’. *JHEP* 07, p. 144, 2016. arXiv:1604.06444.
- [197] A. Freitas, D. López-Val, and T. Plehn: ‘When matching matters: Loop effects in Higgs effective theory’. *Phys. Rev.* D94 (9), p. 095007, 2016. arXiv:1607.08251.
- [198] J. Alwall, D. Rainwater, and T. Plehn: ‘Same-Sign Charginos and Majorana Neutralinos at the CERN LHC’. *Phys. Rev.* D76, p. 055006, 2007. arXiv:0706.0536.
- [199] A. Azatov, C. Grojean, A. Paul, and E. Salvioni: ‘Taming the off-shell Higgs boson’. *Zh. Eksp. Teor. Fiz.* 147, p. 410, 2015. [*J. Exp. Theor. Phys.* 120, p. 354, 2015]. arXiv:1406.6338.
- [200] M. Buschmann, D. Goncalves, S. Kuttimalai, M. Schonherr, F. Krauss, and T. Plehn: ‘Mass Effects in the Higgs-Gluon Coupling: Boosted vs Off-Shell Production’. *JHEP* 02, p. 038, 2015. arXiv:1410.5806.
- [201] A. Azatov, C. Grojean, A. Paul, and E. Salvioni: ‘Resolving gluon fusion loops at current and future hadron colliders’. *JHEP* 09, p. 123, 2016. arXiv:1608.00977.
- [202] I. M. Shoemaker and L. Vecchi: ‘Unitarity and Monojet Bounds on Models for DAMA, CoGeNT, and CRESST-II’. *Phys. Rev.* D86, p. 015023, 2012. arXiv:1112.5457.
- [203] G. Busoni, A. De Simone, E. Morgante, and A. Riotto: ‘On the Validity of the Effective Field Theory for Dark Matter Searches at the LHC’. *Phys. Lett.* B728, p. 412, 2014. arXiv:1307.2253.
- [204] O. Buchmueller, M. J. Dolan, and C. McCabe: ‘Beyond Effective Field Theory for Dark Matter Searches at the LHC’. *JHEP* 01, p. 025, 2014. arXiv:1308.6799.
- [205] G. Busoni, A. De Simone, J. Gramling, E. Morgante, and A. Riotto: ‘On the Validity of the Effective Field Theory for Dark Matter Searches at the LHC, Part II: Complete Analysis for the s -channel’. *JCAP* 1406, p. 060, 2014. arXiv:1402.1275.
- [206] D. Racco, A. Wulzer, and F. Zwirner: ‘Robust collider limits on heavy-mediator Dark Matter’. *JHEP* 05, p. 009, 2015. arXiv:1502.04701.
- [207] M. Bauer, A. Butter, N. Desai, J. Gonzalez-Fraile, and T. Plehn: ‘On the Validity of Dark Matter Effective Theory’, 2016. arXiv:1611.09908.
- [208] J. M. Cornwall, D. N. Levin, and G. Tiktopoulos: ‘Derivation of Gauge Invariance from High-Energy Unitarity Bounds on the s Matrix’. *Phys. Rev.* D10, p. 1145, 1974. [Erratum: *Phys. Rev.* D11, p. 972, 1975].

References

- [209] J. M. Cornwall, D. N. Levin, and G. Tiktopoulos: ‘Uniqueness of spontaneously broken gauge theories’. *Phys. Rev. Lett.* **30**, p. 1268, 1973. [Erratum: *Phys. Rev. Lett.* **31**, p. 572, 1973].
- [210] C. H. Llewellyn Smith: ‘High-Energy Behavior and Gauge Symmetry’. *Phys. Lett.* **B46**, p. 233, 1973.
- [211] H. A. Weldon: ‘Constraints on scalar masses implied spontaneous symmetry breaking’. *Phys. Lett.* **B146**, p. 59, 1984.
- [212] H. A. Weldon: ‘The Effects of Multiple Higgs Bosons on Tree Unitarity’. *Phys. Rev. D30*, p. 1547, 1984.
- [213] J. F. Gunion, H. E. Haber, and J. Wudka: ‘Sum rules for Higgs bosons’. *Phys. Rev. D43*, p. 904, 1991.
- [214] T. Corbett, O. J. P. Éboli, and M. C. Gonzalez-Garcia: ‘Inverse amplitude method for the perturbative electroweak symmetry breaking sector: The singlet Higgs portal as a study case’. *Phys. Rev. D93* (1), p. 015005, 2016. arXiv:1509.01585.
- [215] T. Han, D. Krohn, L.-T. Wang, and W. Zhu: ‘New Physics Signals in Longitudinal Gauge Boson Scattering at the LHC’. *JHEP* **03**, p. 082, 2010. arXiv:0911.3656.
- [216] M. Gillioz, R. Grober, C. Grojean, M. Muhlleitner, and E. Salvioni: ‘Higgs Low-Energy Theorem (and its corrections) in Composite Models’. *JHEP* **10**, p. 004, 2012. arXiv:1206.7120.
- [217] S. Dawson, E. Furlan, and I. Lewis: ‘Unravelling an extended quark sector through multiple Higgs production?’ *Phys. Rev. D87* (1), p. 014007, 2013. arXiv:1210.6663.
- [218] J. Alwall, R. Frederix, S. Frixione, et al.: ‘The automated computation of tree-level and next-to-leading order differential cross sections, and their matching to parton shower simulations’. *JHEP* **07**, p. 079, 2014. arXiv:1405.0301.
- [219] A. Alloul, N. D. Christensen, C. Degrande, C. Duhr, and B. Fuks: ‘FeynRules 2.0 - A complete toolbox for tree-level phenomenology’. *Comput. Phys. Commun.* **185**, p. 2250, 2014. arXiv:1310.1921, URL <https://feynrules.irmp.ucl.ac.be/wiki/ModelDatabaseMainPage>.
- [220] C. Degrande, C. Duhr, B. Fuks, D. Grellscheid, O. Mattelaer, and T. Reiter: ‘UFO - The Universal FeynRules Output’. *Comput. Phys. Commun.* **183**, p. 1201, 2012. arXiv:1108.2040.
- [221] A. Alloul, B. Fuks, and V. Sanz: ‘Phenomenology of the Higgs Effective Lagrangian via FEYN-RULES’. *JHEP* **04**, p. 110, 2014. arXiv:1310.5150.
- [222] A. Djouadi: ‘The Anatomy of electro-weak symmetry breaking. I: The Higgs boson in the standard model’. *Phys. Rept.* **457**, p. 1, 2008. arXiv:hep-ph/0503172.
- [223] B. Hespel and E. Vryonidou: ‘Higgs pair production’. URL <https://cp3.irmp.ucl.ac.be/projects/madgraph/wiki/HiggsPairProduction>.
- [224] B. Hespel, D. Lopez-Val, and E. Vryonidou: ‘Higgs pair production via gluon fusion in the Two-Higgs-Doublet Model’. *JHEP* **09**, p. 124, 2014. arXiv:1407.0281.

- [225] T. Hahn: ‘Generating Feynman diagrams and amplitudes with FeynArts 3’. *Comput. Phys. Commun.* **140**, p. 418, 2001. arXiv:hep-ph/0012260.
- [226] T. Hahn and M. Perez-Victoria: ‘Automatized one loop calculations in four-dimensions and D-dimensions’. *Comput. Phys. Commun.* **118**, p. 153, 1999. arXiv:hep-ph/9807565.
- [227] J. Pumplin, D. R. Stump, J. Huston, H. L. Lai, P. M. Nadolsky, and W. K. Tung: ‘New generation of parton distributions with uncertainties from global QCD analysis’. *JHEP* **07**, p. 012, 2002. arXiv:hep-ph/0201195.
- [228] G. Aad et al. (ATLAS, CMS): ‘Combined Measurement of the Higgs Boson Mass in $p\bar{p}$ Collisions at $\sqrt{s} = 7$ and 8 TeV with the ATLAS and CMS Experiments’. *Phys. Rev. Lett.* **114**, p. 191803, 2015. arXiv:1503.07589.
- [229] Tevatron Electroweak Working Group (CDF, Do): ‘Combination of CDF and Do results on the mass of the top quark using up to 9.7 fb^{-1} at the Tevatron’, 2014. arXiv:1407.2682.
- [230] G. Aad et al. (ATLAS, CDF, CMS, Do): ‘First combination of Tevatron and LHC measurements of the top-quark mass’, 2014. arXiv:1403.4427.
- [231] A. Djouadi, J. Kalinowski, and M. Spira: ‘HDECAY: A Program for Higgs boson decays in the standard model and its supersymmetric extension’. *Comput. Phys. Commun.* **108**, p. 56, 1998. arXiv:hep-ph/9704448.
- [232] V. Silveira and A. Zee: ‘Scalar phantoms’. *Phys. Lett.* **B161**, p. 136, 1985.
- [233] R. M. Schabinger and J. D. Wells: ‘A Minimal spontaneously broken hidden sector and its impact on Higgs boson physics at the large hadron collider’. *Phys. Rev. D* **72**, p. 093007, 2005. arXiv:hep-ph/0509209.
- [234] G. M. Pruna and T. Robens: ‘Higgs singlet extension parameter space in the light of the LHC discovery’. *Phys. Rev. D* **88** (11), p. 115012, 2013. arXiv:1303.1150.
- [235] D. López-Val and T. Robens: ‘ Δr and the W-boson mass in the singlet extension of the standard model’. *Phys. Rev. D* **90**, p. 114018, 2014. arXiv:1406.1043.
- [236] T. Robens and T. Stefaniak: ‘Status of the Higgs Singlet Extension of the Standard Model after LHC Run 1’. *Eur. Phys. J. C* **75**, p. 104, 2015. arXiv:1501.02234.
- [237] T. Robens and T. Stefaniak: ‘LHC Benchmark Scenarios for the Real Higgs Singlet Extension of the Standard Model’. *Eur. Phys. J. C* **76** (5), p. 268, 2016. arXiv:1601.07880.
- [238] J. F. Gunion and H. E. Haber: ‘The CP conserving two Higgs doublet model: The Approach to the decoupling limit’. *Phys. Rev. D* **67**, p. 075019, 2003. arXiv:hep-ph/0207010.
- [239] N. Craig, J. Galloway, and S. Thomas: ‘Searching for Signs of the Second Higgs Doublet’, 2013. arXiv:1305.2424.

References

- [240] M. Carena, I. Low, N. R. Shah, and C. E. M. Wagner: ‘Impersonating the Standard Model Higgs Boson: Alignment without Decoupling’. *JHEP* 04, p. 015, 2014. arXiv:1310.2248.
- [241] A. Delgado, G. Nardini, and M. Quiros: ‘A Light Supersymmetric Higgs Sector Hidden by a Standard Model-like Higgs’. *JHEP* 07, p. 054, 2013. arXiv:1303.0800.
- [242] J. F. Gunion, H. E. Haber, G. L. Kane, and S. Dawson: ‘The Higgs Hunter’s Guide’. *Front. Phys.* 80, p. 1, 2000.
- [243] G. C. Branco, P. M. Ferreira, L. Lavoura, M. N. Rebelo, M. Sher, and J. P. Silva: ‘Theory and phenomenology of two-Higgs-doublet models’. *Phys. Rept.* 516, p. 1, 2012. arXiv:1106.0034.
- [244] S. L. Glashow and S. Weinberg: ‘Natural Conservation Laws for Neutral Currents’. *Phys. Rev.* D15, p. 1958, 1977.
- [245] H. E. Haber, M. J. Herrero, H. E. Logan, S. Penaranda, S. Rigolin, and D. Temes: ‘SUSY QCD corrections to the MSSM ho $b\bar{b}$ vertex in the decoupling limit’. *Phys. Rev.* D63, p. 055004, 2001. arXiv:hep-ph/0007006.
- [246] S. Davidson and H. E. Haber: ‘Basis-independent methods for the two-Higgs-doublet model’. *Phys. Rev.* D72, p. 035004, 2005. [Erratum: *Phys. Rev.* D72, p. 099902, 2005]. arXiv:hep-ph/0504050.
- [247] D. Eriksson, J. Rathsman, and O. Stal: ‘2HDMC: Two-Higgs-Doublet Model Calculator Physics and Manual’. *Comput. Phys. Commun.* 181, p. 189, 2010. arXiv:0902.0851.
- [248] P. Bechtle, O. Brein, S. Heinemeyer, G. Weiglein, and K. E. Williams: ‘HiggsBounds: Confronting Arbitrary Higgs Sectors with Exclusion Bounds from LEP and the Tevatron’. *Comput. Phys. Commun.* 181, p. 138, 2010. arXiv:0811.4169.
- [249] P. Bechtle, O. Brein, S. Heinemeyer, G. Weiglein, and K. E. Williams: ‘HiggsBounds 2.0.0: Confronting Neutral and Charged Higgs Sector Predictions with Exclusion Bounds from LEP and the Tevatron’. *Comput. Phys. Commun.* 182, p. 2605, 2011. arXiv:1102.1898.
- [250] F. Mahmoudi: ‘SuperIso v2.3: A Program for calculating flavor physics observables in Supersymmetry’. *Comput. Phys. Commun.* 180, p. 1579, 2009. arXiv:0808.3144.
- [251] P. Bechtle, S. Heinemeyer, O. Stål, T. Stefaniak, and G. Weiglein: ‘HiggsSignals: Confronting arbitrary Higgs sectors with measurements at the Tevatron and the LHC’. *Eur. Phys. J. C*74 (2), p. 2711, 2014. arXiv:1305.1933.
- [252] M. Carena, S. Heinemeyer, O. Stål, C. E. M. Wagner, and G. Weiglein: ‘MSSM Higgs Boson Searches at the LHC: Benchmark Scenarios after the Discovery of a Higgs-like Particle’. *Eur. Phys. J. C*73 (9), p. 2552, 2013. arXiv:1302.7033.
- [253] P. M. Ferreira, J. F. Gunion, H. E. Haber, and R. Santos: ‘Probing wrong-sign Yukawa couplings at the LHC and a future linear collider’. *Phys. Rev.* D89 (11), p. 115003, 2014. arXiv:1403.4736.

- [254] M. Buschmann, C. Englert, D. Goncalves, T. Plehn, and M. Spannowsky: ‘Resolving the Higgs-Gluon Coupling with Jets’. *Phys. Rev.* D90 (1), p. 013010, 2014. arXiv:1405.7651.
- [255] U. Baur, T. Plehn, and D. L. Rainwater: ‘Probing the Higgs selfcoupling at hadron colliders using rare decays’. *Phys. Rev.* D69, p. 053004, 2004. arXiv:hep-ph/0310056.
- [256] J. Baglio, O. Eberhardt, U. Nierste, and M. Wiebusch: ‘Benchmarks for Higgs Pair Production and Heavy Higgs boson Searches in the Two-Higgs-Doublet Model of Type II’. *Phys. Rev.* D90 (1), p. 015008, 2014. arXiv:1403.1264.
- [257] W. Hollik, T. Plehn, M. Rauch, and H. Rzehak: ‘Supersymmetric Higgs Bosons in Weak Boson Fusion’. *Phys. Rev. Lett.* 102, p. 091802, 2009. arXiv:0804.2676.
- [258] J. Berger, J. Hubisz, and M. Perelstein: ‘A Fermionic Top Partner: Naturalness and the LHC’. *JHEP* 07, p. 016, 2012. arXiv:1205.0013.
- [259] S. Dawson and E. Furlan: ‘A Higgs Conundrum with Vector Fermions’. *Phys. Rev.* D86, p. 015021, 2012. arXiv:1205.4733.
- [260] S. Fajfer, A. Greljo, J. F. Kamenik, and I. Mustac: ‘Light Higgs and Vector-like Quarks without Prejudice’. *JHEP* 07, p. 155, 2013. arXiv:1304.4219.
- [261] S. A. R. Ellis, R. M. Godbole, S. Gopalakrishna, and J. D. Wells: ‘Survey of vector-like fermion extensions of the Standard Model and their phenomenological implications’. *JHEP* 09, p. 130, 2014. arXiv:1404.4398.
- [262] C.-Y. Chen, S. Dawson, and I. M. Lewis: ‘Top Partners and Higgs Boson Production’. *Phys. Rev.* D90 (3), p. 035016, 2014. arXiv:1406.3349.
- [263] I. Low, R. Rattazzi, and A. Vichi: ‘Theoretical Constraints on the Higgs Effective Couplings’. *JHEP* 04, p. 126, 2010. arXiv:0907.5413.
- [264] D. Pappadopulo, A. Thamm, R. Torre, and A. Wulzer: ‘Heavy Vector Triplets: Bridging Theory and Data’. *JHEP* 09, p. 060, 2014. arXiv:1402.4431.
- [265] A. Kaminska: ‘Improving LHC searches for strong EW symmetry breaking resonances’. In ‘Proceedings, 50th Rencontres de Moriond Electroweak Interactions and Unified Theories’, p. 113, 2015. arXiv:1505.04645.
- [266] V. D. Barger, W.-Y. Keung, and E. Ma: ‘Doubling of Weak Gauge Bosons in an Extension of the Standard Model’. *Phys. Rev. Lett.* 44, p. 1169, 1980.
- [267] N. Arkani-Hamed, A. G. Cohen, and H. Georgi: ‘Electroweak symmetry breaking from dimensional deconstruction’. *Phys. Lett.* B513, p. 232, 2001. arXiv:hep-ph/0105239.
- [268] L. Berthier and M. Trott: ‘Towards consistent Electroweak Precision Data constraints in the SMEFT’. *JHEP* 05, p. 024, 2015. arXiv:1502.02570.

References

- [269] O. Bessidskaia Bylund, F. Maltoni, I. Tsirikos, E. Vryonidou, and C. Zhang: ‘Probing top quark neutral couplings in the Standard Model Effective Field Theory at NLO in QCD’. *JHEP* 05, p. 052, 2016. arXiv:1601.08193.
- [270] F. Maltoni, E. Vryonidou, and C. Zhang: ‘Higgs production in association with a top-antitop pair in the Standard Model Effective Field Theory at NLO in QCD’. *JHEP* 10, p. 123, 2016. arXiv:1607.05330.
- [271] L. Berthier and J. T. Nielsen: ‘Statistics of predictions with missing higher order corrections’, 2016. arXiv:1610.01783.
- [272] K. Cranmer: ‘Machine Learning and Likelihood Free Inference in Particle Physics’, 2016. Keynote at the Thirtieth Annual Conference on Neural Information Processing Systems (NIPS). URL <https://nips.cc/Conferences/2016/Schedule?showEvent=6195>.
- [273] G. Aad et al. (ATLAS): ‘A neural network clustering algorithm for the ATLAS silicon pixel detector’. *JINST* 9, p. P09009, 2014. arXiv:1406.7690.
- [274] P. Jaranowski and A. Krolak: ‘Optimal solution to the inverse problem for the gravitational wave signal of a coalescing compact binary’. *Phys. Rev. D* 49, p. 1723, 1994.
- [275] B. M. Schäfer and L. Heisenberg: ‘Weak lensing tomography with orthogonal polynomials’. *Monthly Notices of the Royal Astronomical Society* 423, p. 3445, 2012. arXiv:1107.2213.
- [276] L. Wolz, M. Kilbinger, J. Weller, and T. Giannantonio: ‘On the validity of cosmological Fisher matrix forecasts’. *Journal of Cosmology and Astroparticle Physics* 9, 009, 2012. arXiv:1205.3984.
- [277] T. Bringmann, A. Galea, A. Hryczuk, and C. Weniger: ‘Novel Spectral Features in MeV Gamma Rays from Dark Matter’. *Phys. Rev. D* 95 (4), p. 043002, 2017. arXiv:1610.04613.
- [278] A. M. Sirunyan et al. (CMS): ‘Measurement of the top quark mass in the dileptonic ttbar decay channel using the mass observables Mbl, MT₂, and Mblv in pp collisions at sqrt(s) = 8 TeV’, 2017. arXiv:1704.06142.
- [279] F. Ferreira, S. Fichet, and V. Sanz: ‘On new physics searches with multidimensional differential shapes’, 2017. arXiv:1702.05106.
- [280] T. D. P. Edwards and C. Weniger: ‘A Fresh Approach to Forecasting in Astroparticle Physics and Dark Matter Searches’, 2017. arXiv:1704.05458.
- [281] W. K. Newey and D. McFadden: ‘Large sample estimation and hypothesis testing’. *Handbook of Econometrics* 4, p. 2111 , 1994.
- [282] P. Artoisenet and O. Mattelaer: ‘MadWeight: Automatic event reweighting with matrix elements’. In ‘Proceedings, 2nd International Workshop on Prospects for charged Higgs discovery at colliders (CHARGED 2008)’, volume CHARGED2008, p. 025, 2008.
- [283] O. Mattelaer: ‘A new approach to matrix element re-weighting’. Ph.D. thesis, Louvain U., CP3, 2011. URL <http://hdl.handle.net/2078.1/69114>.

- [284] A. Mertens: ‘The automated Matrix-Element reweighting and its applications at the LHC’. In ‘Proceedings, 15th International Workshop on Advanced Computing and Analysis Techniques in Physics Research (ACAT 2013)’, volume 523, p. 012028, 2014.
- [285] K. Cranmer: ‘Practical Statistics for the LHC’. In ‘Proceedings, 2011 European School of High-Energy Physics (ESHEP 2011)’, p. 267-308, 2015. arXiv:1503.07622.
- [286] T. Han and Y. Li: ‘Genuine CP-odd Observables at the LHC’. Phys. Lett. B683, p. 278, 2010. arXiv:0911.2933.
- [287] N. D. Christensen, T. Han, and Y. Li: ‘Testing CP Violation in ZZH Interactions at the LHC’. Phys. Lett. B693, p. 28, 2010. arXiv:1005.5393.
- [288] G. Aad et al. (ATLAS): ‘A morphing technique for signal modelling in a multidimensional space of coupling parameters’, 2015. Physics note ATL-PHYS-PUB-2015-047. URL <http://cds.cern.ch/record/2066980>.
- [289] T. Plehn, P. Schichtel, and D. Wiegand: ‘Where boosted significances come from’. Phys. Rev. D89 (5), p. 054002, 2014. arXiv:1311.2591.
- [290] F. Kling, T. Plehn, and P. Schichtel: ‘Maximizing the significance in Higgs boson pair analyses’. Phys. Rev. D95 (3), p. 035026, 2017. arXiv:1607.07441.
- [291] K. Cranmer and T. Plehn: ‘Maximum significance at the LHC and Higgs decays to muons’. Eur. Phys. J. C51, p. 415, 2007. arXiv:hep-ph/0605268.
- [292] T. Plehn, D. L. Rainwater, and D. Zeppenfeld: ‘A Method for identifying $H \rightarrow \tau^+ \tau^- \rightarrow e^\pm \mu^\mp p_T$ at the CERN LHC’. Phys. Rev. D61, p. 093005, 2000. arXiv:hep-ph/9911385.
- [293] G. Aad et al. (ATLAS): ‘Evidence for the Higgs-boson Yukawa coupling to tau leptons with the ATLAS detector’. JHEP 04, p. 117, 2015. arXiv:1501.04943.
- [294] G. Klamke and D. Zeppenfeld: ‘Higgs plus two jet production via gluon fusion as a signal at the CERN LHC’. JHEP 04, p. 052, 2007. arXiv:hep-ph/0703202.
- [295] S. Bolognesi, Y. Gao, A. V. Gritsan, et al.: ‘On the spin and parity of a single-produced resonance at the LHC’. Phys. Rev. D86, p. 095031, 2012. arXiv:1208.4018.
- [296] F. Kling, T. Plehn, and M. Takeuchi: ‘Tagging single Tops’. Phys. Rev. D86, p. 094029, 2012. arXiv:1207.4787.
- [297] A. P. Dawid: ‘Further comments on some comments on a paper by Bradley Efron’. Ann. Statist. 5 (6), p. 1249, 1977.
- [298] K. M. Carter, R. Raich, W. G. Finn, and A. O. Hero: ‘FINE: Fisher Information Non-parametric Embedding’, 2008. arXiv:0802.2050.
- [299] G. ’t Hooft and M. J. G. Veltman: ‘Scalar One Loop Integrals’. Nucl. Phys. B153, p. 365, 1979.

References

- [300] A. Denner: ‘Techniques for calculation of electroweak radiative corrections at the one loop level and results for W physics at LEP-200’. *Fortsch. Phys.* **41**, p. 307, 1993. arXiv:0709.1075.
- [301] M. J. G. Veltman: ‘Second Threshold in Weak Interactions’. *Acta Phys. Polon.* **B8**, p. 475, 1977.
- [302] D. Toussaint: ‘Renormalization Effects From Superheavy Higgs Particles’. *Phys. Rev. D* **18**, p. 1626, 1978.
- [303] J. M. Frere and J. A. M. Vermaseren: ‘Radiative Corrections to Masses in the Standard Model With Two Scalar Doublets’. *Z. Phys. C* **19**, p. 63, 1983.
- [304] W. Grimus, L.avoura, O. M. Ogreid, and P. Osland: ‘A Precision constraint on multi-Higgs-doublet models’. *J. Phys. G* **35**, p. 075001, 2008. arXiv:0711.4022.
- [305] W. Hollik: ‘Nonstandard Higgs Bosons in SU(2) X U(1) Radiative Corrections’. *Z. Phys. C* **32**, p. 291, 1986.
- [306] W. Beenakker and W. Hollik: ‘The Width of the Z Boson’. *Z. Phys. C* **40**, p. 141, 1988.
- [307] C. D. Froggatt, R. G. Moorhouse, and I. G. Knowles: ‘Leading radiative corrections in two scalar doublet models’. *Phys. Rev. D* **45**, p. 2471, 1992.
- [308] H.-J. He, N. Polonsky, and S.-f. Su: ‘Extra families, Higgs spectrum and oblique corrections’. *Phys. Rev. D* **64**, p. 053004, 2001. arXiv:hep-ph/0102144.
- [309] W. Grimus, L.avoura, O. M. Ogreid, and P. Osland: ‘The Oblique parameters in multi-Higgs-doublet models’. *Nucl. Phys. B* **801**, p. 81, 2008. arXiv:0802.4353.
- [310] F. del Aguila, J. de Blas, and M. Perez-Victoria: ‘Electroweak Limits on General New Vector Bosons’. *JHEP* **09**, p. 033, 2010. arXiv:1005.3998.
- [311] J. Watkins: ‘Introduction to the Science of Statistics’. URL <http://math.arizona.edu/~jwatkins/statbook.pdf>.
- [312] S. Chatrchyan et al. (CMS): ‘First results on Higgs to gamma gamma at 13 TeV’, 2016. Note CMS-PAS-HIG-15-005.